



HAL
open science

Development of biomimetic systems for the study of molecular motor oscillations

Jonathan Lee Tin Wah

► **To cite this version:**

Jonathan Lee Tin Wah. Development of biomimetic systems for the study of molecular motor oscillations. Agricultural sciences. Université René Descartes - Paris V, 2012. English. NNT: 2012PA05T062 . tel-00798304

HAL Id: tel-00798304

<https://theses.hal.science/tel-00798304>

Submitted on 8 Mar 2013

HAL is a multi-disciplinary open access archive for the deposit and dissemination of scientific research documents, whether they are published or not. The documents may come from teaching and research institutions in France or abroad, or from public or private research centers.

L'archive ouverte pluridisciplinaire **HAL**, est destinée au dépôt et à la diffusion de documents scientifiques de niveau recherche, publiés ou non, émanant des établissements d'enseignement et de recherche français ou étrangers, des laboratoires publics ou privés.

THÈSE DE DOCTORAT DE L'UNIVERSITÉ PARIS V DESCARTES

Spécialité : Biophysique

École doctorale : « Frontières du Vivant »

réalisée

à l'Institut Curie

présentée par

Jonathan LEE TIN WAH

Pour obtenir le grade de

DOCTEUR DE L'UNIVERSITÉ PARIS V DESCARTES

Sujet de la thèse :

**Development of biomimetic systems for the study of
molecular motor oscillations**

soutenue le 28 novembre 2012

devant le jury composé de :

M. Andrea PARMEGGIANI

M. Didier CHATENAY

M. Jean BAUDRY

M. Laurent BLANCHOIN

M. Benoît FORGET

M. Pascal MARTIN

Rapporteur

Rapporteur

Examineur

Examineur

Examineur

Directeur de thèse

Remerciements

Cette thèse fût laborieuse et dure... non seulement à cause de la difficulté inhérente du sujet qui implique des manipulations expérimentales complexes et souvent frustrantes, mais surtout parce que je suis allé à contre-courant de ma formation initiale et en tant que biologiste, étudier des moteurs moléculaires à cette échelle relevait du travail de titan ! J'ai mené la thèse jusqu'à son terme et j'en suis très heureux. Cela rend l'écriture de cette partie « remerciements » d'autant plus compliquée car, en effet, je n'y serais jamais arrivé sans le soutien moral et scientifique des gens qui m'ont entouré et il me semblait donc impératif de rendre hommage à tout le monde comme il se doit ce qui n'est pas chose facile.

Tout d'abord il faut remercier Pascal qui m'a donné l'occasion de faire une thèse aux antipodes de ma formation de base. Nous avons eu nos différends et nos duels épiques mais je pense que nous sommes sortis tous les deux grandis de cette expérience. Puisqu'on en est aux membres d'équipage si je puis dire, je dois aussi remercier Volker qui, de par sa pédagogie, sa patience et son côté « couteau suisse » scientifique, m'a remis le pied à l'étrier dans les moments les plus difficiles. Sans oublier Mathieu, le magicien de l'électronique avec qui on a formé un duo de choc !

Mais je me suis aussi fait des amis en dehors de l'équipe (eh oui je suis très sociable). En tête de file, on retrouve Sabrina, sans doute ma meilleure amie à l'Institut qui, outre son côté maternel me rappelant constamment à l'ordre pour les deadlines administratives, comme remplir ma déclaration d'impôts par exemple, a été d'un soutien moral précieux et d'une loyauté sans faille. Viennent ensuite Fahima ma « tante » du labo, Sandrine « cousine », Philippe, Joël, Matthias, Coco et bien sûr The One and Only Kevin ! Bien entendu, il y a pleins d'autres gens mais tous les mentionner est impossible. J'espère qu'ils sauront me pardonner s'ils lisent un jour ce passage. Complétant le tableau on retrouve mes collègues de bureau, Maeva et Youba. Et là j'en profite pour demander pardon à Maeva parce que partager le bureau de deux garçons aussi subtils que Youba et moi n'a pas été une sinécure pour ses oreilles sensibles.

J'ai également eu l'occasion de travailler et collaborer avec des gens formidables durant thèse. Je pense bien sûr à Ayako, probablement une des personnes les plus professionnelles

que je connaisse – les protocoles qu’elle écrit sont des œuvres d’art de précision. Il ne faut pas non plus oublier François-Damien, FD, mon comparse sur le projet des colonnes magnétiques. Je remercie aussi Evelyne et les gens de l’UMR 144 (avec une petite pensée spéciale pour Priscilla bien sûr) pour le bon accueil qui m’a été fait durant mes manip au bâtiment de la rue Lhomond. J’en profite pour remercier Cécile qui, bien que nous n’ayons pas eu l’opportunité de collaborer directement, a été d’une aide précieuse et d’un grand soutien, de par ses conseils, sa sagesse et son grand sens de l’écoute.

Et maintenant c’est au tour des potes hors-institut ! Honneur aux dames donc, les premiers remerciements iront à V et Cami , avec qui j’ai passé de supers soirées. Merci à V en particulier qui m’a redonné courage durant la période de mon dernier comité de thèse qui a été particulièrement éprouvant et chapeau parce qu’il ne lui aura fallu qu’une seule phrase ! Ensuite les autres, il y en a pleins à commencer par Seb avec qui on aura bien rigolé, A-C, Mamie Agnès, les deux Sabines et pleins d’autres.

Et pour finir, je voudrais remercier ma famille qui m’a toujours soutenu à travers les obstacles et les soucis... plus particulièrement à ma mère qui m’a transmis sa ténacité tenant parfois de l’entêtement mais nous dirons que cela m’a été plutôt utile jusqu’à présent ! Je n’oublie bien entendu pas mes tantes, mes deux grand-mères, mon petit frère et mon père qui ont tous été présents pour moi durant ces années.

En clôture, je remercie les membres du jury pour la soutenance mémorable et pour la discussion enrichissante qui a suivi la présentation.

J’espère n’avoir oublié personne dans cette partie ‘remerciements’ et je souhaite bonne lecture à ceux et celles qui liront ce manuscrit !

Contents

General Introduction

Prologue

| | |
|---|----|
| A/. Introduction to molecular motors | 16 |
| 1) Actin..... | 16 |
| 1.1 Biochemical Properties of Actin | 16 |
| 1.2 Mechanical properties of actin filaments | 19 |
| 2) Myosin | 19 |
| 2.1 Myosin II..... | 20 |
| 2.2 Myosin 1 | 24 |
| B/. Mechanical properties of molecular motors | 26 |
| 1) Experiments on single molecules..... | 26 |
| 1.1 The Three-Bead Geometry..... | 26 |
| 1.2 Two-step force generation by myosins | 29 |
| 1.3 Effects of an external load on myosin activity..... | 30 |
| 1.4 Calcium regulation of myosin 1 activity..... | 33 |
| 1.5 Non-productive attachments | 34 |
| 2) In-vitro Motility Assay | 35 |
| 2.1 General Principle | 35 |
| 2.2 Processivity | 37 |
| C/. Working model for myosin | 40 |

| | |
|--|----|
| 1) The power stroke model..... | 40 |
| 2) A consequence of mechanosensitivity: non-linear stiffness of myosin | 43 |
| D/. Myosin in biological systems | 46 |
| 1) Myosin II in muscles..... | 46 |
| 1.1 Muscle contractions | 46 |
| 1.2 Mechanical properties of muscle fibres : Force-Velocity relation..... | 49 |
| 1.3 Transient response of a muscle fibre to sudden changes in length | 53 |
| 1.4 Partial activation of muscles | 54 |
| 1.5 Stretch activation of muscles | 55 |
| 2) Myosin 1c and the mechanosensitivity of hair cells in the inner ear | 56 |
| 2.1 Mechano-electrical transduction in the inner ear of vertebrates | 56 |
| 2.2 Myosin 1c as an adaptation motor | 57 |
| 2.3 Force-Displacement relation of a hair bundle..... | 59 |
| 3) Spontaneous oscillations of acto-myosin systems | 60 |
| 3.1 Spontaneous oscillations in muscle fibres | 61 |
| 3.2 Spontaneous oscillations of hair cell bundles | 62 |
| 3.3 Summary | 64 |
| E/. An intermediate scale | 66 |
| 1) Evidence for collective motor effects | 66 |
| 2) Theoretical descriptions of collective motor effects and oscillations | 67 |
| 3) Spontaneous motor oscillations in a minimal actomyosin system..... | 68 |

Part I

Part I Chapter I

| | |
|---|----|
| A/. Instrumentation..... | 73 |
| 1) The Optical Tweezers | 74 |
| 1.1 Principle of the Optical Tweezers..... | 74 |
| 1.2 Characteristics of our Optical Tweezers | 77 |
| 2) Acousto-Optic Deflectors | 77 |
| 2.1 Principle of Acousto-Optic Deflectors..... | 77 |
| 2.2 Characteristics of our AODs | 78 |
| 3) The Detection Method | 80 |
| 3.1 Photodiodes..... | 80 |
| 3.2 Calibration..... | 81 |
| 4) Controlling the set-up | 86 |
| 4.1 Moving the laser | 86 |
| 4.2 Moving the stage..... | 86 |
| B/. Biochemical Tools..... | 86 |
| 1) Myosins..... | 87 |
| 1.1 Myosin II..... | 87 |
| 1.2 Myosin 1b | 87 |
| 2) Actin..... | 90 |
| 2.1 Polymerisation | 90 |

| | | |
|-----|---|----|
| 2.2 | Actin bundles | 91 |
| 3) | Functionalization of the beads | 91 |
| 4) | Protein Attachment | 93 |
| 4.1 | Nitrocellulose Surfaces | 93 |
| 4.2 | Antibody-treated Surfaces | 94 |
| 4.3 | Silanized Surfaces | 94 |
| 5) | Additional molecular cocktails | 96 |
| 5.1 | Anti-Bleaching Mixture | 96 |
| 5.2 | ATP regeneration | 97 |
| 6) | Experimental Procedure | 97 |
| 6.1 | Flow Cell Preparation | 97 |
| 6.2 | Molecular Motor Attachment | 98 |
| 6.3 | Incubation of actin and functionalized beads..... | 98 |
| 6.4 | Injection of the experimental solution and starting the experiment..... | 99 |
| 6.5 | Recording the collective effects of the motors..... | 99 |

Part I Chapter II

| | | |
|-----|--|-----|
| A/. | Characterization of the molecular motors | 101 |
| 1) | In-vitro motility assay | 101 |
| 1.1 | Nitrocellulose surfaces | 102 |
| 1.2 | Silane surfaces | 104 |
| 2) | Force generation..... | 104 |

| | |
|--|-----|
| B/. Spontaneous oscillations under elastic loading | 106 |
| 1) With single actin filaments | 107 |
| 2) With polarized actin bundles | 108 |
| C/. Mechanical stimulus : Alternating steps..... | 110 |

Part I Chapter III

| | |
|---|-----|
| A/. Motility Assay | 115 |
| B/. Force exerted by the motors | 116 |
| C/. Spontaneous oscillations and stimulation..... | 116 |

Part II

Part II Introduction

| | |
|--|-----|
| A/. The Need for a New Molecular Force Sensor..... | 119 |
| B/. Auto-Assembled Magnetic Columns | 122 |
| C/. Magnetic columns as force sensors | 123 |

Part II Chapter I

| | |
|---|-----|
| A/. Making the magnetic bead pattern | 125 |
| 1) PDMS substrate fabrication | 125 |
| 1.1 – Making the moulds | 125 |
| 1.2 – PDMS casting | 126 |
| 2) Depositing nucleator beads by capillary assembly | 126 |
| B/. Formation of the columns..... | 129 |
| 1) The Magnetic Beads | 129 |

| | |
|---|-----|
| 2) The Electromagnet | 130 |
| 2.1 Making the Electromagnet | 131 |
| 2.2 Calibration of the Electromagnet | 131 |
| 2.3 – Limits of the Electromagnet | 132 |
| C/. Characterization of the properties of the columns | 133 |
| 1) The Experimental Set-Up | 133 |
| 1.1 – The custom stage | 135 |
| 1.2 – The Cooling System | 137 |
| 1.3 - The detection system | 138 |
| 2) Observation of the columns from the side | 138 |
| 3) Experimental Procedure | 140 |
| 3.1 Procedure with the electromagnet | 140 |
| 3.2 – Procedure with the permanent magnet | 142 |
| 3.3 – Viewing the profile of the columns | 143 |

Part II Chapter II

| | |
|---|-----|
| A/. Mechanical properties of magnetic columns | 145 |
| 1) Stiffness | 145 |
| 1.1 Variation of stiffness along the length of a column | 145 |
| 1.2 Viewing the deformation profile of the columns: | 149 |
| 2) Stiffness as a function of column length | 150 |
| 3) Responsiveness and drag coefficients of the columns. | 152 |

| | |
|--|-----|
| 4) Influence of the external magnetic field on stiffness | 153 |
| B/. Theoretical behaviour of a magnetic column: interactions between magnetic dipoles | 154 |
| 1) Formation of the columns | 154 |
| 2) Rotation of the beads in the magnetic field | 157 |
| 3) Orientation of the individual dipoles in a deflected column | 158 |
| 4) Stiffness of a column | 159 |
| 5) Linearity of the force-displacement relation | 163 |
| 6) Friction on a pivoting column | 165 |
| C/. Towards biological applications | 166 |

Part II Chapter III

| | |
|---|-----|
| A/. Viability of the magnetic bead columns as force sensors | 168 |
| B/. A magnetic column as a biomimetic stereocilium | 169 |
| C/. Control of the height of the columns | 170 |
| D/. Future developments | 171 |

Conclusion

| | |
|--|-----|
| A/. Part I: Molecular motor oscillations under elastic loading | 172 |
| B/. Part II: Auto-assembled magnetic bead columns as force sensors | 173 |

General Introduction

“An oscillation is the repetitive variation over time of a measure around an equilibrium position and two or more different states.” This is the definition one is likely to find in any physics textbook and the most obvious examples one can find are mechanical oscillators. The latter include pendulums, tuning forks and the ever classical spring-mass system. However as any physicist will point out, there exist other types of oscillations such as electrical, optical etc... In biology, the most common type of oscillation is the biochemical oscillation where the concentration of a molecule will vary over time in a cyclic manner, like the circadian oscillator for instance.

Over the years, several studies have demonstrated the ability of biological systems to act as mechanical oscillators as well. Whether this was driven by a chemical oscillation within the living system as one would expect from a biological organism, or due to the intrinsic mechanical properties of the biological system, remained a valid question. Moreover if it was indeed due to the mechanical properties of the biological system, at what scale should one investigate the origin of this oscillatory behaviour?

Most of the biological systems that exhibit mechanical oscillations have molecular motors as one of their characteristic components. Molecular motors are remarkable biological molecules with amazing mechanical properties, making them prime candidates in the investigation of this phenomenon. Molecular motors, however, have been studied extensively in their own right and as a result, we have a fairly well-documented knowledge of their working mechanism. The enormous work that has been done by various teams those last decades has deciphered the biochemical and biomechanical cycle of individual motors and defined the various characteristics of each kind of motor making concepts such as “duty ratio”, “power stroke” and “processivity” common knowledge. Knowing the mechanochemical properties of molecular motors at the single molecule level gives us important information. In complex biological systems, however, motor molecules often work in groups, which can give rise to collective effects that are not easily predicted from single-molecule properties. Understanding biological systems as mechanical oscillators requires investigations at intermediate scales between that of the single motor and that the complete

system (e.g. a muscle fibre) to determine how molecular motors team-up to produce oscillations.

The initial goal of this thesis was to follow-up the work of Pierre-Yves PLACAIS in the investigation of small molecular motor collections under elastic loading. However it evolved during the course of those three years into finding new ways both biochemical and physical to probe the molecular motors, to circumvent the weaknesses of the initial set-up and to mimic naturally occurring biological systems more accurately, more specifically the hair cell bundle which is the research spearhead of our team at the Curie Institute.

The thesis is divided into three main parts. The prologue introduces the molecular motors we have used during the project, namely myosin II and Ib and their substrate, actin. We discuss their implication in the oscillations observed in biological systems, followed by a theoretical approach of the subject. The next two parts deal with our experimental endeavours to develop the new tools and testing them. Part I discusses the biochemical and chemical additions made to an already existing set-up used to demonstrate oscillations in a minimal acto-myosin system. In Part II, we develop a new mechanical sensor for forces exerted at the molecular scale. It is based on self-assembling columns of magnetic beads, which are usually used in micro-fluidic devices for medical diagnosis research. And last but not least, the final part of the thesis summarizes the results and perspectives for future research in the field.

Prologue

Molecular Motors and Oscillations

Molecular motors are fascinating biological nanomachines that can convert chemical energy, in the form of adenosine triphosphate (ATP) into mechanical work. In cells, those motors work conjointly with molecular structures which form part of the cytoskeleton. Those structures consist of three families of filaments, namely microtubules, actin filaments and the lesser known intermediate filaments. As its name implies, the cytoskeleton is responsible for the general architecture of the cell but far from being a static scaffold, it is a highly dynamic structure. Actin filaments and microtubules are constantly assembling and disassembling. The dynamic properties of the cytoskeleton combined with molecular motor activity are involved in many of the mechanical activities of the cell, such as cell motility, mitosis, intracellular transport, etc....Understanding the mechanism behind the force generation capabilities of molecular motors and their interaction with their substrates are essential to investigate their role in the oscillatory behaviour of the biological systems harbouring them.

In this chapter, we review the state of the art on the study of molecular motors and their role in bio-mechanical oscillations while concentrating our efforts on myosins, which we use in our experiments. We start by introducing molecular motors and their substrates and give a description of their main characteristics. Following this, we discuss the emergence of oscillations in naturally occurring biological structures and then delve into some theoretical concepts on the biophysics of individual molecular motors and molecular motor collections. In the final part, we talk about the investigation of the properties of molecular motor collections under elastic loading which lies at an intermediate scale between single molecule experiments and organized biological structures, which was previously done in the lab and upon which this thesis is built. We thus end the chapter by detailing the main objectives of the thesis and how those objectives were met or have evolved over the course of the three years.

A/. Introduction to molecular motors

1) Actin

Actin is the natural substrate of the molecular motor myosin and serves as a molecular ‘highway’ on which the myosin can move. Actin filaments possess some interesting properties of their own due to their dynamic nature and are entirely capable of some mechanical feats in the right conditions. Understanding the biochemistry and the mechanical properties of actin is hence essential in the study of actomyosin interactions.

1.1 Biochemical Properties of Actin

Monomeric actin (G-actin) is a globular protein with a molecular weight of 43 kDa and consisting of 375 amino acids. It is made up of four sub-units, has a nucleotide binding site which can bind ATP or ADP and is also able to bind divalent ions such as calcium and magnesium (Cooke, 1997).

G-actin can spontaneously polymerize to form filaments; in this form, actin is known as F-actin. The G-actin monomers can bind with each other via hydrophobic interactions. As a result, actin polymerizes in high-salt solutions. The ions present in high-salt solutions shield the electrostatic repulsive forces between monomers, which bear a negative charge, thus promoting polymerization. Actin is able to polymerize into a filament because of a difference in the polymerization and depolymerization rates at both ends of the filament. An actin filament thus sports two different ends, the ‘plus’ end or barbed end and the ‘minus’ end or pointed end. As the name suggests, the ‘plus’ end is more dynamic than the ‘minus’ end due to the higher polymerization and depolymerization rates there.

During the elongation phase of a filament, the net growth rate at the ‘plus’/barbed end ($\frac{dn_b}{dt}$) and the ‘minus’/pointed end ($\frac{dn_p}{dt}$) can be expressed as the difference between the polymerization rate $k_{on} \cdot C$ (where C is the concentration of free monomers) and the depolymerization rate, k_{off} . The relation at the two ends is shown below:

$$\frac{dn_b}{dt} = k_{on,b}C - k_{off,b} \quad \text{Eq. 0.1.1.}$$

$$\frac{dn_p}{dt} = k_{on,p}C - k_{off,p} \quad \text{Eq. 0.1.2.}$$

Each end of an actin filament is characterized by a critical concentration $C_C = \frac{k_{off}}{k_{on}}$ of monomers at which there is no filament growth. In the absence of ATP, there is no energy source and the filament is at thermal equilibrium. Because adding a monomer at the plus end gives rise to the same filament than adding the monomer to the other end, the critical concentrations, which correspond to the dissociation constant of the associated reaction, must be equal at both ends: $C_C^+ = C_C^-$. In the case of ATP-bound monomers, however, the polymer gets out of equilibrium. This is because, following polymerization, the ATP is hydrolysed and the phosphate is released giving rise to ADP-bound monomers within “old” parts of the filament. As a result, the two ends of the filament are not equivalent and $C_C^+ \neq C_C^-$.

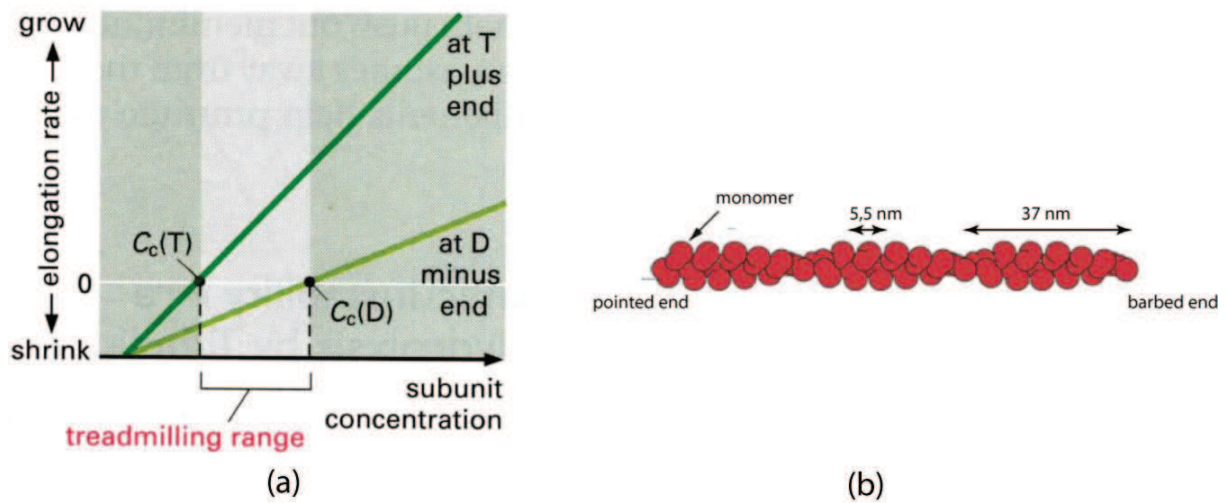


Figure 0.1.1. Growth dynamics of an actin filament. (a) When ATP is present, the critical concentrations are different at the two ends of the filament and we reach a treadmilling state when the monomer concentration $C_c(T) < C < C_c(D)$. (b) Diagram of an actin filament (Alberts, 1994).

Figure 0.1.1 shows the dynamics of actin in presence and absence of ATP: we can observe the behaviour of monomers bound to ADP, where the critical concentrations at both ends are equal ($C_C^+ = C_C^- = 2 \mu\text{M}$). In this case, given a sufficient amount of monomers $C > C_C$ in solution, filaments are formed until an equilibrium state between, G-actin and F-actin is reached when $C = C_C$. In contrast, when ATP is present in solution, the critical concentration

at the plus end is smaller than that at the minus end: $C_c^+ < C_c^-$. If the monomer concentration is intermediate between those two critical concentrations then an active non-equilibrium phenomenon known as “treadmilling” takes place. It involves the continuous addition of monomers at the ‘plus’ end and the continuous loss of monomers at the ‘minus’ end with no net change in length but with a net displacement of the filament. Treadmilling is involved in force-generation by the actin cytoskeleton and cell motility and is regulated by a complex network of proteins ((Plastino & Sykes, 2005), (Blanchoin, Pollard, & Mullins, 2000)).

Sub-figure (b) shows a diagram of the structure of an actin filament. The filament is a double helix, with a helical repeat every 37 nm. It consists of two parallel protofilaments in which the actin monomers are arranged periodically every 5.5 nm. An actin filament due to the orientation of the protofilaments is structurally polarized.

Actin filaments in in-vitro conditions are difficult to work with. At equilibrium, they tend to form dense, entangled networks and when diluted to avoid network formation, they depolymerize rather fast. To avoid this issue, it is customary to stabilize F-actin by using phalloidin. Phalloidin is a toxin obtained from the poisonous deathcap mushroom (*amanita phalloides*) and binds specifically to F-actin. The dynamic properties of the actin filaments are drastically reduced and they can be stored for a longer duration, even at low concentrations. Moreover since the filaments have a mean diameter of 7 nm, orders of magnitude below the resolution of even the best optical microscope, phalloidin labeled with a fluorescent dye is routinely used to bind F-actin, thus making the filaments visible via common fluorescence microscopy.

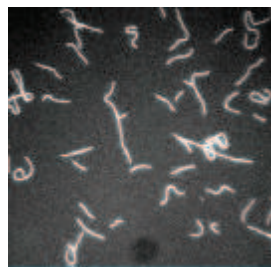


Figure. 0.1.2. Individual actin filaments stabilized by labeled phalloidin and observed using fluorescence microscopy.

This technique makes it relatively easy to visualize and handle actin filaments in-vitro.

Actin filaments are also the prime substrate of myosins which are one of the most important molecular motor families. The interaction between actin and myosin catalyzes the enzymatic activity of myosin motors.

1.2 Mechanical properties of actin filaments

Actin filaments as structural components of the cytoskeleton have also been studied for their mechanical properties. The measurements were performed in in-vitro conditions, on filaments stabilized by phalloidin. The latter can modify the mechanical properties of actin. Indeed, it has been shown that the persistence length of a phalloidin-stabilized actin filament is twice as large as that of a normal actin filament (18 μm and 9 μm respectively (Isambert et al., 1995)). Consequently it is important to bear in mind that the mechanical properties measured should not be taken at face value due to them being measured on such filaments but should be used cautiously depending on the context. The mechanical properties that have been deduced include (and not limited to) longitudinal stiffness with experiments performed on 1 μm -long filaments (Kojima, Ishijima, & Yanagida, 1994), torsional rigidity ((Tsuda, Yasutake, Ishijima, & Yanagida, 1996), (Yasuda, Shindo, & Ishiwata, 1996)) and bending stiffness ((Gittes, Mickey, Nettleton, & Howard, 1993),(Yasuda et al., 1996)). The question that arises is how we should think of an actin filament from a purely mechanical point of view.

Several experiments and theoretical calculations have shown that the way an actin filament behaves largely depends on various external mechanical factors. When the filament is pulled taut by a large tension, (≥ 200 pN, (Kojima et al., 1994)) like in muscular fibres, the filament can be modeled as a rigid beam. However under lower tension, actin behaves like a semi-flexible filament and thermal fluctuations have a major influence on its behaviour. It is thus important to consider the configuration of the actin in the studied system and the external conditions before applying any of the above assumptions to our reasoning.

2) Myosin

Myosins, being molecular motors, use the energy produced during ATP hydrolysis to produce mechanical work via an interaction with an actin filament. This interaction also catalyzes the enzymatic activity which brings about ATP hydrolysis. There are about 150 different types of myosins that have been discovered and classified, with differing amino acid sequences in their

motor domain, however, we will mostly talk about two different types of myosin, myosin II and myosin I.

2.1 Myosin II

Myosin II is the most widely studied type of myosin. It was the first to be discovered and is dubbed conventional myosin for historical reasons. Myosin II is located in muscles where they form the bulk of the total proteins (~45%). Their role is to ensure contractility of muscular fibres when working with actin filaments. Myosin II can also be found in non-muscular cells. In such cells, they intervene in force generation in the cellular cortex ((Bray & White, 1988),(Salbreux, Joanny, Prost, & Pullarkat, 2007)), adhesion (Cai et al., 2006) and motility (Jay et al.,2008). It has also been suggested that mechanical contraction by highly concentrated myosin II could potentially promote active depolymerization of actin filaments (Haviv, Gillo, Backouche, & Bernheim-Groswasser, 2008; Reymann et al., 2012).

(a) General Structure of Myosin II

The full-length myosin II is a large protein with a molecular weight of approximately 500kDa. It consists of two heavy chains (~2000 amino acids each) and of two different types of light chains (< 200 amino acids), with each type having a duplicate within the protein.

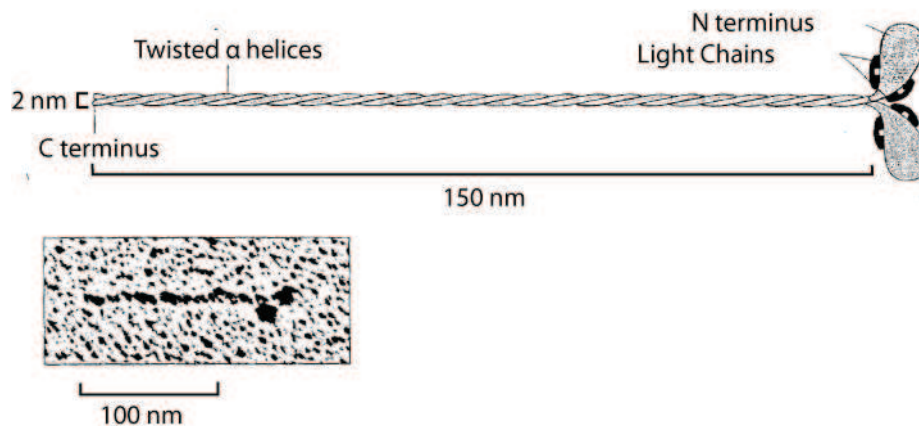


Figure. 0.1.3. General structure of myosin II; The lower figure shows an electron microscopy picture and the upper one shows a diagram of the whole molecule. The heavy chains form the myosin heads and twist upon themselves between the junction point to form the myosin tail. The light chains are found in close proximity to the heads (Alberts, 1994).

Electron microscopy imaging has shown that the molecule is made up of two globular heads and a 150 nm-long and 2 nm-wide tail (See Figure. 0.1.3).

In physiological conditions, at a saline concentration of less than 0.5 M, myosin II is insoluble and assembles spontaneously via their tail to form bipolar filaments if one of the two light chains is phosphorylated. When the light chain is dephosphorylated, the tail is curled around the head and the myosin is inactive. Phosphorylation unfolds the tail which activates the myosin and allows the spontaneous assembly into filaments. In in-vivo conditions, the phosphorylation is catalyzed by myosin light chain kinase, a calcium-dependent enzyme. Consequently, an increase in the cytosolic concentration of calcium brings about an activation of myosin in muscles and the formation of transient myosin II filaments in non-muscle cells (Alberts, 1994).

Trypsin can separate myosin II into two fragments by cleaving the protein in the middle of its tail. The fragments are : heavy mero-myosin (HMM) with a molecular weight of 350kDa and light mero-myosin (LMM) which weighs 150 kDa.

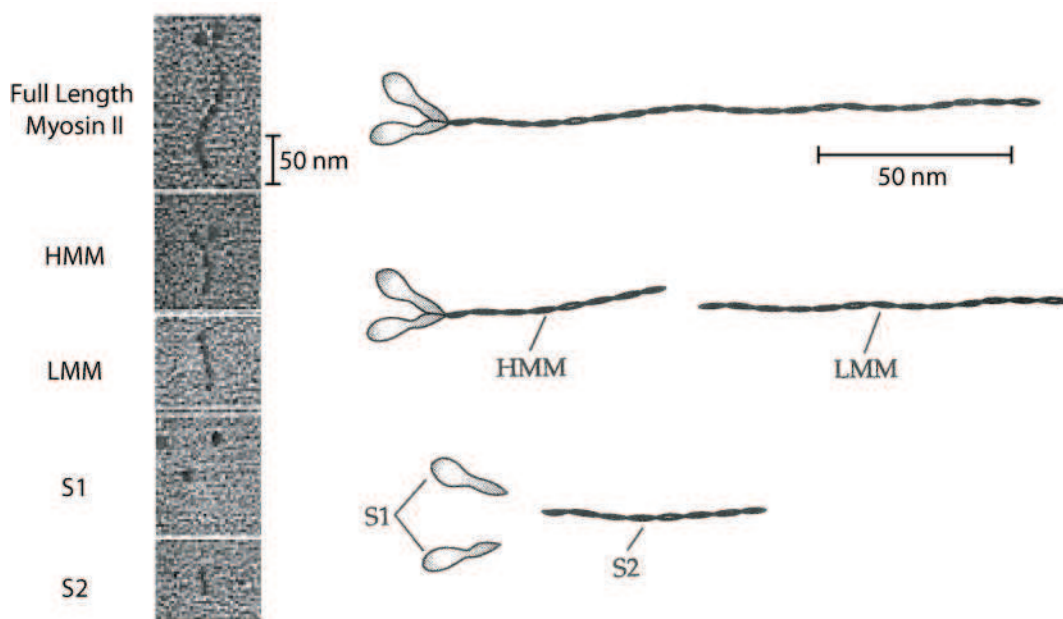


Figure. 0.1.4. Myosin II and its subfragments after enzymatic digestion (Howard, 2001; Lowey, Slayter, Weeds, & Baker, 1969).

HMM is made up of the two heads and part of the tail. LMM consists of what is left of the tail. LMM is soluble in high salt solutions, similar to the full-length protein and is able to assemble into filaments in low salt conditions. They are devoid of ATPase activity. HMMs, however, are soluble at any saline concentration, can bind actin and have an ATPase activity. Further separation can be performed by treating HMM with papain. This results in two

subfragments S1 and S2 ((Lowey et al., 1969),(Margossian & Lowey, 1982)) (Figure. 0.1.4). The S1 are the individual myosin heads and possess an ATPase and actin-binding activity. It has thus been deduced that the myosin heads bear the actin-binding site and the nucleotide-binding site.

(b) The Myosin Head

Since it contains the sites which gives myosin its most defining properties, the subfragment S1 has naturally attracted interest and its structure has been obtained in great detail at high resolution (Cooke, 1997).

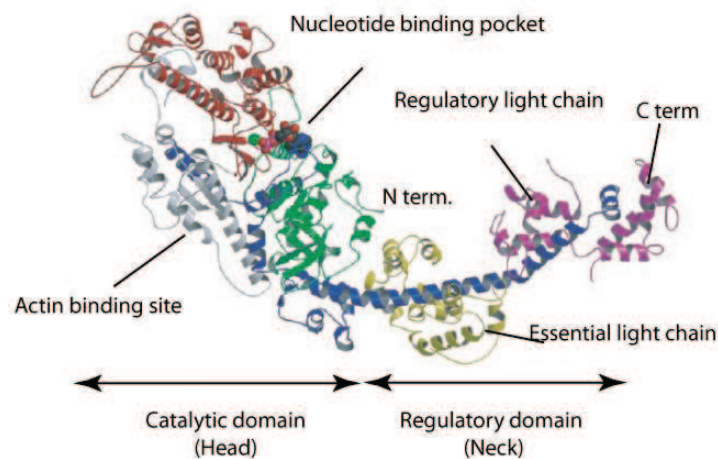


Figure. 0.1.5. 3D model of the S1 subfragment of myosin II

The S1 fragment can be considered as the catalytic component of the protein. It contains the binding sites of actin and nucleotides and a regulator domain, often nicknamed the myosin neck which spans from the catalytic domain itself to the junction region it makes with the tail. The catalytic domain corresponds to the heavy chain of myosin II. Structurally speaking, the heavy chain ends with an α helix which links the catalytic domain to the tail. This helix is the central element of the neck (Figure. 0.1.5) and is stabilized by two light chains, the essential light chain and the regulating chain. The two chains are curled around the helix. This is highly conserved across the members of the myosin family.

(c) Enzymatic Activity

When not bound to actin, myosin II has a low ATP hydrolysis rate ($\sim 0.1 \text{ s}^{-1}$). The hydrolysis reaction can be divided into a number of steps. The myosin first binds to an ATP molecule,

hydrolyzes it into ADP and inorganic phosphate (P_i), and liberates the phosphate and the ADP, in that order. The limiting step is the liberation of the inorganic phosphate. Actin catalyzes the ATPase activity of myosin. In presence of actin, the hydrolysis of ATP by myosin increases to 25 s^{-1} . In absence of ATP, myosin binds strongly to actin in a state known as rigor mortis with a low detachment ($\sim 1\text{ s}^{-1}$, (Howard, 2001)). ATP increases this detachment rate a thousand-fold, implying that the binding of an ATP molecule catalyzes the dissociation of actin and myosin.

(d) Mechano-chemical activity of myosin

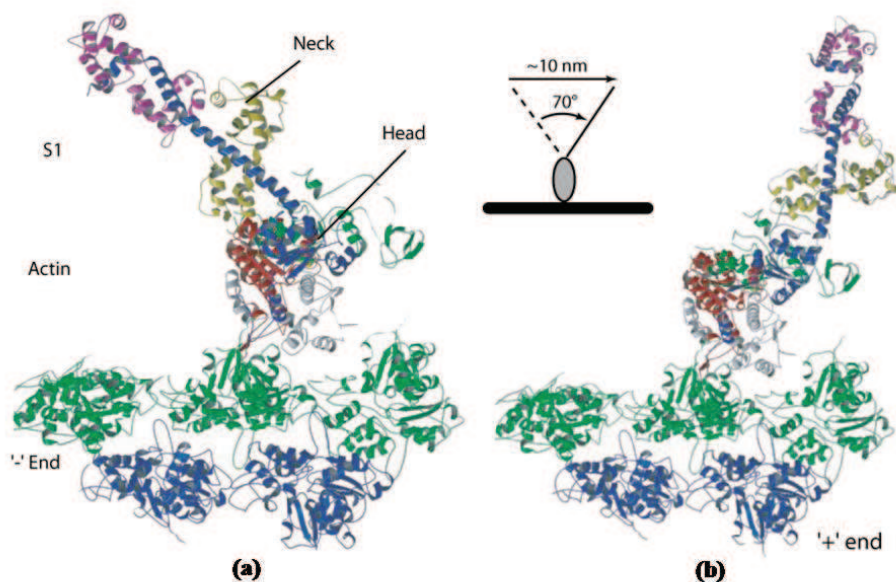


Figure 0.1.6. 3D models of the structure of an S1 fragment from myosin II (skeletal muscle) bound to actin and to two different nucleotides. (a) S1 with an ADP-vanadate complex which is an ADP- P_i analog. (b) S1 fragment with an ADP- BeF_3 complex, which mimics an ADP-bound structure. There is a 70° in the next angle between the two states. This corresponds to a displacement of the tip of the head of $\sim 10\text{nm}$ (Adapted from (Geeves & Holmes, 1999)).

Myosin is able to produce mechanical work because the biochemical modifications undergone by myosin during the ATPase cycle are accompanied by conformational changes of the actomyosin complex. When the S1 fragment shifts from the ADP- P_i state to the ADP state, there is a conformational shift of the molecule which pivots the neck about an angle of 70° . This angle corresponds to a displacement of approximately 10nm towards the barbed end of an

actin filament. Interestingly, an additional rotation has also been observed during the liberation of ADP giving rise to a rigor state ($\sim 20^\circ$ in smooth muscle myosin using S1 fragments (Whittaker et al., 1995). A similar behavior, but with a rotation of 33° , has been reported for myosin 1c (Batters, Arthur, et al., 2004) and brush-border myosin 1 (James D. Jontes, 1995). As we will discuss later in this chapter (Section B/. 1.2), these observations suggest that the conformational change associated with ATP hydrolysis can happen in two steps; this property has important functional consequences because it implies that an external load can affect the ability of the myosin to release ADP.

From a purely structural point of view, the mechanical work done by the molecular motors can be seen as coming from the rotation of the neck domain. This view was reinforced in single molecule experiments by producing mutant myosin II with neck domains of varying lengths. It was demonstrated that the size of the conformational change associated with ATP hydrolysis is directly proportional to the length of the neck domain (Ruff, Furch, Brenner, Manstein, & Meyhofer, 2001). This suggests that the neck acts as a lever arm, thus amplifying the small movements occurring in the catalytic domain during the conformational changes.

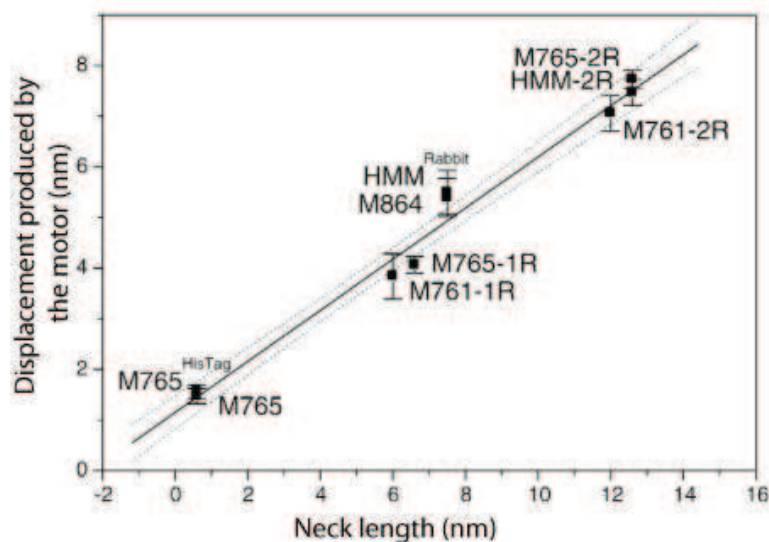


Figure 0.1.7. The displacement produced by a motor is proportional to the length of its neck domain. This implies that the regulator domain acts as a lever arm to amplify small movements. Adapted from (Ruff et al., 2001).

2.2 Myosin 1

Myosin 1 is one of the members of the “unconventional” myosins. Unconventional myosins were named this way for historical reasons to distinguish them from “conventional” myosins,

i.e. myosin II. While their basic functions remain highly similar, it is interesting to note that there are certain differences both in structure and organisation compared to myosin II. In this thesis, we considered two closely related members of the myosin-1 family: myosin 1b and myosin 1c. The latter is a prime candidate for the motor that drives adaptation and spontaneous oscillations of the hair-cell bundle in the inner ear, which is one if not the major point of interest of our research group.

Myosin 1 is a single-headed myosin motor with a relative molecular weight of approximately 110 – 130kDa and has a single heavy chain (Pollard, Doberstein, & Zot, 1991). In contrast to myosin II, they do not form filaments. Myosins 1 can be divided into two subclasses : ‘the long-tailed’ myosin 1 class and the ‘short-tailed’ class comprising myosin 1b and 1c. The latter are among the most widely expressed and studied forms of myosin 1.

Myosin 1b is especially interesting in that its enzymatic cycle has some notable differences with myosin II. The maximum rate of ATP binding is about more than 30 times slower than myosin II and its ADP release, while the myosin is in a strongly-bound state, is also very slow and is accompanied by a rotation of the lever arm. This last observation suggest that myosin 1b may play a role in tension sensing, for a force opposing the conformational change associated with ADP release would be expected to increase the lifetime of myosin attachment to actin.

Apart from the conserved motor domain, myosin 1 consists of a regulatory domain and a tail. The regulatory domain serves as a lever arm to amplify conformational changes in the production of the power stroke (Geeves & Holmes, 1999). It contains IQ motifs which vary in number depending on the isoform of the myosin 1 (myosin 1c has 3 IQ motifs (Houdusse, Silver, & Cohen, 1996) and myosin 1b can have splice isoforms of 4,5 or 6 IQ motifs (Ruppert, Kroschewski, & Bähler, 1993)). IQ motifs bind calmodulin. Calmodulins are intermediate messenger proteins that modify their affinity for target proteins by binding calcium. In the case of myosin 1, the addition of calcium ions weakens the affinity of calmodulin for the IQ motifs located close to the myosin head (Zhu, Beckingham, & Ikebe, 1998). Since it has been shown that calmodulin binding increases the stiffness of the regulatory domain and hence the lever arm of the motor (Rayment et al., 1993), the mechanical activity of myosin 1 is widely believed to be regulated by calcium (see more evidence (Section B/ 1.4)).

B/. Mechanical properties of molecular motors

In the previous section, we have seen an overview of molecular motors, mostly myosins along with a description of their substrate, actin filaments. This allowed us to appreciate how biochemistry and spatial molecular structure could mesh together to create a molecular machine, capable of producing mechanical work. This section attempts to shed light on the mechanical properties of molecular motors, by describing some of the major experiments that have provided considerable information and, in some cases, have become cornerstones of the field.

1) Experiments on single molecules

1.1 The Three-Bead Geometry

Single molecule experiments have given rise to considerable breakthroughs in the study of molecular motors by allowing us to monitor directly the interaction of a single myosin molecule with an actin filament. The most common set-up used is based on optical tweezers and is known as the “Three-bead geometry” or the “dumbbell geometry”.

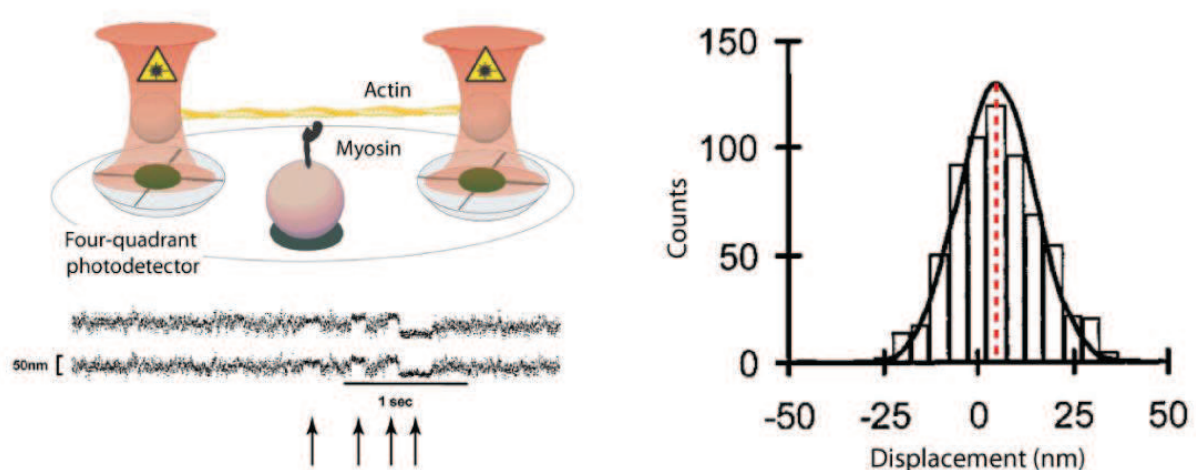


Figure 0.1.8. (a) Two beads with an actin filament under tension in-between them are manipulated using optical tweezers. They are used to move the actin filament closer to a single myosin molecule held in place by a third bead. The photodiodes can monitor any interaction by detecting the bead position with nanometer resolution. ((Batters, Wallace, Coluccio, & Molloy, 2004) The timecourse below the diagram shows the Brownian noise with interaction events being evidenced by a reduction in the bead fluctuations (indicated by arrows).((C Veigel, Bartoo, White, Sparrow, & Molloy, 1998). (b) Distribution of the displacements induced by a single HMM. The histogram is fitted with a Gaussian function and its width is the result of the Brownian fluctuations of the beads. The central value has a value of 5nm which gives the mean displacement produced by one motor ((C Veigel, Bartoo, et al., 1998)

The “three-bead geometry” (Finer, Simmons, & Spudich, 1994) has been used to characterize myosin I and II. Two beads are made to adhere to each ends of an actin filament and are individually trapped by a pair of optical tweezers. They are pulled apart from each other until the actin filament between them is under tension and taut. A third bead is affixed to the surface and was treated so as to obtain statistically one myosin motor over a desired surface area. This bead acts as a pedestal to elevate the single myosin motor relatively high above the surface. The experiment itself involves lowering the taut actin filament until it is in the vicinity of the myosin motor in a solution containing ATP (Figure. 0.1.8). The photodiodes record the bead position and allow measurement of the forces acting on the bead (Neuman & Block, 2004).

The timecourse of the fluctuations of the beads reflects the Brownian motion of the bead dumbbell. During the experiment itself, when the taut actin filament is located near the single myosin motor, the fluctuations are stochastically interrupted by events where the fluctuations are dramatically reduced. This indicates that the motor has bound to the actin filament, thus limiting the fluctuations of the bead-actin-bead system (shown by the arrows on Figure. 0.1.8). The duration of the binding event is proportional to the concentration of ATP in solution according to a first order rate equation (C Veigel, von Maydell, Kress, Molloy, & Fink, 1998), which is logical since the binding of ATP in the nucleotide-binding site of myosin promotes the detachment of the motor from actin. Consequently those experiments are performed at low ATP concentrations (a few μM) to facilitate detection of the binding events.

A binding event is also associated with a shift in the baseline of the mean position of the bead. However the displacement itself can be difficult to evaluate accurately due to the fluctuations of the system (Molloy et al., 1995). The baseline shifts differ in both amplitude and direction and as a result, it is convenient to plot them as a histogram to observe how they are distributed. Their distribution follows a Gaussian rule where the width of the Gaussian fit represents the amplitude of the bead fluctuations and the distance of the peak value with respect to the base position (labeled as ‘0’ on the histogram) is the actual displacement of the bead from the baseline. In the study by Claudia Veigel and her collaborators in 1998, the displacement produced (see part (b) of Figure. 0.1.8) was 5nm. The mean force produced by a myosin motor during such an experiment can be measured using a displacement clamp i.e.

measuring the external opposing force required to prevent the myosin from generating a displacement. Several studies have been performed in that regard and the results differ as shown in the table below.

| <u>Force developed by one myosin</u> | <u>Reference</u> |
|---|--|
| 3 – 4 pN | (Finer et al., 1994) |
| 2.1 pN | (Ishijima et al., 1996) |
| 1.7 pN | (Molloy et al., 1995) |
| 9 pN | (Takagi, Homsher, Goldman, & Shuman, 2006) |

Figure. 0.1.9. Table of forces generated by a single myosin molecule measured by various studies over the years.

By analysing the amplitude of bead fluctuations during a binding event, one can estimate the stiffness of the myosin-actin link. The stiffness values obtained, however, varied over a relatively large range, from 0.2 – 2 pN/nm ((C Veigel, Bartoo, et al., 1998),(Mehta, Finer, & Spudich, 1997),(Ishijima et al., 1996),(Takagi et al., 2006),(Nishizaka, Seo, Tadakuma, Kinoshita Jr., & Ishiwata, 2000)). Proper stiffness estimation of the acto-myosin stiffness requires corrections that take into account the compliance of elements in series with the myosin, namely the links between beads and actin filament and those between the motor molecule and the substrate. Difficulties in estimating these series compliances may explain in part the large range of measured values. A recent study (Lewalle, Steffen, Stevenson, Ouyang, & Sleep, 2008) found ways to alleviate these limitations, indicating that a crossbridge stiffness of 1.8 pN/nm. This value is in reasonable agreement with estimates resulting from mechanical studies of muscle fibers (Linari, Caremani, Piperio, Brandt, & Lombardi, 2007).

1.2 Two-step force generation by myosins

The displacement and force brought about by myosin motors are caused by the conformational change in the molecule and the myosin neck acts as a lever arm to amplify it into a noticeable movement. After measuring the forces developed and the stiffness of the myosin-actin interaction, it was only natural to start exploring the finer details of this conformational change. The spotlight in this endeavour was on myosin I because it was slower than the relatively fast myosin II, making the observations easier. The experiments were performed using the three-bead geometry and the optical tweezers were used to measure the mechanical transitions made by a single myosin I head while it is attached to the actin filament (C Veigel et al., 1999). The start and end of an interaction event were synchronized (since the duration of the individual events is random, the middle sections of the interaction timecourse were ignored) and averaged in order to remove the noise due to thermal fluctuations. The amplitudes of the bead position at the beginning and end of the averaged interaction events were compared (see Figure. 0.1.10).

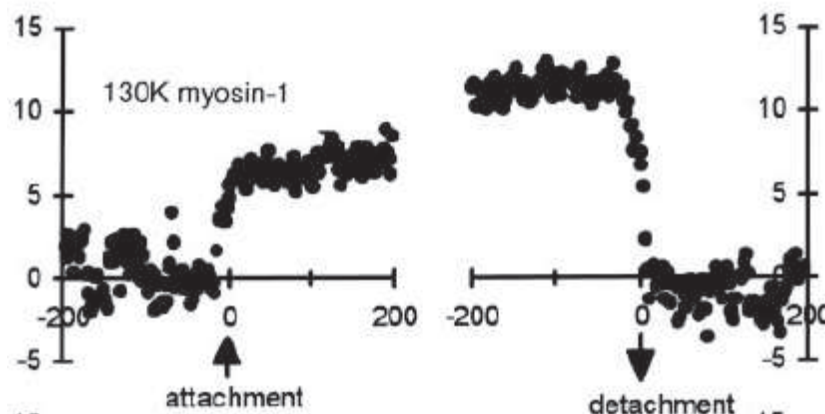


Figure. 0.1.10. The beginning and ends of n interaction events were synchronized and averaged. The myosin used in this experiment was brush-border myosin I. ($n=63$). Adapted from (Claudia Veigel et al., 1999)

It was shown that the working stroke of myosin I is made up of two steps (Claudia Veigel et al., 1999). The first step occurs within 10 ms of the actomyosin interaction and has an amplitude of 6.5nm. It is followed by a shorter step of 5.5 nm. The duration of the second step is ATP-dependent and decreases when the ATP concentration increases, falling from 305.5ms to 50.6ms as ATP increases from 3 μ M to 100 μ M.

Since then, considerable efforts have been made to investigate if this two-step working stroke is a peculiar feature of myosin 1 or a characteristic common to members of the myosin family. Further studies have demonstrated the presence of the two steps in the working stroke of myosin 1c (Batters, Wallace, et al., 2004), smooth muscle myosin II (Claudia Veigel, Stephan Schmitz, 2005) and skeletal muscle myosin II (Capitanio et al., 2006), although the second step is considerably smaller in myosin II.

In agreement with structural observations, the presence of the two steps suggest that the working stroke can effectively be divided into two distinct biochemical states corresponding to two successive conformational changes upon interaction of myosin with actin. The first conformational change occurs after actin binds to the myosin. As phosphate is released after ATP hydrolysis, the system transits to a tightly bound force-generating state (the ‘actin-myosin-ADP’ state). The loss of ADP then leads to another tightly bound complex (‘actin-myosin’). Additional movement can be generated during this process, making up the second step of the working stroke. The binding of an ATP molecule to myosin ends the mechanical event by causing the detachment of the myosin motor from the actin filament as evidenced by the decreased lifetime of the second step when the ATP concentration was increased.

1.3 Effects of an external load on myosin activity

Single-molecule experiments have demonstrated an intimate coupling between the biochemical states and the conformational states of the myosin molecule during its mechanical cycle and a conformational change associate with ADP release while the myosin occupies a strongly-bound state on actin. Remarkably, the detachment rate of a myosin II molecule in an ADP-bound state was shown to be affected by an external force (C Veigel, Molloy, Schmitz, & Kendrick-Jones, 2003) (Guo & Guilford, 2006) This phenomenon has also been confirmed in myosin I (Batters, Wallace, et al., 2004). In both cases, it was found that a force opposing the myosin movement associated with ADP release lengthened the lifespan of attachment or, equivalently, that the detachment rate decreased: the myosin behaves like a “catch-bond”. This effectively stops or slows down the motor as it goes through the various stages of its enzymatic cycle, hence allowing myosin to adapt its hydrolysis rate to the external mechanical conditions (C Veigel et al., 2003). Interestingly, a similar mechanism has been observed in muscles, where it is known as the “Fenn effect” (Fenn, 1923). The ability to ‘lock’ myosin heads into a tightly bound state to actin is an energy-saving method (ATP-wise) to keep a biological system under tension in-vivo.

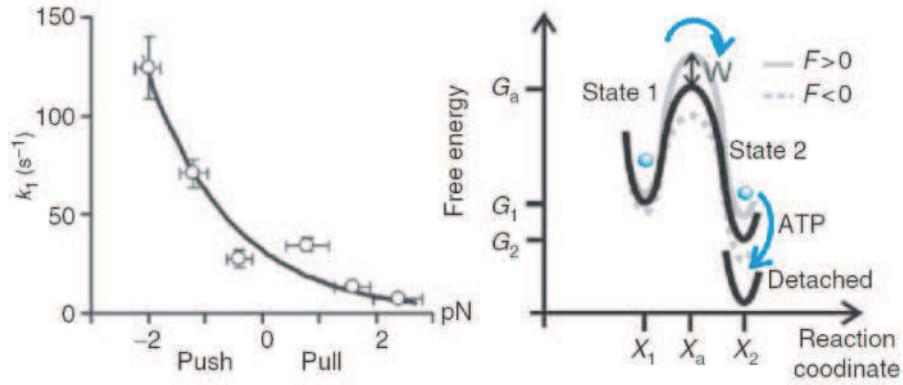


Figure. 0.1.11. Left : The graph shows that k_1 (the transition rate constant between the first state and the second state) varies exponentially with the force applied. Push refers to a force in the direction of the myosin movement and Pull refers to a force opposing the myosin movement. Right : Energy profile of the myosin motor during actin interaction. The black curve shows the default activation energy barrier from state 1 to state 2 in absence of force. This activation energy can be lowered (grey dotted line) or increased (full grey line) depending on the direction in which the external load is applied (C Veigel et al., 2003).

In single molecule experiments, the transition rate constant, k_1 between the first (ADP-bound) and the second (no nucleotide bound) state of the bound myosin was shown to depend exponentially on the external force applied (left hand side of Figure. 0.1.11):

$$k_1 \propto \exp\left(-\frac{Fd}{k_B T}\right),$$

in which d is a distance that characterizes the mechanosensitivity of the myosin molecule. With myosin 1b, $d = 12$ nm (Joseph M. Laakso, John H. Lewis, Henry Shuman, 2008). Correspondingly, the rate of myosin detachment from actin decreases by more than 75-fold when an opposing tension of 2pN or less is exerted on the motor. Myosin 1b thus appears as a very sensitive molecular force sensor. In contrast, myosin II is much less sensitive to force ($d = 1.3$ nm; see Veigel et al, 2003).

These observations can be interpreted by representing the acto-myosin interaction by a two-state energy profile comprising an energy barrier between the two states (right hand side of Figure. 0.1.11). The energy barrier between state 1 and 2 can be lowered or raised depending on the direction of the force applied. A force in the direction of the myosin movement lowers the energy barrier and promotes transition into the second state. Conversely, a force opposing the movement of the myosin increases the energy barrier and tends to ‘trap’ the myosin in

state 1. The second step is accompanied by ADP release and because ADP release kinetically limits the detachment rate of myosin from actin (Lewis, Lin, Hokanson, & Ostap, 2006), the external opposing load can prevent the second step from completing its rotation and mechanical cycle, hence inhibiting ADP release and actin detachment.

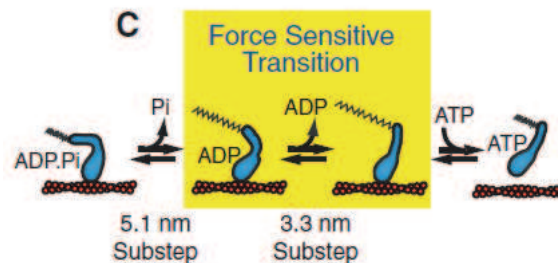


Figure 0.1.12. A diagram of myosin 1b (blue) bound to actin (red) showing the two steps of the working stroke. The spring symbol signifies a tension on the actomyosin complex. An opposing tension opposes the natural movement of the second step and as such prevents the myosin from completing its mechanical cycle which inhibits ADP release and eventually actin detachment (highlighted in yellow)(Joseph M. Laakso, John H. Lewis, Henry Shuman, 2008).

This tension-sensitivity and the load-dependent kinetics of myosin 1 imply that the role of myosin 1 in biological systems is to generate and sustain tension over long periods.

Until recently, it was thought that this mechanism could be applied to all short-tailed myosin 1 isoforms. However a recent article has put this assumption on hold. This article proposes that force sensing step in myosin 1c is not the ADP release step like in myosin 1b but an isomerization that follows ATP binding (Figure. 0.1.13).

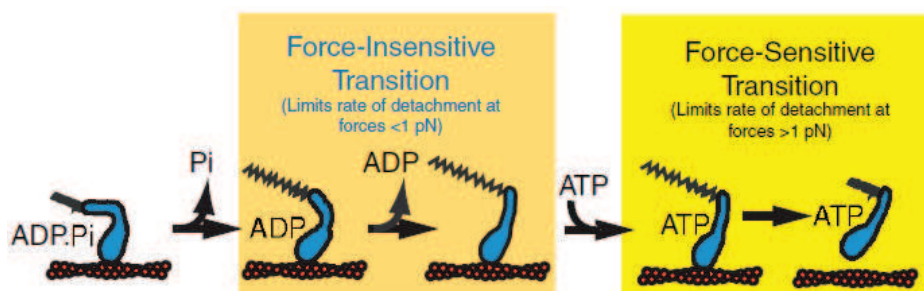


Figure 0.1.13. Diagram of the working stroke of myosin 1c. Contrary to the general idea that the force-sensitive step for myosin 1 isoforms was the ADP release step (in orange). It has recently been suggested that the isomerization following ATP binding would in fact by the force-sensing step in myosin 1c (Greenberg, Lin, Goldman, Shuman, & Ostap, 2012).

The authors arrived to this conclusion by comparing the rate constants of the various steps of the enzymatic cycle with theoretical rates obtained from a model. They found that the rate corresponding to ADP release for myosin 1c was numerically similar to the value of the force-independent step of their model. Moreover single molecule experiments similar to those performed on myosin 1b provided some of the evidence. It was inferred that the force-dependent transition took place after ADP release and that addition of ADP did not influence the detachment of myosin 1c from actin. However, since there is still no evidence of any visible and measurable conformational change linked to this isomerization, this new development has yet to be confirmed.

1.4 Calcium regulation of myosin 1 activity

We have previously discussed that calcium has potentially a major influence on the mechanics of myosin 1 by lowering the affinity of calmodulin for the regulatory domain of myosin 1, hence directly affecting the stiffness of the neck and the motor domain. Further evidence was first provided by studying the biochemical details of the working stroke. It was found that calcium increases the detachment rate of calmodulin from the IQ motifs close to the motor domain which regulates ATPase activity (Manceva et al., 2007). The influence of calcium was confirmed in another study which demonstrated that the presence of calcium increased the rate of ADP release of myosin 1c by ten times and produced a 7-fold inhibition of the ATP hydrolysis step. This accelerates the detachment of the actomyosin crossbridge and increases the lifetime of the detached ATP-loaded myosin (Adamek, Coluccio, & Geeves, 2008).

A more direct demonstration of calcium regulation of myosin 1 was published recently using myosin 1b and single molecule experiments using the three-bead configuration (Lewis, Greenberg, Laakso, Shuman, & Ostap, 2012). The ensemble averaging method used to analyze and interpret the data was described previously in section B 1.2. The synchronization of the onset of the attachment events gives the average displacement of the first sub-step (called here time-forward averages) and the averaging synchronization at the end of the events gives the average displacement of the whole step (called here time-reverse averages). In absence of calcium, the size of each substep was similar to what was reported in the literature, however in presence of 9 μ M calcium, the size of both substeps were dramatically reduced (fivefold for the first one, from 5.2nm to 1.1nm and 15-fold for the second one, from 13nm to 0.89nm). This is illustrated below.

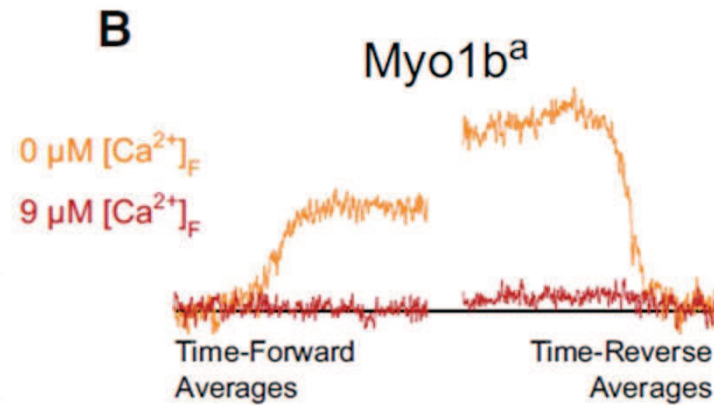


Figure 0.1.14. The diagram shows the average size of the two substeps of the myosin 1b working stroke with and without calcium (Lewis et al., 2012).

Such a drastic decrease in the size of the working stroke and the substeps indicate that calcium had a major influence on the lever arm. Overall, these results indicate that calcium weakens the motor (smaller power stroke and lower duty ratio). Although, myosin 1b behaves as a “catch bound” in the absence of Ca^{2+} , this effect is lost in the presence of Ca^{2+} . An increase of Ca^{2+} thus favors detachment of the motor under load.

1.5 Non-productive attachments

In the case of slower myosins such as myosin 1c, about 80% of the actomyosin binding events produce neither force nor displacement and are said to be non-productive (Batters, Wallace, et al., 2004). Those events have a duration of 100ms or less, are ATP-independent and are shorter than their productive counterparts which can last for several seconds in 20 μM ATP. They can be thought of as transient reversible binding events which do not generate a force and where the myosin detaches from the actin without ATP hydrolysis.

A similar mechanism has been observed between actin filaments and myosin II in muscle fibres. When a fast extension is exerted on a relaxed fibre (a fibre in biochemical conditions where there is no contraction), there is an unusually high apparent stiffness, suggesting the presence of actomyosin cross-bridges (see Figure 0.1.15) (Brenner, Schoenberg, Chalovich, Greene, & Eisenberg, 1982).

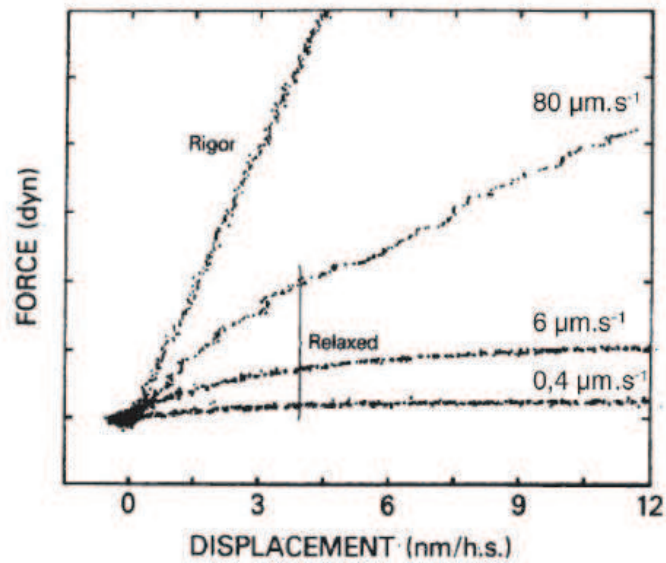


Figure. 0.1.15. When a rapid extension ($80\mu\text{m/s}$) is applied to a muscle fibre, force increases linearly with respect to the extension suggesting a Hookean stiffness present in the fibre. When the extension speed is reduced to $6\mu\text{m/s}$, this apparent stiffness decreases and disappears completely if the speed is further reduced to $0.4\mu\text{m/s}$ (Brenner et al., 1982).

This stiffness depends on the speed at which the extension is exerted. This suggests that a fast extension can deform the myosin crossbridges in the muscle fibre. In this case, the crossbridges are analogous to rigid springs. However when a slow extension is applied, the myosins have enough time to detach themselves from the actin filaments thus explaining the absence of any noticeable stiffness at low extension speeds.

2) In-vitro Motility Assay

2.1 General Principle

This section deals with another milestone in molecular motor study, the motility assay. In a typical motility assay, fluorescent filaments are brought into contact with a surface covered with a layer of myosin molecules (Figure. 0.1.16). The filaments can be seen to glide across the surface, carried by the motors in a continuous and directed motion.

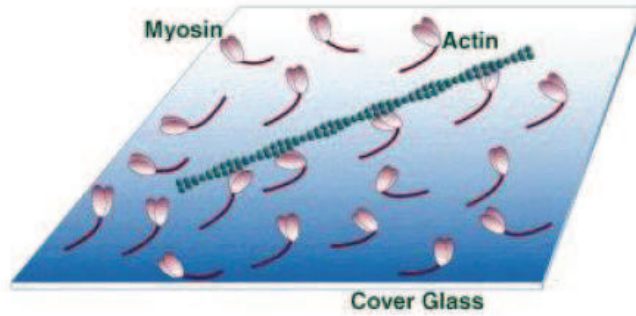


Figure. 0.1.16. Diagram of a typical motility assay – the actin filaments are carried by the myosin layer distributed on the surface. The fluorescent actin filaments can be seen to move in a continuous and directed motion. (<http://physiology.med.uvm.edu/warshaw/TechspgInVitro.html>)

The main advantage of the motility assay is that it can be performed in minimal and easy-to-control conditions, i.e. with purified proteins and in appropriate ATP-enriched buffers. So far, a motility assay has been devised for every possible type of myosin and also for microtubule-specific motors such as kinesin and dynein. A motility assay is not only useful to test for the viability of molecular motors but also provides valuable information on the motility of the motors adsorbed.

In the first historical motility assay experiment (Kron & Spudich, 1986), the motors used were myosin II and they were adsorbed on the surface. In those conditions, the average velocity of the actin filaments increased when the ATP concentration increased until 200 μM ATP where the filament velocity saturated at about 3 to 4 $\mu\text{m/s}$.

Over the years, several improvements and variations have been introduced. In the original assay, the myosins were adsorbed non-specifically on the surface. It is possible to control the density of the myosins on the surface by specific binding using antibodies (Winkelmann, Bourdieu, Ott, Kinose, & Libchaber, 1995). The antibodies themselves can be targeted towards different parts of the myosin molecule and, as one would expect, have an effect on the motility of the motors and the velocity of the actin filaments. Other parameters, such as temperature have also been tested (Figure. 0.1.17).

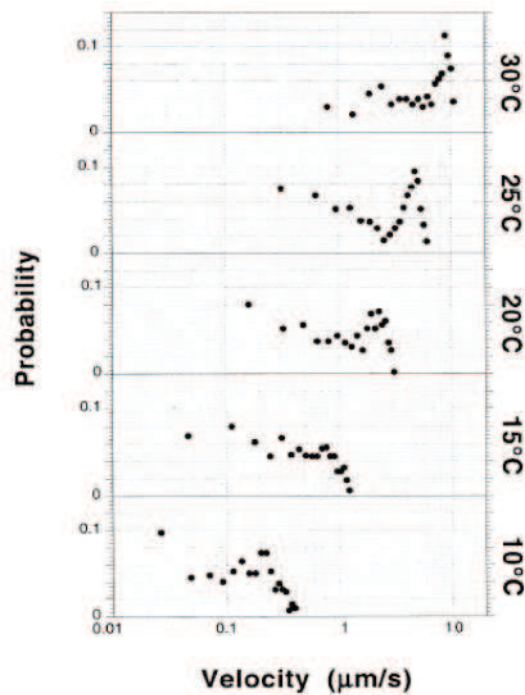


Figure 0.1.17. –Velocity distribution of myosin II-driven actin filaments in a motility assay at different temperatures. (Bourdieu, Magnasco, Winkelmann, & Libchaber, 1995)

At low temperatures (10°C), the velocity distribution is quite large, with no defined peak and tends to be in the low range of velocities. As temperature increases above 17.5°C, a more defined peak can be identified allowing us to define an average velocity. At 30°C, the velocity can reach high values up to 10μm/s (Bourdieu et al., 1995).

2.2 Processivity

The distribution and average velocity of actin filaments in motility assays depend strongly on the motor density on the surface (Bourdieu et al., 1995). With myosin II, a clearly defined average velocity is observed above 300 motors/μm². When the motor density exceeds 450 motors/μm², the average velocity saturates at about 5 μm/s (Figure. 0.1.18).

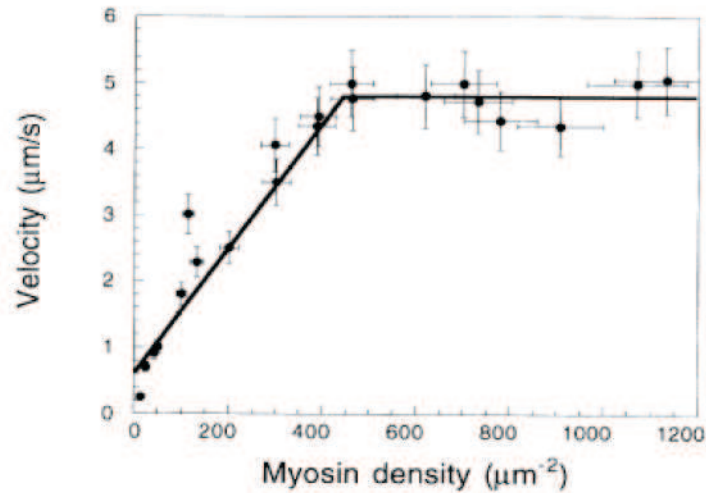


Figure 0.1.18. Variation of filament velocity in a motility assay with motor density (Bourdieu et al., 1995).

However, when similar experiments were performed with kinesin and microtubules, it was found that the velocity of the microtubules remained more or less constant whatever the density of the motors on the surface (Figure. 0.1.19(Howard, 2001)).

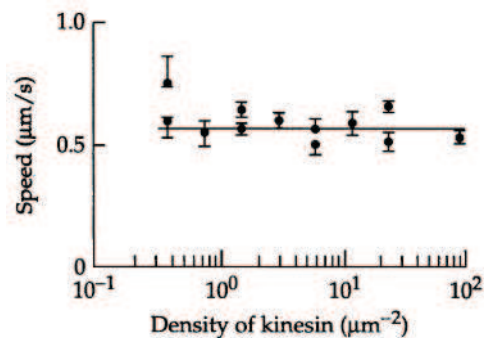


Figure 0.1.19. The velocity of microtubules in a motility assay with a kinesin-covered surface. (Howard, 2001)

This different behaviour of kinesin can be explained by the concept of processivity. Kinesin is said to be “processive” because a single kinesin motor can move a microtubule (Howard, Hudspeth, & Vale, 1989). In contrast, myosin II like most members of the myosin family such as myosin 1b and 1c, is non-processive, i.e. a single myosin motor cannot move an actin filament over an appreciable distance by itself. This motor molecule must act collectively

with other myosin motors to induce a continuous motion of an actin filament. It should be noted here that not all myosins are non-processive. Myosin V, for instance, is a notable processive myosin. Processivity can be further understood by introducing the concept of “duty ratio”.

The duty ratio can be defined as the ratio of the time a motor domain remains attached to its substrate to the total duration of its enzymatic cycle (Howard, 2001). Processive motors have a high duty ratio and can thus work individually by maintaining a constant attachment to their substrate. Non-processive motors have a low duty ratio and since they spend a long time detached from their substrate (which is then free to diffuse), they need to work in groups to produce a continuous movement. A given motor contributes a working distance to the moving filament and detaches itself. When this particular motor is detached, the other motors move the filament along the rest of the way. This process is often compared to the way a millipede ‘walks’.

The duty ratio r of a generic molecular motor can be written as:

$$r = \frac{\tau_{on}}{\tau_{on} + \tau_{off}} = \frac{\tau_{on}}{\tau_{total}} ; \quad \text{Eq. 0.1.3.}$$

where τ_{on} is the time the motor spends attached to its substrate and τ_{off} is the time spent detached from its substrate. Because the cycle is driven by ATP hydrolysis, we have $k_{ATP} = 1/(\tau_{on} + \tau_{off})$ and thus:

$$r = k_{ATP} \tau_{on} , \quad \text{Eq. 0.1.4.}$$

where k_{ATP} is the rate of ATP hydrolysis by one motor head. Let’s now consider a gliding assay in which there are enough motor heads to drive a continuous movement of actin filaments at velocity v . If each head moves over a distance δ during the time τ_{on} , then $v = \delta/\tau_{on}$ and in turn:

$$r = \frac{\delta \cdot k_{ATP}}{v}. \quad \text{Eq. 0.1.5.}$$

Considering an ATPase rate of 20/s per myosin II head, a working distance δ of 5nm and a filament moving at $5\mu\text{m/s}$, we can deduce that myosin II has a duty ratio r of 0.02, meaning that a myosin II motor head stays attached for only 1ms to an actin filament.

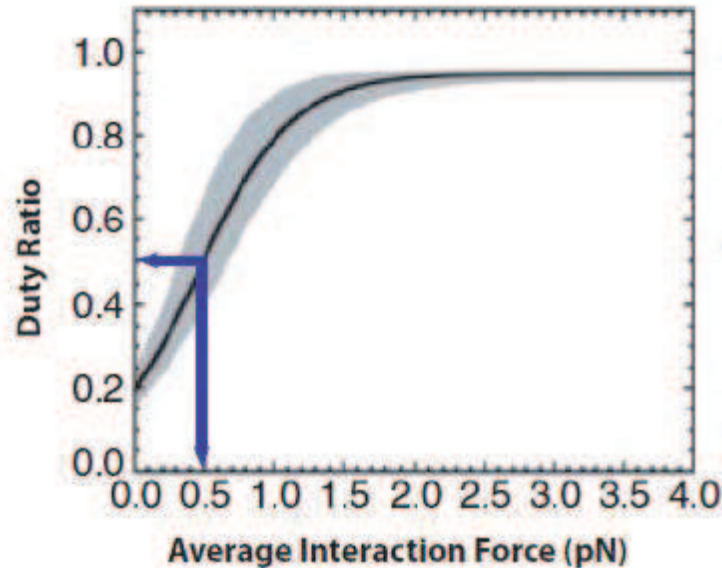


Figure 0.1.20. Predicted myo1b duty ratio as a function of the load applied. The arrows show the amount of force necessary (0.5pN) to shift myosin1b from a low duty ratio motor to a high duty ratio motor (Joseph M. Laakso, John H. Lewis, Henry Shuman, 2008).

This duty ratio, while an inherent property of a given molecular motor, is by no means fixed. It can indeed be changed by the application of an external force (Figure. 0.1.20). We have already seen in section B/. 1.3 that, in single molecule experiments on myosin I, it is possible to change a low duty ratio myosin into a high duty ratio myosin by applying an external force (C Veigel et al., 2003) (Joseph M. Laakso, John H. Lewis, Henry Shuman, 2008). This observation provides a molecular explanation to the “Fenn effect”, the phenomenon by which a muscle fiber adjusts its ATP consumption to the load to which the muscle is subjected: the ATPase rate decreases at increasing loads (Fenn, 1923; Duke, 1999).

C/. Working model for myosin

1) The power stroke model

The different observations gathered in both motility assays and single molecule experiments have led to the development of a working model for the force producing mechanism of a

myosin head. The model is known as the ‘power stroke model’. It is based on the coupling between the biochemical states of myosin and the mechanical events of the myosin enzymatic cycle.

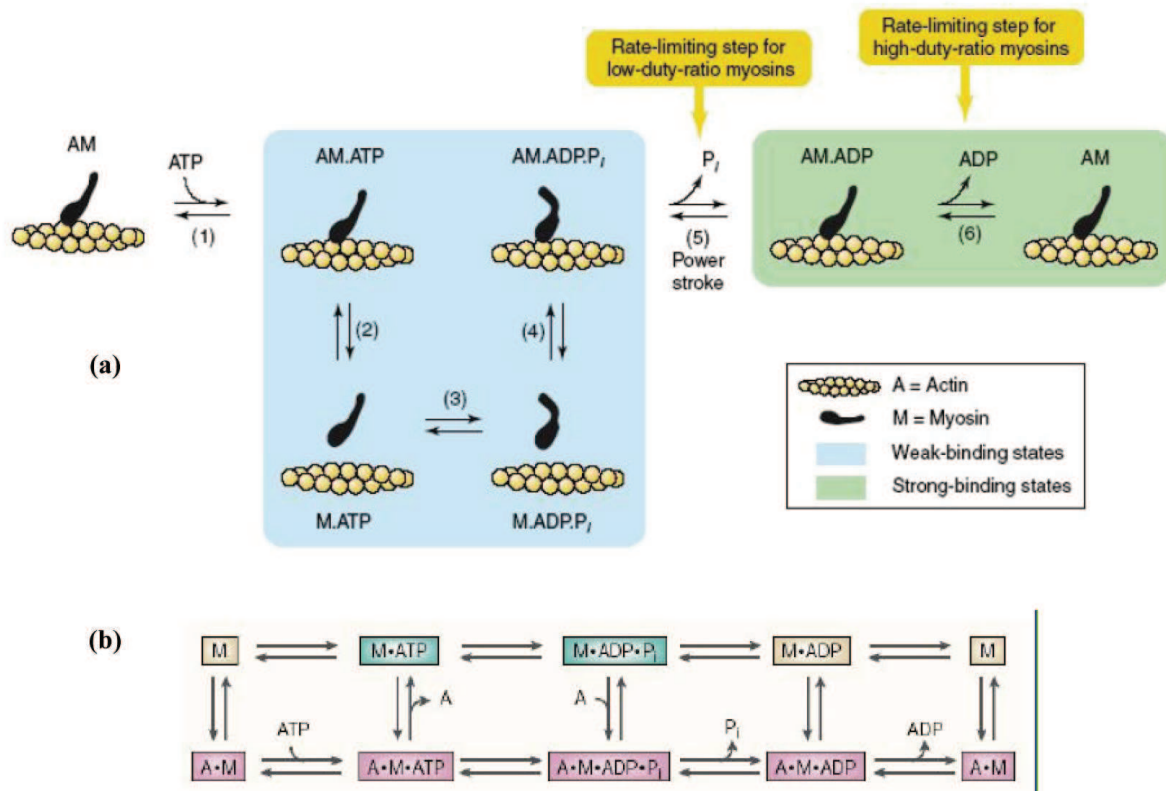


Figure 0.1.21. (a) The classical power stroke model showing the different biochemical states of myosin with respect to the mechanical events (De La Cruz & Ostap, 2004). (b) Diagram of the different actin-myosin-nucleotide states possible and their reaction pathways (Spudich, 2001).

Figure 0.1.21(a) shows the essential steps of the power stroke model. In absence of ATP, myosin is strongly bound to actin (AM state). When ATP binds to myosin (AM.ATP), the affinity of myosin for actin decreases and causes the dissociation of the actomyosin complex (M.ATP). ATP hydrolysis into ADP and P_i bring about a conformational change which prepares the myosin for force generation at a later stage of the mechanical cycle. At this point, myosin is in rapid equilibrium with loosely bound state (AM.ADP. P_i). The power stroke itself occurs via a force-producing conformational change which is associated with the liberation of P_i , leading to a tightly bound state (AM.ADP). Subsequent liberation of ADP then brings the myosin back to the start of the cycle. This schematic view is simplified in that the force is shown to be generated in only one step but as we have already seen earlier when

investigating the mechanical properties of the myosin molecule in single molecule experiments, the power stroke of myosin is made up of two consecutive sub-steps corresponding to two conformational changes brought about by the liberation of P_i and ADP respectively (See Figure. 0.1.22).

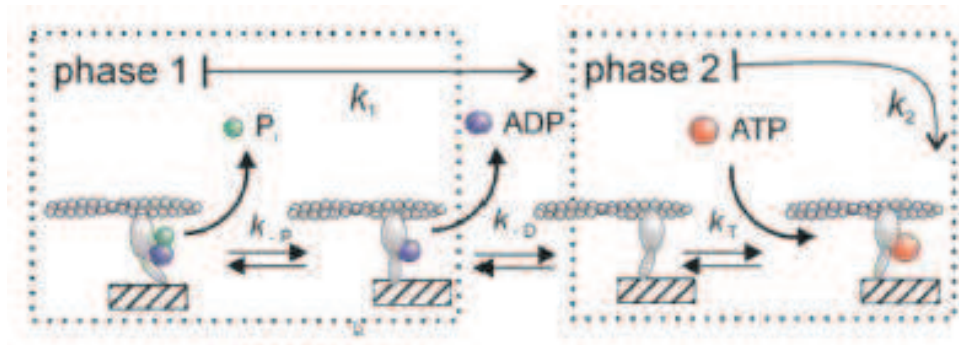


Figure. 0.1.22. Diagram of the myosin power stroke showing the two sub-steps (Capitanio et al., 2006).

It is also possible to explain the power stroke model with mechanical terms.

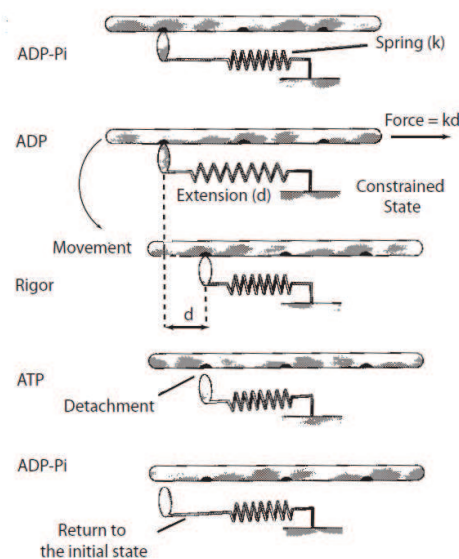


Figure. 0.1.23. Mechanical model of the power stroke. The liberation of P_i and ADP bring about internal conformational changes in the molecule, of amplitude δ , hence placing an internal spring of stiffness k . When the spring exerts a force, the actin filament moves and the spring is released. The binding of an ATP molecule causes detachment of the myosin (Howard, 2001).

The hydrolysis of an ATP molecule causes a conformational change which puts the internal spring of a myosin molecule under tension (See Figure. 0.1.23). In this constrained state,

myosin exerts a force $k\delta$ on the actin filament. If we consider a myosin adsorbed on a surface like in a motility assay, the force developed moves the actin filament, releasing the mechanical energy stored in the molecule. The relevant spring here can be any flexible element coupled to the tail of the myosin and in series with it. Note that the motility assay configuration (fixed myosin molecule exerting a force on a mobile actin filament) can be ‘reversed’ i.e. myosin can carry a ‘cargo’ bound to its tail along a fixed actin filament.

The model is in reality mitigated by thermal fluctuations at the microscopic scale at which those processes actually take place. As such, the various steps of the mechanical cycle we have described cannot be thought of as purely deterministic in nature. Without going into the statistical physics and thermodynamics needed to fully describe the system, one can think of the mechano-chemical stage which involved ATP hydrolysis and force production as the most probable pathway among the other possible states of the actomyosin complex (See Figure. 0.1.21(b)).

This cycle is common to the whole myosin family. The differences between the different types of myosins come from differing values of transition rates through the various stages of the mechano-chemical cycle. This is linked to the role of each given motor in the physiological system in which they are involved (De La Cruz & Ostap, 2004).

2) A consequence of mechanosensitivity: non-linear stiffness of myosin

A molecular system is said to be mechanosensitive if it can exist in two different states with a probability to be in one of the two states that can be shifted one way or the other by the application of a force to the system. In order to do so, the force must input mechanical energy to the system by being associated to a conformational change in the direction of the force (Howard, 2001). Let us consider a simple mechanical bi-stable system possessing an internal elastic degree of freedom of a given stiffness k . This system can transition between two states 1 and 2 via a displacement δ .

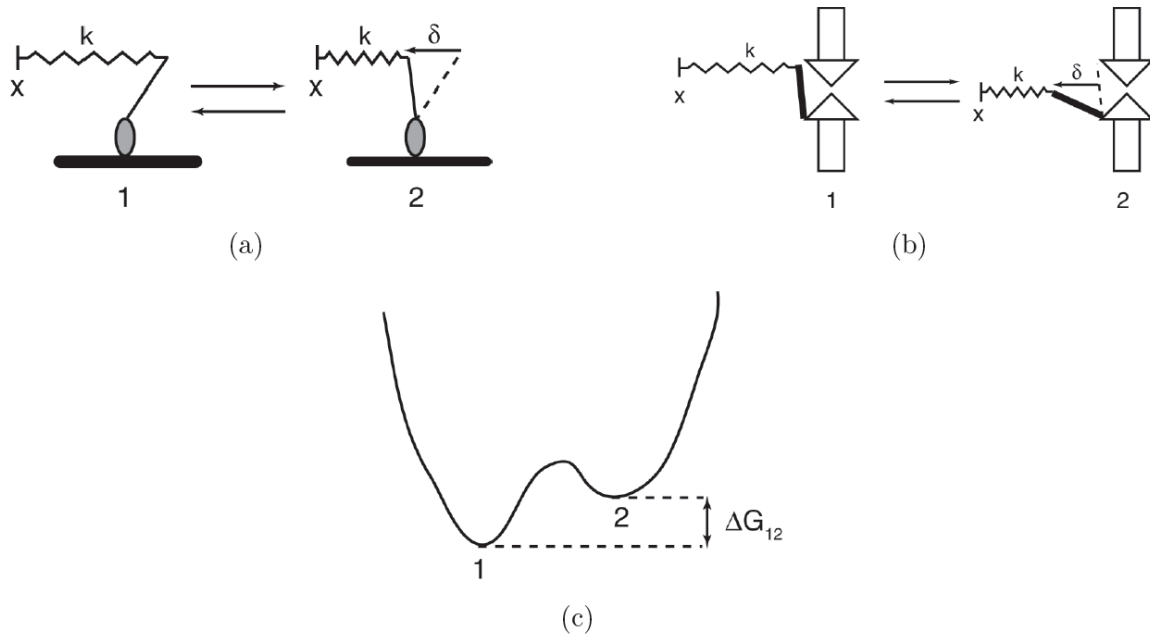


Figure 0.1.24. (a) Diagram showing two possible states of a myosin motor, rigor state (1) and ADP (2). An imposed displacement x of a spring element of stiffness k is energetically favourable to state 2. This implies that an opposite displacement δ relaxes the system with respect to state (1). (b) A mechanosensitive system similar in principle to (a) applied to an ion channel linked to an elastic element which is able to be in a closed (1) or open (2) state. (c) Energy profile of a bi-stable mechanosensitive system. The two states 1 and 2 are separated by an energy barrier. The ratio of probabilities of the system being in state 1 or 2 is given by their free enthalpy difference, ΔG_{12} . Adapted from (Plaçaïs, 2008).

Such a model fits the behaviour of an actin-bound myosin motor in rigor state (no nucleotide attached) and in ADP state. It can also be applied to a mechanosensitive ion channel, in which a spring is coupled to the channel which can be either closed or open (Figure. 0.1.24). Figure. 0.1.24(c) shows the energy profile of this model. The two states 1 and 2 can be characterized by their free enthalpies G_1 and G_2 respectively:

$$G_1 = \mu_1 + \frac{1}{2}kx^2 \quad \text{Eq. 0.1.6.}$$

$$G_2 = \mu_2 + \frac{1}{2}k(x - \delta)^2 \quad \text{Eq. 0.1.7.}$$

; where μ_1 and μ_2 are the free enthalpies intrinsic to each of the two states and x is the extension of the elastic component of the system. At thermodynamic equilibrium, the ratio of probabilities gives:

$$\frac{p_2}{p_1} = e^{-\left(\frac{\Delta G_{12}}{k_B T}\right)} \quad \text{Eq. 0.1.8.}$$

; where $p_2 + p_1 = 1$

By substituting $\Delta G_{12} = G_2 - G_1 = -k\delta(x - x_0)$, where $x_0 = \frac{\delta}{2} + \frac{(\mu_2 - \mu_1)}{(k\delta)}$ corresponds to the spring extension at which the system displays equal probabilities to occupy either of the two states ($p_1 = p_2 = 0.5$), we get the following :

$$p_2 = \frac{1}{1 + e^{\left(\frac{-k\delta(x-x_0)}{k_B T}\right)}} \quad \text{Eq. 0.1.9.}$$

This relationship is graphically shown in Figure. 0.1.25(a).

The average force f one has to apply on the system to maintain it at position x is written as :

$$\langle f \rangle = p_1 \frac{dG_1}{dx} + p_2 \frac{dG_2}{dx} = kx - k\delta p_2 \quad \text{Eq. 0.1.10.}$$

The force-displacement relationship is non-linear and the width of the non-linear zone is given by δ (Figure. 0.1.25(b)).

The stiffness of this system can be expressed as :

$$\bar{k} = \frac{d\langle f \rangle}{dx} = k - \frac{(k\delta)^2}{k_B T} p_2 (1 - p_2) \quad \text{Eq. 0.1.11.}$$

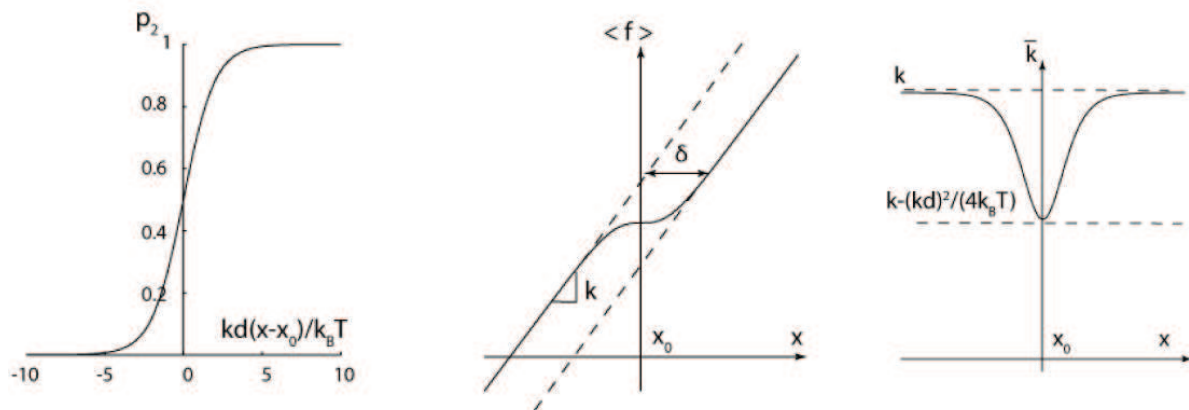


Figure. 0.1.25. (a) Graphical representation of the probability of the system being in state 2. (b) Non-linear force-displacement relation of the system. The two asymptotic branches of slope k are separated by δ which determines the width of the non-linear zone. (c) In the vicinity of x_0 , the stiffness of the system decreases. Adapted from (Plaçaïs, 2008)

This stiffness is not constant and varies with x . Due to the system consisting of two possible states and to the fact that the probability of the system being in either state is dependent on the force, the system as a whole appears more flexible than its elastic component (See Figure. 0.1.25(c)). A similar softening of the acto-myosin crossbridge has been observed with single myosin1 molecules within a narrow region of displacements (Batters, Wallace, et al., 2004). This observation suggests that the conformational change associated with the second step of the myosin's working stroke can be reversed by an external force. This inference is also supported by a recent study with myosin V, in which power-stroke reversals were observed (Sellers & Veigel, 2010).

D/. Myosin in biological systems

1) Myosin II in muscles

1.1 Muscle contractions

There are three kinds of muscles in vertebrates: skeletal muscles which are anchored to bones by tendons and are responsible for skeletal movements and posture maintenance, smooth muscles involved in unconscious motion and contractions and cardiac muscles. Skeletal and cardiac muscles are striated muscles. In all those muscles, contractions are based on the molecular interactions between actin filaments and myosin-II molecular motors.

It is easier to visualize the organization of a muscle fibre by taking a top-down approach and gradually stream down to the most basic functional components. A muscle fibre or myocyte is a multi-nucleated cell is made up of parallel arrangements of myofibrils which are cylindrical structures as long as the muscle fibre and about 1 to 2 μm in diameter and are themselves made up of long chains of sarcomeres. A sarcomere is the basic contractile unit of the muscle. It consists of two disc-like structures known as Z-lines at each end and an arrangement of thin and thick filaments which overlap over a certain distance. The thin filaments are actually actin filaments linked to regulatory proteins, tropomyosin and troponine chief among them. The troponine-tropomyosin complex is bound to actin via troponine such that tropomyosin occupies the myosin-binding groove of actin. The thin filaments are linked to the Z-lines by their barbed ends and their pointed ends are directed towards the centre of the sarcomere.

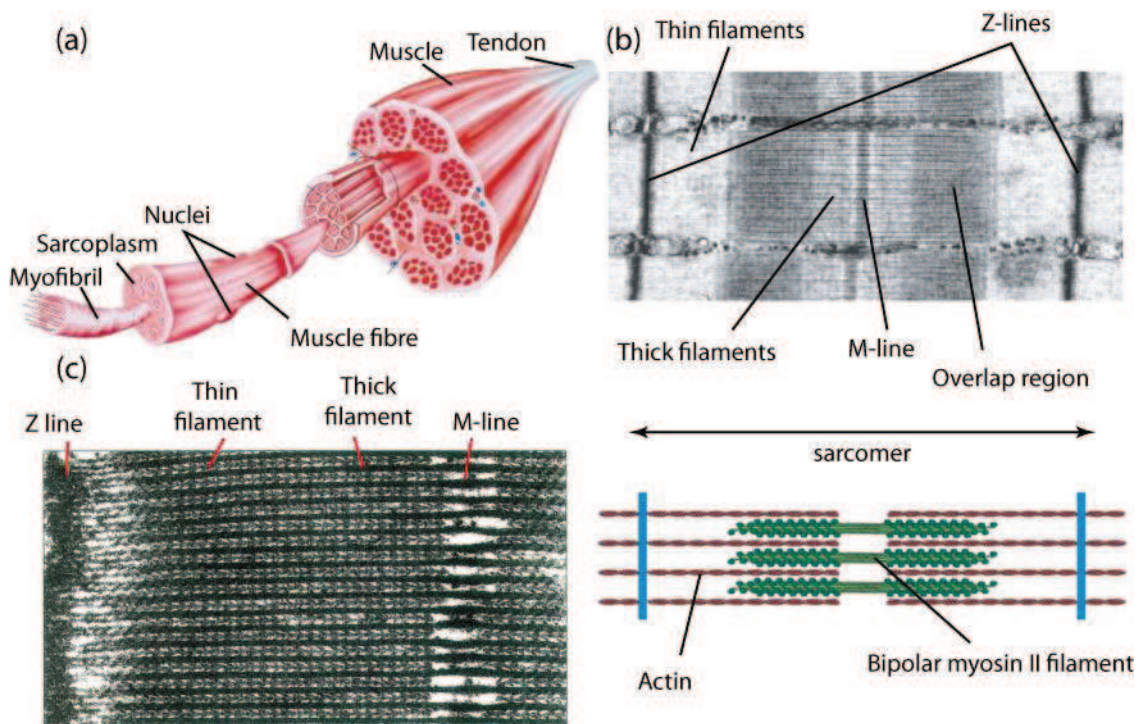


Figure 0.1.26. Structure of a skeletal muscle. (a) A skeletal muscle and its constituents (<http://www.shelfieldpeonline.co.uk/>). (b) Electron microscope image of a sarcomere (<http://www.ks.uiuc.edu/>) and just below, a diagram showing the different components of a sarcomere. (c) Insect sarcomere – alternating actin and myosin filaments can be seen, along with myosin crossbridges between the filaments.

The thick filaments are bipolar myosin II filaments linked together by their tails and proteins of the M-line, a linear structure running in the middle of the sarcomere. They are also

connected to the Z-line by titin. The myosin heads are oriented away from the M-line and towards the Z-line. In the overlap region, myosin interacts with the actin filaments and contraction of the sarcomere takes place when the thin and thick filaments slide over each other under the action of myosin driven by ATP hydrolysis (Figure. 0.1.26(a)).

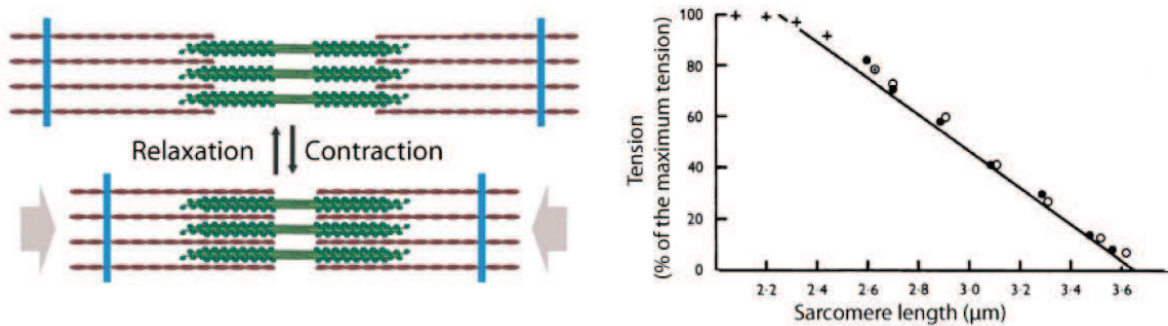


Figure. 0.1.27. (a) The myosin from the thick filaments interact with the actin filaments and exert a force which causes the thick filament to slide over the thin ones ultimately resulting in the contraction of the sarcomere. (b) Tension produced by a muscle fibre as a function of the imposed length of the sarcomere. Above $2.3\mu\text{m}$, an increase in the length of the sarcomeres induces a decrease in the overlap between the thick and the thin filaments meaning a decrease in the available pool of myosin heads (Gordon, Huxley, & Julian, 1966).

A muscle needs to be activated to trigger contraction and tension. The activation mechanism involves an increase in the intracellular calcium concentration in response to a nervous impulse. Calcium binds to troponin which in turn induces a conformational change in tropomyosin that frees the myosin-binding groove of the actin filament. Myosin can then bind to actin and give rise to force generation. Under complete activation conditions ($p\text{Ca} = 5$ and $p\text{MgATP} = 2.5$ where $pX = -\log[X]$), the force exerted by a muscle fibre decreases linearly when the average length imposed to the sarcomeres increases enough to affect the size of the overlap region between thick and thin filaments (Figure. 0.1.27). This observation suggests that the force produced by a muscle is proportional to the number of myosin heads in interaction with the actin filaments, as if the active total tension were the sum of the forces produced by each individual motor.

1.2 Mechanical properties of muscle fibres : Force-Velocity relation

(a) Hyperbolic Behaviour

Muscle mechanics has been extensively studied over the past decades. There are two types of measurements commonly used to characterize the properties of muscles at steady state: isometric contraction and isotonic contraction. In the former, the length of the muscle is fixed and the force required to maintain the length constant is measured. Isotonic contraction does the reverse, a constant force is applied to the muscle and the length is measured over time.

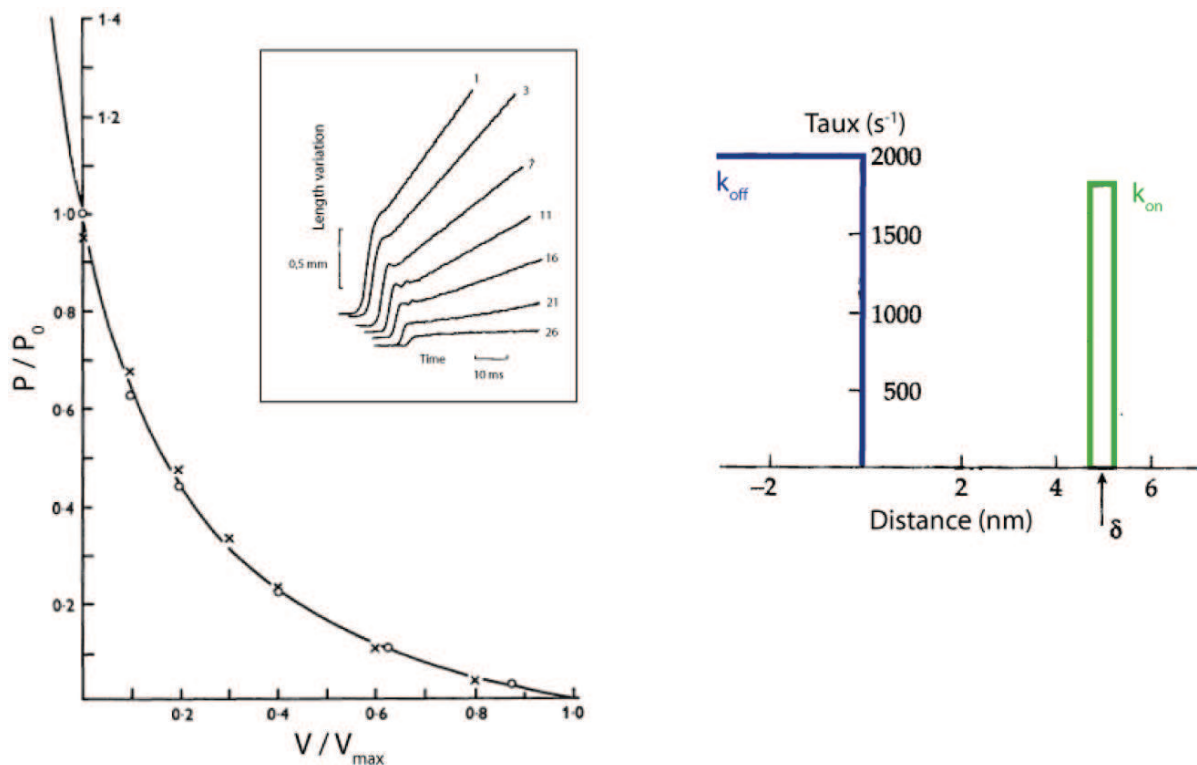


Figure 0.1.28. Force-velocity relation of skeletal muscles. Left: The insert shows the timecourse of a muscle fibre's length to which different loads were applied. The numbers next to each curve correspond to the mass in grams attached to the fibre. After an initial 'jump' which is due to the elastic response of the tendons when the force is applied; the muscle contracts at constant speed with respect to the load. The contraction speed can be drawn as a function of load, giving the force-velocity relation of the muscle. The graph itself shows a hyperbolic fit (Hill's relation) of the experimental data obtained on frog muscle (Huxley, 1974). Right: The hyperbolic relation of the force-velocity relation can be described by the power stroke model by assigning to myosin binding (k_{on}) and unbinding (k_{off}) rate constants that are dependent on the relative position of the myosin and the filament. This model relies on the assumption that the myosin molecule is elastic, hence the rate constants depend on the force applied to the motor ((Howard, 2001).

The force-velocity relation is obtained from the contraction speed as a function of the force applied (see Figure. 0.1.28). The contraction speed is maximum when the muscle has no load applied to it and is null at isometric tension. The contraction speed varies with the force according to a hyperbolic rule known as the Hill Equation :

$$(P + a)(V + b) = (P_0 + a)b \quad \text{Eq. 0.1.12.}$$

; where P is the load on the muscle, V is the contraction speed, P_0 is the isometric tension and a and b are empirical constants which depend on the animal from which the muscle being studied has been extracted and on the temperature.

This behavior has been describe by the classic cross-bridge model of muscle contraction (Huxley, 1957). This model states that each myosin crossbridge produces a force independently from each other. The myosin heads are modeled as elastic elements that produce a force on the filament proportional to their extension. Each myosin head has attachment and detachment rates with respect to actin called k_{on} and k_{off} , respectively. The rate constants depend on the relative position of the thick and thin filaments and thus on the load exerted on myosin. On Figure. 0.1.28 (Right), we can see that using this model, myosin shows characteristics of the power stroke model. Myosin has a high k_{on} in the extension region δ where it generates a large force. When this constraint is removed by the displacement of the filament, the k_{off} increases, preventing force production in the opposite direction.

The model has been tested experimentally. It was demonstrated that both the mechanical work produced and the heat liberated by a muscle increase when the muscle is allowed to shorten. This behavior, which is known as the Fenn Effect (Fenn, 1923), implies that when a muscle contracts in response to a decrease in the imposed load, the average ATPase rate k_{ATP} increases. Because

$$\frac{1}{k_{ATP}} = \frac{1}{k_{on}} + \frac{1}{k_{off}} \quad \text{Eq. 0.1.13.}$$

the load dependence of k_{ATP} implies that of k_{on} and k_{off} .

We can now link the experiments performed on muscles with those performed on single myosin molecules. It was shown that the stiffness of a muscle fibre decreases when the contraction speed increases (Ford, Huxley, & Simmons, 1985) and that the stiffness in absence of load represented about 35% of the stiffness in isometric conditions, implying that the average number of myosin motors bound to actin rises when a force opposes contraction. The number of motors attached is the product of the duty ratio and the total number of motors. Consequently, the duty ratio must increase when the motors experience an opposing force. Because the duty ratio can be written as:

$$r = \frac{1}{1 + \frac{k_{off}}{k_{on}}} \quad \text{Eq. 0.1.14.}$$

these experiments are also consistent with the idea that the attachment and detachment rates depend on the external load. The force produced by the motors is thus adjusted to the speed at which the contractile system operates. In the case of a muscle, when the load applied on it is low, the force produced is also low and the contraction speed is high. Conversely, when the load is high, the contraction speed is low but the force produced is large. As we have seen earlier (see Section B/. 1.2), single molecule experiments have shed light on the molecular mechanism that may explain the mechanosensitivity of myosin.

(b) Anomalous behaviour near isometric conditions

The hyperbolic behaviour of muscle fibres is convenient to understand the mechanosensitivity and force-dependent kinetics of myosin motors in organized systems but it should be noted that in the range of tensions near isometric tension, muscle fibres (obtained from frogs) do not follow Hill's hyperbolic rule (Edman, Mulieri, & Scubon-Mulieri, 1976) (See Figure. 0.1.29). The experiments were performed on frog muscles kept at 0°C.

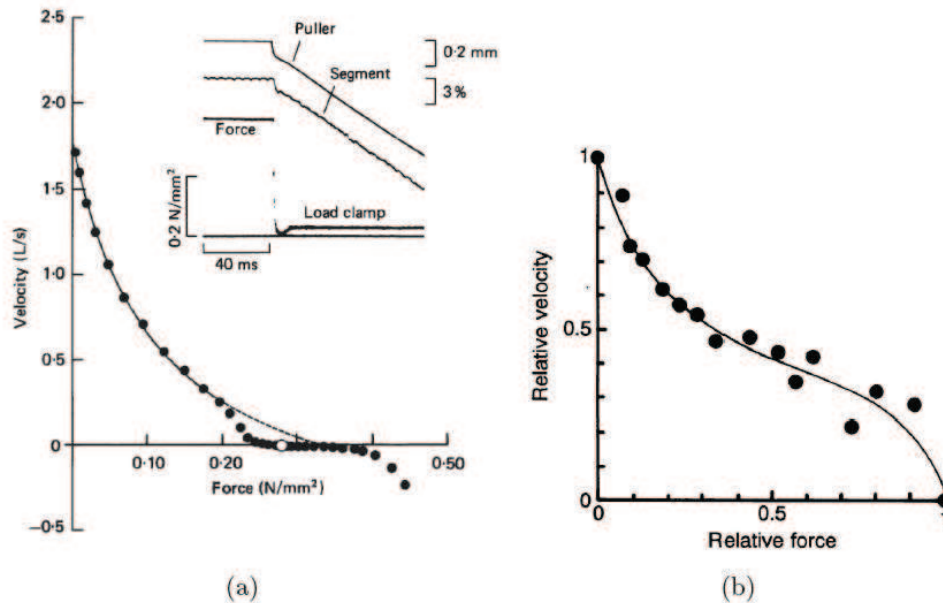


Figure 0.1.29. Force-Velocity relation near isometric conditions. (a) Until 80% of the isometric tension, the force-velocity relation of a frog muscle follows Hill's relation. The insert shows the protocol of an isotonic contraction experiment. The whole fibre (puller) and a segment of fibre contract at constant speed (Edman, 1988). (b) A similar behaviour was observed on in-vitro myosins. The isometric force is 15pN ((Oiwa, Chaen, Kamitsubo, Shimmen, & Sugi, 1990).

Above 80% of the isometric tension, the speed decreases faster than what the Hill relation predicts and the isometric force is also lower than expected. The force-velocity relation continues with very low speed variations for forces higher than isometric tension. At some point, however, at higher loads, the elongation speed increases again (Edman, 1988). This suggests that near isometric tension, there is a change in the behaviour of the muscle fibre. At high strength and low speed, there is an increase in the density of myosin heads attached to actin making it difficult for unattached myosin heads to find a free binding site. The attachment rate decreases near isometric tension (Edman, 1988).

Further experiments performed on myosin molecules in-vitro have shown that this biphasic behaviour might be an intrinsic property of the acto-myosin system. In this study, force-clamp experiments were performed on myosin-covered beads (about 4 – 40 molecules in interaction) running on actin 'rails' (Oiwa et al., 1990). They found that at low forces, the force-velocity relation followed the hyperbolic Hill relation but near the stall force of the motors, the hyperbolic relation is no longer valid.

1.3 Transient response of a muscle fibre to sudden changes in length

When subjected to a sudden change in length, the tension in an isolated muscle fibre varies in three phases (Figure. 0.1.30).

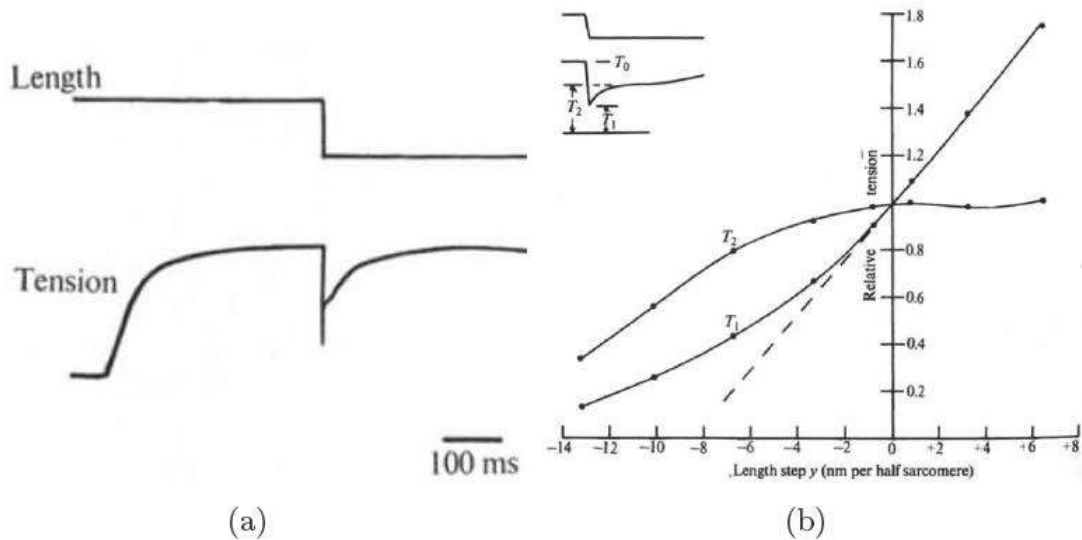


Figure. 0.1.30. (a) Recording of the response of the muscle fibre in response to a sudden decrease in length. The fiber is first activated by calcium and develops an active tension T_0 . In response to the length change, after an elastic response from T_0 to T_1 , we can see a relaxation to the control value in two phases: a fast relaxation from T_1 to T_2 , followed by a slower relaxation from T_2 to T_0 . (b) Graph of phases 1 and 2 as a function of the length step. Insert : Zoom of the initial timecourse of relaxation (from Huxley and Simmons, 1971).

In phase 1, there is a large variation of the tension upon application of the length change. This is due to the response of the passive elastic component of the actomyosin crossbridges ($T_0 \rightarrow T_1$). Phase 2 is a fast recovery of the tension over a timescale of a few ms ($T_1 \rightarrow T_2$). Finally there is a slow return to the base tension ($T_2 \rightarrow T_0$). The relation between T_2 and the step length is non linear: for small displacements, the tension is nearly completely relaxed after the rapid phase of relaxation but for large displacements, there is a marked increase in the slope.

The stiffness can be deduced by obtaining the derivative of T_2 . It is much lower for small displacements than for large ones. This non-linear behaviour has been interpreted as evidence for the existence of different conformational states of the actomyosin crossbridges and related to the mechanosensitivity of actomyosin systems (see section C/. 2) and (Huxley & Simmons,

1971). The overall stiffness of the system drops in the range of displacements that evoke significant rearrangement of the myosins between their different conformational states (2 in a minimal model).

1.4 Partial activation of muscles

Muscle fibres need to be activated by calcium to induce contraction and force generation. By using an intermediate calcium concentration ($pCa \sim 5.5 - 6.5$) lying between the concentration at a relaxed state and concentration at complete activation, it is possible to activate the muscle partially. Partial activation means that the tension developed by the fibre is a fraction of the maximum tension one can obtain during total activation.

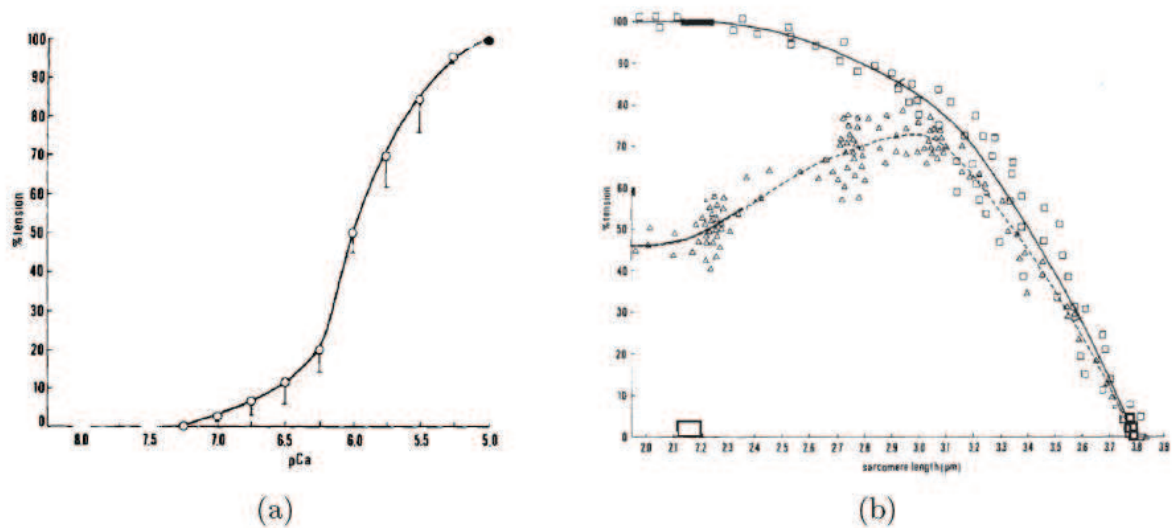


Figure 0.1.31. Partial activation of a muscle fibre. (a) Tension measured in a muscle fibre from the heart of a frog with a sigmoidal relation with respect to calcium. Tension reaches 50% of its maximum value for $pCa=6$. (b) Measurements of the isometric tension on similar fibres at different sarcomere length. Squares : active tension generated by fully activated fibres. Force decreases continuously when the average length of the sarcomeres increases. Triangles : same experiments but with partially activated fibres. The relation is non-monotonous. Between 2.3 and $3\mu m$, tension increases with sarcomere length. Above $3\mu m$, tension falls with rising tension ((Fabiato & Fabiato, 1978).

For a fully activated fibre, isometric tension decreases linearly with an increasing sarcomere length. However a different behaviour emerges in partial activation conditions. When the sarcomere length lies between 2 and $3\mu m$, the force increases when the average length of the sarcomere increases (Endo, 1972; Fabiato & Fabiato, 1978) (Figure. 0.1.31). Above $3\mu m$, the force decreases with an increasing sarcomere length. It is also possible to achieve partial

ADP activation of muscle fibres with (Cooke & Pate, 1985) or without calcium activation (Shimizu, Fujita, & Ishiwata, 1992). In those conditions, the relation between tension and sarcomere length is also non-monotonous (Shimamoto, Kono, Suzuki, & Ishiwata, 2007).

So far we have assumed that each crossbridge was an independent force generator. While this is consistent with the isometric force being proportional to the overlap length between thick and thin filaments at total activation, it fails to explain the events occurring at partial activation i.e. an increase in the tension when the sarcomere length increases. This observation suggests that the crossbridges actually work as cooperative activators and that this becomes apparent during partial activation. A model has been put forward (Ishiwata, Shimamoto, Suzuki, & Sasaki, 2007) involving a decrease of the interfilament spacing in response to a stretch of the sarcomeres and the cooperativity of ADP-bound crossbridges. The latter induces a lowering of the stiffness of the actin filament and hence an increase in its fluctuation amplitude. The combined effect of the two effectively increases the local density of motors that can interact with actin, thus augmenting force production.

1.5 Stretch activation of muscles

When a muscle fibre is stretched, the induced tension developed by the fibre can increase after a transient relaxation phase, and even rise beyond the tension developed by the muscle under control conditions (Pringle, 1978). In insect muscles and cardiac muscles, the tension is maintained at this peak value and does not return to its initial lower value as long as the muscle remained stretched.

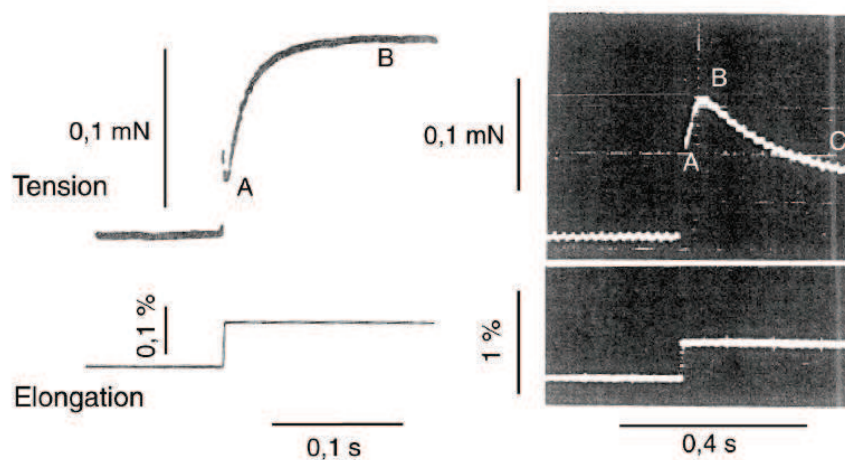


Figure 0.1.32. Stretch activation of muscle fibres. When subjected to a sudden stretch, the tension developed by an insect flight muscle (left) after a relaxation phase (A), reaches a

stationary value which is higher than the control value (B). In the skeletal muscles of the rabbit (right), the same mechanism can be seen except that after a short time, the tension relaxes (C) to his original value (image was cropped and this is not shown) (Pringle, 1978).

2) Myosin 1c and the mechanosensitivity of hair cells in the inner ear

2.1 Mechano-electrical transduction in the inner ear of vertebrates

Hair cells are located in the inner ear of vertebrates. They are responsible for the transduction of mechanical stimuli into nervous impulses in the hearing process. The most striking organelle of those cells is the hair bundle that extends from the apical surface of each hair cell. The hair bundle acts as a mechano-receptive antenna. A hair bundle is made up of stereocilia, which are rigid cylindrical processes containing bundled parallel actin filaments. The stereocilia are arranged by increasing height similar to the pipes of a church organ (Figure. 0.1.33). They are connected to each other by lateral links, including diagonal tip links going from the top of one stereocilium to the flank of the nearest taller neighbour.

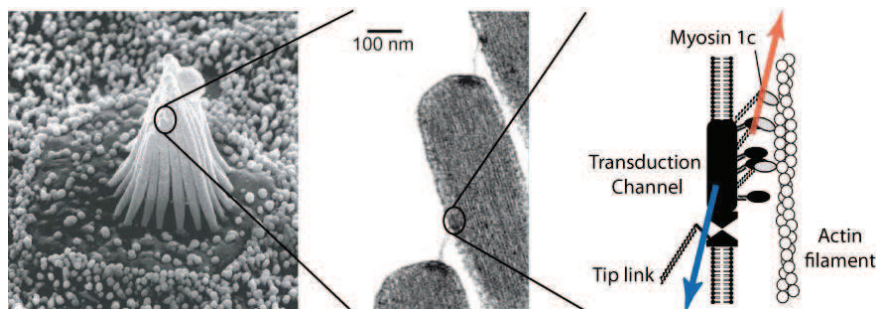


Figure. 0.1.33. Electron micrograph of the hair-cell bundle of a bullfrog (the cell body is embedded in the epithelium and the stereocilia located on top protrude out of the epithelium). By zooming in on the top of a stereocilium we can see the tip links connecting the stereocilia from different rows. The tip links are connected to the transduction complex. Myosin 1c exerts a force on the actin filament towards the top of the stereocilium (red arrow). At rest, this active force is balanced by the tension in the tip link (blue arrow) and determines the open probability of a mechano-sensitive channel.

In-vivo, the hair cells are embedded in an epithelium forming a field of protruding hair bundles. The latter are surrounded by a fluid serving as a propagation medium for the mechanical stimuli brought from the outside by the rest of the hearing apparatus. Thanks to interstereociliary links, a mechanical stimulus can move an entire hair bundle as one single structure from the shortest to the tallest stereocilia (this direction is defined as positive by convention). A deflection of the hair bundle triggers the opening of the ion channels found on the membrane of the stereocilia. The resulting entry of cations in the hair bundle initiates a

signaling cascade which starts with the depolarization of the cell and ends with the liberation of neurotransmitters at an afferent synapse at the base of the cell body.

Mechano-electrical transduction is remarkably fast – human beings can hear frequencies up to 20 kHz. This high speed indicates that the ion channels of the hair bundles are directly activated by the mechanical stimuli without any biochemical secondary messengers which are markedly slower. In the gating spring model (Corey & Hudspeth, 1983), the open probability of the channel is directly controlled by the tension in the elastic element to which it is coupled (Figure. 0.1.33). At low or null tension, the channels are closed. A deflection in the positive direction increases the tension and increases the open probability of the transduction channels.

The channels present significant open probability at rest (Corey & Hudspeth, 1983). This observation implies that there is an active mechanism to maintain the tip link under enough tension. This tension could be coming from the myosin-1c motor molecules that anchor the transduction complex to the actin filaments of the stereocilia (Figure. 0.1.33) (Hudspeth & Gillespie, 1994). The number of myosins has been estimated to about 50 – 150 per transduction complex which produces a tension of about 14pN in each link (P. Martin, 2008).

2.2 Myosin 1c as an adaptation motor

Like all sensory systems, the hair cells are endowed with an adaptation mechanism that allows them to remain sensitive to small transient stimuli in presence of persistent and constant saturating stimuli. The adaptation mechanism can be studied by imposing steps to the hair bundles and observing the transduction current.

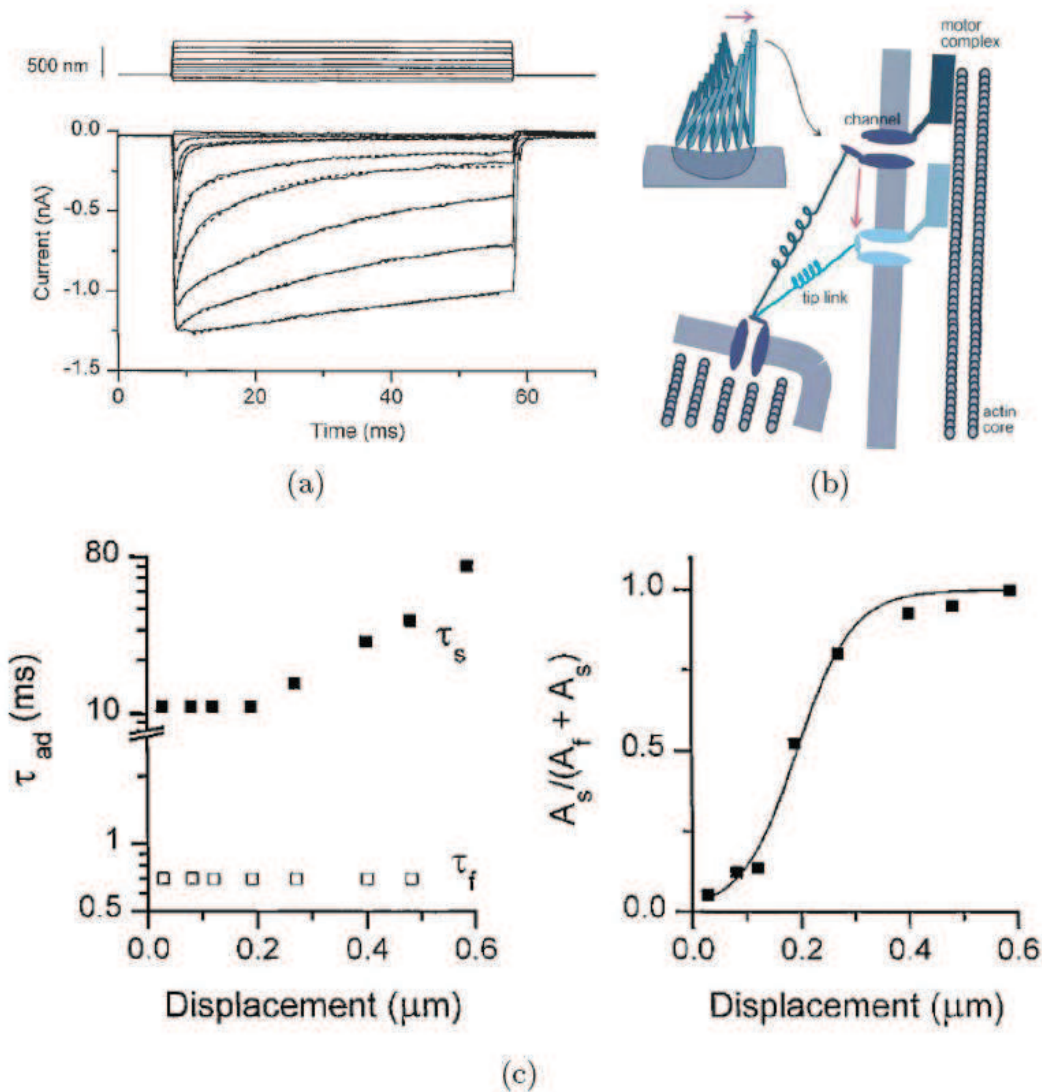


Figure 0.1.34. Adaptation in the inner ear. (a) The transduction current from turtle hair cells in response to increasing steps over a relatively long timecourse. After the maximum is reached, the fall in current is fitted with a bi-exponential relation in (c) (Wu, Ricci, & Fettiplace, 1999). (b) After a positive deflection, the excess tension in the elastic element is relaxed when the channel slides towards the base of the stereocilium which promotes the closed state ((Gillespie & Corey, 1997). (c) Left: time constants τ_c (slow) and τ_f (fast) obtained by the fit performed in (a). Right: Ratio of the slow exponential to the sum of the two VS the displacement. The ratio determines the fraction of adaptation that can be attributed to the slow phase.

In response to positive deflections, the absolute value of the current increases meaning that the channels open. The current then gradually decreases to its initial value, indicating that the channels are reclosing (Figure 0.1.34(a)). The role of adaptation is to return the open probability of the channels to its resting value in order to restore sensitivity of the hair bundles to transient stimuli.

The kinetics of the adaptation process can be described by two time constants. The fast time constant varies from tens of microseconds in the rat to a few milliseconds in the frog. The slow timescale of adaptation varies between 10 to 100 ms. For weak displacements, the rapid phase is largely responsible for adaptation. Conversely, it does not intervene for large displacements (Figure. 0.1.34(c)).

According to the gating-spring model of mechano-electrical transduction, the channels open in response to a positive stimulus due to an increase in the tension in the elastic element coupled to the channel. Adaptation can be explained by a mechanism which releases the tension in the gating spring during a static positive stimulus, leading to reclosure of the channels. In the case of a negative stimulus, such a mechanism would be required to increase tip-link tension and must thus be active. Myosin 1c is a strong candidate for the role of adaptation motor in the inner ear (Gillespie & Cyr, 2004). This motor is indeed necessary for adaptation to take place (Stauffer et al., 2005). However, it remains uncertain that myosin motors are fast enough to mediate adaptation in the submillisecond timescale. For fast adaptation, electromechanical feedback of the Ca^{2+} component of the transduction channel on the state of the transduction channels appear to be necessary (Wu, Ricci & Fettiplace, 1999)

2.3 Force-Displacement relation of a hair bundle

The mechanical properties of the hair-cell bundle can be studied by measuring its force-displacement relation. This is done by imposing displacement steps to the bundle and measuring the force necessary to maintain this displacement (P Martin & Hudspeth, 2001). The measurements are performed over short timescales (~3ms after application of the first step) in order to avoid the influence of adaptation as much as possible. For large displacements both positive and negative, the force-displacement curve is linear showing behaviour analogous to a simple Hookean spring. However, near the resting position of the hair cell bundle, the relation is no longer linear and a zone of negative stiffness can be observed.

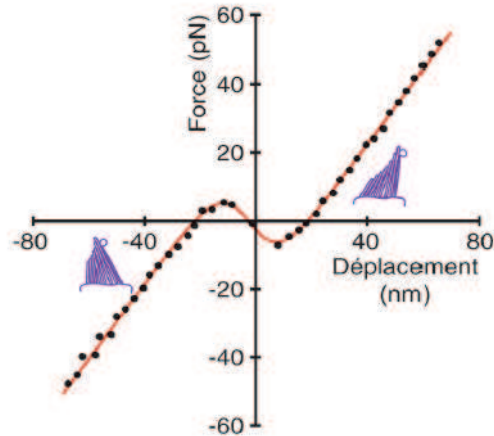


Figure 0.1.35. Force-displacement curve of a hair cell bundle. For small displacements, the relation is non-linear and can become negative. This zone of negative stiffness is mechanically unstable (data from Martin et al, 2000).

This region of negative stiffness is mechanically unstable and represents a range of positions where the hair cell bundle cannot remain at rest.

This negative stiffness can be explained by a phenomenon called “gating compliance” (Howard and Hudspeth, 1988), in which gating of the mechanosensitive transduction channel create force in the direction of the applied stimulus. This model is highly similar to the interpretation of the non-linear behaviour of the T2 curve obtained in experiments on muscles (see section D/. 1.3), suggesting a common mechanism between the two. Using a similar reasoning, it can be said that the reduced stiffness is due to the fact that the system can exist in two stable states (open channel and closed channel) separated by a conformational change. The difference here is that, contrary to what was observed in muscles, the magnitude of the conformational change is large enough to overcome the stiffness of the elastic component of the gating spring, effectively making the overall stiffness of the system negative.

By using equation 0.1.11 detailed in section C/. 2) , it is possible to calculate the stiffness of the gating spring and the conformational change. For the hair cell bundles of the bullfrog sacculus, the gating spring has a stiffness of 0.57 pN/nm and the magnitude of the conformational change is 8.2 nm (P Martin, Mehta, & Hudspeth, 2000).

3) Spontaneous oscillations of acto-myosin systems

We have described the general architecture of muscles and hair-cell bundles, as well as their mechanical properties. Both biological systems are organized myosin-based systems and both

show interesting properties thanks to the action of the actomyosin system. Those two systems are also known to oscillate spontaneously under certain conditions and there is strong evidence that myosins have an active role in these oscillatory properties.

3.1 Spontaneous oscillations in muscle fibres

In some insects, the flight muscles display oscillations that are asynchronous to the activating nervous impulses they receive (Pringle, 1978). Similar spontaneous oscillations are present in cardiac muscles (Fabiato & Fabiato, 1978; Fukuda, Fujita, Fujita, & Ishiwata, 1996) and more surprisingly in skeletal muscles (Okamura & Ishiwata, 1988). In the latter, the oscillations do not occur in physiological conditions.

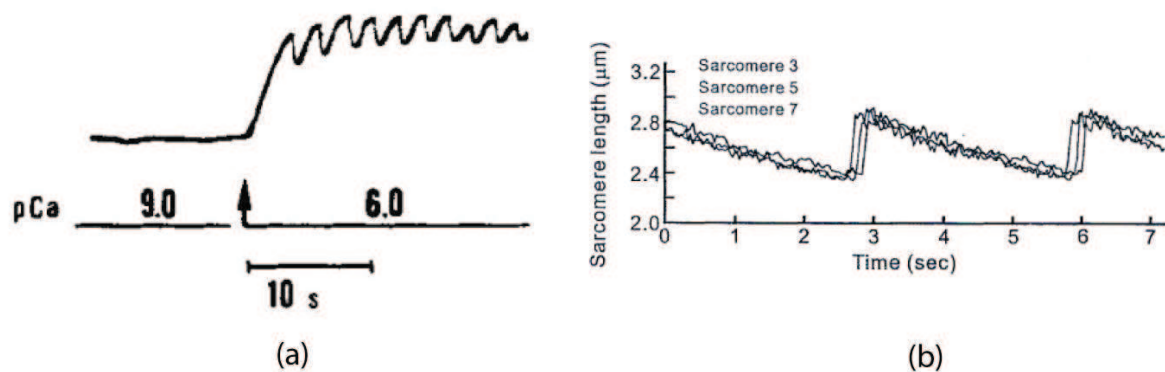


Figure 0.1.36. (a) Oscillations of isometric tension of cardiac muscle fibre (rat) under partial calcium activation (arrow). Upon partial activation, the tension increases and oscillates around its new mean value (Fabiato & Fabiato, 1978). (b) Length of three sarcomeres over time in a myofibril (skeletal muscle, rabbit) suspended between two glass fibres. The triangular shape is characteristic of skeletal muscle fibre oscillations (Ishiwata et al., 2007).

In in-vitro experiments, the oscillatory behaviour of muscle fibres can be observed by spontaneous tension oscillations in isometric conditions (Figure 0.1.36(a)) or by monitoring spontaneous oscillations in the length of sarcomeres (Figure 0.1.36(b)). These oscillations have a characteristic triangular shape, with a slow phase in the direction of the natural mechanical motor activity and a rapid phase in the opposite direction. For the spontaneous oscillations to appear in skeletal and cardiac muscle fibres, a number of conditions must be met:

- The fibre must be partially activated either by calcium (Fabiato & Fabiato, 1978) or ADP (Okamura & Ishiwata, 1988). The need for activation implies that myosin is involved in the oscillation process.
- The average length of the sarcomeres must be lower than $3\mu\text{m}$.
- A load must be applied to the fibre. Oscillations are never observed in-vitro on free-floating muscle fibres.

It is interesting to note that the conditions necessary for oscillations to occur are identical to those in which the relation between tension and sarcomere length is non-monotonous (See Section 1.4 and Figure. 0.1.31). Moreover, the range of sarcomere lengths over which oscillations appear coincides with the range of sarcomere lengths in which the isometric tension in a partially activated muscle fibre increases, strongly suggesting a link between the two phenomena.

Oscillations were also recorded on cardiac muscle fibres where the thin filaments (i.e. actin and its regulatory proteins) were replaced by naked actin filaments (Ishiwata, S, Funatsu T, 1998). In this configuration, actin is no longer regulated by its associated proteins. Oscillations were observed in presence of 2,3-butanedione 2-monoxime (BDM), a molecule which partially interferes with myosin activity by mimicking the tropomyosin-troponin complex. These experiments suggest that the auto-oscillatory behaviour of myofibrils are an intrinsic property of the actomyosin system, irrespective of regulatory proteins.

3.2 Spontaneous oscillations of hair cell bundles

(a) Characteristics of hair cell bundle oscillations

When a hair cell from the sacculus of a bullfrog is placed in-vitro in an environment mimicking its physiological working conditions, the hair-cell bundle oscillates spontaneously (P Martin, Bozovic, Choe, & Hudspeth, 2003; Pascal Martin & Hudspeth, 1999).

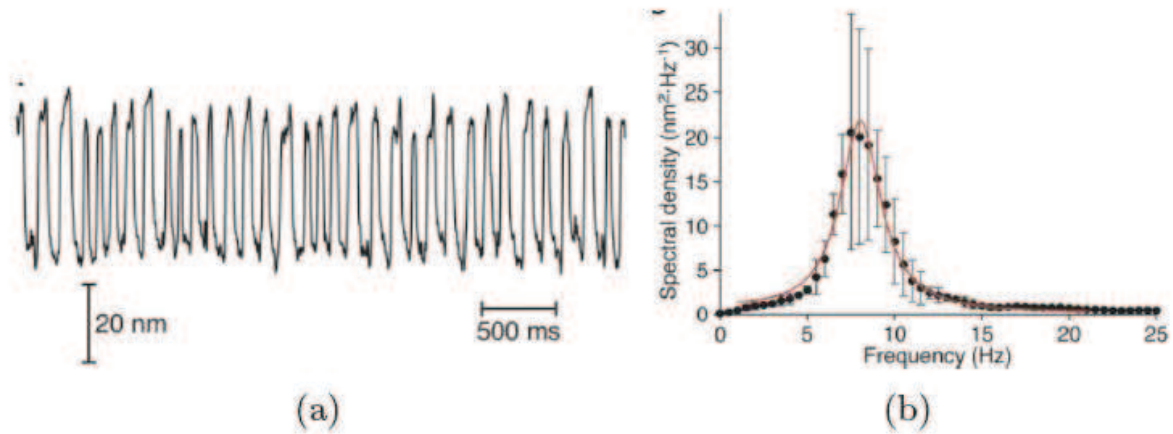


Figure 0.1.37. (a) Square-shaped oscillations of hair cell bundle (Peak-to-peak amplitude = 28nm). It was recorded by monitoring the movement over time of a flexible glass fibre attached to the kinociliary bulb of the bundle. (b) The power spectrum of the signal recorded in (a) with a peak centered at 8Hz. Quality factor = 2 (P Martin, Hudspeth, & Jülicher, 2001).

The oscillations have a rectangular shape; each half-period consists of a slow phase in one direction and a rapid transition in the opposite direction. The frequency lies usually between 5 and 50 Hz and the peak-to-peak amplitude can go up to 100 nm.

The oscillatory motion operates within a calcium concentration range from 100 μM and up to 1 mM. In this range, the frequency increases with an increasing calcium concentration. If a flexible glass fiber is placed into close contact with the kinociliary bulb, the frequency and amplitude of the oscillations depend on the rigidity of the fiber with a more rigid fiber causing faster oscillations with lower amplitudes (P Martin et al., 2003). Above a fibre stiffness of approximately 1 $\mu\text{N}/\text{nm}$, the oscillations disappear.

The joint study of the spontaneous motion and the response of oscillating hair cell bundles to sinusoidal stimuli has shown that the fluctuation-dissipation theorem is violated near the characteristic oscillation frequency (P Martin et al., 2001). This implies that spontaneous oscillations are caused by active components, suggesting that the adaptation motors, myosin 1c are most likely to be involved. It has been shown that the oscillations can enhance the mechanosensory functions of the hair cells (P Martin et al., 2001).

(b) Model for the spontaneous oscillations of hair cell bundles

In the gating spring model, the open probability of the channel P_0 depends on the force exerted by myosin 1c on the elastic element linked to the channel. A dynamic instability can arise when gating compliance is strong enough to yield negative stiffness (see section C/. 2) . To take into consideration the calcium regulation of the open probability of the channels at rest and of the adaptation kinetics, the stall force F_s of the motors is assumed to be a decreasing function of the calcium concentration. This relation can be described as :

$$F_s = F_{max} (1 - SP_0) \quad \text{Eq. 0.1.15.}$$

where S is a numeral parameter defining the impact of the calcium feedback on motor activity. The fact that the oscillations only appear within a certain range of calcium concentrations means that it is highly analogous to what happens in muscle fibres, i.e. oscillations only appear in partial myosin activation conditions.

Figure. 0.1.38 shows a model for the oscillation of hair cell bundles based on the above assumptions. In this model, the force-velocity relation of the motors is linear and no oscillations are observed if the activity of the myosin motors is not calcium-regulated. Experimentally, when the channels are blocked by gentamicin, the oscillations stop and the force-displacement relation becomes linear (P Martin & Hudspeth, 2001)

3.3 Summary

The two systems we have described exhibit spontaneous oscillations. Oscillations are caused by two different motors, myosin II in muscles and myosin 1c in the hair cells but yet the characteristics of each system are intriguingly similar. In both cases, the motors are non-processive and thus they have to work together. Another condition necessary for the oscillations to occur is the presence of an elastic force in the system which opposes the force produced by the motor assemblies. In the muscle fibres, this was due to the load imposed and in the hair cell bundles, the elastic element of the gating spring.

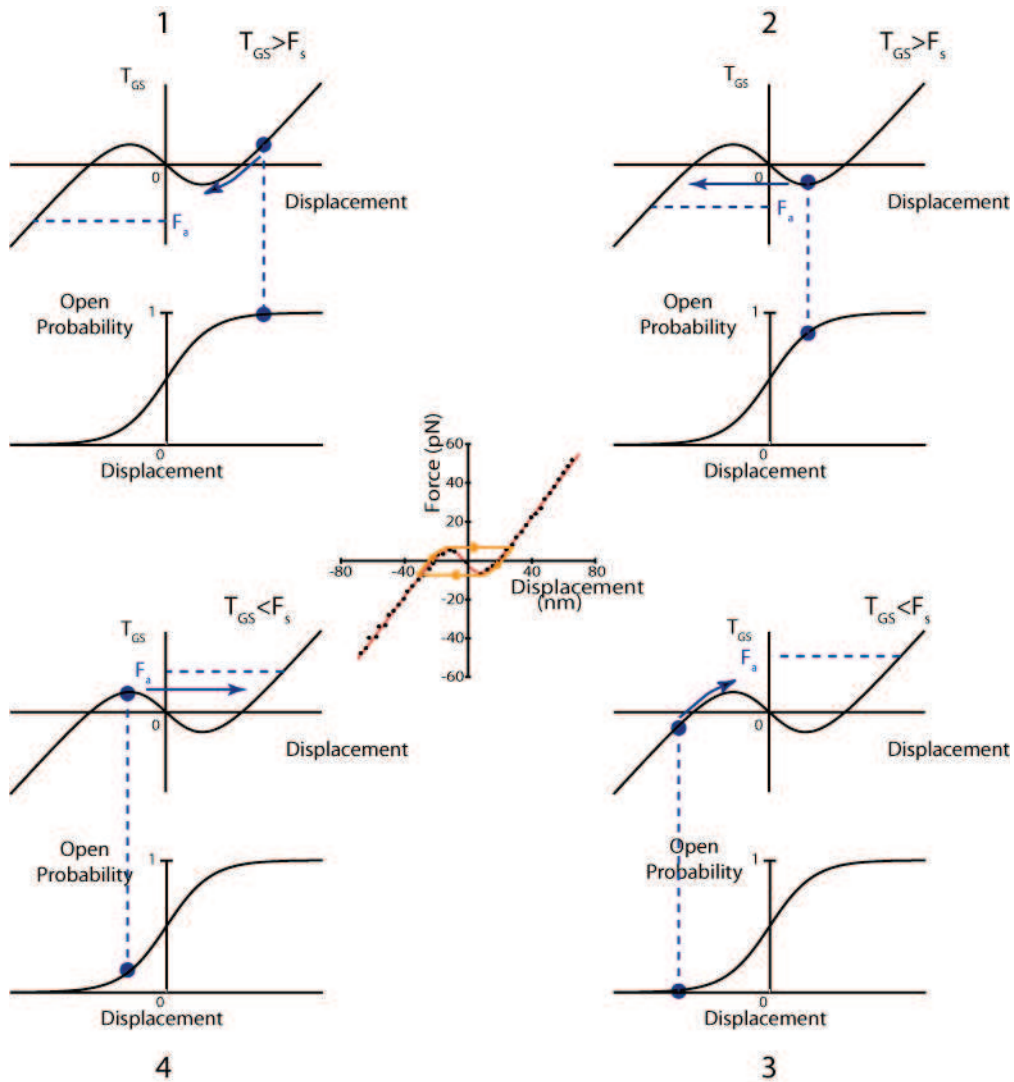


Figure 0.1.38. Model for the spontaneous oscillation of the hair-cell bundle. In state 1, the bundle is deflected in the positive direction, the tension T_{GS} in the gating spring is high and the channels are open. This implies that calcium can flow in and that the concentration of calcium near the motors is high and hence the stall force of the motors is low. As such, the motors slide towards the base of the stereocilium to close the channel. We now arrive at state 2, near the unstable region of negative stiffness. Since the channels are now closing, the stall force of the motors has increased but not enough to stop the motors. The hair cell bundle then 'jumps' to the other side of the unstable region and we reach state 3. Here the open probability is much lower and the channels are mostly closed reducing the calcium concentration which causes an increase in the stall force of the motors. The motors are now 'strong' enough to climb up the stereocilium to reopen the channels until we reach state 4 where the hair cell bundle reaches the unstable region again and jumps towards the other side (positive deflections side). The oscillations are due to the effects of the calcium feedback on the stall force of the motors and the presence of an unstable zone. This means that the motors never reach a stable position where $F_s = T_{GS}$ which drives the hair cell bundle to perform cycles around the unstable region of negative stiffness.

E/. An intermediate scale

1) Evidence for collective motor effects

From the mechanical properties of single molecular motors, we have tried to move up the organization ladder and to look at the properties of more complex actomyosin systems. However the properties of complex systems directly derive from single molecule properties only if one supposes that each basic component can perform its function independently from one other. Several of the observations we have seen previously on muscle fibres and hair cell bundles have proved that such an approach is too simplistic concerning myosin since we cannot fully explain them using the properties of single motors.

- Under complete activation conditions, a myofibril produces a force proportional to the number of motors involved. In this case, the isometric tension of the fibre decreases with the length of the sarcomere. Under partial activation conditions, however, there is a range of sarcomere lengths where the isometric tension produced by the fibre increases when the average sarcomere length increases (see section D/. 1.4).
- Spontaneous oscillations occur in actomyosin systems when a load is applied. Those oscillations appear under the same conditions for which the force-displacement relationship of sarcomeres is non monotonic.
- While the independent force generator model (Huxley, 1957) can describe the hyperbolic force-velocity relation of muscle fibres at small loads, it fails to predict the biphasic behaviour observed near isometric load. When muscle fibres operate near isometric tension, i.e. near the anomalous region of the force-velocity relation, they spontaneously oscillate.

These observations in muscle point towards properties that emerge from the collective action of myosins and that cannot be properly explained from the characteristics of single motors. Signatures of collective effects have also been obtained in vitro. One of them was performed by observing NK11, a mutant form of the motor NcD that belongs to the kinesin superfamily and interacts with microtubules (Endow & Higuchi, 2000). Collections of NK11 motors were shown in gliding assays to power bidirectional movements of the microtubules, with comparable velocities: a movement directed along a direction abruptly reversed its direction in a stochastic manner. Although a single NK11 motor is non-processive, a sufficiently high number of motors pulling in one direction increases the probability that the others will follow

suit, giving rise to directed motion. Bidirectional motion was also reported in the case of actin filaments gliding over myosin-II motors in one-directional grooves in the case where the negatively-charged actin filaments were subjected to an electric field (Riveline et al., 1998). Finally, as detailed below, our group has previously shown that myosin-II molecules can give rise to spontaneous oscillations when subjected to elastic loading (Plaçais et al, 2009).

2) Theoretical descriptions of collective motor effects and oscillations

We will now give a theoretical view of how oscillations can arise from collective motor. The model (Jülicher & Prost, 1995, 1997) differs from the power stroke model in that it ignores the molecular details of the mechano-chemical cycle of individual motors and focuses instead on the essential characteristics of molecular motors: the motors interact with a filament and exert a force that is powered by ATP hydrolysis.

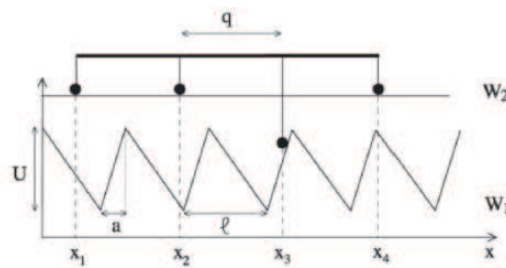


Figure. 0.1.39. Diagram showing motors periodically spaced with a period q and rigidly coupled to each other. The motors interact with the filament via the potentials W_1 and W_2 , where W_1 has a period of l . W_1 is asymmetric in this case.

The model considers a collection of N motors rigidly coupled to each other and periodically spaced. Each motor can exist in two energy states, a free state (State 2) of potential energy W_2 and a bound state (State 1) with a periodic potential W_1 . The periodicity of this potential is equal to the periodicity of the filament and W_1 represents the interaction potential between motor and filament (Figure. 0.1.39). Even if the filament (in the case of myosin motors, the filament is actin) is polar and thus asymmetric, W_1 can be symmetric depending on the type of motor being studied. The periodicity of motors and filaments are incommensurate. This is the case in muscles but also in any situation where the motors are randomly distributed such

as in in-vitro experiments (for this assumption to hold, N must be large). Remarkably, it was shown that the activity of the system can give rise to non-monotonic force-velocity relations.

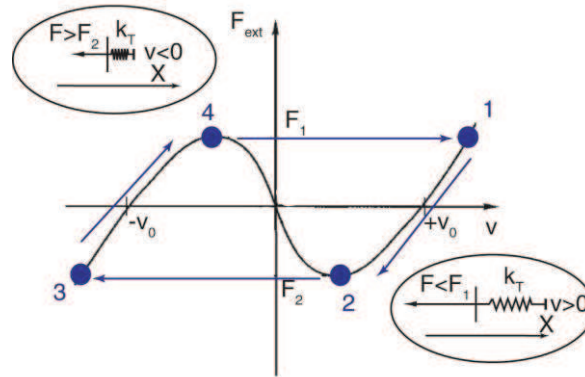


Figure 0.1.40. Oscillations of a collection of molecular motors coupled to a spring.

We shall now give a simplified description of the occurrence of the oscillations according to the model. It should be noted that since the model is based on a force-velocity relation and not a force-displacement relation, the oscillations predicted can be large compared to the displacement produced by a single motor. Figure 0.1.40 shows the force-velocity relation of a collection of motors under an elastic load and the oscillation cycles. At point 1, the velocity of the motors is positive, i.e. pushes the motors in their natural direction of motion, and the force exerted by the spring is F_1 . Since the motors move in the positive direction, the elastic pushing force will decrease with respect to F_1 which will tend to slow the motors down until we reach point 2 (the spring now opposes motor movements) at the threshold of the unstable zone. The motors will then undergo a transition at constant force F_2 to the opposite part of the unstable zone and will now be in the negative velocity domain (point 3). The motors are now moving in the opposite direction which will trigger an increase in the elastic force until the system reaches point 4. The system will then return to point 1, thus completing the cycle.

3) Spontaneous motor oscillations in a minimal actomyosin system

(Plaçais, Balland, Guérin, Joanny, & Martin, 2009)

As we have discussed earlier, there are a number of phenomena arising from the collective effect of myosin motors, the oscillatory property being the most interesting. Those effects have been mostly studied either from the physiological point of view involving relatively

complex biological structures such as sarcomeres and hair-cell bundles or from the molecular side by putting into play a single motor interacting with a single strand of its substrate namely one actin filament. While those experiments and studies have provided valuable insight into the workings of molecular motors in general, studies at the intermediate scale between those two extremes have been lacking, bringing forth the question: how do molecular motors behave when made to work collectively in small assemblies? If one could study this intermediate regime experimentally, would the results match the theoretical expectations?

This study was conducted in our lab prior to my arrival by Pierre-Yves PLACAIS. The goal was to test the ability of a minimal actomyosin system to generate spontaneous oscillations under an elastic loading. The set-up used was a modified motility assay where biotinylated actin filaments carried streptavidin-coated beads. The beads served a dual purpose, both as handles for optical tweezer and as probes to visualize any movement of the filament. The tweezers provided the elastic load opposing the movement of the motors.

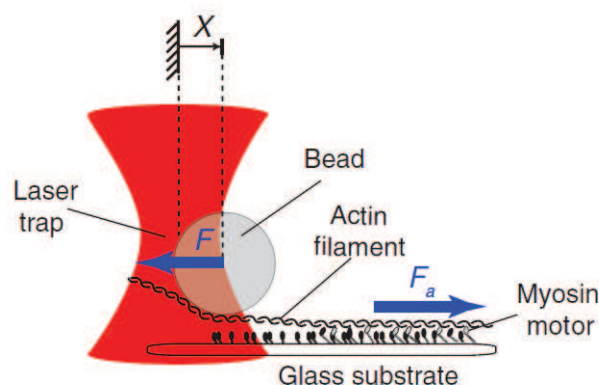


Figure. 0.1.41. Gliding assay with elastic loading. The motor molecules develop an active force F_a on the actin filament in a direction defined here as positive. The optical trap imposes an elastic restoring force $F = -k_T \times X$ in the negative direction. k_T represents the trap stiffness and X the position of the bead with respect to the center of the trap.

During the experiment itself, a filament carrying a bead was brought to the myosin II-covered surface until the motors started to pull the filament away from the trap centre. The trap exerted a restoring force on the bead and the motors. The system then exhibited noisy spontaneous oscillations as shown on Figure. 0.1.42 (the characteristics of these oscillations are also shown).

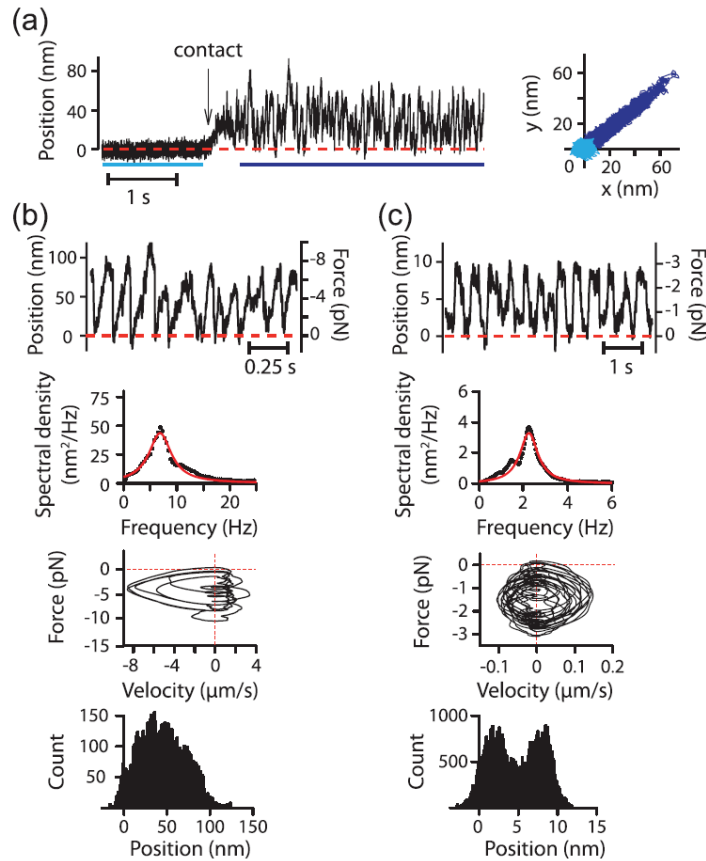


Figure 0.1.42. Time course of bead position at the onset of interaction between actin and myosin (left) and bead trajectories in the horizontal plane before and after contact (right). (b) and (c) from top bottom, spontaneous oscillations, the spectral density, the force-velocity relation and the position histogram of the bead position. (b) Mean position, +50 nm; rms magnitude, 29 nm; peak-to-peak magnitude ~80 nm; spectrum peak at 6.9 Hz. The trap stiffness was 0.083 pN/nm. (c) Mean position, 4.8 nm; rms magnitude, 3.2 nm; peak-to-peak magnitude, 8.5 nm; spectrum peak at 2Hz, Trap stiffness was 0.31 pN/nm

The oscillations observed could be classified into two main groups: asymmetric and triangular, which resembles the oscillations of muscle fibres, and square-shaped like in hair-cell bundles. The set-up involved a relatively large number (15-130) of randomly distributed motors working in groups and the motors were rigidly coupled via the glass surface used in the experiments. The results were compared with stochastic simulations based on the two-state model described earlier. The simulations showed results coherent with the experimental results; with oscillations appearing as asymmetric triangular in some cases and more symmetric in others suggesting that the oscillations arise due to the dynamical properties of the motor assembly as predicted by the model. However the appearance of the oscillation waveform could not be controlled experimentally implying that it depends on an unknown or uncontrollable parameter.

This study demonstrated that a minimal actomyosin system under elastic loading could effectively replicate both oscillation types from two apparently dissimilar organized biological systems. This suggests that the ability to oscillate under an elastic restoring force opposing the movement of the motors is an intrinsic ability of the actomyosin system.

Our objective is to expand on this work, by first reproducing the experimental observations seen and seek to have a better control of the oscillations by trying to uncover the parameters influencing its characteristics. The parameters that could have an influence on the properties of the oscillations are the stiffness of the system, the number of the motors engaged and the type of motors. During this endeavour, we sought to address those questions and develop new biochemical and technological tools to stimulate and study the molecular motor oscillations in-vitro and this eventually became a major aspect of this work over the three years of the PhD.

PART I

Molecular motor oscillations
under elastic loading.

Part I

Chapter I: Materials and Methods

This chapter describes the technical and biochemical tools necessary to our experiments. It is divided into two main parts. The first part gives a description of the instruments and experimental set-up to interact with the acto-myosin system and measure its characteristics. The second part, which is devoted to the biological molecules themselves, details the biochemical recipes and the construction of our in-vitro acto-myosin system.

A/. Instrumentation

The set-up, which was built during the PhD thesis of Pierre-Yves Plaçais and the postdoc of Martial Balland, has been described at length previously (PhD thesis of P.Y. Plaçais, 2008). While, over time, there have been some enhancements, whether voluntary (mostly thanks to my fellow colleagues, especially Volker BORMUTH and our engineer, Mathieu RICHARD) or due to the passage of time such as wear and tear, the set-up as a whole remains largely unchanged. Its design was constrained by the fact that single molecular motors typically exert forces in the piconewton range and involve displacements on the order of nanometers, which motivated the use of optical tweezers as force transducer.

A summary diagram of the set-up is shown on Figure 1.1.1. The continuous light beam of an infra-red laser ($\lambda = 1064 \text{ nm}$) is enlarged ten times by two telescopes (L1-L2 and L3-L4), directed to the back focal plane of a high numerical-aperture ($\text{NA} = 1.35$) $\times 60$ objective and focused in the sample plane. The acousto-optic deflectors found in the optical path of the laser beam allow us to control the position and intensity of the laser. Our microscope is equipped with two arc-lamps: a xenon lamp is used to illuminate the sample and a mercury lamp is used to visualize Alexa-594 fluorescence via special filters (excitation filter F2 (HQ560/40), emission filter F3 (HQ630/60)). The xenon lamp is used to image a bead in the sample plane onto piezo-mounted four-quadrant photodiodes, thus allowing position measurement of the bead. A CCD camera is mounted on the microscope to visualize the bead in bright field or fluorescence from the actin structures (see inset).

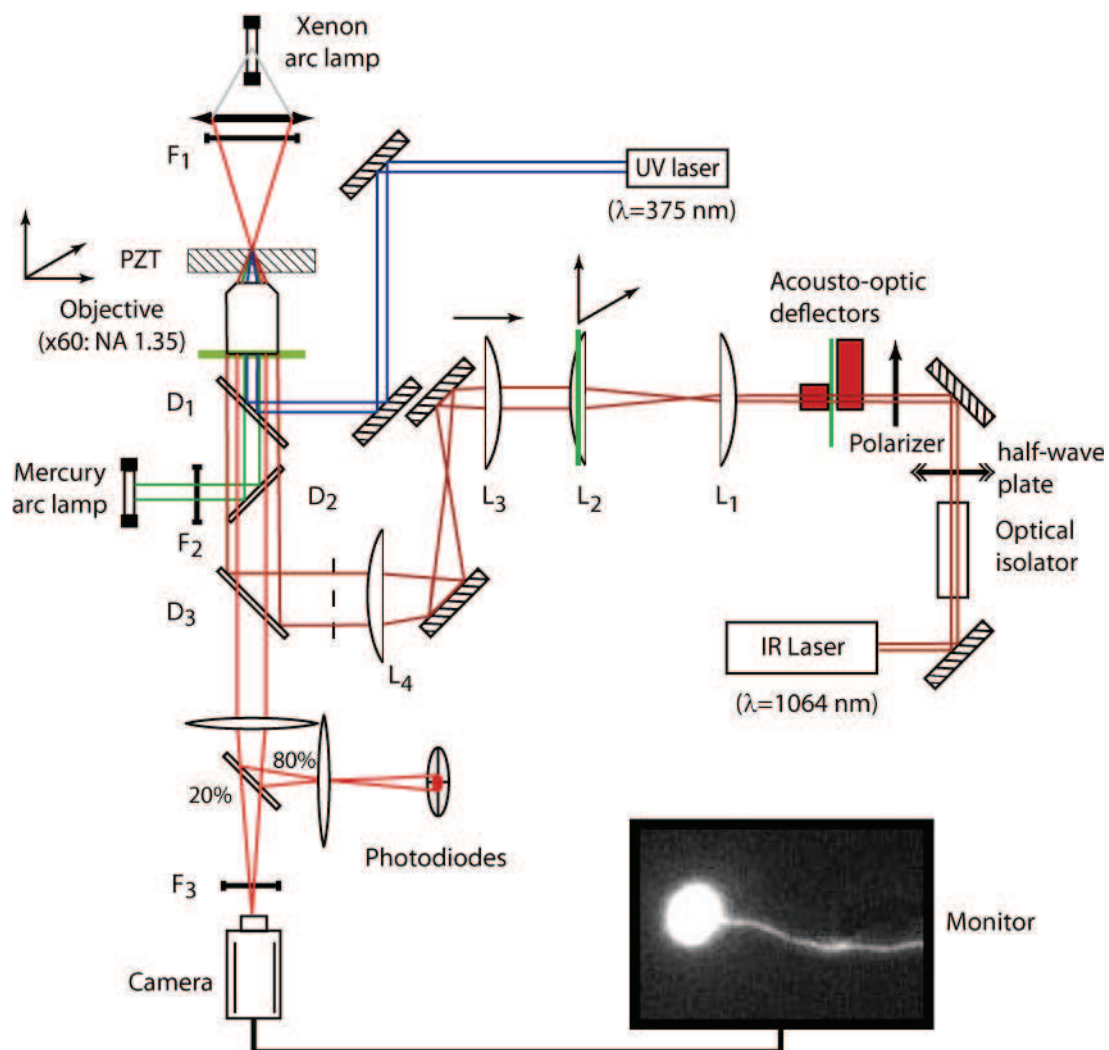


Figure 1.1.1 General schematic view of the optical tweezers set-up.

Having taken a quick overview of the set-up, we shall now zoom in on the major components of the system in order to have a more in-depth appreciation of their characteristics.

1) The Optical Tweezers

1.1 Principle of the Optical Tweezers

Optical tweezers can exert force on a dielectric object based on a difference in refractive indexes between the object and the fluid in which it is immersed by shining a focused laser through the object. In a dielectric particle, positive and negative charges are able to move

within the material. Hence, upon application of an electric field, the positive charges move towards the lower potential and the negative charges move towards the higher potentials. In an inhomogeneous field, this distribution of charges gives rise to a dielectrophoresis event, whereby the particle is attracted by the region of maximum field intensity.

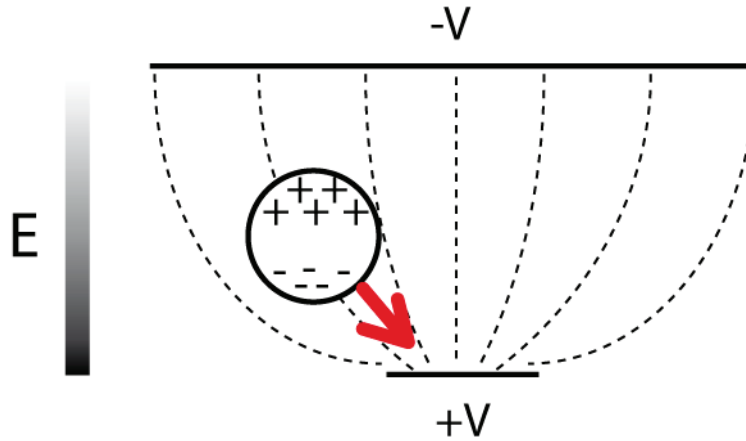


Figure 1.1.2 Schematic drawing of the principle behind dielectrophoresis. A dielectric particle in a non-uniform field E moves towards the region where the field intensity is maximal.

In the case where the diameter D of a spherical dielectric particle is significantly smaller than the wavelength λ of a focused light beam (Rayleigh Regime where $\lambda \gg D$), the particle can simply be treated as a point dipole \vec{p} in an inhomogeneous electric field \vec{E} . The force \vec{F} applied on the particle is then given by:

$$\vec{F} = \frac{1}{2} \alpha \vec{\nabla}(E^2),$$

where α is the electric susceptibility of the particle. The square of the magnitude of the electric field represents the intensity of the beam. Because the force is proportional to the gradient of the beam intensity, it is advantageous to use a microscope objective with a high numerical aperture to highly focus the beam in the sample plane.

In the opposite case (Mie regime where $\lambda \ll D$), the trapping phenomenon can be explained by ray optics. As shown in Figure 1.1.3, when a bead is placed within a focused laser beam, light will be refracted as it enters and exits the bead. There is thus a change in the momentum of the light which gives rise to an equal and opposite momentum change in the particle according to Newton's Third Law of Motion.

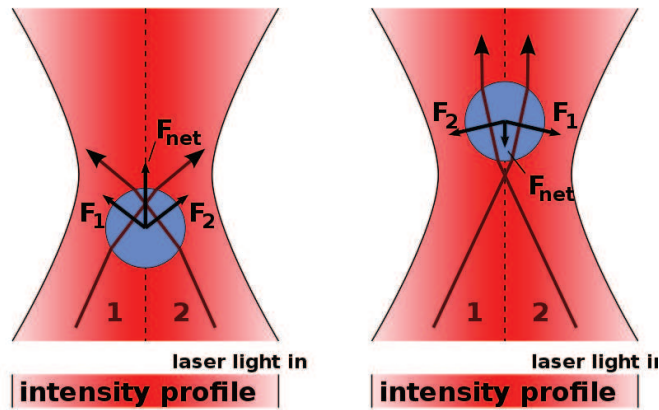


Figure 1.1.3 Principle of the optical tweezers in the Mie regime ($\lambda \ll D$). By refraction through the bead, the laser beam loses momentum which is transferred to the bead via a force. The diagram shows the trap in the axial direction. The same principle applies in the two radial axes.

The change in momentum gives rise to a net force directed towards the laser focus, whether the bead is in front or behind the focus. This net axial force compensates for the scattering force of the laser and keeps the bead stably trapped in the axial direction. In the lateral plane, if the bead is at the centre of the laser beam, the light rays are refracted symmetrically resulting in no net lateral force on the bead. In contrast, when the bead is moved away from the trap centre in the lateral plane, the stronger beams at the centre impose a larger momentum shift towards the centre of the beam than the momentum shift directed away from the centre as imposed by the weaker beams. The resultant force brings the bead back to the centre of the beam.

Because we work with light in the infra-red ($\lambda=1064$ nm), our trapping regime belongs to an intermediate regime ($\lambda \approx D$) and the force exerted by the laser on the bead cannot be easily computed. Nevertheless, for small displacements Δx , the force F applied to the bead is linear with respect to its displacement from the trap centre. This is analogous to Hooke's Law:

$$F = -k\Delta x$$

Consequently, it is common to define a trap stiffness k for optical tweezers similar to a spring. Although we cannot calculate this stiffness, we will see later that it can be estimated from the thermal fluctuations of position of a trapped bead. The stiffness of optical tweezers depends

on various factors, including the power of the laser, the numerical aperture of the objective, the refractive index of the medium and the bead used.

1.2 Characteristics of our Optical Tweezers

The laser we use as the basis of our optical tweezers emits in the infrared (IR) domain of the electromagnetic spectrum. IR is only marginally toxic to biological samples, which largely motivated its implication in our set-up. The laser emits in a continuous wave of wavelength 1064 nm and has a power rating of 4 W. The beam is pumped by a laser diode and the current in the diode determines the IR power output as show in Fig. 1.1.4.

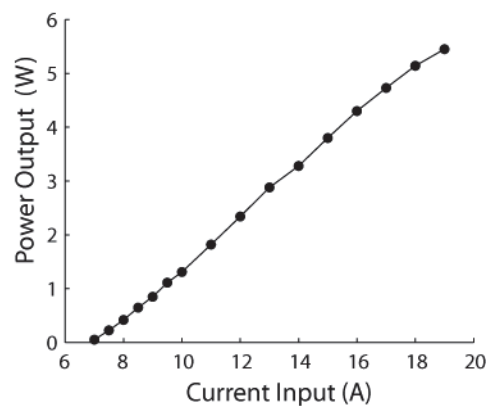


Figure 1.1.4 Power output of the laser with respect to the input current in the diodes.

Since the laser is designed to work optimally at a nominal power of 4 W, we usually work at 16A. The intensity of the beam is controlled using another device which we shall describe in the following section.

Currently, our optical trap has a stiffness of 0.12 pN/nm at maximum laser power when trapping a silica bead of 1 μm in diameter (Bangs Laboratories). The bead, which we have coupled to the acto-myosin system by biochemical means (these will be detailed further in this chapter), serves as the ‘handle’ of the optical tweezers.

2) Acousto-Optic Deflectors

2.1 Principle of Acousto-Optic Deflectors

An acousto-optic deflector (AOD) is a device which can control the direction of a laser beam. It consists of an anisotropic crystal with a piezo-electric actuator mounted on one side. When

a sinusoidal voltage is applied to the actuators, an acoustic travelling wave (with the same frequency as the sinusoidal voltage) is produced in the crystal and propagates transversely to the direction of propagation of the laser going through the crystal. The acoustic wave in the crystal acts as a diffraction grating and is thus able to diffract the laser beam. When the angle between the light and the acoustic wave is precisely equal to the Bragg angle, diffraction is efficient only in the first order.

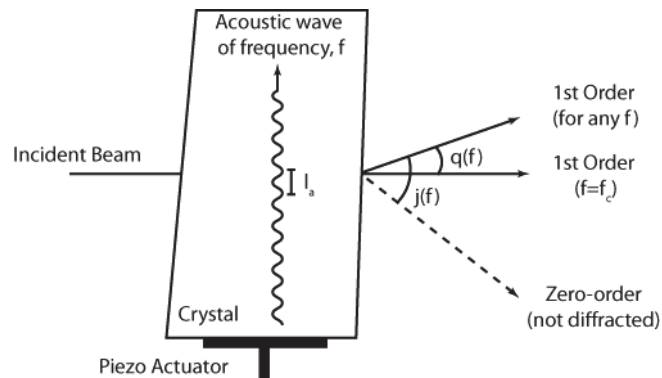


Figure 1.1.5 Diagram showing the principle of the AODs. The acoustic wave in the crystal is analogous to a diffraction grating. The side at which the beam enters the crystal is not perpendicular to it, such that the 0th order beam is deviated by refraction. At the central frequency f_c of the acoustic wave, the 1st order is not deviated. The angle the 1st order makes with the 0th order depends on the frequency of the acoustic wave.

The frequency of the acoustic wave is directly proportional to the angle of deflection of the laser beam. As a result, one is able to effectively move the laser over a certain angular range by varying the frequency.

2.2 Characteristics of our AODs

In order to control the incidence angle of the laser beam and hence the position of the trap in the focal plane of the objective, we make use of two AODs arranged perpendicularly to each other, one for each axis of the experimental working plane. Our AODs consist of a tellurium oxide crystal (TeO_2) and maximizes light intensity in the first order diffraction.

They also exhibit a large bandwidth of 30 MHz, from 60 to 90 MHz with a central frequency of 75.5 MHz.

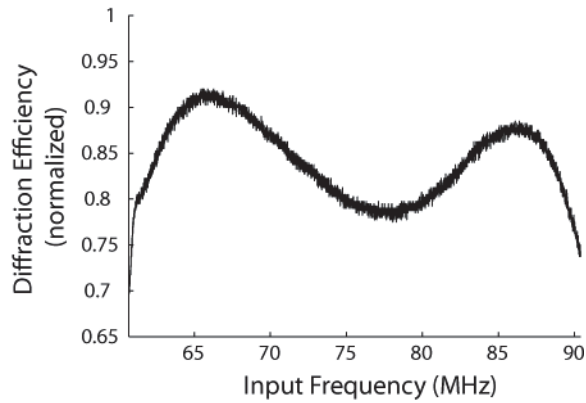


Figure 1.1.6 Efficiency of the 1st Order diffraction by one deflector. At the central frequency, there is a 80% transmission.

A large bandwidth is advantageous because it also results in a larger angle through which the laser can be deflected. Our AODs having a bandwidth of 30 MHz implies that we have an angular range of deflection of 49 mrad giving us a range in terms of distance on the experimental plane of 15 μm when taking into consideration the magnification factors from the telescopes and the focal length of the objective (3mm). We can modulate the laser deflection by using a frequency generator (DDS.62-92.D47.2out, AA Optoelectronics) that we control using our computer interface.

The frequency generator is also able to impose a voltage from 0 to 10 V to both axes. This determines the amplitude of the signal sent to the piezo actuators and consequently determines the amplitude of the acoustic wave, allowing us to control the intensity of the diffracted laser beam of the first order.

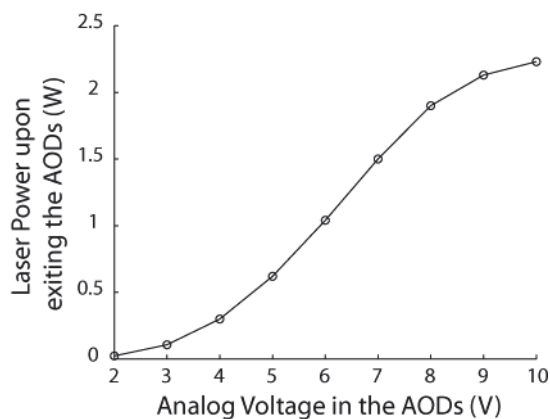


Figure 1.1.7 Effect of the amplitude of the acoustic wave on the intensity of the diffracted beam.

3) The Detection Method

As we have described earlier, we use beads coupled to the acto-myosin system as a handle for the optical tweezers. Hence, to measure the activity of the molecular motors, it is necessary to be able to measure the displacement of those beads in the nanometer range.

3.1 Photodiodes

We currently use photodiodes as our primary detection tool to track and measure the movements of the coupled bead. Photodiodes are devices which convert light into an electric current. The detection method hence consists in projecting an image of the bead on the photodiodes and measuring the current related to the bead motion.

Our photodiodes have four quadrants and have a photo-sensitive zone of 1mm. The principle underlying the measurement of bead motion using such photodiodes is explained below (Fig. 1.1.8)

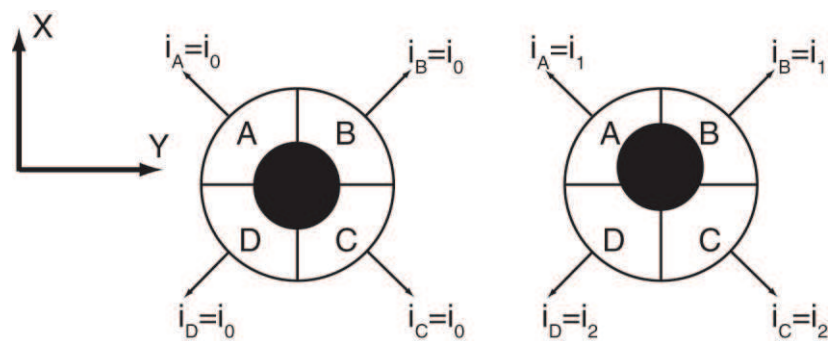


Figure 1.1.8 Principle of four-quadrant photodiodes when applied to bead detection. Left : When the bead is centered, the four quadrants receive an identical light input and as the equations below demonstrate, the signal generated is nought. Right : When the bead is moved (here in the X direction), the upper quadrants and the lower quadrants receive different light inputs and we can thus obtain a signal which is proportional to the displacement of the bead.

Each quadrant produces a current proportional to the light intensity it receives. The current from the four quadrants can be combined according to the equations below in order to deduce the bead motion in the X and Y directions of the plane.

$$X \propto (i_A + i_B) - (i_C + i_D) \quad \text{Eq 1.1.1}$$

$$Y \propto (i_A + i_D) - (i_B + i_C) \quad \text{Eq 1.1.2}$$

The currents i are in fact first converted into a voltage signals u by a pre-amplification circuit (with a conversion factor of $10^7 \Omega$) and are then treated by an analog circuit to perform the appropriate arithmetics to deduce bead motion in the two directions of the plane.

$$X \propto (u_A - u_C) + (u_B - u_D) \quad \text{Eq 1.1.3}$$

$$Y \propto (u_A - u_B) + (u_D - u_C) \quad \text{Eq 1.1.4}$$

The two signals are then filtered by a low-pass filter (8-pole Bessel filter, 3384 model, Krohn-Hite Corp.) and recorded on our computer. The signals are also sent to our oscilloscopes to allow real-time monitoring of the bead motion during the experiments.

3.2 Calibration

(a) Calibration of the photodiodes

To effectively use the photodiodes as a means to measure motor-driven bead motion, it is necessary to translate the voltage variations into displacement. The photodiodes are mounted on a piezo stage that can be moved along two axes. The calibration itself is done by projecting the image of a bead on the photodiodes such that the bead is at the centre of the linear range of the photodiodes ($\pm 150 \text{ nm}$ from the center in the sample plane, corresponding to $\pm 90 \mu\text{m}$ in the plane of the photodiodes) and by applying alternating steps of increasing amplitude to the position of the diode and observing the corresponding variation in the voltage signal.

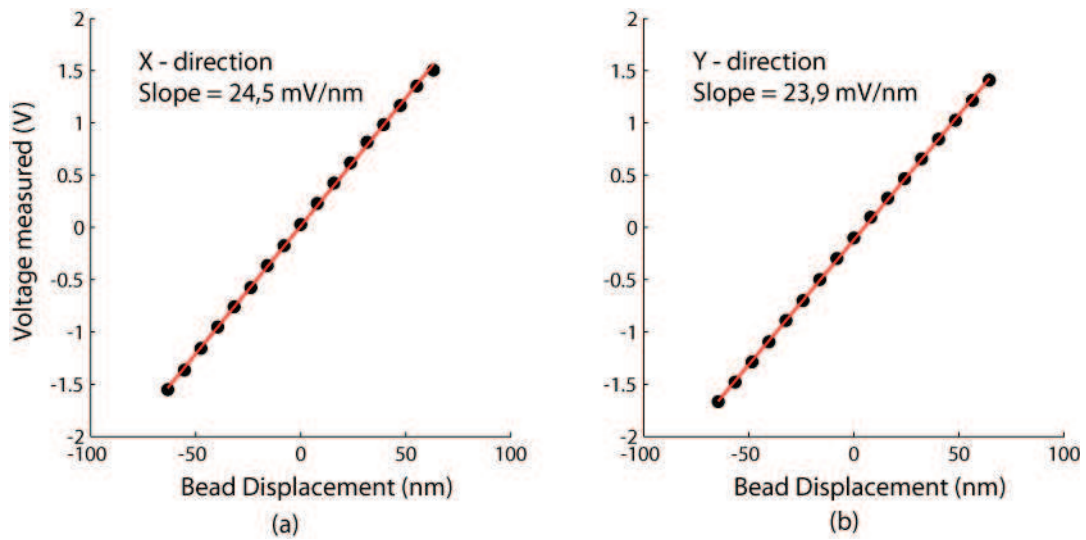


Figure 1.1.9 Typical calibration curves. Left : Calibration in the X direction, calibration factor = 24.5 mV/nm. Right : Calibration in the Y direction, calibration factor = 23.9 mV/nm. A magnification factor of $\times 600$ has been applied to go from the sample plane to the plane of the photodiodes.

For each step and in both directions, the voltage signal is averaged and plotted with respect to the recorded displacement of the diode (Figure 1.1.9). The slope of the graphs gives the calibration factor for each respective direction, after the diode is divided by the multiplicative factor ($\times 600$) between the sample and the diode.

(b) Calibration of the trap

Optical tweezers behave like a linear spring over small displacements of the dielectric bead relative to the centre of the laser beam (see Figure 1.1.10)

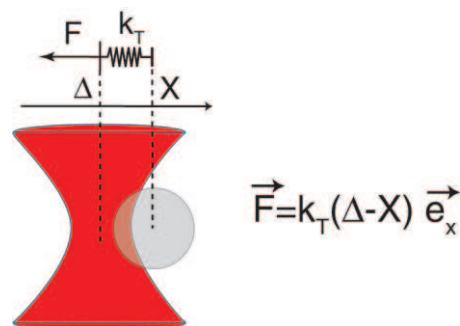


Figure 1.1.10 The laser trap is analogous to a spring. Following Hooke's Law, the trapped bead is subjected to a restoring force proportional to its displacement from the centre of the trap.

In a given direction x , the force exerted by the trap on the bead can be written as :

$$\vec{F} = k (\Delta - X)\vec{e}_x, \quad \text{Eq 1.1.5}$$

where Δ is the trap position and X is the bead position.

Based on this equation, if we want to measure the forces developed by the molecular motors to which our bead is coupled, it is imperative to know the value of k , the stiffness of the trap. The stiffness of the trap can be deduced from the thermal fluctuations of bead position: the greater the fluctuations, the softer the trap is. Using Langevin's equation for Brownian motion when applied to the thermal fluctuations of a bead in a viscous regime (for simplicity's sake, we shall only consider one axis), we get :

$$m.\ddot{x} = -k.x - \gamma.\dot{x} + \eta(t), \quad \text{Eq 1.1.6}$$

where m is the mass of the bead, x is the position of the bead, k is the stiffness of the trap, γ is the drag coefficient on the bead by the surrounding fluid and $\eta(t)$ is the resultant force of the random bombardment due to the surrounding molecules of the fluid.

Considering the small size of the bead, we can assume that the system is overdamped and we can hence neglect $m.\ddot{x}$. The equation can be rewritten as:

$$\eta(t) = k.x + \gamma.\dot{x} \quad \text{Eq 1.1.7}$$

The transfer function χ for this system can be written as :

$$\underline{\chi}(\omega) = \frac{\underline{X}(\omega)}{\underline{\eta}(\omega)} = \frac{\frac{1}{k}}{1 + i.\frac{\gamma}{k}.\omega} \quad \text{Eq 1.1.8}$$

$$\text{where } \underline{X}(\omega) = \int x(t).e^{-i.\omega.t}.dt$$

According to fluctuation-dissipation theorem, the auto-correlation of the noise can be written as :

$$\langle \eta(t) \cdot \eta(t') \rangle = 2 \cdot k_B T \cdot \gamma \cdot \delta(t - t') \quad \text{Eq 1.1.9}$$

During the calibration of the trap, a trapped bead is imaged at the centre of the linear range of the photodiodes as described in Section 3.2 and after calibration of the photodiodes, we record the bead position in the two axes during a time T_{exp} at a sampling frequency f_e . We can then obtain the discrete spectral density of the signal as follows :

$$P_n = \frac{|X_n|^2}{T_{exp}} = \frac{\frac{1}{k^2} \cdot |\eta_n|^2}{T_{exp} \cdot \left(1 + \frac{\gamma^2}{k^2} \cdot \omega_n^2\right)}, \quad \text{Eq 1.1.10}$$

$$n \in [0, 1, \dots, N - 1]$$

where n is the n^{th} sample, the frequency is defined as $\omega_n = \frac{2 \cdot \pi \cdot n}{T_{exp}}$, X_n and η_n are Fourier components at the discrete angular frequency ω_n of the recorded signal and the noise respectively, and N is the number of points recorded.

Performing a Fourier transform on equation 1.1.9 for a finite recording time T_{exp} , we get:

$$|\eta_n|^2 = 2 \cdot k_B \cdot T \cdot \gamma \cdot T_{exp} \quad \text{Eq 1.1.11}$$

Finally, the spectral density of the bead motion is given as:

$$P_n = \frac{2 \cdot k_B \cdot T \cdot \gamma / k^2}{(1 + \frac{\gamma^2}{k^2} \cdot \omega_n^2)} \quad \text{Eq 1.1.12}$$

In order to obtain γ and k , the power spectrum obtained from our recorded data is fitted with a Lorentz function of the form (see also Figure 1.1.11):

$$F(f) = \frac{a}{1 + b \cdot f^2} \quad \text{Eq 1.1.13}$$

We can thus extract the two parameters a and b , and in turn (from Equation 1.1.12) γ and k .

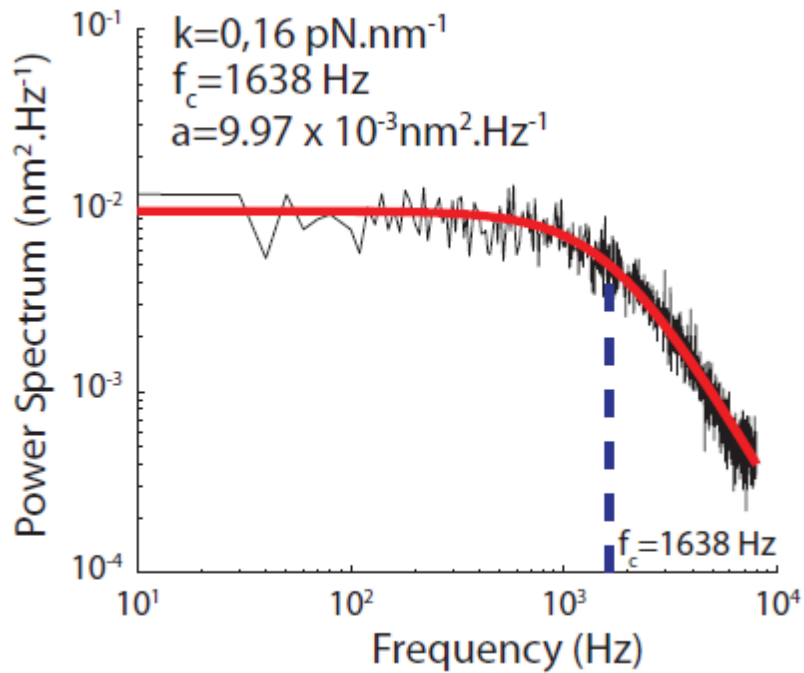


Figure 1.1.11 A typical power spectrum obtained during the calibration of the trap stiffness. In black : The averaged power spectrum obtained by recording the thermal fluctuations of the bead. In red : Fitting the power spectrum with a Lorentz function.

4) Controlling the set-up

This section will describe shortly the various possibilities of the set-up and the main characteristics of our control interface. We control our experiments with LabView software (National Instruments) using a series of custom-made programs to communicate with our physical devices.

4.1 Moving the laser

Our Labview program allows us to control the frequency and amplitude of the acoustic wave travelling in the AODs (Section 2.1) and thus to vary the intensity of the laser beam and move the laser across the sample plane. In addition, we can also apply a variety of pre-programmed stimulation routines via LabView. These include (but are not limited to) application of steps of differing sizes and durations, triangular waveforms of stimulation, again with variable characteristics, and frequency sweeps. A feedback system has also been implemented for experiments where we want to keep a parameter such as bead position or the trap force constant.

4.2 Moving the stage

The sample is mounted on a PZT stage, allowing fine (with nanometer precision) position control of the stage in the X, Y and Z axes. This is particularly useful during calibration or any finer manipulations that might be required. The stage is interfaced with our computer via LabView. Our programs can control the stage using relative values input using the keyboard or in real time using the mouse motion for the X and Y axes and the mouse wheel for the Z axis.

B/. Biochemical Tools

In this part of the thesis, we detail the various biochemical protocols that we used in our experiments. Those protocols, for the most part, have already been described and used by many well-established teams around the world. This section will thus be used to list and give a moderately detailed description of the biochemical tools involved in our work. The exact composition of the buffers (in bold font) will be given in the appendix. I will, however, lay

more emphasis on the new protocols that I have developed in the laboratory and that had not been implemented before starting this PhD.

1) Myosins

1.1 Myosin II

We use myosin II Heavy Mero-Myosin (HMM), purified from rabbit skeletal muscles. They were graciously prepared by Karin VOGT in the laboratory headed by Professor Mathias RIEF (Physik Department, Technische Universität, München).

The HMMs are stored in 1 μ L aliquots at 6.75 mg/mL. A stock solution is prepared by adding 13 μ L of **AB**. The resulting mixture is then kept on ice. The motors stored in this fashion are functional for approximately two weeks.

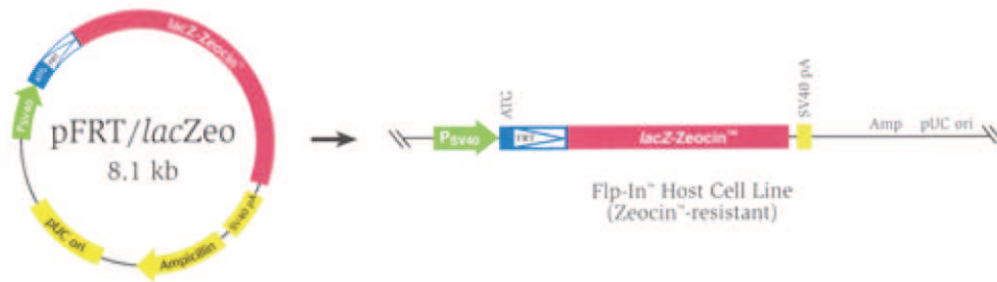
1.2 Myosin 1b

Myosin 1b is purified by our team on the premises of UMR144 of the Curie Institute using a stable cell line expressing myosin 1b. The cell line, immortalized HEK (Human Embryonic Kidney) 293 Flp-In cells, was graciously provided by Evelyne COUDRIER, Ayako YAMADA and Claudia ALMEIDA.

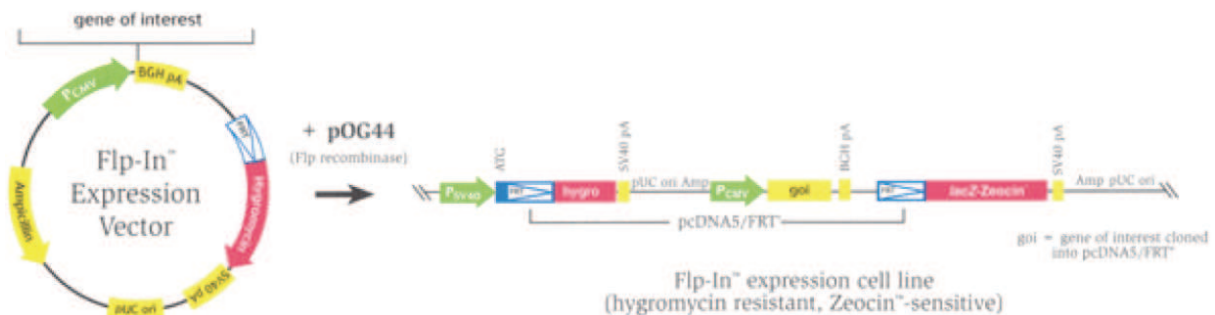
(a) Expression of myosin 1b

The integration of myosin 1b with a Flag tag into the genome of the HEK 293 was previously done successfully by the team of Evelyne COUDRIER in Daniel LOUVARD's group. The integration itself was performed using the commercially available Flp-In system from Life Technologies. The Flp-In system introduces a gene of interest in the genome of a chosen mammalian cell line via the inclusion of a Flp Recombination Target site into said genome. This is done by a Flp recombinase-mediated DNA recombination at the FRT site (See Fig. 1.1.12).

pFRT/lacZeo is stably transfected into the mammalian cells of interest to generate the Zeocin™-resistant Flp-In™ Host Cell Line(s).



The psDNA5/FRT expression vector containing the gene of interest (goi) is cotransfected with pOG44 into the Flp-In™ Host Cell Line. The Flp recombinase expressed from pOG44 catalyzes a homologous recombination event between the FRT sites in the host cells and the pcDNA5/FRT expression vector.



Integration of the expression construct allows transcription of the gene of interest (goi) and confers hygromycin resistance and Zeocin™ sensitivity to the cells.

Figure 1.1.12 Diagram from Life Technologies detailing the integration of a gene of interest in the genome of a host cell using their commercial Flp-In System.

After stable expression of myosin 1b has been confirmed, the cells are frozen in DMSO and stored at 80°C.

(b) Cell Culture of the HEK 293-Flp-In

The first step in the purification process is to carefully thaw a frozen HEK 293 Flp-In Myosin 1b aliquot. The cells are then transferred in 25mL culture flasks filled with a culture medium (Dulbecco's Modified Eagle Medium (DMEM) from Gibco and Life Technologies) and kept in an incubator at 37°C with 5% CO₂. The medium is supplemented with 10% fetal calf serum to boost cell growth and 0.18mg/mL HygroGold (an antibiotic from Life Technologies) was added from the second day on.

The cells adhere on the flask surface and divide. When the cell layer reaches 80% confluence, Trypsin-EDTA is added to detach the cells from the walls of the flasks and the growing cell culture is successively transferred into 75 mL, 150 mL and finally 300 mL culture flasks. Once the cells on the walls of the 300 mL culture flasks reach maximum confluence, the contents are transferred into a 1L spinner flask in order to perform cell culture in bulk. The cell concentration is then measured regularly by counting the amount of cells in 1mL of medium with a Countess Automated Cell Counter (Invitrogen). Once the cell concentration reaches between 800,000 – 1,000,000 cells/mL, the contents of the flask are divided into four spinner flasks and the process is repeated. When the cell concentration in all four spinners reaches 800,000 – 1,000,000 cells/mL, the cells are harvested by centrifugation. We obtain one pellet from each spinner and each pellet has an expected weight of approximately 4g. The cell pellets are weighed, labeled and frozen at 80°C to await purification.

(c) Purification of myosin IB

The purification process is relatively long and takes three days in all. We start by choosing an appropriate cell pellet and melting it on ice. The cell suspension is then lysed using a **lysate buffer** for 30min at 4°C on a rocking platform. The supernatant is collected and incubated with Anti-Flag Peptide Agarose Beads (Invitrogen) for 2h at 4°C on a rotator. The myosin Ib will bind to the agarose beads via their Flag tag. The beads are gathered (by centrifugation at 1000g for 3 min) and incubated overnight at 4°C with an **elution buffer** containing 0.24mg/mL 3× Flag peptides. The latter will compete with the myosin 1b for the Anti-Flag antibody at the bead surface and, due to their high concentration and high affinity, will eventually occupy all of them, freeing myosin 1b into solution. The next day, the solution is centrifuged at 1000g for 4 min at 4°C and the supernatant containing the myosin Ib is then dialysed overnight against a **dialysis buffer** at 0.1% methyl cellulose. Afterwards, the solution inside the dialysis tubing is collected and snap-frozen in liquid nitrogen in 10µL aliquots. The aliquots are then stored at -80°C and can be used within a few months.

The presence of myosin 1b in monomeric state is confirmed by using a blue native gel electrophoresis (see Fig. 1.1.13).

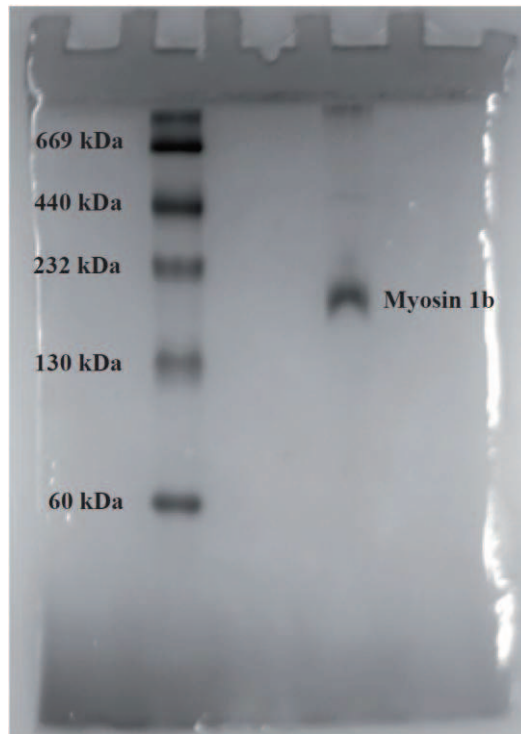


Figure 1.1.13 Blue native gel confirming the presence of Myosin 1b after the purification process has been completed. The molecular weight of myosin 1b appears to be higher than the expected 130 kDa due to the presence of calmodulin, a protein that binds to the myosin neck.

The concentration of the myosin 1b is measured using a Bradford colorimetric assay. The concentration is usually approximately of the order of 2 μ M.

2) Actin

Filamentous F-actin is obtained from monomeric G-actin by undergoing a polymerization reaction in a high-salt buffer known as **F-buffer**. The filaments are then decorated with phalloidin labeled with Alexa-594 to make them visible in fluorescence. We use commercially available G-actin (Cytoskeleton) stored at 42 μ M in **G-buffer** at -80°C. Biotinylated actin is also bought from cytoskeleton and kept in the same buffer at 8 μ M.

2.1 Polymerisation

We start the polymerization reaction by adding 16 μ L of **F-buffer** to 2 μ L of G-actin at 42 μ M and to 2 μ L of biotinylated actin at 8 μ M. The mixture is left for 2h at room temperature. We then add 1 μ L of fluorescent phalloidin (kept at a stock concentration of 100 μ M at -20°C) and

leave the mixture for 1h on ice. We accordingly obtain fluorescent actin filaments with an unbiotinylated actin to biotinylated actin ratio of 1:5.

2.2 Actin bundles

Actin bundles are built using fascin as a cross-linker. Fascin is an actin cross-linking protein which has the ability to form polarized and rigid actin bundles (Ishikawa, Sakamoto, Ando, Higashi-Fujime, & Kohama, 2003). 20 μL of the biotinylated F-actin solution is mixed with 10 μL of fascin at 2 μM in **AB**. The resulting mixture is stored on ice overnight prior to use.

3) Functionalization of the beads

One of the most important step of our experiment is the procedure that leads to strong attachment of an actin filament to a bead, which then serves as a handle for the optical tweezers. The streptavidin–biotin bond is a biochemical interaction which is commonly used to provide specific attachment in research. As such, we covalently bind streptavidin to the surface of our beads to attach them to biotinylated actin bundles and/or filaments.

Our protocol is based on Sulfo-NHS (Sulfo N-hydroxysuccinimide)/EDC (ethyl dimethylaminopropyl carbodiimide) coupling which is routinely used to covalently bind proteins to carboxylated substrates. Our protocol is adapted from a similar coupling process developed by Volker BORMUTH and Horatio FONTANA at the Max Planck Institute in Dresden. Their protocol involves the addition of a Polyethylene Glycol (PEG) spacer between the streptavidin and the hydrophobic surface of the beads in order to avoid denaturation of the streptavidin. Shorter PEG molecules are also coupled to the bead to act as a passivating agent protecting the beads against non-specific interactions. We initially tried to couple the streptavidin directly to the carboxylated groups of the bead. The result, however, was less than satisfactory: after mixing functionalized beads with biotinilated actin filaments, less than 30% of the beads were attached to a filament and we could not manually stick a functionalized bead to a biotinilated actin filament by manipulating the bead with optical tweezers. Upon the implementation of the PEG spacer, the functionalized beads performed much better: the percentage of attached beads rose to ~80% and we could now attach beads to filaments at leisure using the optical tweezers.

The principle of the chemical coupling between a carboxylated substrate (1) and a protein of interest (2) is shown in Figure 1.1.14. The final product is an amide of the form (1)CONH(2).

The addition of EDC is necessary to create a highly reactive intermediate which reacts with Sulfo-NHS to give the amide linkage.

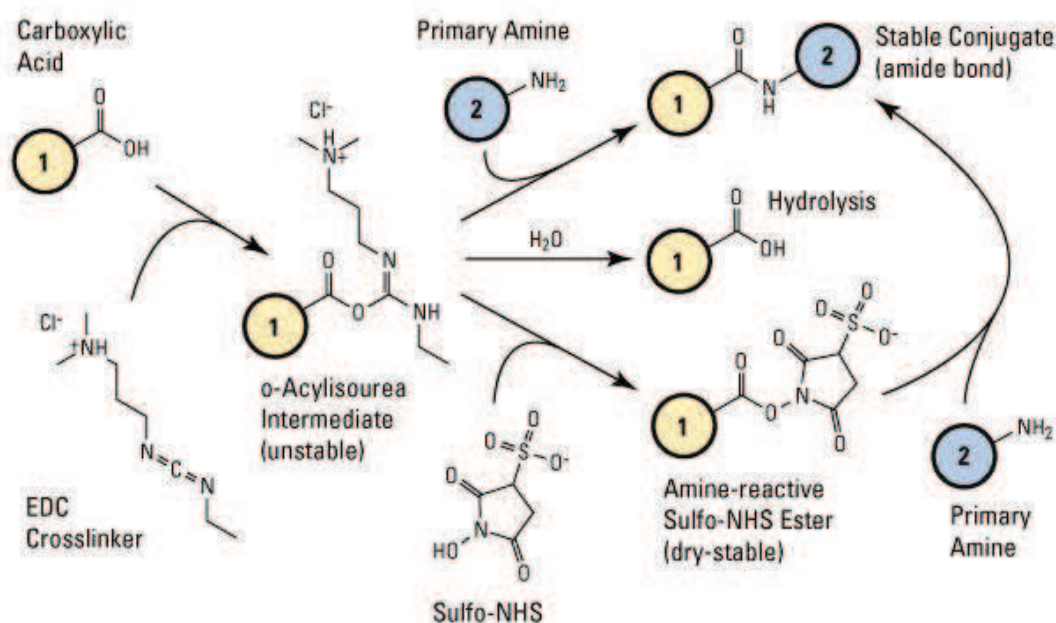


Figure 1.1.14 Diagram showing the Sulfo-NHS/EDC coupling. The three possible reactional pathways after formation of the unstable intermediate are shown. (Image taken from the website of Pierce Chemicals)

The first step is an esterification reaction between a carboxylated substrate and the EDC which produces a reactive unstable intermediate known as O-Acylisourea ester. The latter can then follow three reactional pathways :

- (i) A condensation reaction with the N-terminal of the protein of interest thus covalently binding the substrate and the protein of interest with a stable amide bond.
- (ii) A hydration reaction which regenerates the initial carboxyl group.
- (iii) If Sulfo-NHS is present in the reaction medium, it can react with the reactive intermediate to form a semi-stable NHS-ester which can then react with the amine function of the N-terminal of the protein of interest to form a stable amide linkage between (1) and (2).

Reaction pathway (iii) is usually favoured by adding sulfo-NHS in the reaction medium before EDC in order to preferentially induce the formation of the semi-stable NHS-ester.

The beads used are carboxylated silica beads from Bangs Laboratories (SC03N, 1 μ m in diameter). The protocol reads as follows: 2.5 mg of silica beads are first washed in **MES buffer** (centrifuged two times in 1 mL **MES** at 4000 rpm at 4°C for 3 min and resuspend in 250 μ L of **MES**) and sonicated to minimize the presence of aggregates. Then sulfo-NHS (1.62 mg in **MES**) and EDC (1.42 mg in **MES**) are added in that order. The mixture is then left to incubate for 15min at 37°C at 600rpm on a thermomixer to activate the beads by forming the semi-stable NHS-ester coupled to the bead. After activation, the beads are washed with **MES** (two times in 500 μ L) and resuspended in 150 μ L of **Borate Buffer**. We then add 5kDa amino-carboxy-PEG (2.6 mg) and 2kDa amino-PEG (9.36 mg) and the mixture is left to incubate for 2h at 37°C at 600 rpm on a thermomixer. The amino-carboxy-PEG acts as the spacer and also carries a carboxyl group to carry out another coupling reaction with streptavidin (of course, it can be done with any protein or any substrate carrying an amino group) while the shorter 2kDa amino-PEG serves as a passivating shell around the bead.

To attach streptavidin, the beads are washed five times with 500 μ L of borate buffer (4000 rpm, 4°C for 3 min) and resuspended in **MES**. Another activation via sulfo-NHS and EDC is performed as described earlier and the beads are then resuspended in 250 μ L of **PBS** with 1mg/mL streptavidin (Sigma). After an overnight incubation at 4°C on a rotator, the beads are washed with PBS, resuspended in 250 μ L of PBS and stored on ice. They are functional for about 1 month.

4) Protein Attachment

4.1 Nitrocellulose Surfaces

To attach our myosin II to a glass surface, we coat the latter with a thin layer of nitrocellulose. We prepare a 0.1% (w/v) of nitrocellulose in a volatile solvent, amyl acetate. 20 μ L of this solution is applied and uniformly spread on a 22 \times 22 mm coverslip that has been cleaned with acetone. The solvent is then allowed to evaporate at room temperature for approximately 1h. They are usable for one day. The myosin II after dilution to the appropriate concentration (0.4 μ M) in **AB** is flowed onto the treated surface and left to incubate for 4min. The uncovered parts of the coverslip are then passivated by **AB-BSA**.

4.2 Antibody-treated Surfaces

Attaching myosin 1b poses some challenges because non-specific adhesion via nitrocellulose-treated surfaces is not enough to guarantee a functional motility assay, in contrast to myosin II. It may be that myosin 1b is too short to prevent strong interaction between the myosin head and the surface, so that the motor protein cannot orient itself to properly interact with actin and mediate motility. To circumvent this problem, we use specific binding through anti-myosin 1b antibodies directed towards the tail domain of myosin 1b. The antibody is thought to direct the coupling between the myosin and the substrate in a way that positions the motor domain away from the solid surface.

The antibodies are either purified by Maité PROSPERI from Evelyne COUDRIER's team or bought from Santa Cruz. The antibodies are dissolved in **AB** to 0.08 μ M and applied to nitrocellulose-coated coverslips for 10min. The uncovered parts of the coverslip are then passivated with **AB-BSA**. After washing the coverslip with **AB**, myosin 1B is added and left to incubate for 5min twice.

4.3 Silanized Surfaces

In an attempt to optimize our motility assays, we searched improved means of attaching motor proteins to glass surfaces and new passivating protocols. In their publication, Albet-Torres et al. (Langmuir 2007) discussed the use of silanized surfaces in in-vitro motility assays. The main advantages of such surfaces are the specific attachment of the hydrophobic tail domain of myosin II HMMs on the hydrophobic silane, thus increasing the probability of having myosin II motor heads free to interact with incoming actin filaments.

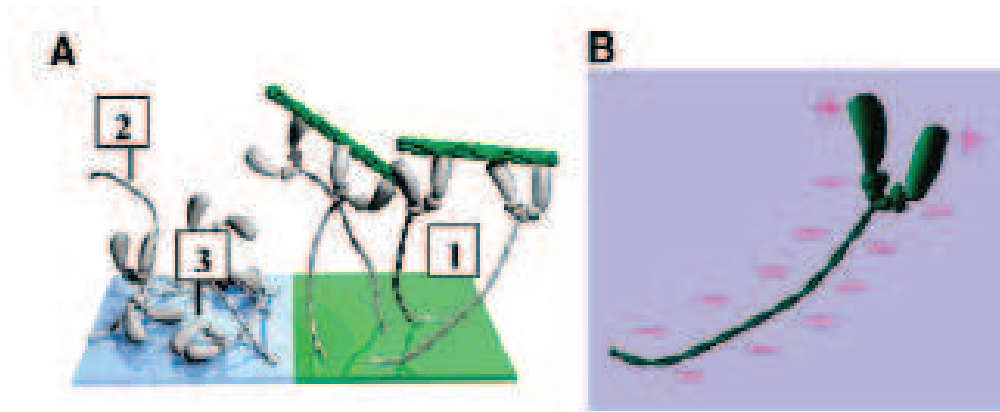


Figure 1.1.15 A : Non specific adhesion of HMM on nitrocellulose-treated surfaces (2 and 3) compared to specific adhesion of the tail domain on hydrophobic surfaces (1). B : Charge distribution on the surface of a HMM. (Albet-Torres et al., 2007).

In addition, Pluronic F-127, a tri-block polymer which consists of a hydrophobic central block flanked by two PEG blocks, can be used to efficiently passivate the silanized surfaces. . The hydrophobic central part binds itself readily to the hydrophobic silane. The two PEG blocks act will then form a polymer brush which will effectively passivate the surface.

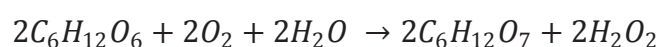
Our protocol is largely adapted from Albet-Torres et al.. The main difficulty of the protocol is the cleaning process which is necessary to obtain a homogeneous silanization. We start by washing 22×22 coverslips by sonicating them for 1min in chloroform in order to remove all organic impurities on the surface. They are then rinsed with milliQ water and subjected to plasma cleaning for 30 s. Following this step, they are placed in Piranha solution at 80°C for 10min. Piranha solution is a highly corrosive solution obtained by mixing hydrogen peroxide and sulphuric acid in a 3:7 ratio. Afterwards, the coverslips are rinsed with milliQ water and dried with a stream of nitrogen gas. The coverslips then go back to plasma cleaning for 30s and are then completely immersed in a freshly prepared trimethylchlorosilane (TMCS) dissolved to 0.5% in chloroform. After this step, the coverslips are rinsed with ethanol and dried with a clean nitrogen gas stream.

The hydrophobic nature of the coating is tested by placing a small drop of water on it. The contact angle of the droplet is estimated and gives an indication of the hydrophobicity of the surface. The coverslips were deemed sufficiently hydrophobic when the contact angle was superior to 90°.

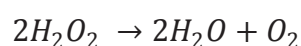
5) Additional molecular cocktails.

5.1 Anti-Bleaching Mixture

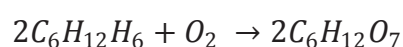
Photobleaching occurs when a fluorescent dye loses its emission properties after several cycles of excitation/emission. Excitation occurs when a fluorescent dye absorbs enough energy to move from its fundamental state to an excited state. From this excited state, the dye either returns to the fundamental state by emitting a photon or it can transit to a triplet state which cannot return to the fundamental state by way of a simple electronic transition, thus increasing its lifespan. This eventually leads to an overall loss of fluorescence. The triplet state can indeed generate free radicals that can react with the dissolved oxygen in the solution. Such reactions can severely damage the dye and the structure to which it is bound, here, the actin filaments. To avoid this, we can either reduce the lifetime of the triplet state or reduce the concentration of oxygen in the medium. We chose the latter, prompting us to use the synergetic action of two enzymes, glucose oxidase and catalase. In the first step, glucose oxidase catalyses the oxidation of glucose into gluconic acid and hydrogen peroxide according to the following equation:



Catalase then removes hydrogen peroxide from the experimental medium as shown below :



While this reaction produces oxygen, the overall equation is written as :



The stoichiometry of the equation shows that, on the whole, oxygen is removed from the reaction medium.

We refer to this enzyme cocktail as **AB-GOC**. It is prepared by adding 20 μ L of 5 mg/mL glucose oxidase, 20 μ L of 1.25 mg/mL catalase and 10 μ L of 1 M DTT to 200 μ L of **AB**. **AB-GOC** remains functional for approximately 3 hours when kept on ice. **AB-GOC** is activated by the addition of 4 μ L of 230 mg/mL glucose just prior to the experiment.

5.2 ATP regeneration

During a typical experiment, ATP is consumed by the active molecular motors, hence reducing the ATP concentration in the experimental medium. It is important to regenerate ATP in the medium because since the concentration of ATP in solution is relatively low ($\sim 2\text{mM}$), the ATP will be rapidly consumed, thus ending the experiment prematurely. Moreover, ATP concentration is, in this experimental context, an important parameter which should be kept constant.

To achieve this, we make use of creatine phosphokinase which produces ATP from ADP and creatine phosphate. We refer to our experimental buffer enriched with the ATP regenerator cocktail as **AB-GOC-CP**. We prepare it by adding $12.5\ \mu\text{L}$ of $40\ \text{mM}$ creatine phosphate and $7.5\ \mu\text{L}$ of $5\ \text{mg/mL}$ creatine phosphokinase to $250\ \mu\text{L}$ of **AB-GOC**.

6) Experimental Procedure

6.1 Flow Cell Preparation

Our flow cell consists of a $18\times 18\ \text{mm}$ coverslip and a $22\times 22\ \text{mm}$ coverslip separated by two parafilm strips close to each other. The $3\ \text{mm}$ spacing between the two strips form a channel. The parafilm is slowly melted on a heating plate to seal the channel walls. The end result is a flow cell with a channel with two open ends. The channel itself is $\sim 100\ \mu\text{m}$ high and $\sim 300\ \mu\text{m}$ wide.

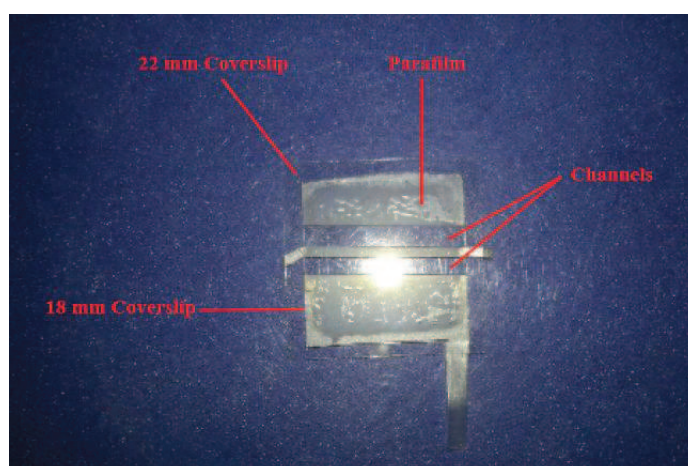


Figure 1.1.16 Example of a typical flow cell. On this example, there are two channels. The number of channels can be varied depending on the experiment and is convenient to test different conditions on the same flow cell for instance.

Before building the flow cell, the 22×22 mm coverslip is coated appropriately with either nitrocellulose or tetra-methyl chlorosilane, depending on the experiment.

6.2 Molecular Motor Attachment

(a) Myosin II HMM

At the start of the experiment, 2 μL of the HMM stock solution (6.75 mg/mL) are mixed with 3 μL of **AB**. The mixture is injected into the flow cell (built using the nitrocellulose-treated coverslips) and allowed to stand for 4min at room temperature. The flow cell is then passivated by injecting **AB-BSA** and left for 4min at room temperature.

The attachment protocol, if one wishes to attach HMMs to silanized surfaces, has some minor differences. The dilution of myosin in **AB** is done in the same way but the incubation time in the flow cell is 5 min and the flow cell is then washed with **AB** and passivated with F-127 in **AB** at 1% (w/v) for 15min.

(b) Myosin 1b

In the case of myosin 1b, we also use nitrocellulose-coated coverslips. The anti-myosinIb antibodies are diluted to 0.08 μM in **AB** and injected in the flow cell. They are left to stand for 10min. The flow-cell is then washed with **AB** and passivated with **AB-BSA** for 4min. Myosin 1b, brought to the appropriate concentration in **AB** (usually 0,4 μM) is injected into the flow cell and left to incubate for 5 min at room temperature. The flow cell is washed and the previous myosin Ib incubation step is repeated.

6.3 Incubation of actin and functionalized beads

(a) With actin filaments

Prior to the experiment per se, a solution of biotinylated actin filaments is prepared by diluting 1 μL of a stock solution of actin at 4 μM into 49 μL of **AB**. The mixture to be injected into the flow cell is prepared as follows : in 80 μL of **AB-GOC-CP**, we dilute 1 μL of the streptavidin-coated bead solution , 4 μL of 230 mg/mL glucose and 2 μL of 100 mM ATP. 10 μL of the biotinylated actin solution is then added. The solution obtained is gently mixed with a pipette tip and left to incubate for 5 min at room temperature and in the dark.

(b) With actin bundles

The preparation of a solution of biotinylated actin bundles is quite similar as the protocol described above. The main difference is that we do not pre-dilute the bundle solution before preparing the final experimental mixture. The preparation is as follows: in 89 μL of **AB-GOC-CP**, we dilute 1 μL of the streptavidin-coated bead solution, 4 μL of 230 mg/mL glucose and 2 μL of 100 mM ATP. 1 μL of the biotinylated, fascin-crosslinked actin bundle solution is then added. The solution is then gently mixed with a pipette tip and left to incubate for 5 min at room temperature and in the dark.

6.4 Injection of the experimental solution and starting the experiment

Once the flow cell is ready, we inject 20 μL of the bead-actin mixture we have just prepared into the flow cell. The latter is then mounted on the microscope stage and the surface where we attached the motors is observed in fluorescence. The initial step is to check the motility of the actin filaments or bundles on the surface (depending on which of the two possible experimental mixtures we have injected into the flow cell), which is a direct test of the viability and functionality of the molecular motors. Once we have checked this, we search for a bead attached to a filament/bundle. However even if a bead unattached to any filament/bundle has been trapped, it is possible to instantaneously bind free filaments/bundles to the trapped bead by manipulating the stage such that the trapped bead and a free-floating filament/bundle come into physical contact with each other. This allows the streptavidin on the bead to bind to the biotinylated filament/bundle. Since the formation of the streptavidin-biotin link is quasi-instantaneous, it is quite simple to do and is more convenient than relying on luck looking for the correct bead-actin configuration.

Once we have found and trapped a suitable bead, we approach it as close to the surface as possible without touching said surface. The bead is then centred on the photodiodes. Afterwards we calibrate the photodiodes and the trap.

6.5 Recording the collective effects of the motors

After the calibration process is complete, the bead is slowly and carefully lowered to the substrate until the motors exert a force. This is monitored using the photodiode signal on the oscilloscopes as shown below (Fig. 1.1.17). A shift in the baseline of the bead motion and an

increase in the amplitude of the bead motion indicate that the motors are acting upon the actin filament/bundle. We refer to this observation, colloquially, as an event.

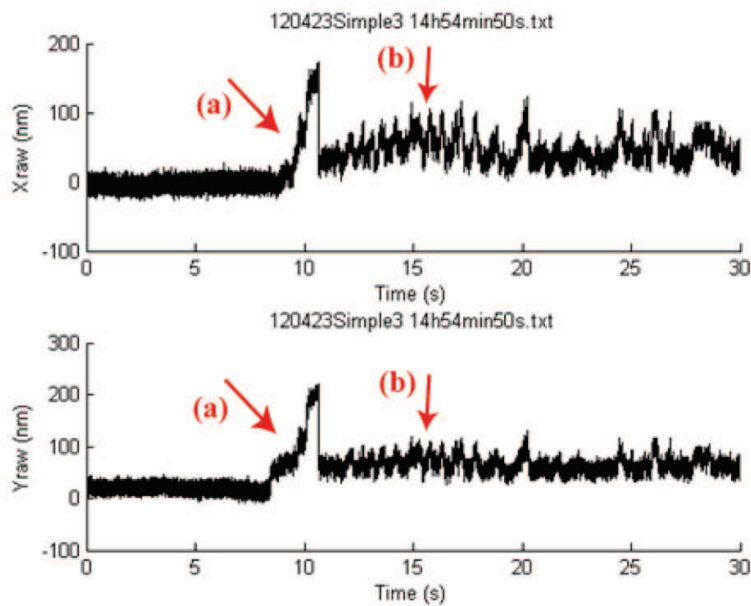


Figure 1.1.17 Recording of an event onset in the X (top) and Y (bottom) directions. There is a shift in the baseline and an increase in the amplitude of the bead fluctuations. The red arrows show different occurrences which can take place during a single event. (a) shift in the baseline indicates that the motors have exerted a force. Here we observe a baseline shift of 50nm which corresponds to a force of 6pN (Trap stiffness = 0.12pN/nm). (b) a possible oscillation event.

The recording program is then engaged in order to characterize the characteristics of the event. Once a satisfactory and sufficiently stable event has been identified, we can then stimulate the system using the other routines written.

Part I

Chapter II: Behaviour of molecular motor assemblies under elastic loading

In this chapter, we report our experimental results on the mechanical properties of molecular motor collections. We start by characterizing the motor systems in motility assays, namely by measuring the gliding velocity of actin filaments as the result of the activity of different myosins (myosin II or myosin 1b) and for different substrates. Under elastic loading, our acto-myosin systems show noisy oscillations; they are here described when using single actin filaments or fascin-crosslinked actin bundles. Our observations on the mechanical stimulation of bundles interacting with myosin-II motors are then detailed.

A/. Characterization of the molecular motors

The in-vitro performance of molecular motors can vary considerably from one experiment to the next. Their functionality depends largely on a number of parameters such as temperature, purification method and even the skill of the experimenter. It is thus useful to characterize any protein (whenever possible or practical) prior to experimentation.

1) In-vitro motility assay

The collective action of myosins can be monitored using the in-vitro motility assay (“gliding assay”). With this assay, we test the functionality of the motors and their average speed. The surface where the myosins are adsorbed/attached plays an important role in the velocity of the actin filaments because they can heavily influence the orientation of the myosin heads. Moreover the surface also dictates the type of passivation treatment that can be applied in order to minimize non-specific interactions with the surface. The temperature at which those tests were performed is room temperature, about 25°C and was assumed as such throughout. However local temperature variations could vary within the flow cell due to the laser and the light from the arc-lamps.

1.1 Nitrocellulose surfaces

Nitrocellulose surfaces are the most commonly used surfaces in our lab. They were used to great effect in the modified in-vitro assay that uncovered spontaneous oscillation in minimal acto-myosin systems (Plaçais et al., 2009). As such they are considered as our default surface treatment in myosin attachment protocols and were used in the majority of our experiments. The velocity of the filaments was first measured in in-vitro motility assays with myosin II HMMs, which are the molecular motors that we have most often used and the most readily available to us (Figure 1.2.1).

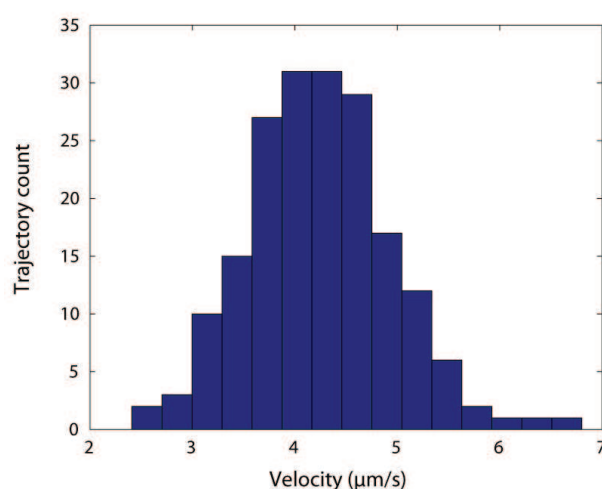


Figure 1.2.1. Speed distribution of actin filaments on myosin II HMMs in a flow cell. The average velocity was $4.2 \pm 0.7 \mu\text{m/s}$ ($n=188$ filaments).

The average gliding velocity was of the order of approximately 4 to 5 $\mu\text{m/s}$ which is slightly lower than the reported HMM-mediated actin filament velocity of approximately 7.5 $\mu\text{m/s}$ (Yoko Yano Toyoshima, Stephen J. Kron, Elizabeth M. McNally*, Kenneth R. Niebling, 1987). The velocity was recorded on thirty more flow cells and the velocities obtained from all of them was considered similar within 95% confidence bounds by a Student's t-test, confirming that our myosin coating can be considered reliable and reproducible. The fascin-crosslinked bundles behaved in a similar fashion and moved with a similar velocity as that of single filaments on myosin II HMMs. The bundles glided with an average velocity of $4.57 \pm 0.65 \mu\text{m/s}$ (obtained from different flow cells). Variation of bundle velocity from flow cell to flow cell was checked using a Student's t-test and proved similar within 95% ($n=.20$).

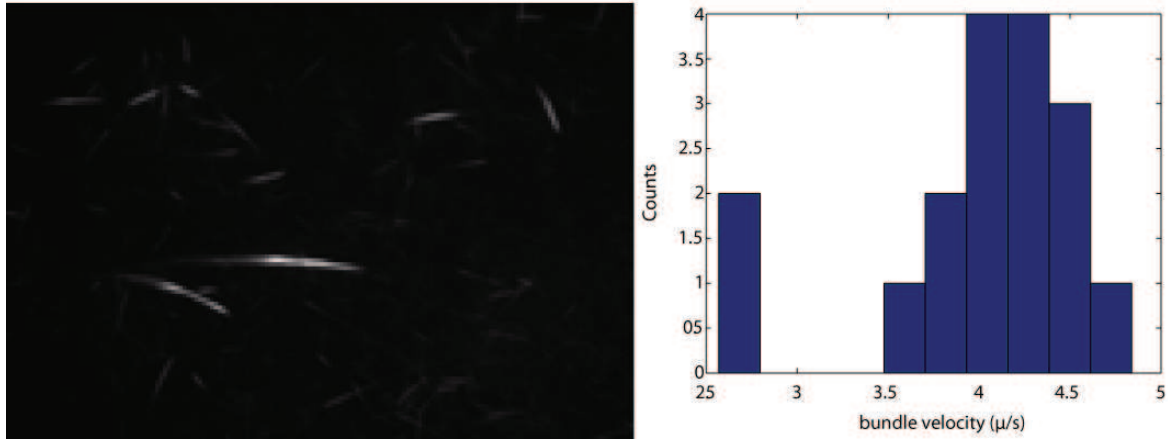


Figure 1.2.2. Left: Photograph from a motility assay showing gliding of fascin-crosslinked actin bundles. Right: Distribution of velocities of fascin-crosslinked actin bundles on myosin II HMMs in in-vitro motility assay. Average velocity = $4.25 \pm 0.8 \mu\text{m/s}$ ($n=17$ bundles)

Contrary to what is observed with myosin II, passive adsorption of myosin1b on nitrocellulose surfaces is not enough in our case for actin motility to occur. The myosin 1b has to be orientated by using anti-myosin1b antibodies directed towards the tail domain of the motor; the antibody is adsorbed on nitrocellulose surfaces prior to the addition of the motor protein.

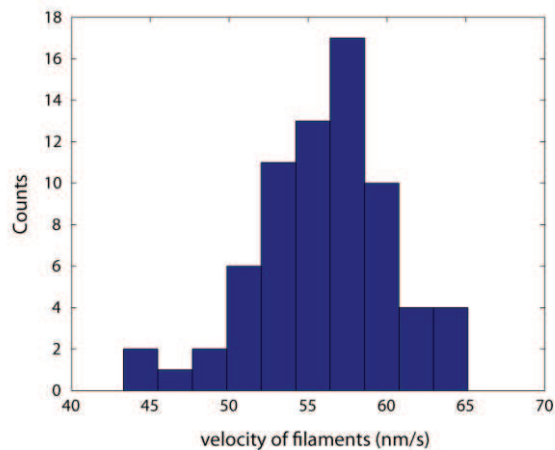


Figure 1.2.3. Speed distribution of actin filaments on a myosin1b-covered surface obtained via attachment of the motors via antibodies. The latter are themselves adsorbed on nitrocellulose-treated surfaces. The average velocity of the myosin 1b is here around 57 nm/s ($n=73$), which is the fastest velocity that we measured.

The velocity of filaments on myosin 1b-covered surfaces was measured at approximately 25 – 57 nm/s (Mean = $37 \pm 0.9 \text{ nm/s}$, $n=12$) which is coherent with the literature although the

velocities we have observed lie in the lower range of velocities reported (Zot, Doberstein, & Pollard, 1992).

1.2 Silane surfaces

One of the main advantages of silane surfaces is that they promote specific adhesion of the myosin tails thus favouring orientation of the head away from the surface and easing their interaction with the actin filament. We then performed tests on silanized surfaces using myosin II HMMs.

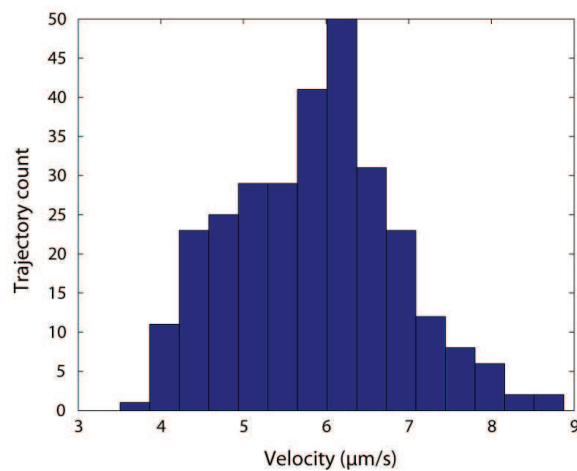


Figure 1.2.4. Distribution of velocities on HMMs on silane-treated surfaces. The velocity is here $8.3 \pm 3 \mu\text{m/s}$ ($n=494$).

As expected, the velocity is higher than what was recorded on myosin adsorbed non-specifically on nitrocellulose surfaces, with a value of approximately $7 \mu\text{m/s}$ on average ($n=5$ different flow cells).

2) Force generation

Force generation is one of the most fundamental characteristics of molecular motors and it is hence important to characterize the average force developed by the myosins we use before starting our experiments. In our set-up a bead attached to an actin filament or bundle is brought down on a myosin-covered surface and the fluctuations of the bead over time are recorded. A shift in the baseline of the timecourse indicates that the motors have interacted with an actin filament and are actively exerting a force on the bead-actin system. This is also evidenced by the larger amplitude of the fluctuations of the bead. At steady state, the force

generated by the myosins is equal to the elastic restoring force exerted by the optical trap, hence this force is also known as the “stall force”. The force developed can be calculated from the baseline shift by knowing the stiffness of the trap (~ 0.13 pN/nm) and the average number of motors involved can be deduced by assuming that a single motor develops a force of 1.5 pN and has a duty ratio of 0.1 (Howard, 2001; Molloy et al., 1995). Here we test our myosin II motors on single filaments and then on fascin-crosslinked actin bundles.

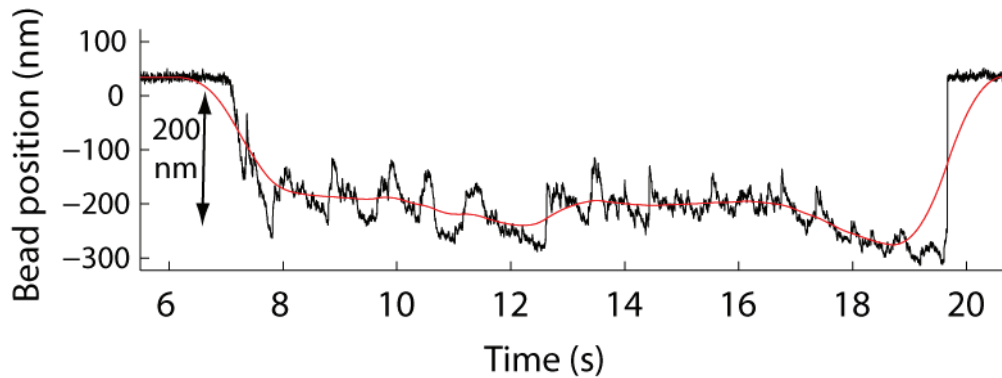


Figure 1.2.5. Graph showing a 200-nm shift in the baseline using single actin filaments and myosin II HMMs. Since the optical trap has a stiffness of ~ 0.13 pN/nm, the force exerted by the motors here is 26 pN which amounts to 160 motors of which about 10 interact with actin filament at any given time (assuming a single motor generates a force of 1.5pN and a duty ratio of 0.1).

The forces generated by myosin II on single filaments lie between 5 and 26 pN ($n=5$). This range is similar to that previously reported by our team (between 4.7 and 22.3 pN (Plaçais et al., 2009)).

The next part of the testing process was to test the forces that would be exerted on fascin-crosslinked bundles. We used bundles mainly to obtain a more rigid system compared to the single filaments and to recruit more motors and hence exert a greater force. As a bonus, fascin crosslinks actin filaments in a polar fashion producing polarized bundles which can be used to mimic the hair-cell stereocilium more accurately than single filaments. With a ratio of actin to fascin of 2:1, we expected to have bundles of approximately a few tens of actin filaments on average (Ishikawa et al., 2003), leading us to believe that polarized actin bundles would lead to much larger stall forces than with single filaments.

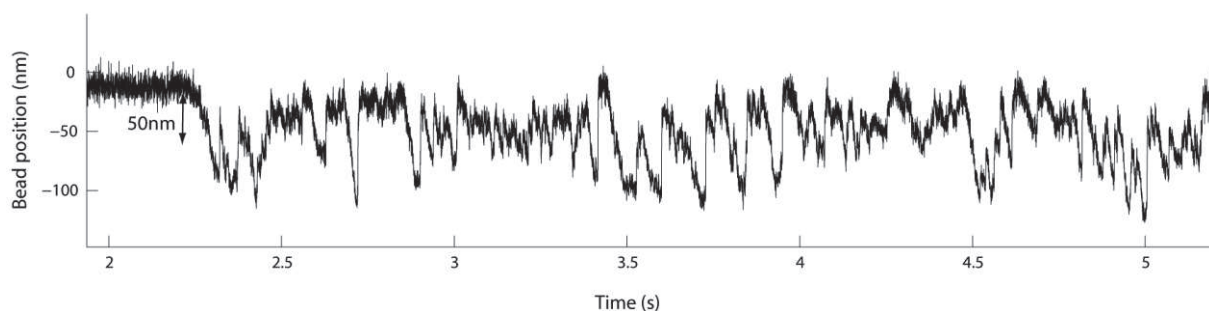


Figure 1.2.6. Graph showing a maximum baseline shift of 100 nm using fascin-crosslinked bundles, corresponding to a force of 12 pN and hence 80 motors.

Quite surprisingly, we found that the forces generated by myosin II motors on bundles were in the range of 6.5 to 26 pN ($n=15$) which is nearly identical to the forces observed using single filaments. It should be noted, however, that a large number of bundles escaped from the tweezers when brought into contact with myosin, meaning that our trap was not strong enough to retain those bundles (the bundles that escaped the trap developed forces that were larger than ~ 30 pN). This implies that the bundles we are able to study are subjected to forces exerted by the myosin II motors that are within the sustainable force range of our optical tweezers. At the moment, our tweezers cannot oppose the forces generated by myosins on large bundles; we thus select “weak” bundles only.

During the course of this project, reproducing oscillations using single filament experiments proved difficult, which is why our focus was quickly placed on using the bundles. The actin bundles were easier to handle and events were observed more regularly and more often than with single filaments.

B/. Spontaneous oscillations under elastic loading

When the actin filament/bundle is brought in contact with molecular motors, we have seen that the motors exert an active force that evokes a shift in the baseline of the bead position (Figure 1.2.5 and Figure 1.2.6). Knowing the trap stiffness, one can monitor this force as a function of time; a steady state would result from force balance between the active motor force and the elastic restoring force exerted by the trap. This stall condition, however, appears to be unstable and noisy spontaneous oscillations of the actomyosin system are often observed (Plaçais et al., 2009). The power spectrum of the oscillation is drawn in order to determine the characteristic frequency of the oscillation from the presence of a clear peak.

However the oscillations recorded are often very noisy and as such appear as bands with no clearly defined peak in the power spectrum. As a means to discriminate ‘valuable’ oscillations, a quality factor is defined. The power spectrum is fitted with a Lorentz function; the central frequency f_0 and the width of the peak at half its height Δf are extracted from the fit. The quality factor Q is then defined as : $Q = \frac{f_0}{\Delta f}$. We consider movements with a quality factor larger than 1 as being true oscillations.

1) With single actin filaments

The spontaneous oscillations reported in our laboratory in 2009 by Pierre-Yves Plaçais were successfully reproduced using a similar protocol. There are two main differences in the current protocol: 1/ we used a different batch of purified myosin II HMMs and 2/ beads were functionalized with streptavidin using the Sulfo-NHS/EDC coupling protocol instead of using commercially available streptavidin-coated beads (that did not work in my hands).

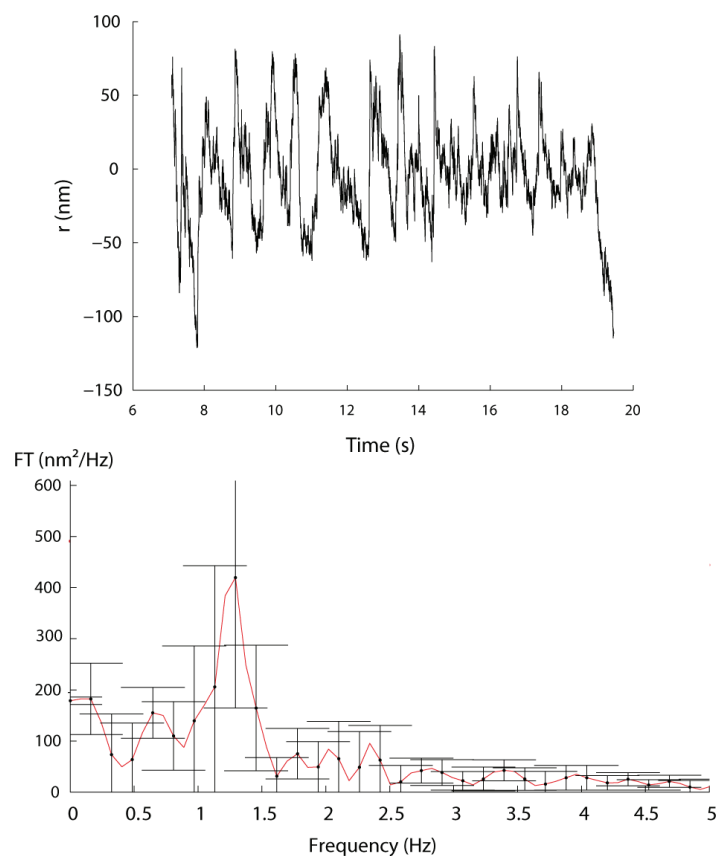


Figure 1.2.7. Top: Oscillation of an actomyosin system with a single filament. Bottom: Power spectrum of the oscillation (Frequency of 1.27Hz with a quality factor of 1.8).

The oscillations previously reported displayed three types of waveforms. The most striking ones were the triangular form similar to what is observed in muscles and the rectangular form which is analogous to hair cell bundle oscillations. However, the most common form recorded was intermediate between triangular and rectangular and has no defined shape. In our case, the latter was the only pattern observed using single actin filaments. The range of frequencies we recorded varied between 1.27 and 5.6 Hz (n=5).

As mentioned earlier, the issues with actin filaments were numerous. The molecular interaction events and the subsequent oscillations were quite short-lived often stopping before we could even start recording. For this reason and also to test how the different properties of a bundle could affect the oscillatory behaviour of the system, we focused mainly on the use of bundles in our experiments.

2) With polarized actin bundles

The actin bundles behave essentially like single filaments during the typical experiment (apart from the lack of visible buckling and their greater ease of use) with some differences that are important to point out.

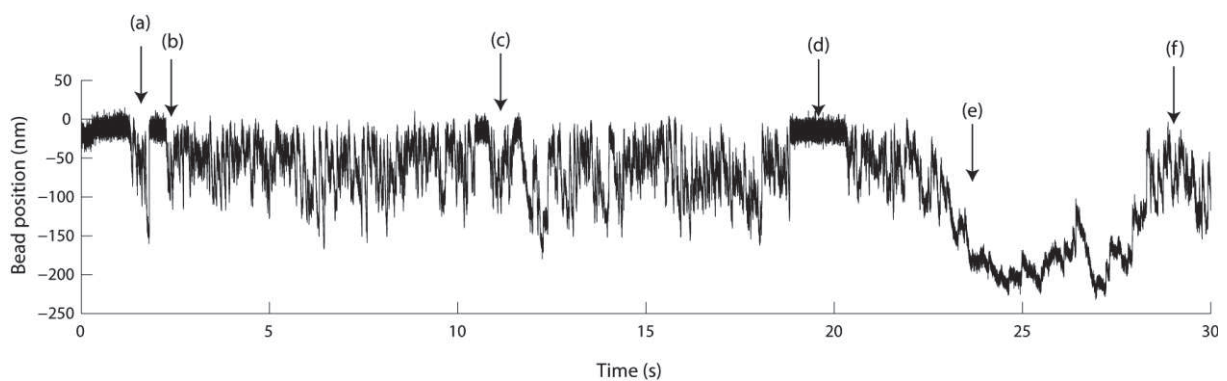


Figure 1.2.8. Timecourse of a fascin-crosslinked bundle under elastic loading interacting with an assembly of myosin II HMMs. The labels (a) to (f) show different events that can occur over time during such an interaction and are described in greater detail in the main text.

The timecourse above shows a typical bead motion over time with a “bundled actin and myosin II HMM” configuration under elastic load from the optical tweezers. The various occurrences that can take place are listed below and refer to Figure 1.2.8 (Note that those

examples belong to that particular event and can take place individually during others. This timecourse was chosen because all these occurrences took place during its recording):

(a): There is a shift in the baseline and an increase in the fluctuation amplitude indicating interaction with the motors and force generation. Before the maximum force is reached, the bundle apparently detaches.

(b): Another shift occurs and this time, the motors reach a steady state and we record an oscillation.

(c) and (d): The bundle detaches again, reattaches and another oscillation is initiated.

(e): During the oscillatory behaviour, the baseline shifts further and further indicating that an increasing force is being exerted on the bundle. Moreover, the amplitude of the fluctuations decreases markedly implying an increase in the stiffness of the system. The bundle may have recruited other filaments or come closer to the substrate to interact with more and more motors. After some time, the force decreases and the system resumes the oscillatory behaviour as observed before the force increase.

(f): An oscillation appears and persists for several minutes.

One of these oscillations was singled out and analyzed to showcase the typical behaviour of a myosin II-driven actin bundle under an elastic load. This particular oscillation ranks among the fastest we have recorded; it has a frequency of 6.5 Hz.

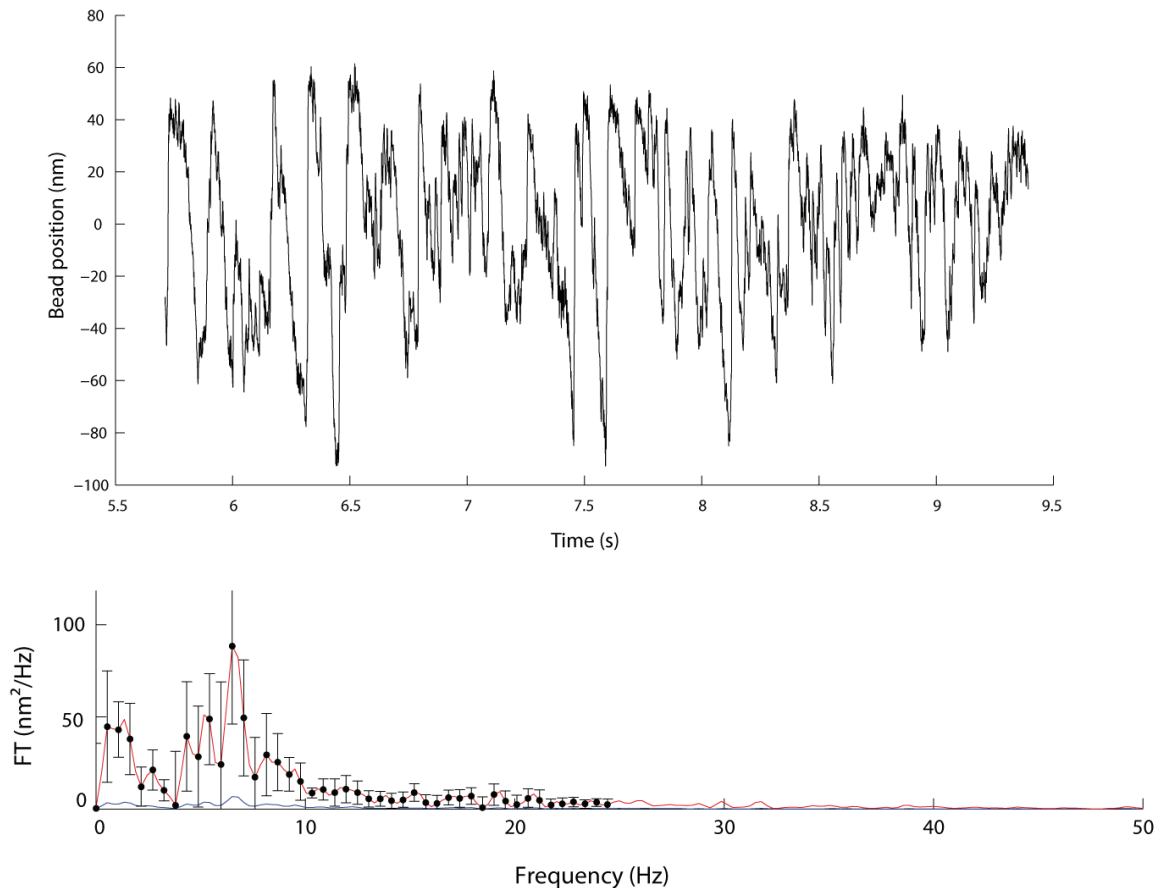


Figure 1.2.9. Top: Timecourse of oscillations as seen on actin bundles interacting with a collection of myosin II motors. Bottom: Power spectrum of the oscillation (frequency of 6.5 Hz and quality factor of 2.1).

The oscillations recorded on bundles have a frequency that varies between 1.3 and 7 Hz (with an average of 4.5 ± 1.7 Hz ($n=25$), again similar to actin filaments. However, the events last much longer, of the order of several minutes (~ 7 min, events during experiments involving bundles usually end because the bundle escapes the trap after some time) compared to at most 1 or 2 min for the single filaments. Since the oscillations last for longer periods of time, it is possible to apply mechanical stimuli for relatively long periods of time.

C/. Mechanical stimulus : Alternating steps

To stimulate the system, we imposed alternating step displacements to the laser trap. The steps increased in amplitude in the positive and negative directions until the final step reached 100 nm. The series was then repeated ten times during one run. Each lasted for 0.5 s with a

pause of 0.5 s between two consecutive steps.

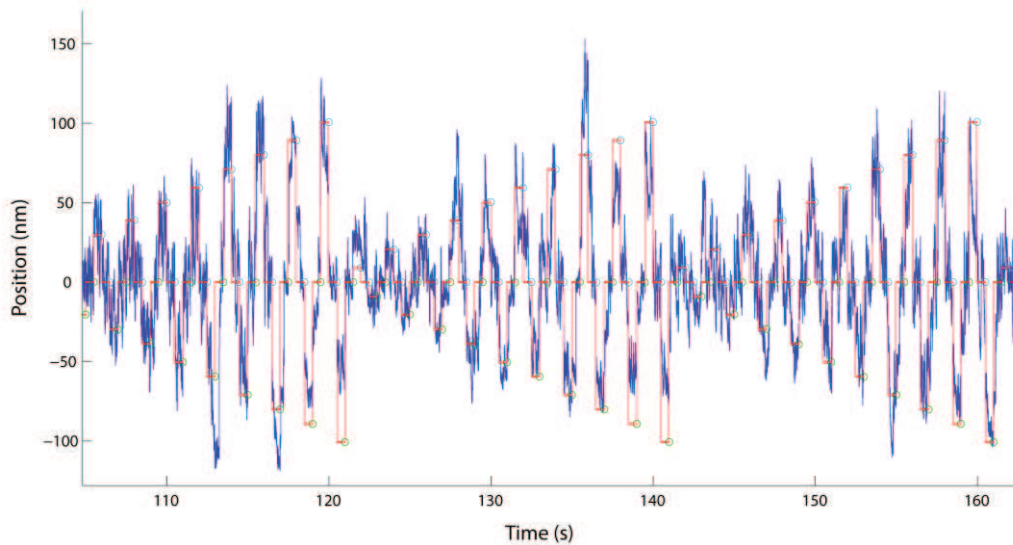


Figure 1.2.10. Position of the bead (in blue) over time when subjected to alternating steps of the laser trap (in red). This figure shows three alternating step series of a timecourse consisting of ten. Although there is a shift between the average trap and bead positions as a result of active force production by the motors, we have here realigned the traces to more clearly see how the acto-myosin system responds to the stimulus. The bead position, averaged over the 0.5-s interval between two steps is artificially aligned with the trap position before each step.

Figure 1.2.10 shows three iterations of alternating steps out of ten series. For a passive system consisting of, for example, molecular motors with no ATP in interaction with the actin-bead structure held by the tweezers, one would expect a movement of the bead following the direction of stimulation and reaching a stable position that is lower than the position of the trap (in absolute values) (Figure 1.2.11). This also implies that the force reaches a plateau at a non-zero value showing that the actomyosin system has an inherent stiffness. Conversely when ATP is added, hence activating the motors, the latter adapt to the force applied and relax to stall force. In that case, the bead should reach a position that is on average equal to the position of the trap (in absolute values; after the offset corresponding to stall force has been subtracted). Both are illustrated in Figure 1.2.11 when the experiment was performed on single filaments (Plaçais, 2008).

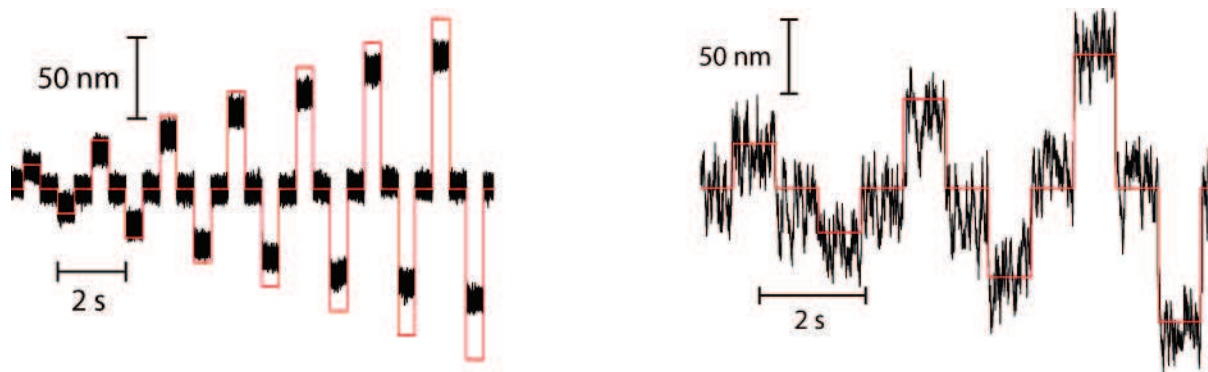


Figure 1.2.11. *Left : Response of passive motors (in black) to alternating steps imposed by the trap position (in red). The bead reaches a position that is inferior to the trap position. Right : Response of active (in black) to alternating steps imposed by the trap position (in red). The motors relax to stall force upon application of the stimulus; the bead can thus be observed to move up to a position that is on average equal to the trap position. Taken from (Plaçaïs, 2008).*

Polarized actin bundles seem to behave in a similar fashion as demonstrated in Figure 1.2.10 where we can clearly observe that the bead position actively moves towards the trap position after stimulation. One notable peculiarity in our observations is that in some cases, the bead reaches a position beyond the trap position. However we reason that this might be due to a calibration error. Since we calibrate our photodiodes by imaging the bead slightly above the myosin-covered surface, there is a possible bias induced when we now image the bead in the plane of the myosin-covered surface during the actual experimental event.

By averaging the ten series, we can observe the general behaviour of the system at each step with respect to time in both displacement and force (knowing the stiffness of the optical trap which is 0.12 pN/nm in this case) (Figure 1.2.12).

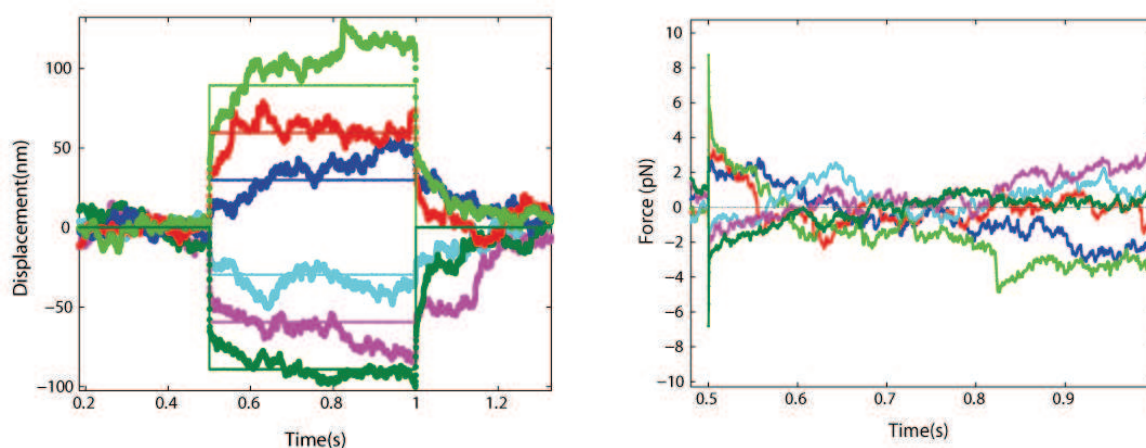


Figure 1.2.12. Signals obtained from averaging ten series of alternating steps. Left: signals of the mean bead displacement over time (noisy signals) superimposed on the trap position (perfect steps). The steps and the bead displacement are colour-coded. We can see the anomaly where the final bead position lies beyond the trap position. Right: Forces exerted by the trap. The force relaxes to zero on average due to motor activity but as expected from the displacement-time relation shown on the left, the force sometimes continues to non-zero values. This is particularly noticeable from 0.8 s onwards. Both anomalies are attributed to a calibration error.

The relaxation time of the motors can be estimated from the time needed for the bead to reach the laser trap position. It was previously established that this relaxation time consisted of two phases, a rapid phase and a slow phase (Plaçais, 2008). The two characteristic time constants of those two phases can be deduced by adjusting a double-exponential curve to the force signal of the form $F(t) = A_1 e^{-t/\tau_1} + A_2 e^{-t/\tau_2}$ where τ_1 is the rapid phase and τ_2 is the slow phase. The rapid phase is linked to passive relaxation due to the viscous drag while the slow phase is linked to the motors actively relaxing the force. Earlier works in our laboratory characterized those times as being of the order of 100 - 200 μ s for the rapid phase and having ranging from 11 to 30 ms for the slow phase. In our case however, the values of τ_1 and τ_2 are larger, of the order of the millisecond for both time constants. We have 100 ms for τ_1 and 300 ms for τ_2 , implying that our system consisting of bundled polarized actin is markedly slower than a similar system based on single actin filaments. Strangely, the relaxation times are sometimes larger than the actual duration of the step. This means that in those cases, the step was too brief to the bead reaching a “steady” position and as such it would be interesting to repeat those experiments with longer-lasting steps. Moreover their value does not seem to be correlated to the direction or amplitude of the steps. More importantly, due to the bundles being stiffer than single filaments, we were expecting a faster time constant. Unfortunately, it is difficult to deduce and conclude anything concerning this within reasonable confidence bounds due to the low amount of data we have on the bundles and the large fluctuations of the system.

Figure 1.2.12 can also be used to obtain the force-displacement behaviour of the system at different moments of the step duration.

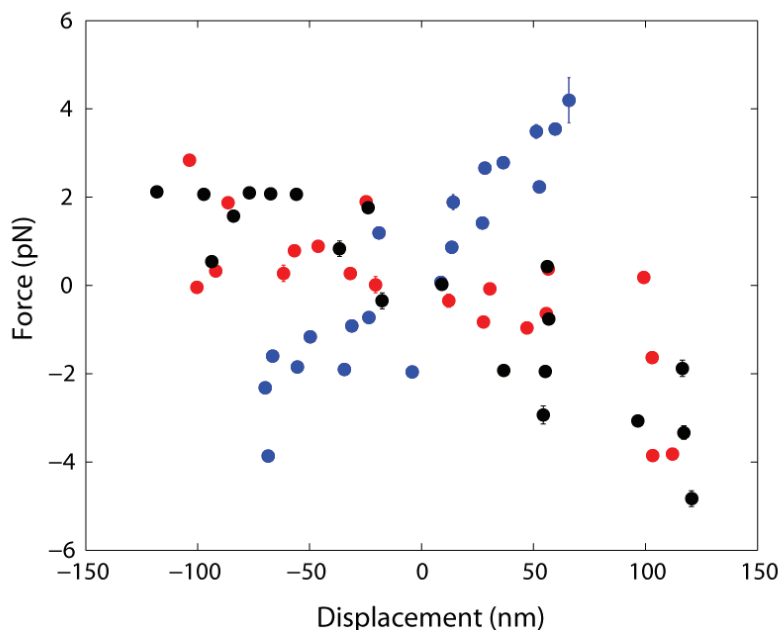


Figure 1.2.13. Force-displacement relation of the system at different moments of the step duration during the alternating steps protocol. The force-displacement relation was plotted for a time window of 3 ms at 7 ms (blue), 247 ms (red) and 457 ms (black) after the start of the steps.

The data points are quite widespread and as a result, performing a linear fit through the appropriate points makes little sense but it is still possible to observe a trend in the data points. The relation remains roughly monotonous for each value of time. Shortly after the start of the step, the force-displacement relation has a positive slope. As the step progresses, the bead reaches its “stable” position located on average beyond the trap position as shown in Figure 1.2.13 by the negative slopes of the force-displacement relation at 247 ms and 457 ms after the start of the step. As mentioned previously, this is due to a probable negative bias in our calibration technique.

Part I

Chapter III: Discussion & Perspectives

In this chapter, we discuss our observations on the oscillatory behaviour of the molecular motors. Our main interest was to expand on the work performed previously (Plaçais, 2008). The spontaneous oscillations of a minimal acto-myosin system were a novel finding and demonstrated that the oscillatory behaviour of many biological systems could be attributed to an intrinsic oscillatory instability of motor collections under elastic loading. The parameters that controlled the properties of the oscillation (shape of the waveform, frequency, etc...), however, were not clearly identified. It was speculated then that using stiffer actin structures would improve our ability to control the oscillation, for instance by varying the stiffness of the elastic load (optical trap) on the acto-myosin system. In this thesis, we used polarized actin bundles to obtain a stiffer system. We also hoped that actin bundles would recruit more motors giving rise to more robust oscillations.

However, because of experimental difficulties with both the instrumentation and the biochemistry, we were able to reproduce the basic oscillation experiments quite late. We focused our efforts on experiments with actin bundles for the aforementioned reasons, but also because the events using single filaments proved to be short-lived despite the passivating PEG layer on our beads. It is also interesting to note that using polarized actin bundles could be a good test for future use with myosin 1c to better emulate the hair cell bundles of the inner ear.

A/. Motility Assay

One of our main achievements was to purify fully functional myosin 1b. The perspectives will be to use myosin 1b in place of myosin II in the elastic loading experiment with the optical tweezers. Because the mechanosensitivity of this motor makes it behave as a catch bond, we expect that myosin 1b would not oscillate under our usual experimental conditions: the opposing force of the tweezers should prevent ADP release in the ATPase cycle of the myosin, thereby blocking the motor in a strongly attached state to actin. This inference, however, still awaits for experimental confirmation. Another important achievement of the

present work was the development of silane surfaces, which preferentially orient the myosin heads away from the surface, hence increasing the average velocity of gliding filaments by decreasing the density of nonfunctional myosin heads. While the silanization process that we currently use remains unreliable, with a low success rate, it confirms the effectiveness of hydrophobic surfaces in the preferential orientation of myosin II and should be perfected in our laboratory for future use.

B/. Force exerted by the motors

In our hands, the force developed by the motors in presence of polarized actin bundles was similar to what is observed on single filaments. Fascin is a cross-linker that binds actin filaments into polarized bundles. In our current experiments we should have on average about 10-15 filaments per bundle for a total width of approximately 130nm with on average 9nm between each filament (Ishikawa et al., 2003). The average length of the actin bundles in our experiment was around 10 μm (n=7). Compared to single filaments which have on average a similar length but have an average diameter of 7-8 nm, we expected a larger force from bundle-myosin interaction due to the larger number of motors that should be in contact with the bundle. However, our current optical tweezers appear to be too weak to hold acto-myosin systems that develop forces larger than a few tens of piconewton. It often happened that a bundle traversed the optical trap. Because the tweezers are unable to retain the ‘stronger’ bundles, we have probably selected bundles that recruit a relatively small number of motors, comparable to that of single filaments. To really benefit from the potential of the actin bundles, it is thus required to improve our current optical-trap setup to make it stiffer. This is feasible, considering that our current maximal stiffness (0.13 pN/nm) is significantly smaller than those reported by others in the literature (up to 1 pN/nm).

C/. Spontaneous oscillations and stimulation

We were able to reproduce spontaneous oscillations under elastic loading with single filaments and the frequencies we have measured were consistent with what was previously found (Plaçais, 2008). Our latest addition to this system was to replace single actin filaments by rigid fascin-crosslinked polarized actin bundles. We found that the bundles could oscillate with frequencies similar to actin filaments. Their behaviour under mechanical stimulation remains more difficult to interpret due to the low amount of data. The system exhibits large

fluctuations making rigorous statistical analysis paramount to better understanding it. As such, we could only make qualitative observations. We have found that the rapid phase of the relaxation by the motors is slower with bundles than with single filaments but future experiments will have to determine if this is really the case over a large number of experiments or just a peculiar feature of that particular motor event.

Nevertheless, this system remains promising to test the kinetics of myosin response to external stimulation. In particular, it could provide useful insight into muscle experiments that probe tension changes in response to fast length changes of the muscle (see section D/ 1.3 of the Prologue and the so-called T2 curve) as well as myosin-based adaptation in the hair-cell bundle (see section D/ 2.2 of the Prologue).

PART II

Self-assembled magnetic bead columns as molecular force sensors

(in collaboration with François-Damien DELAPIERRE, Laurent
MALAQUIN and Jean-Louis VIOVY)

Part II

Introduction

A/. The Need for a New Molecular Force Sensor

In part I, we have discussed the use of optical tweezers to measure forces exerted by molecular motors. We described how a focused laser beam produces an elastic restoring force on a dielectric micron-sized bead, which can then be used as a handle for mechanical stimulation of a minimal acto-myosin system. We also saw that a photometric system containing photodiodes can track nanometer-scale displacements of the bead with a sub-millisecond time resolution.

The main disadvantage of this setup is that the optical trap can only manipulate one single bead, and consequently track one event, at a time. This is rather inefficient considering that the large amount of molecular motors adsorbed to a relatively large surface area and the high number of actin filaments in solution implies that there are potentially hundreds of events that could take place while we are probing just one.

This prompted us to think about ways of studying acto-myosin systems under elastic loading in large numbers. Such a system would contain a large number of identical force sensors, each capable of performing the job of an optical trap (i.e. apply forces in a range of 1-100 pN). As a consequence, the system should also include a position monitor capable of recording several motor interactions at the same time.

We were initially inspired by work on two-dimensional arrays of flexible micro-pillars, which have been extensively used over the past decade to probe active force production by adhering cells. The measurement of the force in the case of the micro-pillars results from their cantilever-like mechanical behaviour. Cantilevers were used as force sensors in a horizontal configuration (Galbraith C, 1997) but it was limited by the density of sensors that could be built on the surface. Another configuration, which has become the basis of cellular force sensors today, was then devised using an array of vertical silicone (polydimethyl siloxane known as PDMS) elastomer microneedles (Tan et al., 2003) (See Figure 2.0.1). The pillars

are made by molding liquid PDMS pre-polymer onto a silicon wafer patterned with an array of cylindrical pits. The wafer is patterned by a combination of conventional photolithography followed by a deep etching process.

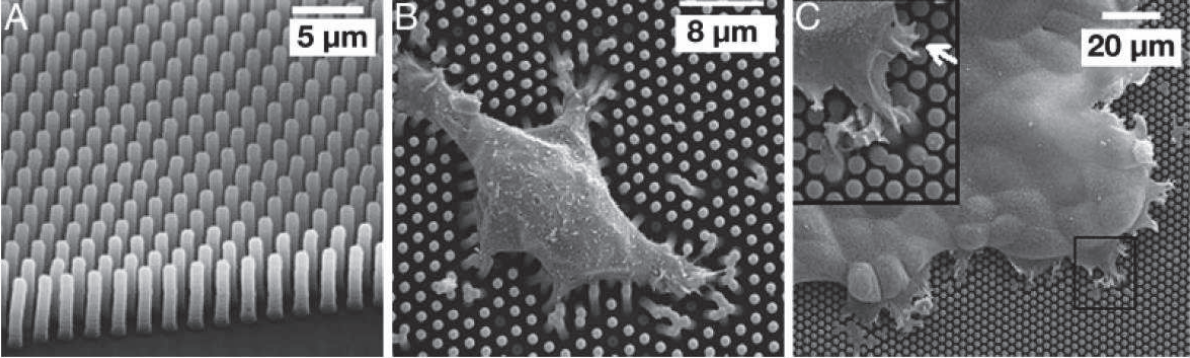


Figure 2.0.1. Scanning electron micrographs of the micropillars. (A) Microfabricated pillars after PDMS molding. In this particular case, the pillars are densely packed to mimic a continuous surface as closely as possible, but the packing density of the micropillars can be changed according to experimental needs. (B) Individual cells on the array. (C) A cell monolayer on the array. (du Roure et al., 2005).

The geometry of a parallel pillar arrangement that would be appropriate for our experiment is shown in Figure 2.0.2.

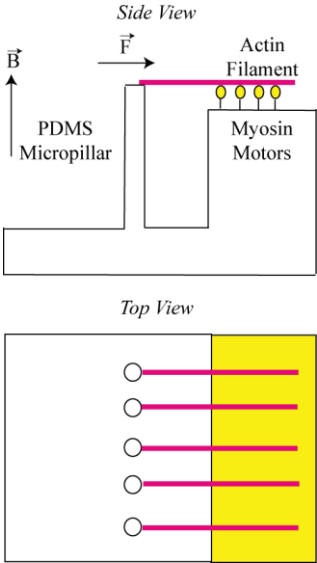


Figure 2.0.2. Diagram of an idealized set-up using PDMS micropillars to probe molecular motor collections mounted on a pedestal opposite the pillars.

Over small displacements, the displacement of a pillar is directly proportional to the force. If we consider a flexible cylinder of radius r , and length L bent by a force F exerted at its tip, the linear elastic theory gives us the following cantilever equation:

$$F = \left(\frac{3}{4} \pi E \frac{r^4}{L^3} \right) \Delta x; \quad \text{Eq 2.0.1.}$$

where E (~ 1 MPa) is the Young modulus of the elastomer and Δx is the deflection of the pillar upon application of an horizontal force at its extremity.

Since each pillar is completely independent of its neighbours, the equation above can be applied to any given micropillar with no ambiguity, further simplifying things. It is possible to vary the mechanical stiffness of the pillars over three orders of (du Roure et al., 2005) by tinkering with the dimensions of the pillars (see Eq 2.0.1), which makes it able to sense a wide range of forces (from 0.47 to 174 nN/ μm).

The typical stiffnesses of the micropillars lies between 1.3 and 21.8pN/nm for pillars of 1 to 2 μm in diameter and 5.2 to 6 μm in length (du Roure et al., 2005). Because cells exert forces in the range of a few nanonewtons, the pillars are deflected by more than a few tens of nanometers, which can easily be detected by video-microscopy. However, our goal is to study molecular motors, particularly myosin II and hopefully in the near future myosin 1b and 1c. Those motors, when working in small groups, develop forces up to a few tens of piconewtons only (Plaçais et al, 2009). Although modifying the dimensions of the pillars to get lower stiffnesses ($\sim 0.1\text{--}3$ pN/nm) may be feasible, the pillars seem too rigid for our purposes, unless we work with much larger motor assemblies. In addition, with this type of force sensor, it is not possible to change the stiffness in situ; one has to make a new PDMS chip with an aspect ratio of the pillars that yields the desired value of the stiffness.

During discussions on the subject with Laurent MALAQUIN and Julien HUSSON (both from the group of Jean-Louis VIOVY), our team came across micro-fluidic devices involving the self assembling of superparamagnetic beads into columns under the action of an external magnetic field. We wondered whether such columns would display mechanical properties that are appropriate for our own purposes.

B/. Auto-Assembled Magnetic Columns

Magnetic beads are commonly used in research, especially in biology. An impressively detailed review on the subject was written by Martin GIJS and his collaborators in 2010 (Gijs, Lacharme, & Lehmann, 2010). They are often combined with microfluidics technology as a way to study protein interaction (Le Nel et al., 2008) and/or to identify and profile target proteins in the diagnosis of diseases (Mohamadi et al., 2010).

Upon application of an external magnetic field, the beads align along the field lines and pile onto one another to form linear structures. When magnetic beads are stuck on a PDMS surface, they nucleate the formation of columns, thus forming a network of magnetic columns regularly distributed over the PDMS chip. Such networks, using specifically functionalized beads, are used as elaborate traps to capture cells for diagnosis in our research unit by the Viovy group (Saliba et al., 2010).

Magnetic beads have already been used as force sensors at the molecular scale. The beads were recently used to measure and characterize the well known force generation induced by actin polymerization (Brangbour et al., 2011)

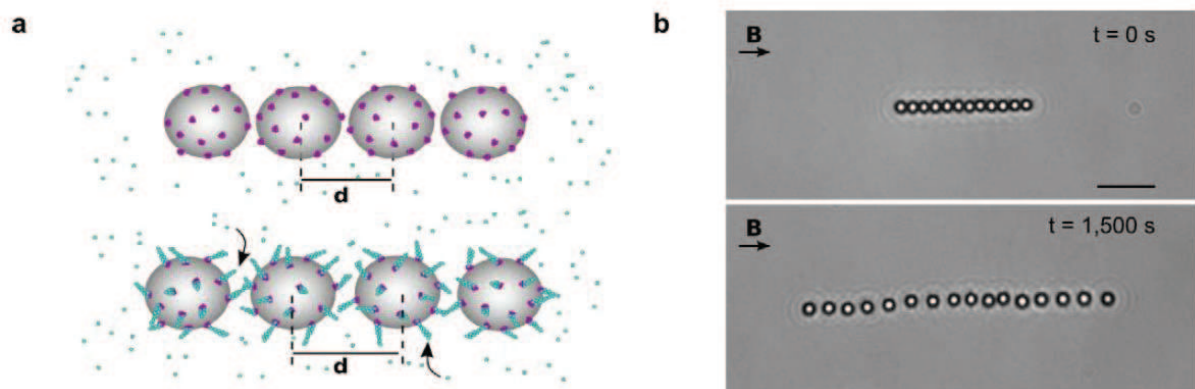


Figure 2.0.3. The beads are coated with gelsolin which initiates actin polymerization which pushes the beads apart. (b) Bright field images of aligned magnetic beads under a magnetic field of 0.5mT before (top) and after (bottom) actin polymerization. (Brangbour et al., 2011).

The magnetic beads were functionalized with gelsolin, a capping protein of the barbed end of actin. Gelsolin directs pointed end growth of the filament in presence of G-actin. On application of a homogenous magnetic field, the beads align along the field lines (See Figure 2.0.3). When G-actin is added, the filament starts to grow and the filament growth along the

axis of the bead alignment causes the beads to move apart from each other. The distance between the beads and the magnetic attractive force were carefully monitored through the application of a homogeneous magnetic field. They were able to obtain magnetic attractive forces of about 0.1 to 100pN with the distance between the beads varying from a few nanometers to several microns.

C/. Magnetic columns as force sensors

To probe acto-myosin interactions, we plan to use the ‘cantilever array’ shown in Figure 2.0.2 but by using magnetic bead columns instead of elastomeric micro-pillars. An ideal concept diagram of the set-up is shown in Figure 2.0.4. One advantage of a magnetic column over a pillar fabricated with soft lithography is that its stiffness can easily be tuned by adjusting the strength of the external field and/or by controlling the number of beads in the column. As with the pillars, the columns will seek to realign themselves with the field in response to external stimulation to return to their original position and thus exert a restoring force. This behaviour is analogous to a Hookean spring and optical tweezers. We thus plan to use this property to obtain high throughput force sensors due to the large number of columns that can be generated on a micro-pattern.

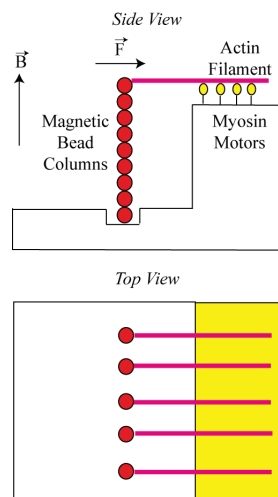


Figure 2.0.4. Concept diagram for the set-up. An actin filament bound to the topmost bead is brought into interaction with a myosin field on an elevated PDMS block. The motors will pull on the filament, deflect the column, which will exert a restoring force on the filament.

The core of the idea is to attach an actin filament by biochemical means to the topmost bead of a column and bring the filament into contact with a myosin “carpet” that had been previously formed onto an elevated PDMS platform. The myosins will then exert force on the actin filament, deflecting the column, which in turn exerts a restoring force. This condition mimics the elastic loading that optical tweezers provide to our molecular motor collections (see Part I). The obvious advantage of this set-up is the large amount of interaction events that we could potentially probe at the same time, thanks to the large number of columns that we can form on a single micro-patterned surface.

However, before we can do that, it is important to characterize the mechanical properties and the behaviour of the columns. This part of the thesis deals with our experimental endeavour to better understand this new set-up and investigate if the columns can act as force sensors that are appropriate for probing acto-myosin interactions.

Part II

Chapter I: Materials and Methods

In this chapter, we describe the methods used to assemble columns of magnetic beads. We detail the characteristics of the various components of the set-up and describe the experimental procedure we use to characterize this system as a molecular force sensor.

A/. Making the magnetic bead pattern

The substrate for column formation is made through capillary-assisted deposition of magnetic beads in microcavities of a patterned surface of Poly(DiMethylSiloxane) (PDMS), a silicone-based elastomer. The PDMS substrates are prepared by replication on master mould prepared via photolithography on a silicon wafer.

1) PDMS substrate fabrication

1.1 – Making the moulds

The moulds are prepared by François-Damien DELAPIERRE in the clean room prior to the experiments. For that purpose, silicon wafers (2'' diameter, 325 μ m thick), are first oxidized in an oxygen plasma cleaner for 1min and then heated on a hot plate at 120°C for 10min to dehydrate the surface. A layer of photosensitive resist (SU8-2002) is then applied to the wafer using a spin-coater (3000rpm, 30s). The coated wafer is baked at 65°C for 1min and then at 95°C for 2min. It is then placed under an optical mask on which a hexagonal pattern has been drawn and irradiated by UV light via a mask aligner system (Karl Suss MJB3). After another round of post-bake at 65°C (1min) and 95°C (1min), the samples are developed (using SU8 developer) and cleaned with isopropanol. SU8 is a negative resist meaning that the exposed region of the sample will reticulate and solidify whereas the unexposed area will be selectively removed by the developer. The developing time depends on the density of the structures on the substrate and on the thickness of the resist. Adjustment of the development time was done by optical monitoring on a microscope. The typical developing time ranges from 30 to 60 s for a resist thickness of 2.5 – 3 μ m. Finally, the wafers are cleaned with an oxygen plasma treatment and silanized with trimethylchlorosilane (Sigma/ABCR) through

vapour phase deposition. The sample is briefly placed in a dessicator containing a flask with 500 μ L of silane for 10min. The pressure of the dessicator is adjusted to around 100mbar. The trichlorosilane molecules bind covalently to the silicon surface and spontaneously form a self-assembled monolayer that behaves as an anti-sticking layer (passivation layer) and prevents PDMS adhesion to the master during the molding step.

1.2 – PDMS casting

PDMS is a silicone-based elastomer material which is routinely used in micro-fluidics (Figure 2.1.1). In our experiments, we used a commercial material formulation from Dow Corning, Sylgard 184 delivered as a two-part kit. The base material is mixed with the curing agent in a 10:1 ratio. The prepolymer mixture is first degassed in a vacuum for 10min and then directly poured on the mould fabricated by photolithography (engraved resin on a silicon support).

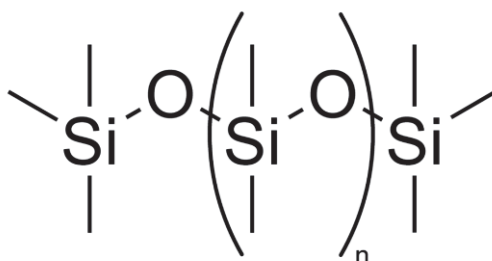


Figure 2.1.1. Chemical formula of Polydimethylsiloxane (PDMS). PDMS is commonly used to make microfluidic chips both for diagnosis and for studying the behaviour of cells in confined spaces. Its inert nature also makes it a material of choice in the manufacture of bio-compatible structures.

The reticulation process is performed by placing the mould and the PDMS mixture in an oven at 65°C for 24h. Once the reticulation of the elastomer is achieved, this slab (1 to 3mm thick) is peeled off the mould. The region of interest i.e. the region containing the pattern is cut off, resulting in a patterned PDMS substrate containing the trapping structures for that particular assembly process. The patterns consist of square-shaped cavities arranged in a hexagonal lattice. The cavities are placed at a distance of 30 μ m to each other.

2) Depositing nucleator beads by capillary assembly

Capillary assembly is a form of self-assembly. Self-assembly is the autonomous organization of objects into ordered structures and is one of the most efficient ways of arranging a large

number of particles in an orderly manner on a surface. Most self-assembly techniques rely on interaction forces between particle and surface to direct the organization, usually using the hydrodynamic drag acting on a drop of particle suspension in direct contact with the surface. However, this can lead to overly dense packaging and makes the precise placement of individual particles difficult. A common solution is to pattern the surface to direct the forces either by chemical means or by altering its topography.

It has been shown that capillary forces can be used effectively to achieve single particle placement on virtually any hydrophobic surface provided that some parameters are controlled such as the particle concentration in the suspension and the contact angle between the drop of particle suspension and the substrate ((Malaquin, Kraus, Schmid, Delamarche, & Wolf, 2007).

Self-assembly is usually performed by dragging a drop of particle suspension over a hydrophobic surface. The moving meniscus confines the particles and exerts a force on them. On hydrophobic surfaces, the component of the force parallel to the surface becomes strong enough compared to the perpendicular one to avoid deposit of the particles on flat surfaces. This force component can be countered by patterning the surface with a vertical structure such as cavity or a wall (Figure 2.0.4).

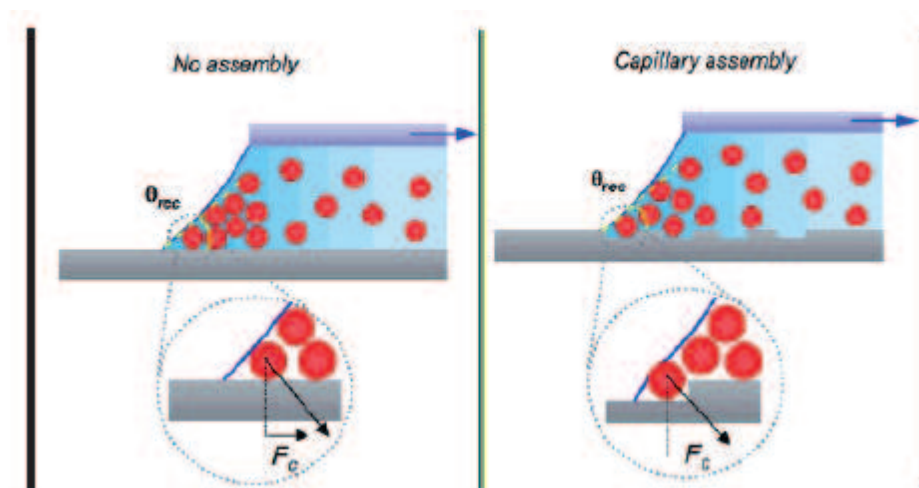


Figure 2.0.4 – Capillary assembly of individual particles on a micro-patterned hydrophobic surface. The combination of the geometrical confinement and capillary forces when the meniscus is pinned on the structures of a patterned surface can be used to deposit only one or just a few particles in the desired location. (adapted from (Malaquin et al., 2007))

While the particle suspension is being dragged across the substrate and over the pattern, the contact line will eventually come into contact with the structures making up the pattern. The

liquid meniscus is then pinned, deforms around the structure, and then breaks. The film breakage combined with the geometrical trapping created by the pattern leads to one or more particles being confined at the vicinity of the pattern structure encountered. In this way, the particles are deposited selectively at the obstacles as per the pattern on the surface and nowhere else. As shown in figure 2.0.4, the contact angle is also important to ensure capillary assembly. It was found that an optimal angle was between 30° and 60° . Any angle lower than 30° promotes convective assembly, where the drying out/evaporation of the meniscus and the confinement effect on the particles by the meniscus and the capillary forces created during the drying process create a continuous 2D particle lattice on the surface (convective assembly is further promoted by a hydrophilic surface). Another important factor is the surface tension of the particle suspension since it has a direct influence on the contact angle and meniscus integrity.

The capillary assembly serves to place magnetic beads, whose properties are described in the following section, in the cavities of the micro-patterned PDMS surface. The patterned PDMS chip is first positioned on a glass slide that has been previously plasma-cleaned to promote the adhesion of the elastomer. The attached chip is then placed on a motorized stage which can be controlled using a computer interface via LabView.

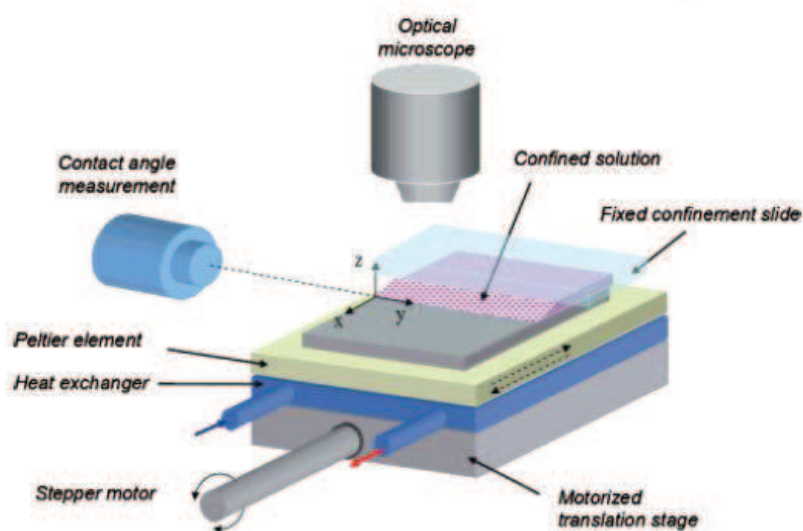


Figure 2.1.2. Diagram of the set-up used to perform controlled capillary assembly on PDMS chips; In our case, the Peltier element and heat exchanger are not used during assembly since the process is performed at room temperature (Malaquin et al., 2007).

A suspension of magnetic beads in surfactant is then placed on the chip at one end of the pattern. The suspension is confined between the chip and a glass slide placed at approximately 30° to the plane of the PDMS surface. The motor is turned on and is made to move relative to the confining slide such that the suspension gets dragged along the pattern and capillary assembly takes place, filling up the cavities with the beads. The whole process is monitored using a microscope objective and a camera.

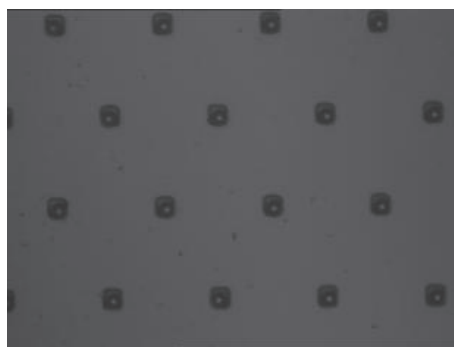


Figure 2.1.3. Appearance of the micro-patterned PDMS chip filled with beads as seen with an optical microscope. Note that there is here one single bead per cavity of the pattern.

The filled PDMS chips can then be stored without any particular precautions. The only major precaution is to take care not to touch or rub the micro-pattern once it is filled.

B/. Formation of the columns

In this section, we detail the formation of the column. We concentrate our attention on two of the main components of the set-up, namely the characteristics of the magnetic beads we use and the methods used to generate the external magnetic field.

1) The Magnetic Beads

The magnetic beads used to build the columns are commercially available (Dynabeads M450, Invitrogen). The beads are 4.5 μm in diameter and have a density of 1600 kg/m^3 . They are made of porous polystyrene filled with nanoparticles (~ 8 nm in diameter; 202 mg/g) of maghemite, an iron oxide ($\gamma\text{-Fe}_2\text{O}_3$) that is ferrimagnetic. Because of its small size, each grain of maghemite displays a single magnetic domain and behaves as a small permanent magnet with a magnetic moment along a preferred direction. However, the orientation of the magnetic moment is subjected to thermal fluctuations and in turn averages out to zero for

observation times significantly longer than the typical switching time (a few nanoseconds). In addition, the particles are free to rotate in the pore of the bead and are thus randomly oriented. Upon application of an external magnetic field, the magnetic moments align with the field resulting in a net magnetization of the bead. Because of the anisotropy of the magnetization, which results in a preferred axis of magnetization within each nanocrystal of maghemite, the grains also tend to reorient under the influence of the external field to align their magnetic moment with this axis (and the external field).

These beads are said to be “super-paramagnetic”, for they show much larger magnetization than standard paramagnetic materials. In addition, retain little to no residual magnetism when the field is removed. The magnetization curve of the beads is shown below:

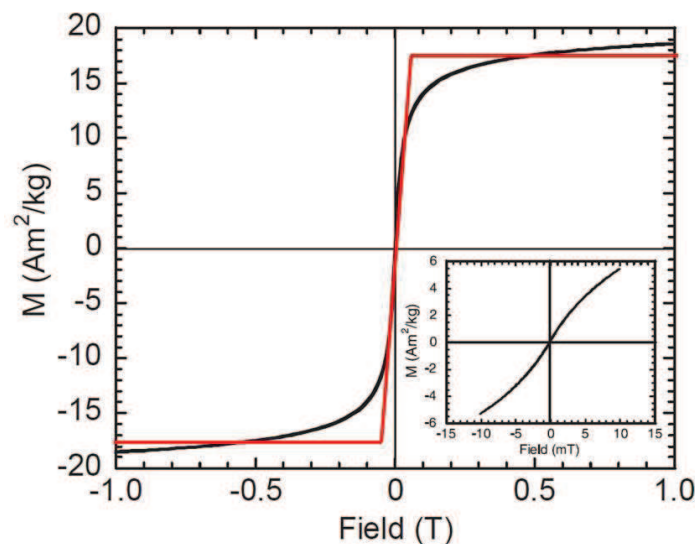


Fig 2.1.4 – Magnetization curve of the Dynabeads M450 as obtained from the Invitrogen website. The graph shows magnetization per unit mass with respect to the external field (Fonnum, Johansson, Molteberg, Mørup, & Aksnes, 2005).

2) The Electromagnet

We used an electromagnet to produce the external magnetic fields (up to 40mT) that force the super-paramagnetic beads to self-assemble into columns. One advantage of this device is that one can easily change the strength of the magnetic field that is produced by changing the current in the wiring of the electromagnet.

2.1 Making the Electromagnet

The electromagnet was built in our laboratory by François-Damien DELAPIERRE and the mechanical workshop of UMR 168. It consists of a solenoid of copper wire that is wound around a brass casing and a steel core. The casing is built so as to allow the operator to change the core from the usual steel to other materials if needed.

2.2 Calibration of the Electromagnet

The strength of the magnetic field at a given point in space depends, of course, on the current in the wiring but also on the distance from the core of the electromagnet. It is thus important to characterize this strength with respect to these two parameters. We used a DC magnetometer (AlphaLab Inc.) held by a clamp connected to a micrometric movable holder. The holder allows us to move the probe the field with relatively good precision, in the submillimeter range. The magnetic field was first measured by holding the probe in direct contact with the core, at its center, and then the probe was raised with increments of 1mm. At each increment, the magnetic field was measured. repeated the measurement for current intensities that varied between 1 and 2 A, with increments of 0.1 A (see Figure 2.1.4).

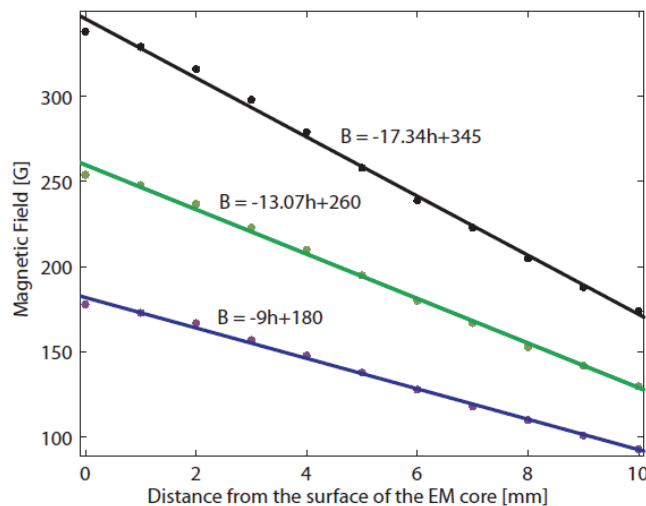


Figure 2.1.4. Calibration of the magnetic field produced by our electromagnet. The field strength is plotted as a function of the distance from the surface of the electromagnet, at the core center. The equations from linear fits are written next to each curve. In black: 2 A, In green : 1.5 A, In blue: 1 A.

The data points obtained were fitted with a straight line since, over the small distances on which we plan to work, the magnetic field strength can be assumed to vary linearly with the distance from the core. In practice, the magnetic beads are positioned 3 - 4 mm from the

surface of the electromagnet. Another important verification to be done is to check for the variation of the field across the width of the steel core.

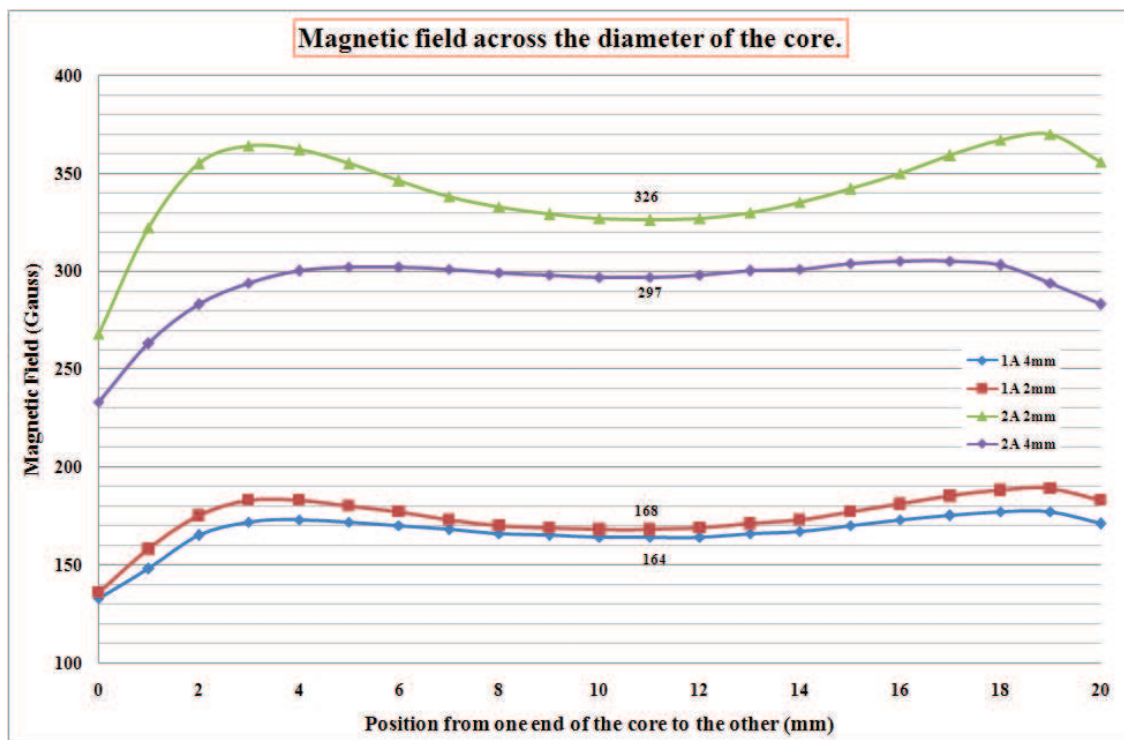


Figure 2.1.5. Variation of the magnetic field across the width of the core of the electromagnet for two values of the current in the solenoid (1 and 2 A) and of the distance to the surface of the electromagnet (2 and 4 mm). For positions near the core center (10 ± 2 mm), the field remains nearly uniform, but increases by up to 10% near the edges of the core.

2.3 – Limits of the Electromagnet

The electromagnet may be a convenient means of applying a changeable magnetic field but it has its drawbacks. The magnetic field it can generate depends on the current flowing in the solenoid. This generates heat due to the resistance in the wires. A cooling system based on a Peltier element and a heat exchanger is used during our experiments (the cooling system will be detailed further in a subsequent section of this chapter) but it has proved to be inadequate to keep up with the temperature rise when the solenoid current rises above 2 A. This effectively imposes a maximum magnetic field that can be generated using the electromagnet; this upper limit is about 300 – 325 G, hence severely limiting any endeavours to investigate the behaviour of the columns at higher fields.

To circumvent this limitation, we also used a set of two powerful permanent magnets to obtain magnetic fields superior to 325 G. The protocols when using them differ only slightly and will be described with more details further.

C/. Characterization of the properties of the columns

We have previously discussed the components necessary to induce column formation namely, the beads, the micro-patterned PDMS chip and the magnetic field. This section is concerned about how those elements are actually arranged in the experimental set-up. We thereby start by giving a description of the instrumentation used (microscope, detection methods, etc...), and we will end by giving an account of our experimental procedure. As for the experiment itself, what we seek to record are the thermal fluctuations of the topmost bead of a column. Since the columns tend to realign with the magnetic field when deflected, which is a behaviour analogous to a stiffness, the thermal motion of the topmost bead with respect to time is related to the stiffness of the column, using the same reasoning as the one we used to determine the optical trap stiffness in section A.3.2 of Chapter I in Part I.

1) The Experimental Set-Up

As stated in the introduction to Part II, our main goal is to characterize the mechanical properties of the bead columns. Consequently the set-up was designed to be able to detect any motion of the columns with good resolution (in the nanometer range) and also to provide stimulation capabilities to observe the response of the columns.

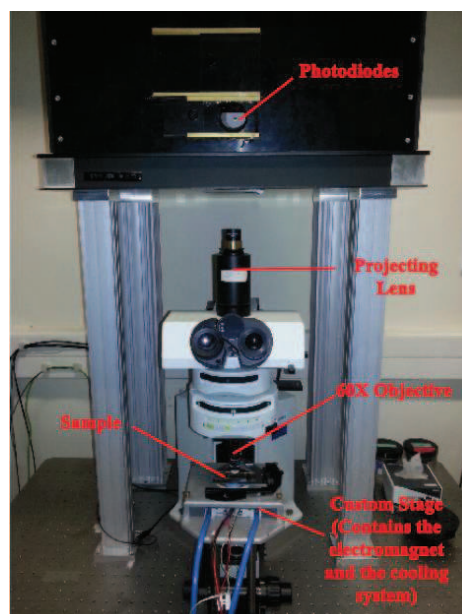


Figure 2.1.6. *Our experimental set-up showing the microscope equipped with our custom-made stage. The electromagnet is placed within the stage compartment with the Peltier element and the cooling system. The PDMS chip is placed on a movable platform which allows us to move the chip relative to the EM when searching for appropriate columns.*

Figure 2.1.6 above shows how the different elements are arranged during an experiment. The set-up itself was adapted from one that is routinely used in our team to study the spontaneous oscillations of hair-cell bundles from the bullfrog sacculus (REF: Tinevez et al (2007)). It is located in a soundproof room to minimize sound interference from outside, which is also highly convenient for our own experiments.

The main component of the set-up is the microscope (BX51WI, Olympus) equipped with a water immersion 60X objective with a numerical aperture of 0.9 (Refer to Figure 2.1.7). The sample is illuminated by a 100 W mercury arc lamp. The reflected light from the sample is then directed to the binocular eyepieces, a CCD camera (LCL-902K, Watec America Corp.) and to two-quadrant photodiodes which serve as our primary detection technique. A comprehensive diagram is shown below:

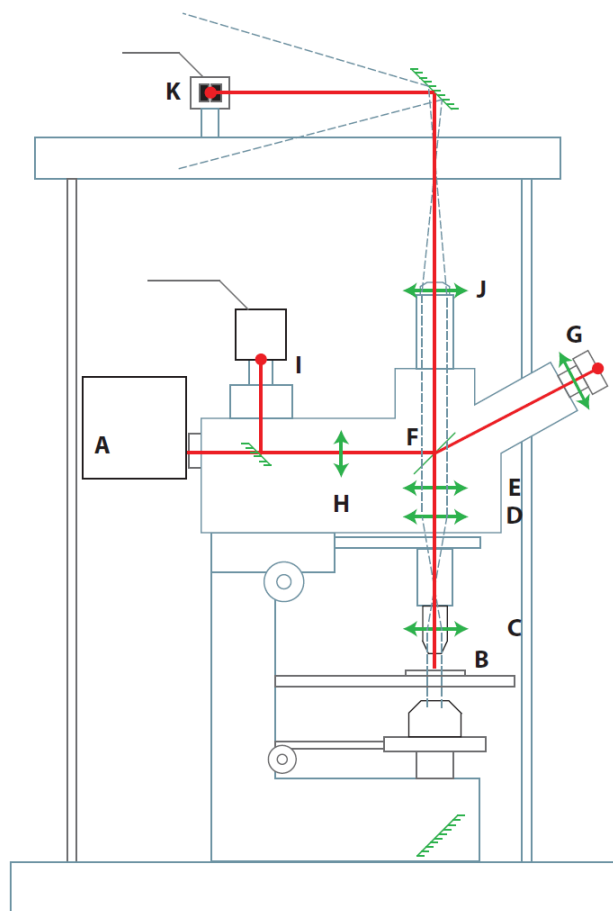


Figure 2.1.7. *Diagram of the optical path on the microscope (adapted from Tinevez 2006)*

Light is provided by a mercury arc lamp (A). Upon reaching the sample (B), the light is then reflected back into the microscope. A lens is able to magnify the image coming from the objective by 2X (D), A moveable optical hub in (F) can direct the image to the binoculars (G), or to the photodiodes (K). A semi reflective mirror can divide the light to a CCD camera (I) and the photodiodes. The light sent to the photodiodes goes through a 5X projecting lens (J). This forms a magnified image (X??) of the sample on the photodiodes.

The magnification factor (X2150) between the sample and its image on the photodiodes is determined by projecting the image of a micrometer on the photodiodes.

1.1 – The custom stage.

In order to accommodate the electromagnet and the cooling system, a special stage was custom-made by our mechanical workshop and adapted to our microscope.

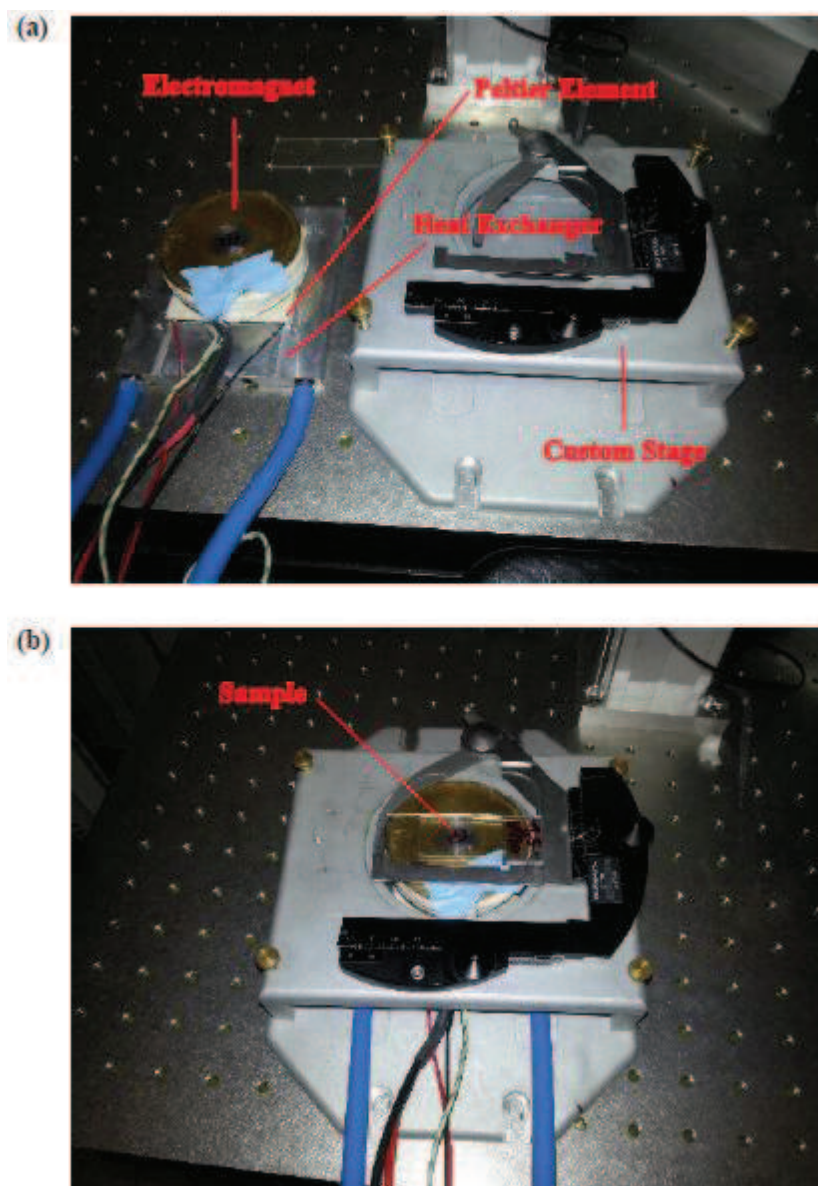


Figure 2.1.8. Photograph of the custom-made stage, (a) Empty and (b) With the electromagnet and the cooling systems.

The stage is made of aluminium and is essentially a compartment to house the electromagnet and the cooling systems. The upper part of the stage is made up of a movable holder for the PDMS chip. This allows us to move the chip relative to the electromagnet when looking for columns to experiment on. As we have seen previously (see Section A of this chapter), note that the magnetic field is nearly uniform over about 2 millimeters from the center of the electromagnet. Because we remained within this zone, we thus assumed that all the columns under investigation are subjected to the same field.

1.2 – The Cooling System

The cooling system used to dissipate the heat build-up when the electromagnet magnet is switched on is basically a heat exchanger regulated by a feedback loop.

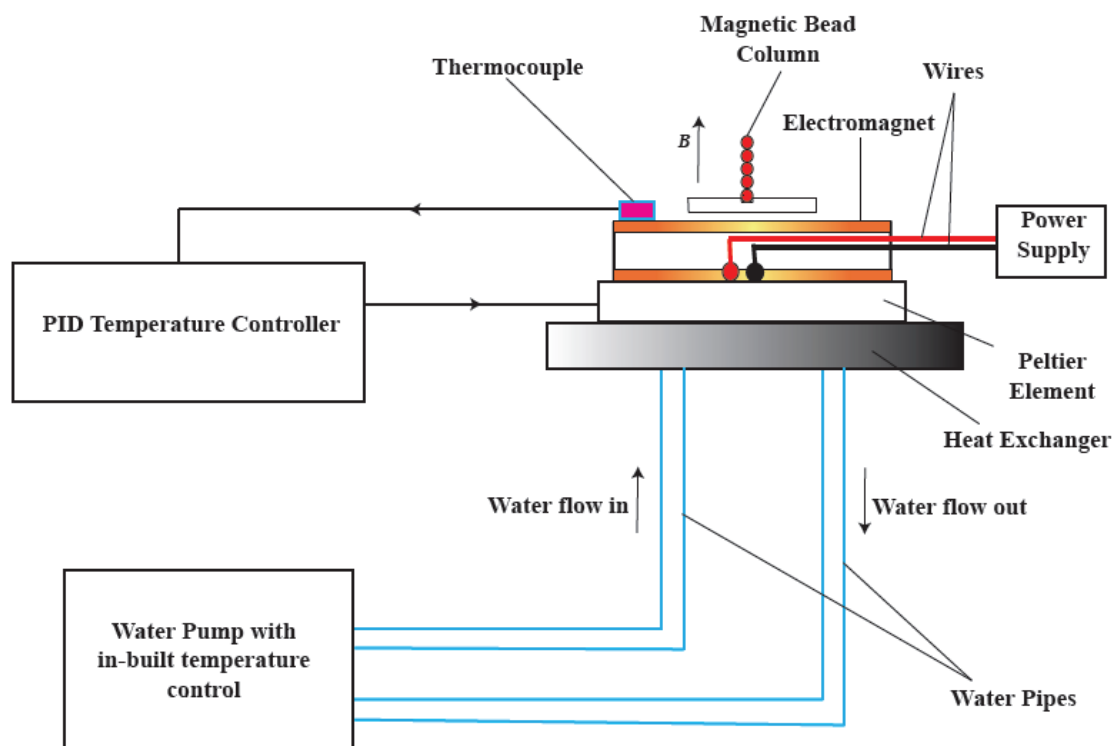


Figure 2.1.9. The electromagnet coupled to the cooling system outside the compartment of the stage.

The temperature is monitored by taping a thermocouple (covered in thermal paste to promote better heat transfer) to the surface of the electromagnet. The thermocouple sends the information to a control panel (Eurotherm) which acts as a PID controller to regulate the temperature. Depending on the temperature change (increase or decrease), the control panel sends the appropriate commands to a Peltier element in direct contact with the electromagnet. The Peltier effect or thermoelectric effect within the element will promote heat exchange from one surface of the Peltier element to the other depending on an electric current. Therefore, we place the Peltier such that the heat exchange occurs from the side in direct contact with the electromagnet to the other side. The latter is placed in contact with a heat exchanger to cool down the surface to which the heat from the electromagnet has just been transferred to. All physical contacts take place via thermal paste to improve the heat conduction. The heat exchanger is a solid plate through which water can flow. The water is pumped using a water

pump which is able to heat or cool down the water to the appropriate temperature. The temperature control of the water is manually controlled with a knob on the pump itself. We usually either leave it at 20°C or cool it to less than 10°C depending on the temperature readings on the control panel.

1.3 - The detection system

As shown in Figure 2.1.7, the light from the sample is reflected on two-quadrant photodiodes which serve as our primary detection method. We have already detailed the principle of detecting the motion of an object with photodiodes in section A.3.1 of the “Materials and Methods” Chapter found in Part I of this thesis. The same principle applies here with one difference: since we have only two quadrants instead of four, we only detect motion along one axis. The calibration method is consequently also highly similar. The programs used to acquire the data are thus also similar in their architecture.

2) Observation of the columns from the side

Fluctuations of the topmost bead in a magnetic column allow us to deduce the stiffness of the columns. However, to describe the origin of this stiffness in a quantitative model, it would be useful to see how the column deforms when it is subjected to an external force: does it bend like a beam or does it behave like a stiff rod that pivots at its base. In order to answer this question, we have designed another type of PDMS chip that allows us to view the columns from the side.

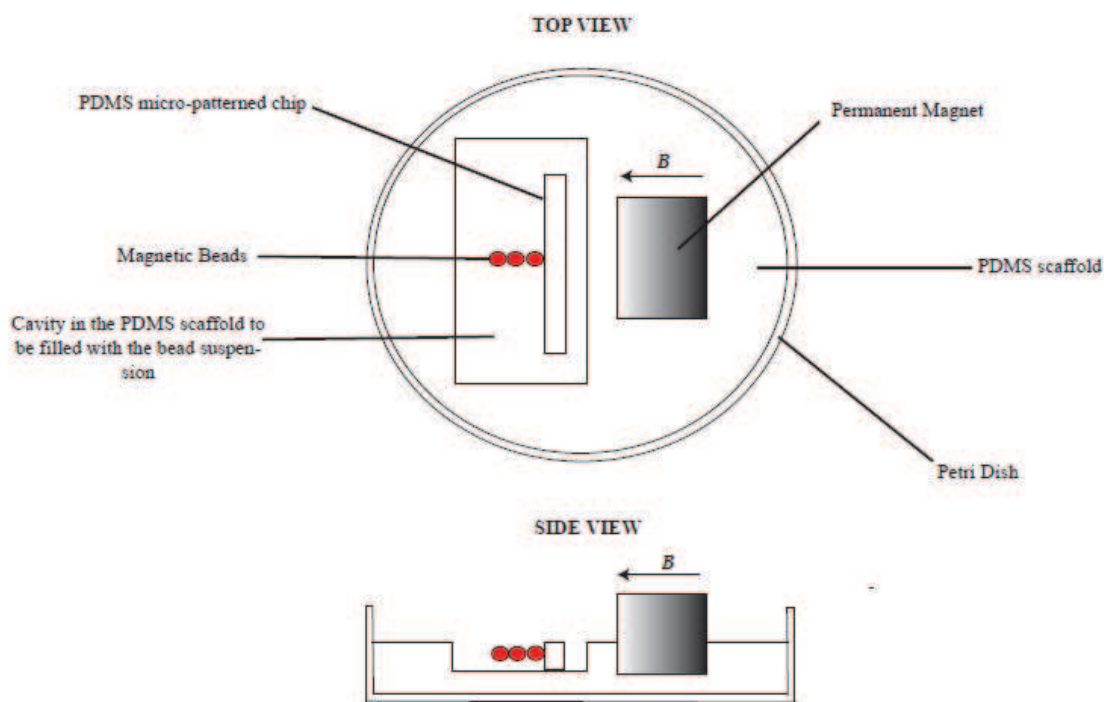


Figure 2.1.10. PDMS chip allowing us to see the columns from the side. The pattern is placed in the rectangular cavity perpendicular to the magnetic field provided by the permanent magnet embedded in the PDMS foundation. It can then be filled with water and the columns can be observed via a water immersion objective.

In this new chip (Figure 2.1.10), the columns form perpendicular to the plane of observation. This is done by orienting the magnet such that the magnetic field lines are also perpendicular to the observation plane. The pattern is, of course, tilted accordingly and lies inside a cavity that can be filled with the bead suspension at an appropriate concentration. The formation of the columns and their behaviour can be monitored using a camera mounted on the microscope. We use a permanent magnet, as opposed to our usual electromagnet, due to the difficulty posed in adapting the cooling system to the sideways configuration and, as a result, it is also not necessary to use our custom-made stage; a normal microscope stage is sufficient.

The whole structure is made by moulding PDMS in a Petri dish with the permanent magnet properly arranged as in Figure 2.1.10. After the PDMS has polymerized, the cavity is formed by cutting out a piece of PDMS with a scalpel.

The PDMS micro-patterned chip is prepared as usual but prior to experimentation, the micro-bead pattern on the chip is carefully cut out with a scalpel and glued to a plasma-cleaned glass slide.

The cut PDMS containing the pattern is adjusted on the slide so as to direct the pattern away from the surface of the magnet, in order to have the magnetic field lines perpendicular to the pattern (Figure 2.1.10). The slide is then placed in the cavity and the latter is filled with the bead suspension whenever an experiment is to take place.

The disadvantages of this chip are mostly that we are limited in terms of range of magnetic fields we can use by the permanent magnet and that this configuration is ill-suited for photodiode detection forcing us to rely on camera recordings for the observations.

3) Experimental Procedure

The previous sections have gone into the details of the micro-fabrication of the PDMS chip, the assembly of the bead network and the characteristics of the different set-ups we use, along with the detection techniques in each case. Once the PDMS chips have been prepared and seeded with the nucleator beads, the experimental procedures to determine the mechanical properties of the columns are rather straightforward; they mostly involve mounting the chips on the appropriate microscopes and observing the fluctuations of the columns after their formation with the occasional stimulation should the need arise. However there are particulars about the different experiments which we shall detail.

3.1 Procedure with the electromagnet

The standard procedure when using the electromagnet as the source of the external magnetic field is to install the custom stage and the cooling system as detailed earlier.

The PDMS chip is mounted on the stage and a drop of water is placed on the pattern. The water immersion objective is lowered into the drop until the bead pattern has been found. Between 50 and 100 μL of a suspension of magnetic beads ($\sim 1/100$ dilution from the stock bead solution; stock concentration = 4×10^8 beads/mL) is then injected into the drop using a micropipette. Immediately upon injection, the power supply is quickly switched on to the current needed for the experiment (between 1 and 2 A) to engage the electromagnet in delivering the corresponding magnetic field. This step has to be done rapidly to avoid any

deposit of the beads on the surface. Once the electromagnet is switched on, the magnetic beads are compelled to align themselves and form the columns.

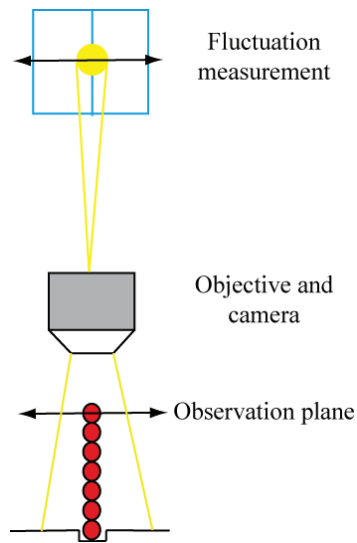


Figure 2.1.11. Diagram of a typical experiment. The optical path has been greatly simplified. The water immersion objective is lowered into the drop and the image of the topmost bead is imaged on the photodiodes. The source of the external magnetic field lies below the stage such that the magnetic field lines generated are perpendicular to the surface. Stylized representation of the observation.

The next step is to identify a suitable column. A suitable column is one that is between 3 to 18 beads high and made of a continuous string of single beads. A column shorter than 3 beads is too stiff and a column longer than 20 beads fluctuates outside the linear range of the photodiodes. We proceed to focus on the equator of the bead. The magnification is then changed so as to increase the size of the image in such a way that a section of the circumference of the bead can be imaged as a straight line on the photodiodes. This is shown below :

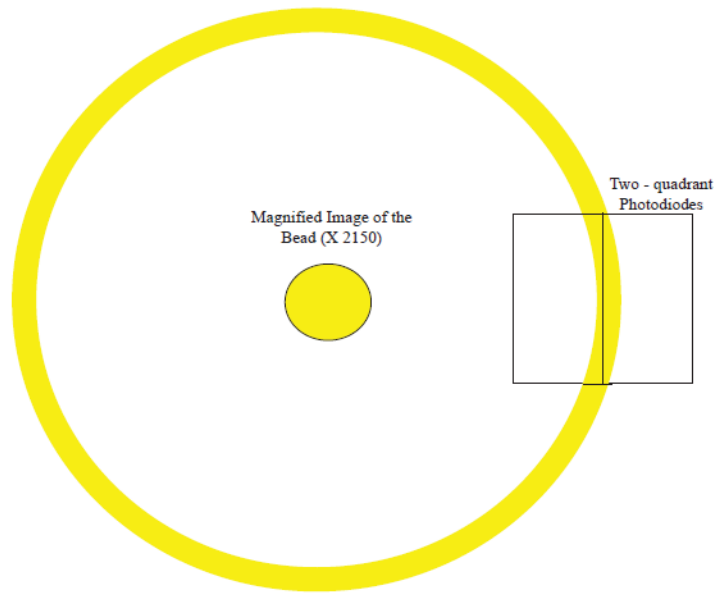


Figure 2.1.12. Diagram of the magnified picture of a bead imaged on the two-quadrant photodiodes. The arc projected on the diodes can be approximated as a vertical band.

The circumference arc of the bead projected on the photodiodes appears as a bright band which can be easily centered and tracked. Once the band has been properly centered, the photodiodes are calibrated and the recording program is run. This program is usually used to calibrate the stiffness of glass fibres used to stimulate the hair-cell bundles of the bullfrog. It records the fluctuation of the bead over a given amount of time (30 s) with a sampling frequency of 25 kHz and gives us the raw displacement against time graph and the power spectrum. We then fit the latter in real time with a Lorentz function and the program automatically extracts the parameters and deduces the stiffness (see Eq.1.1.13 in Section A/3.2(b) of Part I Chapter I).

3.2 – Procedure with the permanent magnet

As we have already discussed previously, the cooling system cannot keep up with the heat building up when the current in the solenoid is higher than 2 A which is equivalent to a magnetic field output of approximately 300 G. We thus use a permanent magnet to generate stronger fields. The experimental procedure is identical to the one with the electromagnet but uses a normal microscope stage and the magnet is instead taped to the glass slide of the PDMS chip just below the micro-pattern. (Figure 2.1.13)

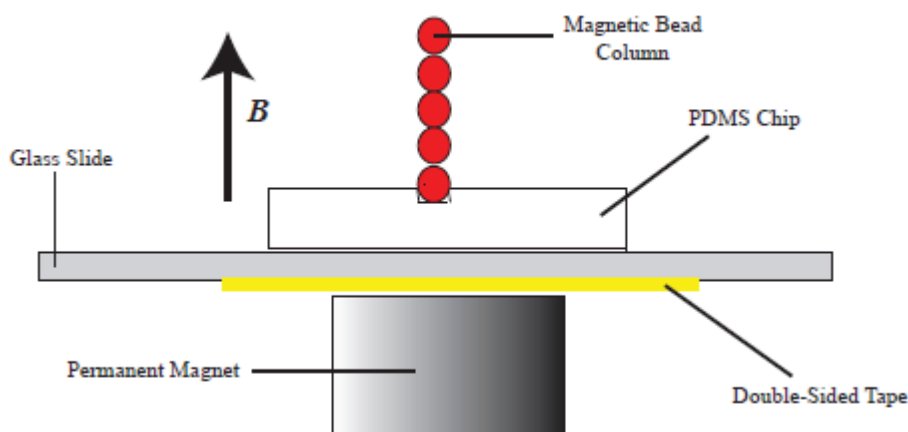


Figure 2.1.13. Diagram of the layout of the permanent magnets with respect to the PDMS micro-patterned surface for the experiments at magnetic fields beyond the range of the electromagnet set-up. For simplicity, only one column was shown.

We used two permanent magnets of differing magnetic fields for our experiments. The effective magnetic field at the micro-pattern was measured by placing the magnetometer in contact of the bead network. The effective magnetic fields for the two magnets were 1000 G for one and 1500 G for the other.

3.3 – Viewing the profile of the columns

In this set-up, we use the tools we have developed to observe the physical deformation of the columns in response to a deflection applied at the topmost bead.

The PDMS chip is placed in the cavity with the magnetic bead pattern facing away from the surface of the magnet. The cavity is filled with water and the water immersion objective is lowered into it until the bead network is found. A bead suspension is injected in the cavity at the vicinity of the pattern. The camera is used to monitor column formation. A micro-pipette is then fitted on the piezo-manipulator and connected to a syringe. The pipette is lowered into the cavity and can be used either to create a flow near the column or to suck in the topmost bead. To create a flow, the piston of the syringe is moved to create a pressure difference which will create a local flow (the direction of the flow can be changed depending on the orientation of the pressure difference) which will deflect the columns. Sucking in the topmost bead applies the same principle but is done by placing the pipette opening tip in contact of the topmost bead and applying a negative pressure. Once the bead is trapped, the column can be deflected at leisure. In both cases, a camera is used to record the movement induced. The

films thus obtained can then be analyzed using a combination of Image J and Matlab programs which have been specially written for the task.

Part II

Chapter II : Mechanical behaviour of the self-assembled magnetic bead columns

This chapter discusses the mechanical properties of self-assembled columns of superparamagnetic beads in an external magnetic field. First, we present our measurements of a column's stiffness and friction coefficient. Second, we give a theoretical description of the column's properties from the magnetic interactions of the beads with respect to each other. We finally discuss the relevance of these columns as molecular force sensors.

A/. Mechanical properties of magnetic columns

1) Stiffness

1.1 Variation of stiffness along the length of a column

In this series of measurements, we measured how the stiffness of a column varied along its length. For a given bead within a column, the image of the equator was projected on the photodiodes and the stiffness at this point was deduced from the thermal fluctuations of bead position, as described previously (Part I and chapter II of Part II). Starting from the topmost bead, the measurement is repeated while going down the column one bead at a time; the stiffness is thus measured every 4.5 μm until the column either becomes too stiff or the image projected becomes too blurry for an accurate measurement. The measurements were performed under different magnetic fields, at approximately 150 G, 300 G, 1000 G and 1500 G.

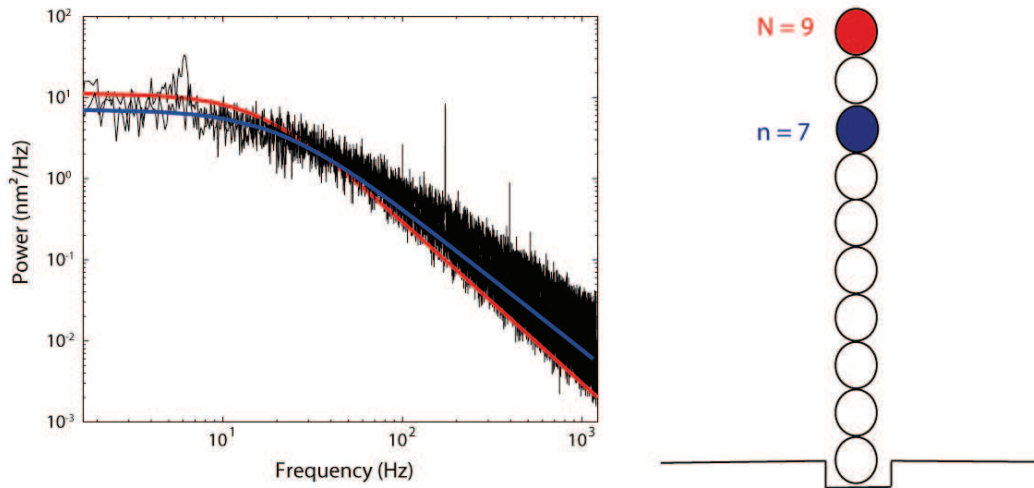


Figure 2.2.1 Power spectra of the 9th bead (topmost, in red) and the 7th bead (in blue) of a 9-bead tall column obtained from fluctuation measurements performed at the equator of the corresponding bead. The two spectra are superimposed. We can see here that, as we go down the column, the amplitude of the fluctuations decrease (smaller area under the curve) implying an increased stiffness. Correspondingly, the low-frequency plateau displays a smaller amplitude and the corner frequency shifts to higher frequency values as we go down the column. The spectra were fitted by a Lorentzian from which we deduced both the stiffness and the friction coefficient of the column. Note that the column behaves as a low-pass filter with a cut-off frequency on the order of a few hundred hertz.

Assuming that all beads have the same diameter, we can calculate the height as: $h = [4.5(n - 1) + 2.25] \mu m$, where n is the index of the bead at which the measurement was made (Figure 2.2.2); for $n = N$, $h = L$ the total length of the column

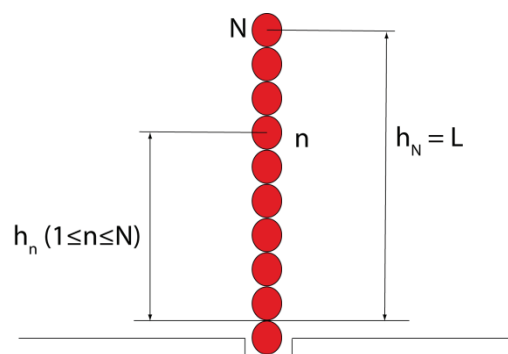


Figure 2.2.2 The height of a given bead is defined by the distance between its equator and the top of the nucleator bead.

In Figure 2.2.3, the stiffness K is plotted as a function of the height h at which it was measured. The stiffness increases when moving towards the base. Its variation is well described by the relation $K = K_p/h^2$, where K_p is a fit parameter.

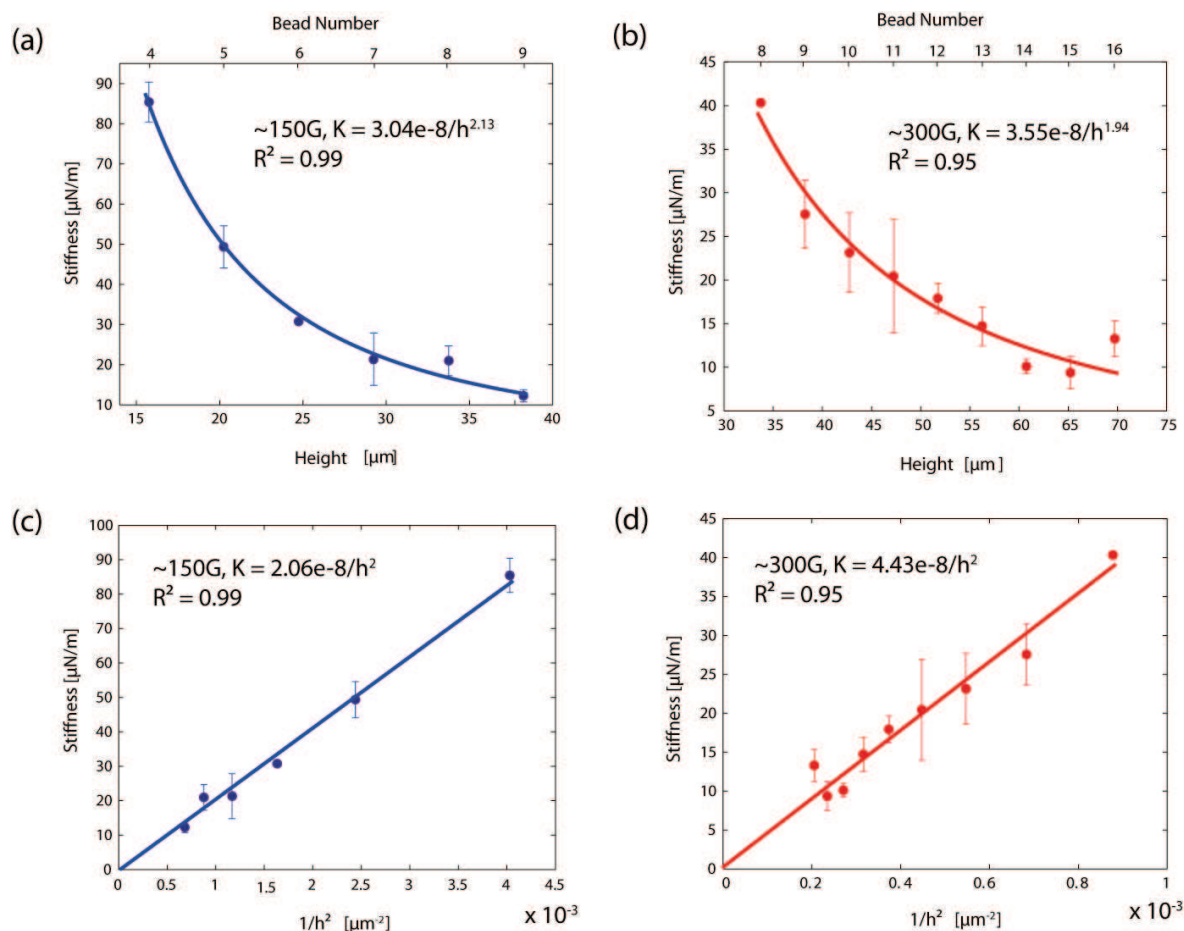


Figure 2.2.3 Variation of stiffness along the height of a column at two different magnetic field strengths. (a) Stiffness variation with respect to the measurement height h for a 9-bead column at 150G fitted with a power law – the power parameter gave a 2.13 value. (b) : Stiffness variation with respect to the measurement height h for a 16-bead column at 300G fitted with a power law – the power parameter was 1.94. (c) and (d) : The data points from (a) and (b) are submitted to a linear law fit in $1/h^2$ highlighting the variation of stiffness as $1/h^2$ within a column within reasonable confidence bounds.

This behavior is consistent with the column behaving as a rigid rod pivoting on the nucleator bead. A pivot spring can be modeled by a rod laid on a fulcrum and connected by a spring of stiffness κ located at a distance l from the fulcrum. The force and the displacement of the rod causes an extension in the spring until the latter has a final length of ε (See Figure 2.2.4) (Howard & Ashmore, 1986).

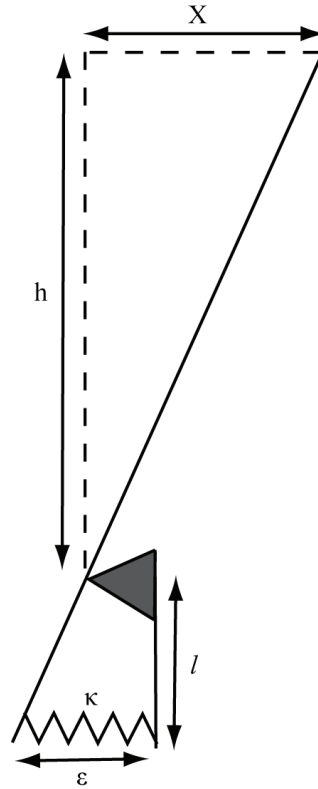


Figure 2.2.4 Diagram of a rigid rod pivoting about a flexible point at its base. Adapted from (Howard & Ashmore, 1986)(Howard, 2001).

The stiffness of the pivoting rod is given by $K=F/X$ according to Hooke's Law. As presented in Figure 2.2.4, the total energy of the deflection is written as:

$$U = \frac{1}{2} KX^2 = \frac{1}{2} \kappa \varepsilon^2 \quad \text{Eq 2.2.1.}$$

As a result, we can write:

$$K = \kappa \frac{\varepsilon^2}{X^2} = \kappa \frac{l^2}{h^2} = \frac{(\kappa \varepsilon^2)}{h^2} = \frac{K_p}{h^2} \quad \text{Eq 2.2.2.}$$

; where K_p is the pivot stiffness and is constant for a given pivoting rod (taken from (Howard, 2001)). One can thus deduce the pivot stiffness K_p from the linear stiffness K by multiplying the later by h^2 . In particular, at the top of the column, where $h = L$, we have:

$$K = K_p/L^2. \quad \text{Eq 2.2.3.}$$

Here, the pivoting point corresponds to the contact point of the last bead on the nucleator bead. K_p is constant for a given column but depends on the external magnetic field, as evidenced by the increasing slopes obtained with increasing magnetic fields. We note that the pivot stiffness nearly doubles when the field increases from 150 G to 300 G.

1.2 Viewing the deformation profile of the columns:

A column was visualized from the side to observe how it deforms in response to a perpendicular fluid flow coming into or out of a micropipette. The micropipette was positioned near the column's top to apply a hydrodynamic force near the topmost bead only. In agreement with the stiffness measurements, the column appeared to pivot about its nucleator bead. To further quantify this motion, we used a bead tracker programmed by Mathieu RICHARD based on a tracking algorithm written by Scott ATWELL (See Figure 2.2.5).

For any given frame of the movie, the tracking program identifies the centre of the beads and records their positions. The analysis program then takes up from there. It has two basic routines. The first one connects the centres of the beads with a straight line and this is done for each successive frame. The straight lines are then superimposed and the point where they intersect gives us the base of the column (Figure 2.2.5). The second routine quantifies how the column deviates from a pivoting rod. The first four bead centres, starting from the base, are fitted with a straight line. The distance B between the center of the topmost bead and this line is compared with the length A between the base to the perpendicular projection of topmost bead's center on the straight line. The ratio B/A is plotted against the angle of deflection of the column (defined by comparison with a linear fit performed on the whole column) to check for a pivoting rigid rod behaviour over a range of angles.

The ratio B/A increased with the angle of deflection and displayed a hysteresis when the movement of the column was reversed. However, we found that $B/A < 6\%$ for relatively large deflections of $\pm 20^\circ$, corresponding to deflections at the top of the column of $\pm 12.5\mu\text{m}$ (more than two bead diameters). This value was small enough to consider that the columns behaved as rigid pivoting rods about the bead anchor, especially at the small angles of deflections

($\sim 0.03^\circ$ for a 10-bead column of $10 \mu\text{N/m}$ stiffness) explored during thermal fluctuations of the columns.

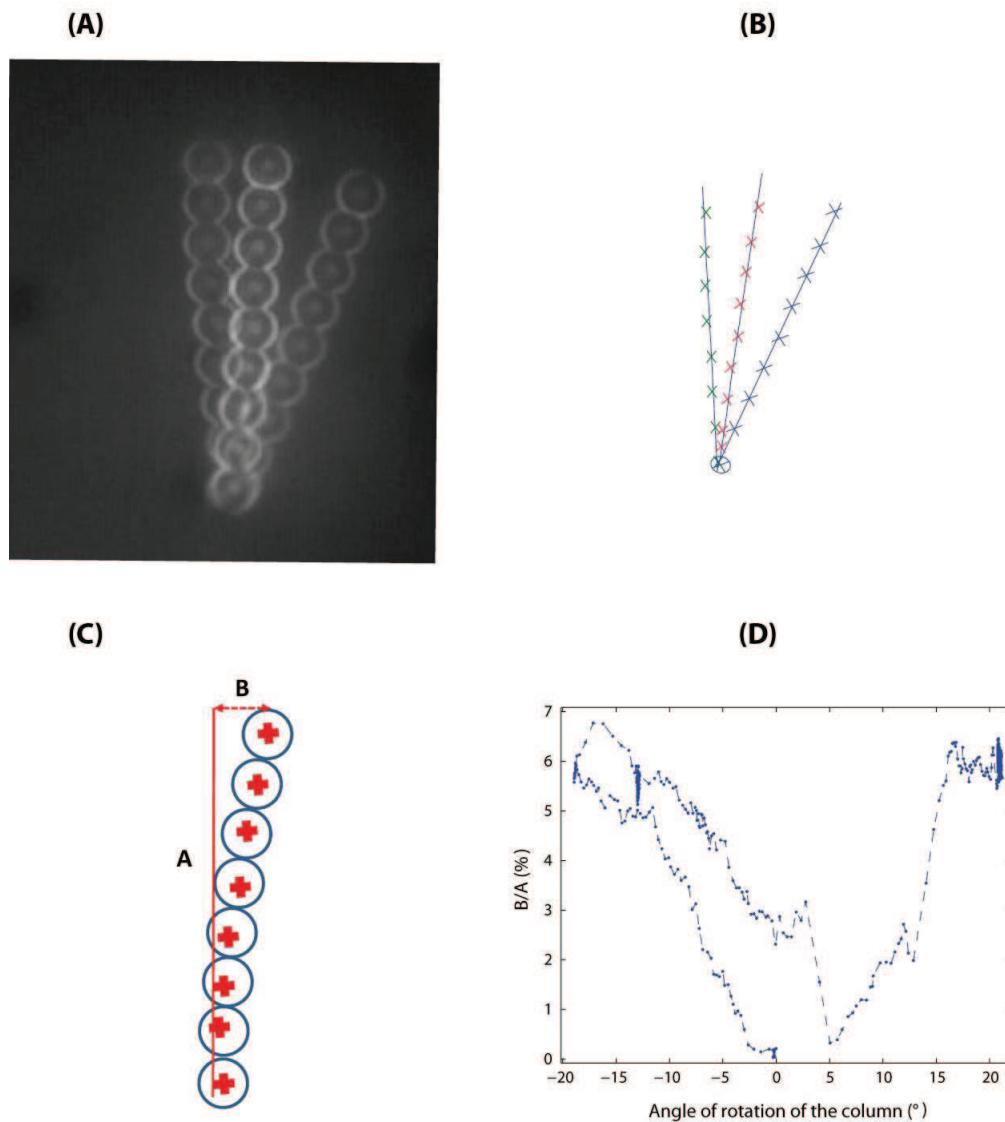


Figure 2.2.5 *A* : Superposition of 3 photographs of a column at different positions when deflected by the fluid flow. *B* : Linear fits through the centre of the beads as detected by the tracking program. *C* : Diagram showing a linear fit made through the centres of the four beads closest to the bead anchor and compared with the deflection of the bead at the tip. The ratio B/A serves to monitor bending of the column. *D* : Graph of B/A as the function of the angle of deflection of the column.

2) Stiffness as a function of column length

The stiffness K of different columns was measured at the topmost bead for columns of various length L .

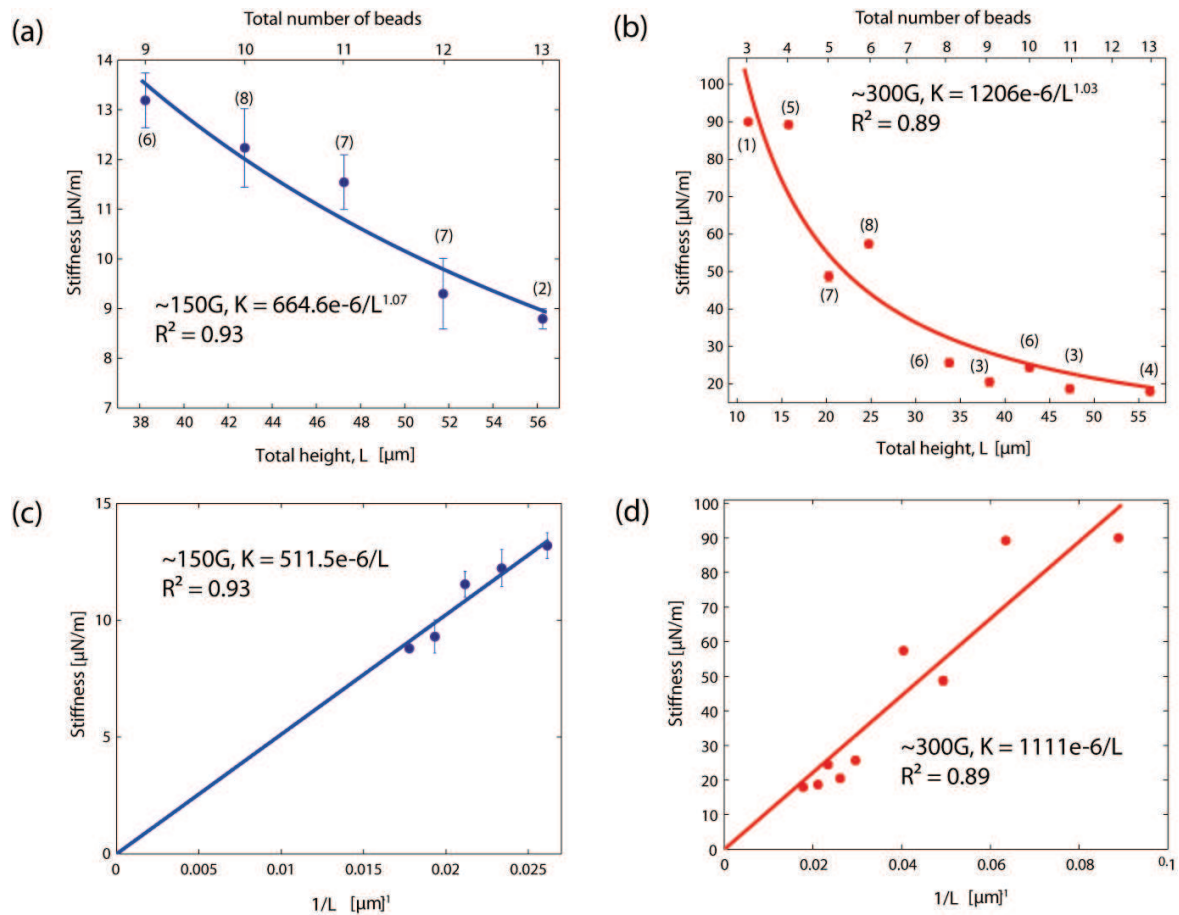


Figure 2.2.6 Plot of the stiffnesses at the top of different columns at 150 and 300G. (a) Stiffness recorded at the topmost bead of different columns at 150G and plotted against their respective lengths – a power law fit revealed a power parameter of 1.07. (b) Stiffness recorded at the topmost bead of different columns at 300G and plotted against their respective lengths – a power law fit revealed a power parameter of 1.03. (c): Linear law fit in $1/L$ for the data points in (a) and (b). The stiffness of each individual column varies as the inverse of its total height. NB: the number of experiments performed per data point is written between brackets next to each data point.

Figure 2.2.6 shows that stiffness measured at the top of the column is inversely proportional to the total length of the column: $K \propto 1/L$. As a consequence, because we also have $K = K_p/L^2$ (see Eq.2.2.3), the pivot stiffness K_p defined in the previous section must be proportional to L . The column with the larger number of beads above the point of measurement will appear stiffer.

From those results, we can extract a physical quantity α that does not depend on the column length or the height at which stiffness is measured. This physical quantity is the pivot stiffness per unit length, given by $\alpha = \frac{K_p}{L} = K \times L$.

3) Responsiveness and drag coefficients of the columns.

The position fluctuations of a column give rise to a power spectrum from which we extract two parameters: the amplitude of the low-frequency plateau and the corner frequency. From those parameters, we have already deduced the stiffness K of the column. In addition, we can also deduce the angular corner frequency ω_c and the drag coefficient or friction γ acting on the columns. The angular corner frequency ω_c is obtained by multiplying the corner frequency f_c by 2π ; its inverse $\tau = 1/\omega_c$ provides a characteristic response time of the system.

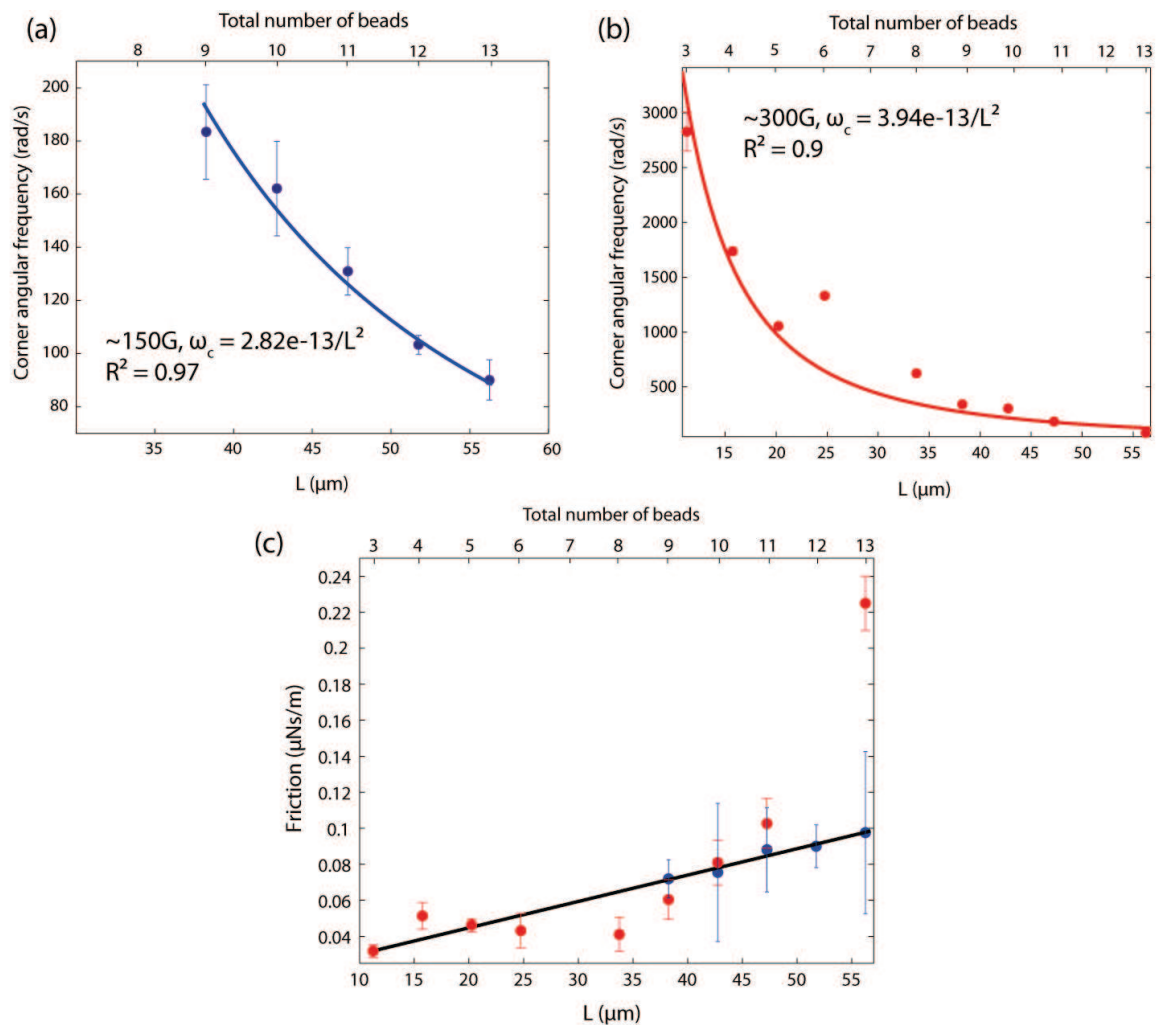


Figure 2.2.7 Graphs of corner angular frequencies and drag coefficients against the lengths of the columns at 150 and 300 G. Data points were obtained from the columns used in Figure 2.2.3. (a) and (b) Corner angular frequencies for different columns at 150 and 300 G as a function of the total length of the columns fitted with a $1/L^2$ fit. (c) and (d) : Friction on the columns deduced from the stiffness and the corner angular frequency against the total length of the columns. The drag coefficients vary linearly with the length irrespective of the external magnetic field strength applied (the outlying data point corresponding to 13 beads at 300 G has not been taken into consideration in the linear fit).

Stiffness and friction are related by the following equation:

$$K = \omega_c \gamma \quad \text{Eq 2.2.4.}$$

The corner angular frequencies range from approximately from 80 – 200 rad/s at 150 G and 400 – 3000 rad/s at 300 G; correspondingly, the cutoff frequencies vary from 13-30 Hz at 150 G to 60-450 Hz at 300 G. The time constants $\tau = 1/\omega_c$ of the system are thus of the order of 1-10 ms. We observe that ω_c varies like $1/L^2$, where L is the column total length (See Figure 2.2.7). We can deduce the friction by using equation 2.2.4. Because $K \propto 1/L$ and $\omega_c \propto 1/L^2$, the friction γ is expected to vary linearly with L according to equation 2.2.4. Figure 2.2.7 confirms that the drag coefficient does increase with L and shows the linear increase (straight lines) that are expected from the relations $K(L)$ and $\omega_c(L)$ shown in Figure 2.2.6 and Figure 2.2.7, respectively; we obtain a reasonable agreement. The drag coefficients of the columns are of the order of 0.05 to 0.2 $\mu\text{Ns/m}$, irrespective of the external magnetic field.

4) Influence of the external magnetic field on stiffness

Now we investigate the influence of the magnetic field by plotting the pivot stiffness per unit length α as a function of the magnetic field at which it was measured.

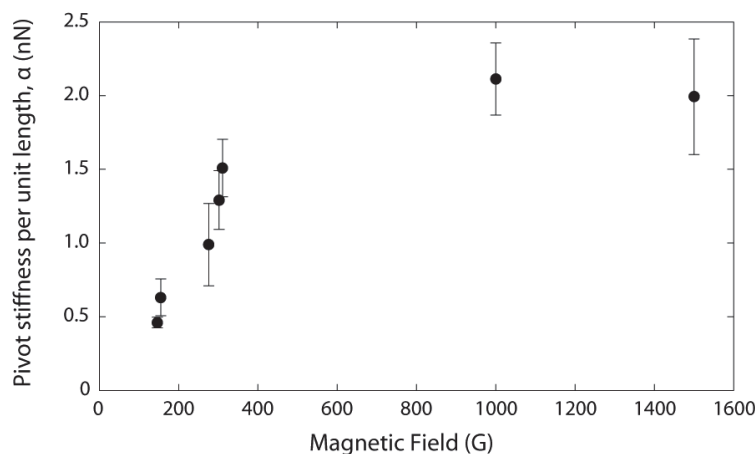


Figure 2.2.8 Graph of α with respect to the external magnetic field. The pivot stiffness per unit length increases and seems to saturate beyond approximately 400G.

The pivot stiffness per unit length increases rapidly until about 400G. It then saturates for high fields (> 1000G).

B/. Theoretical behaviour of a magnetic column: interactions between magnetic dipoles

1) Formation of the columns

Let us consider a suspension of super-paramagnetic beads in a magnetic field. Upon application of the field, the beads get magnetized and in turn interact with each other. Assuming that each bead can be described as a magnetic dipole of moment \vec{m} , the interaction energy U_{12} between a dipole moment \vec{m}_1 positioned at the origin O and a dipole moment \vec{m}_2 positioned at point M of spherical coordinates (r, θ, Φ) (see Figure 2.2.9) can be written as:

$$U_{12} = \frac{\mu_0 \mu_{\text{solvent}}}{4\pi r^3} \left[(\vec{m}_1 \cdot \vec{m}_2) - \frac{3(\vec{m}_1 \cdot \vec{r})(\vec{m}_2 \cdot \vec{r})}{r^2} \right] \quad \text{Eq 2.2.5.}$$

; where μ_0 is the magnetic susceptibility of vacuum, μ_{solvent} is the relative magnetic susceptibility of the solvent ($\mu_{\text{solvent}} = 0.999992 \cong 1$ in the case of water), and $\vec{r} = \overrightarrow{OM}$. The force $\vec{F}_{12} = -\vec{\nabla}U_{12}$ that dipole 1 exerts on dipole 2 is then given by:

$$\vec{F}_{12} = \frac{3\mu_0}{4\pi r^5} \left\{ \left[(\vec{m}_1 \cdot \vec{m}_2) - \frac{5(\vec{m}_1 \cdot \vec{r})(\vec{m}_2 \cdot \vec{r})}{r^2} \right] \vec{r} + (\vec{m}_2 \cdot \vec{r})\vec{m}_1 + (\vec{m}_1 \cdot \vec{r})\vec{m}_2 \right\} \quad \text{Eq 2.2.6.}$$

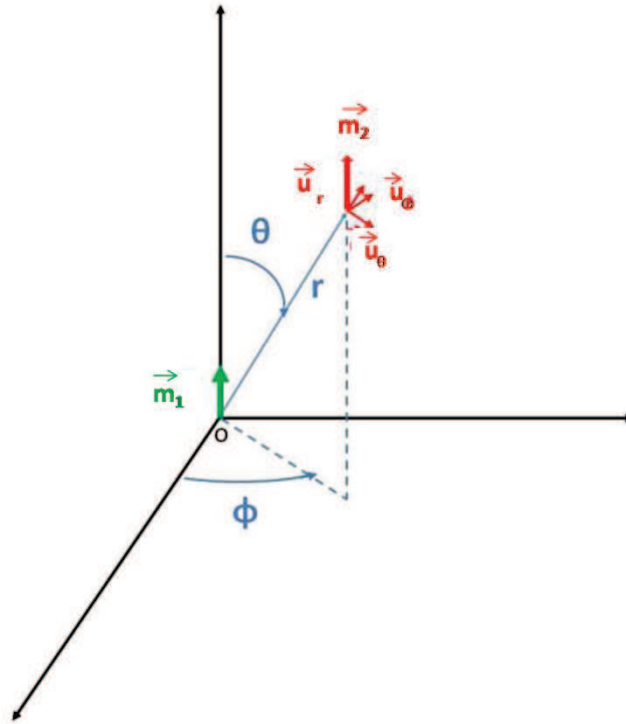


Figure 2.2.9 Diagram showing two parallel magnetic dipoles separated by a distance 'r'. The force exerted by dipole 1 on dipole 2 depends on the angle $\theta = (\vec{m}_1, \overline{OM})$.

In our case, all dipoles result from the magnetization of identical paramagnetic beads by an external field. Considering two equal dipoles with a magnetic moment \vec{m} , we can write the scalar product $\vec{m} \cdot \vec{m} = m^2$. The energy equation can thus be simplified as:

$$U_{12} = \frac{\mu_0 m^2}{4\pi r^3} [1 - 3\cos^2\theta], \quad \text{Eq 2.2.7.}$$

and the force can be expressed as:

$$\vec{F}_{12} = \frac{3\mu_0 m^2}{4\pi r^4} [(1 - 3\cos^2\theta)\vec{u}_r - \sin(2\theta)\vec{u}_\theta] \quad \text{Eq 2.2.8.}$$

From equation 2.2.8, one can deduce a condition on the angle θ to get either attraction or repulsion between the two dipoles, based on the sign of the force component along \vec{u}_r . A

negative radial force, which corresponds to attraction, is obtained for $1 - 3\cos^2\theta < 0$ and in turn $\theta \leq 54.7^\circ \approx 55^\circ$. We can thus deduce that any dipole which lies within 55° of another dipole will be attracted; otherwise it will be repelled (see below):

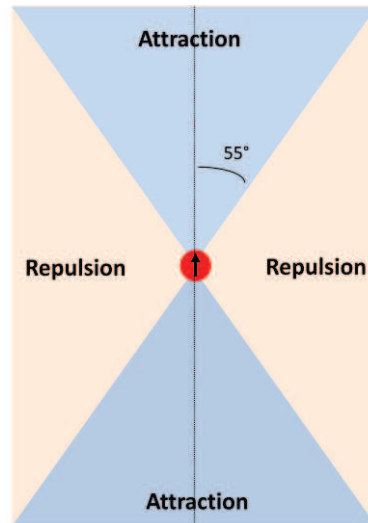


Figure 2.2.10 Diagram showing the attraction and repulsion zone around a magnetic particle which is as represented by a dipole. The attraction zones are approximated by two cones with the apex coincident with the dipole (one cone above and one cone below) and with its sides slanting at 55° with respect to its axis.

As a result, the magnetic beads will attract each other from the top and bottom and repel each other from the sides, which will give rise to the formation of bead columns parallel to the direction of the magnetic field lines.

Those columns, if formed in the bead suspension and left on their own, will spontaneously organize themselves in a hexagonal fashion when they sediment to the surface. However if similar magnetic beads are placed (and stuck) on the surface, they can act as nucleators to direct the formation of the columns. The beads will then preferentially pile up using the nucleator beads at the base of the columns (see Figure 2.2.11) resulting in an organized network of columns. The shape of the network itself is imposed by the way the nucleator beads were arranged.

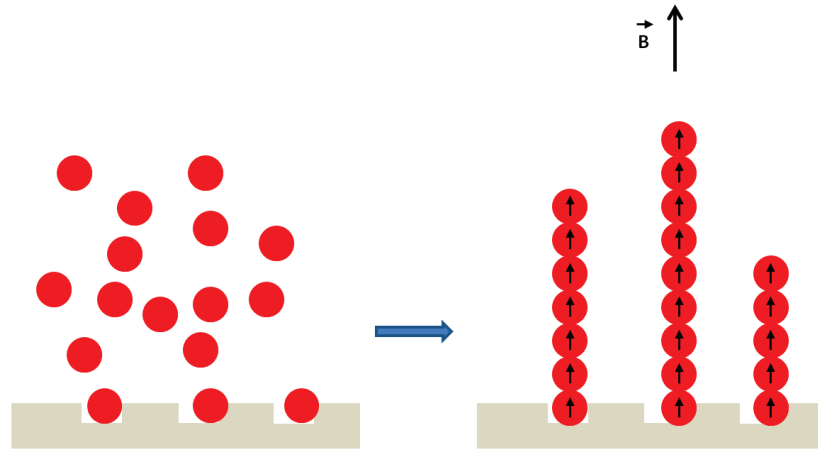


Figure 2.2.11 Formation of the magnetic bead columns using nucleator beads embedded on the PDMS surface.

This allows us to effectively control where the columns will form, giving a measure of versatility to this system.

2) Rotation of the beads in the magnetic field

The magnetic beads are relatively small objects (typically $4.5\mu\text{m}$ in diameter in our case) that are subjected to constant thermal bombardment by the surrounding particles of the fluid in which the beads are immersed. One may thus wonder whether, at this small scale, thermal forces are significant enough to affect dipole orientation by randomly rotating the beads in solution, thus affecting the alignment of the dipoles within a column. We answer this question by comparing the torque exerted by the external magnetic field on the bead/dipole with the thermal energy $k_B T$.

The torque $\vec{\Gamma}$ exerted by a magnetic field \vec{B} on a magnetic dipole \vec{m} immersed in this field is given by:

$$\vec{\Gamma} = \vec{m} \wedge \vec{B} \quad \text{Eq 2.2.9.}$$

At the weakest field strength $B = 150 \text{ G} = 0.015 \text{ T}$ that we used in our experiments, the magnetic moment of the bead is $m = 0.5 \times 10^{-12} \text{ Am}^2$. The maximal torque exerted by the magnetic field ($\theta = \pi/2$) is then $\Gamma = 7.5 \times 10^{-15} \text{ Nm}$. At a room temperature of 25°C , this torque

is $\sim 2 \times 10^6$ times the value of $k_B T$. The effect of thermal fluctuations on the orientation of the dipole is negligible compared to that of the external magnetic field.

3) Orientation of the individual dipoles in a deflected column

When the magnetic beads interact with the magnetic field to form the columns, they seek to attain the configuration of lowest potential energy by aligning with the external field. However each dipole also generates its own magnetic field which affects the other dipoles in the vicinity. If the column is deflected, we can thus expect two possible configurations (See Figure 2.2.12).

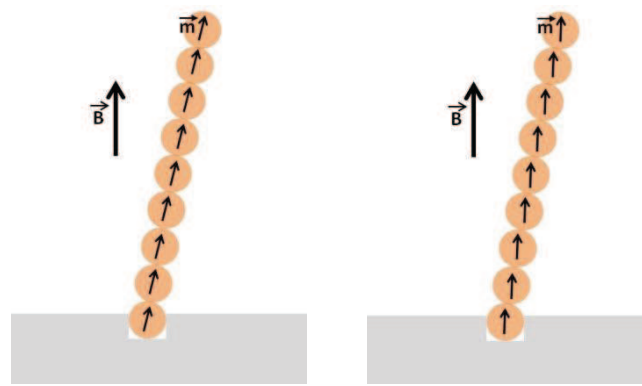


Figure 2.2.12 Left : Dipole-dipole interaction overriding the influence of the external field and the dipoles orient themselves along the field generated by the neighbouring dipoles. Right : Interaction of the dipoles with the external field is higher than dipole-dipole interaction.

If the dipole-dipole interaction is stronger than the interaction of a bead with the external field, the dipoles will orient themselves along the local magnetic field generated by the neighbouring dipoles of the column. Conversely, should the magnetic field prevail over dipole-dipole interaction, the dipoles will preferentially align themselves with the external field. The mechanical properties of the column will depend on which one of those two cases actually occurs. This question can be answered by comparing the torque exerted by a dipole to a neighbouring dipole with the torque exerted by an external magnetic field on a dipole.

We must first consider the magnetic field generated by a dipole 1 on a nearby dipole 2 (See Figure 2.2.9):

$$\vec{B}_{12} = \frac{\mu_0 m_1}{4\pi r^3} (2 \cos \theta \vec{u}_r + \sin \theta \vec{u}_\theta) \quad \text{Eq 2.2.10.}$$

We can then write the torque exerted by dipole 1 on dipole 2 as:

$$\vec{\Gamma}_{12} = \vec{m}_2 \wedge \vec{B}_{12} \quad \text{Eq 2.2.11.}$$

We consider that for maximum torque, the dipoles must be at an angle of $\pi/2$ to each other and at the closest possible distance from each other. Assuming the dipoles are located at the centre of the magnetic beads, and if the two beads are in direct contact, then the minimum distance between the two dipoles r is equal to the diameter d of one bead (4.5 μm). This gives us:

$$\|\vec{\Gamma}_{12}\| = \frac{\sqrt{2}\mu_0 m_1 m_2}{4\pi d^3} \quad \text{Eq 2.2.12.}$$

At 150 G, the torque exerted by dipole 1 on dipole 2 is approximately 4×10^{-16} Nm. When compared, as calculated previously, to the torque $\Gamma = 7.5 \times 10^{-15}$ Nm exerted by the external field on a dipole, we can see that the latter is ~ 20 -fold larger than the dipole-dipole interaction at the weakest magnetic field strength used: the external field prevails over dipole-dipole interaction. The individual dipoles within a column will thus preferentially align with the external field.

4) Stiffness of a column

This section discusses the expected stiffness of magnetic columns, i.e. the property that characterizes its tendency to return to its original position after being deflected at one end. Let us consider a column of N beads deflected through an angle θ and displaced by X at the column's top with respect to the vertical axis. The beads are subjected to a vertical external magnetic field \vec{B} (See Figure 2.2.13). To accord with our experimental results (see ??), we assume here that, for small angles of deflection, the column behaves as a rod that pivots on the first (anchoring) bead.

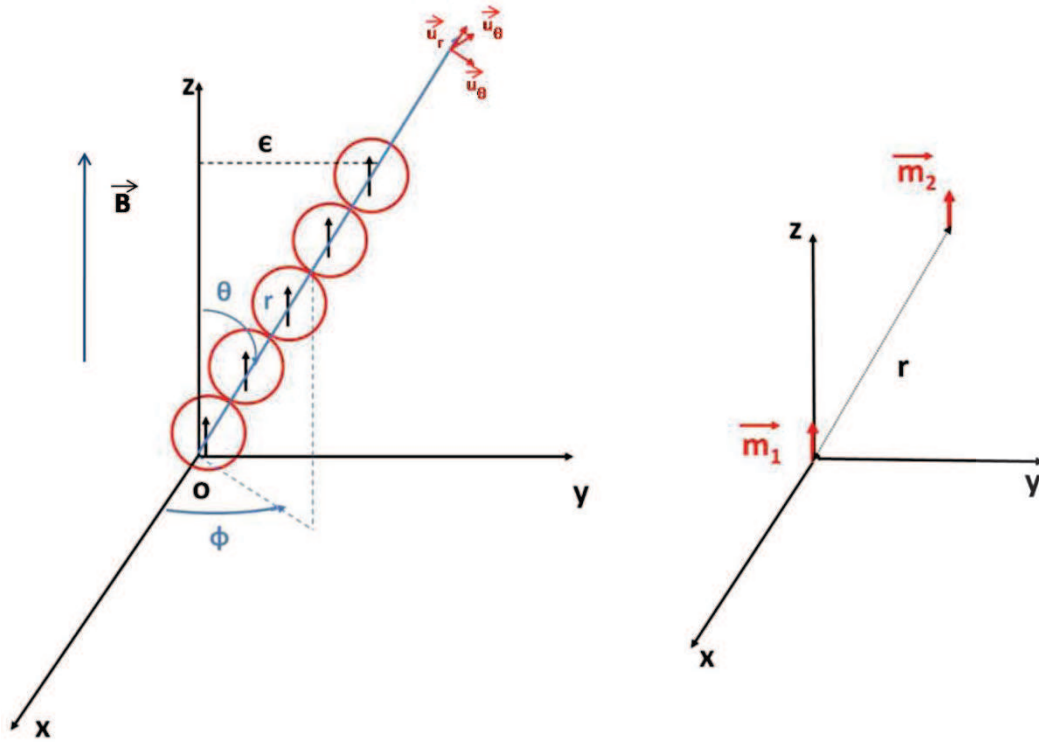


Figure 2.2.13 Left : Column of N beads bent at an angle θ with the vertical axis in an external vertical magnetic field. Right : Diagram showing two dipoles at a distance r from each other.

We now derive an expression for the linear stiffness K . As we have already seen, the individual dipoles are expected to be aligned with the external field. Any given dipole in the alignment is subjected to the magnetic field of the other neighbouring dipoles. In the case of a magnetic bead column, this causes a force which tends to realign the dipoles (beads) with respect to one another and hence the whole column with the vertical magnetic field. The force exerted on the bead 2 (magnetic moment \vec{m}_2) by the magnetic field \vec{B}_{12} created by bead 1 (magnetic moment \vec{m}_1) by definition is given by :

$$\vec{F}_{12} = \vec{\nabla}(\vec{m}_2 \cdot \vec{B}_{12}) \quad \text{Eq 2.2.13.}$$

; where \vec{m}_2 is written : $\vec{m}_2 = m_2(\cos \theta \vec{e}_r - \sin \theta \vec{e}_\theta)$. Using equation 2.2.6, we now have:

$$\vec{m}_2 \cdot \vec{B}_{12} = \frac{\mu_0 m_1 m_2}{8\pi r^3} (3 \cos 2\theta + 1) \quad \text{Eq 2.2.14.}$$

Substituting equation 2.2.14 in equation 2.2.13, we obtain:

$$\vec{F}_{12} = \vec{\nabla}(\vec{m}_2 \cdot \vec{B}_{12}) = -\frac{3\mu_0 m_1 m_2}{8\pi r^4} [(3 \cos 2\theta + 1) \vec{u}_r + 2 \sin 2\theta \vec{u}_\theta] \quad \text{Eq 2.2.15.}$$

From there, we only take the component along unit vector \vec{u}_θ into consideration since it will be responsible for the realignment of the column with the vertical axis and hence the restoring force. The force along \vec{u}_θ can be written as :

$$F_\theta = -\frac{3\mu_0 m_1 m_2}{4\pi r^4} \sin 2\theta \quad \text{Eq 2.2.16.}$$

If the magnetic beads are in direct contact with each other and assuming the centre of the beads as dipoles, the distance r between two dipoles is equal to an integer number of the diameter d of a single bead. We also assume that the magnetic moments of the beads within a column are all equal and can be written as a generic term \vec{m} . Hence, we can write a simplified expression for the force exerted on the topmost bead by the n th bead in the column (with the topmost bead being defined as the first bead).

$$F_n^\theta = -\frac{3\mu_0 m^2}{4\pi (nd)^4} \sin 2\theta \quad \text{Eq 2.2.17.}$$

The total force exerted on the topmost bead is the summation of the forces exerted by all the beads of the column. This total force, which also represents the restoring force of the column to its vertical position is given by:

$$F_{total}^\theta = -\left(\frac{3\mu_0 m^2}{4\pi d^4} \sin 2\theta\right) \sum_{n=1}^{N-1} \frac{1}{n^4} \quad \text{Eq 2.2.18.}$$

The horizontal component of this force can be written as :

$$F_{total}^\theta = -\left(\frac{3\mu_0 m^2}{4\pi d^4} \sin 2\theta \cos \theta\right) \sum_{n=1}^{N-1} \frac{1}{n^4} \quad \text{Eq 2.2.19.}$$

$\sum_{n=1}^{N-1} \frac{1}{n^4}$ is a series which rapidly converges to $S = 1.083$:

$$F_{total}^{\theta} = -\left(\frac{3\mu_0 m^2}{4\pi d^4} \sin 2\theta \cos \theta\right)S \quad \text{Eq 2.2.20.}$$

For small displacements, $\sin \theta \approx \theta \approx \frac{\varepsilon}{L}$ and $\cos \theta \approx 1$. We can then deduce an equation for the stiffness measured at the top of the column :

$$K = \left| \frac{F_{total}^{\theta}}{\varepsilon} \right| = \frac{3\mu_0 m^2}{2\pi d^4 L} S \quad \text{Eq 2.2.21.}$$

The linear stiffness of the column is thus expected to be inversely proportional to its length L . As a consequence, the pivot stiffness $K_p = K \times L^2$ is expected to be proportional to the column length. Because the magnetic moment of the beads depends on the external field, the stiffness should increase with the external magnetic field as the $m^2(B)$. At $B = 150$ G, the magnetic moment of each bead is $m = 0.5 \times 10^{-12}$ A·m². For a 10-bead column, we thus expect a linear stiffness $K \cong 9$ μN/m and a pivoting stiffness $K_p \cong 1.64 \times 10^{-14}$ N·m.

We can then obtain an equation for α , the pivot stiffness per unit length:

$$\alpha = \frac{K_p}{L} = K \times L = \frac{3\mu_0 m^2}{2\pi d^4} S \quad \text{Eq 2.2.22.}$$

Knowing the magnetization curve $m(B)$ of a single bead shown in Figure 2.1.6, we can calculate the variation of the term α with respect to the external magnetic field. As shown in Figure 2.2.14 we get a good agreement between the theory and the measurements, which is quite remarkable considering that there is no adjustable parameter.

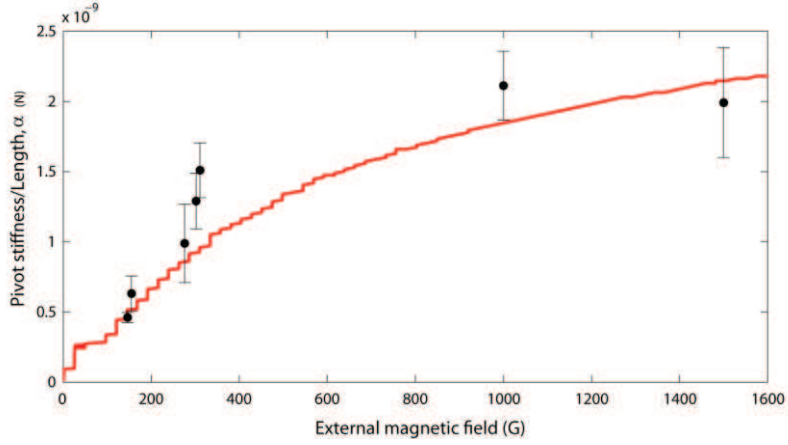


Figure 2.2.14 Variation of α with respect to the external magnetic field. The theoretical expression is drawn in red. The experimental data points are superimposed on the graph for comparison.

5) Linearity of the force-displacement relation

Equation 2.2.15 describes the variation of the force F with respect to the angle of deflection θ . The force exerted at the top of a column varies as $\sin 2\theta$ with a prefactor that depends both on the diameter of the bead ($4.5\mu\text{m}$ in our case) and on the magnetization of the bead in the external field (given by Figure 2.1.6). Considering a column of total height L displaced by an horizontal distance x at the top corresponding to an angle of deflection θ , we can write that $\sin \theta = \frac{x}{L}$. Hence we can write an expression based on equation 2.2.19 for the force F as a function of the displacement of the column x as follows:

$$F(x) = -\frac{\alpha}{2} \sin \left[2 \text{Arcsin} \left(\frac{x}{L} \right) \right] \cos \left[\text{Arcsin} \left(\frac{x}{L} \right) \right] \quad \text{Eq 2.2.23.}$$

We want here to determine the range of displacements x for which the force-displacement relation can be approximated by the linear relation $F_{lin}(x) = -\frac{\alpha}{L} x$ with a deviation that is less than 10% of the true force given by equation 2.2.22.

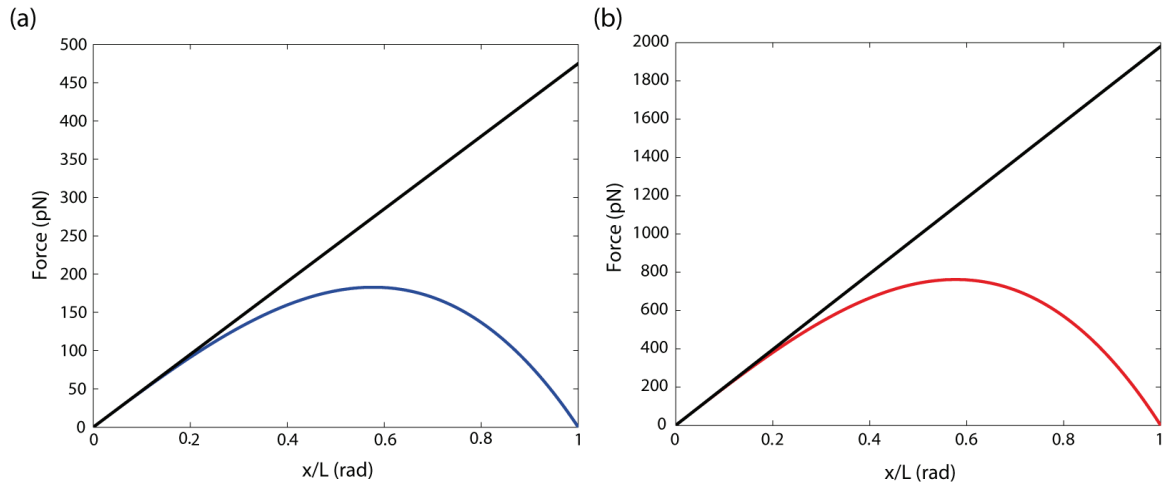


Figure 2.2.15 Plots of force variation with the angle of deflection at 150 G (a) and 1500 G (b)- (black curve). The coloured plots represent the $F(x)$ relation while the black straight lines are the approximated linear relation $F_{lin}(x)$. The dotted arrowed lines show the 10% threshold and show the corresponding angle and forces. At 150G, we have 0.31 rad and ~150 pN and at 1500G, we have 0.31 rad and ~615pN.

On Figure 2.2.15, we compare the force given by equation 2.2.22 to its linear approximation for the lowest and highest magnetic field strengths we have studied, namely 150 and 1500G. The condition $F_{lin} \leq 1.1 \times F$ yields:

$$\frac{x}{L} \leq 31\%$$

In other words, the column behaves as a linear spring as long as it is displaced by a distance x of not more than 31% of its total length, e.g. this means that a 10-bead column can be displaced at its tip by a distance equivalent to approximately four bead diameters. Equivalently, we can write a condition on the external force:

$$F \leq 0.31 \times \alpha$$

Knowing the value of α , linearity is obtained for external forces that are smaller than 150 pN and 615 pN at 150 and 1500 G respectively. It is remarkable to note that while the typical stiffness of our system is rather low (of the order of tens of $\mu\text{N}/\text{m}$), we can conveniently probe a wide range of forces over a wide range of displacements. Moreover, 0.31 rad is approximately equal to 18° which is similar to the angle within which the column does not buckle (20°) as seen in Figure 2.2.5.

6) Friction on a pivoting column

An equation for the friction of a cylinder pivoting in a fluid about a fixed point at one of its end has been proposed by Johannes BAUMGART in his thesis (Baumgart, 2010) based on previous work on the subject (Broersma, 1981). This equation was written to investigate the friction acting on a stereocilium from a hair-cell bundle, which has a similar geometry and can be applied to our magnetic bead columns:

$$\gamma = \frac{4}{3} \pi \eta \frac{L}{\sigma - 1.14 - 0.02\sigma^{-1} - 16\sigma^{-2} + 63\sigma^{-3} - 62\sigma^{-4}} \quad \text{Eq 2.2.24.}$$

, where L is the height of a column, η is the viscosity of the medium – here we consider water i.e. 0.001 Pas, and $\sigma = \ln\left(\frac{2L}{r}\right)$, where $0 < \frac{1}{\sigma} < 0.45$.

In our case, we can express this equation in terms of the number of beads N in a column. The height h where the measurements are performed is equal to L at the top of a column. A general equation for any column made up of beads of any radius r can be written as :

$$L = (N - 1)2r + r = r(2N - 1) \quad \text{Eq 2.2.25.}$$

We can hence rewrite equation 2.2.5:

$$\gamma = \frac{4}{3} \pi \eta \frac{r(2N - 1)}{\sigma - 1.14 - 0.02\sigma^{-1} - 16\sigma^{-2} + 63\sigma^{-3} - 62\sigma^{-4}} \quad \text{Eq 2.2.26.}$$

, where the parameter σ is now written as: $\sigma = \ln[2(2N - 1)]$

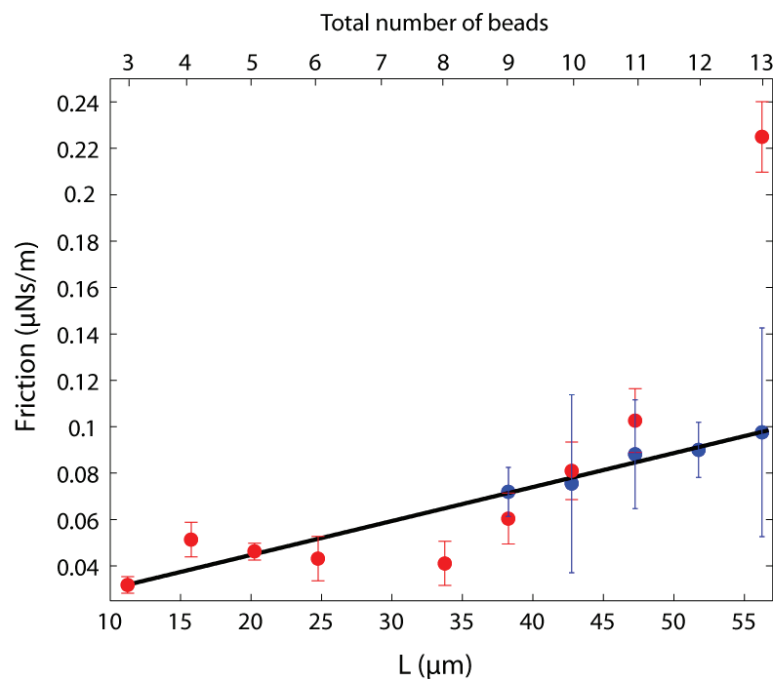


Figure 2.2.16 Theoretical drag coefficient of a solid cylinder (diameter: $4.5\mu\text{m}$) pivoting about one of its ends in water with respect to its length (black line). The experimental data points of drag coefficients of our bead columns were plotted against their heights (at two external magnetic field strengths – 150G in blue and 300G in red) and the plot was superimposed on the theoretical function graph.

Figure 2.2.16 demonstrates that the experimental results on the variation of the friction on the columns with the total length of the columns agree with the theory in the case of a cylinder pivoting about its end in a fluid. This further confirms that the magnetic bead columns can be considered as stiff rigid rods pivoting about their base. The friction coefficient also appears to be independent on the magnetic field in accordance with our findings shown previously (Figure 2.2.7).

C/. Towards biological applications

Now that the mechanical behaviour has been identified and characterized, we can move on to building the actual force sensor. The initial plan was to attach actin filaments or bundles on the topmost bead. We have discussed in Part I about the biotin-streptavidin link that we regularly use to attach the filaments to a silica bead. A similar system could easily be used on magnetic beads. However, the main problem is to attach the bead carrying the actin filament/bundle specifically at the top of the columns.

A solution to this problem is to use functionalized beads to bind actin filaments/bundles and add them to the experimental mix after formation of the columns. To check whether beads added after column formation are located at the summit of the formed columns, we used $1\mu\text{m}$ beads to visually distinguish them from the larger $4.5\mu\text{m}$ beads forming the columns. We have observed that when a suspension of beads of $1\mu\text{m}$ in diameter is added to the observation solution just after formation of the columns, the smaller beads were systematically located at the top of the columns (See Figure 2.2.17) confirming our idea.

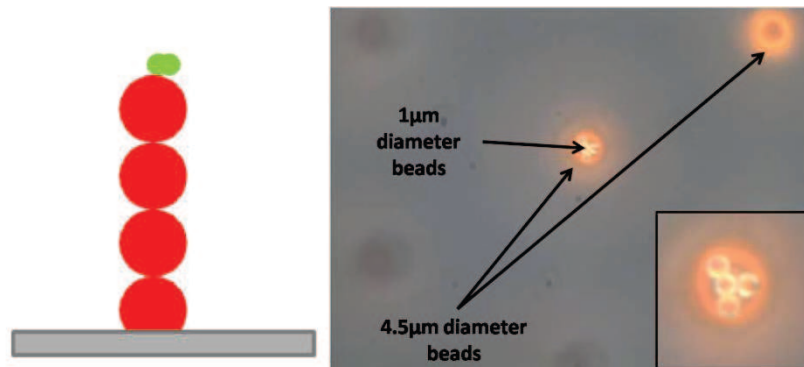


Figure 2.2.17 Left : Diagram of a column of $4.5\mu\text{m}$ beads with the smaller $1\mu\text{m}$ beads on top. Right : a photograph of the same configuration but viewed from the top.

Part II

Chapter III : Discussion & Perspectives

A/. Viability of the magnetic bead columns as force sensors

Could we use bead columns as molecular force sensors to probe the mechanical properties of molecular motors? In typical in-vitro gliding assays, an actin filament interacts with approximately a few tens of motors that exert actively a total force of 5 - 50 pN. Our magnetic columns exhibit a stiffness ranging from 10 $\mu\text{N/m}$ up to 300 $\mu\text{N/m}$, depending on the external magnetic fields (within a range of 150 - 1500 G) and on the height of the column (4 – 16 beads). This range is comparable to that achieved by optical tweezers. For a 10-bead column subjected to an external field of 300 G, we measured a stiffness of approximately 20 $\mu\text{N/m}$ at the column's top. This means that a typical assembly of motors generating a force of 20 pN deflects the column by one micrometer. This deflection can easily be measured using a CCD camera. As long as the deflection remains significantly smaller than half a bead diameter (here 2.25 μm), split photodiodes can also be used but the magnification between sample and imaging planes needs to be adjusted to keep the column movements within the linear range of detection; for a bead of 4.5- μm in diameter, an appropriate magnification would be in the range of $\times 100$ -200. In addition, the column is expected to display linear stiffness as long as the deflection angle remains smaller than $\sim 20^\circ$ (see section A/. 1.2 and B/. 5). Correspondingly, forces up to ~ 600 pN (for a ten-bead column) can in principle be measured at saturation of the bead magnetization. This range is significantly larger than that usually afforded by optical tweezers.

A chief advantage of a magnetic column is that its stiffness can be tuned by varying the external magnetic field without changing the geometrical characteristics (height, diameter) of the column. In practice, the stiffness increases by 4-fold when the field is varied from 150 G to 1500 G. Although a column behaves as a pivot spring, the stiffness of the pivot increases linearly with the column's total length, which contrasts with the behavior of true mechanical pivots. For instance, in the hair-cell bundle, the pivoting stiffness of a stereocilium is set by the bending rigidity of the actin rootlet that anchors the stereocilium into the apical surface of the cell but not on the length of the stereocilium (Howard, 2001). In addition, the friction

coefficient does not appear to depend on the magnetic field and is well described by the friction of a pivoting rod with the same length and diameter as the column. This simple result may seem a priori surprising. Because they magnetize along a preferred axis and remain aligned with the external magnetic field, a pivoting motion of the column must be associated with rotations of the bead to continuously realign the magnetic dipoles. These rotations are expected to create additional friction forces. However, this contribution to friction does not appear to be significant.

A column behaves as a low-pass filter with cutoff frequencies in the range of 30-900 Hz, depending again on the column's length and the magnetic field. Magnetic columns thus appear to be appropriate to monitor the type of motor-driven oscillations that we report in this thesis, with characteristic frequencies of a few hertz. For more dynamic applications, the relatively large friction acting along the column length may become a limitation.

B/. A magnetic column as a biomimetic stereocilium

The unique configuration of magnetic columns makes them interesting candidates in biomimetics. They are already used to build artificial cilia (Coq et al., 2011). Their behaviour as rigid rods pivoting about their base is highly reminiscent of the way an individual rigid stereocilium of a hair-cell bundle pivots on the cell body during mechanical stimulation and spontaneous oscillation (See Figure 2.3.1).

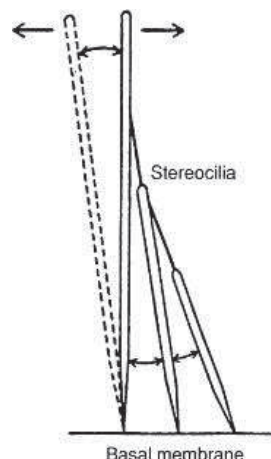


Figure 2.3.1
2007).

Stereocilia of the inner hair cell pivoting about their tapered base (Petrov,

The average stiffness of the whole hair-cell bundle is about $500 \mu\text{N/m}$ (Pascal Martin & Hudspeth, 1999), while that of a single transduction unit (there are ~ 50 units in parallel) is about $10 \mu\text{N/m}$. The latter is comparable to that the column stiffness routinely obtained at 300 G. To match the stiffness of the whole hair-cell bundle, the columns can be rendered stiffer at high fields and by adapting the column's height. The main obstacle would be to create a cooling system that could keep up with the heat build-up in the electromagnet should such a high field be generated. The friction coefficient of the hair bundle (in frogs, with no tip links) is $30 \text{ nN}\cdot\text{s/m}$ (Kozlov et al, 2011), which is only 3-fold smaller than that of a 10-bead column. By combining a field of myosin 1c on opposite pedestals, a rigid actin bundle on the topmost bead and calcium feedback, it could be possible to recreate a biomimetic system of the transduction apparatus of the hair-cell bundle.

C/. Control of the height of the columns

With our current protocol of bead self-assembly, the columns display random lengths. We used this random distribution to study, within one chip, the stiffness and friction coefficient of a column as a function of length. For applications, however, the column's height ought to be precisely controlled to comply with geometrical constrains, e.g. the height of a pedestal with adsorbed molecular motors (Figure 2.0.2), and afford another means to set the sensor stiffness, in addition to varying the magnetic field.

Achieving control over the height of the columns would involve controlling the number of beads within all the columns. This can be done using a modified microfluidic chip with a flexible (PDMS) ceiling.

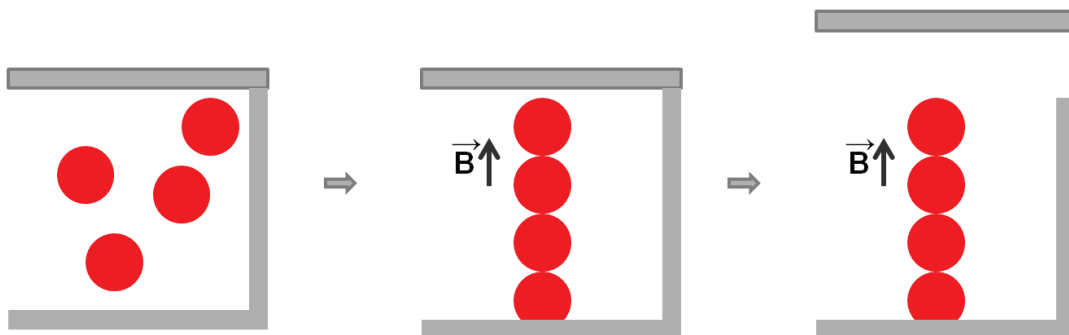


Figure 2.3.2 Diagram of a possible microfluidic set-up to control the height of the columns. The 'ceiling' of the chip could consist of a perpendicular channel where a pressure variation could move the (elastic) ceiling up or down.

The number of beads incorporated in a column can be adjusted by confining the whole chip under a ceiling, thus imposing a limited height and consequently a limited number of beads. The ceiling could be made from a PDMS membrane spread on the network and its vertical position could be controlled by applying positive or negative pressure on it (Figure 2.3.2). This system is based on microfluidic ‘Quake’ valves (Unger, 2000).

D/. Future developments

The perspectives of this work are mostly technological in nature. The first main task is to perfect the Quake valves to control the height of the columns. This would in turn lead to the design and building of a chip containing myosin-covered pedestals to achieve an experimentally ready set-up.

Once this is complete, an actual experiment would require functionalized beads capable of attaching actin filaments. Since these are already routinely produced in the laboratory, the problem would be to orient them towards the myosin-covered surfaces. A directed flow from a syringe pump could effectively orient fluctuating actin filaments in the correct direction.

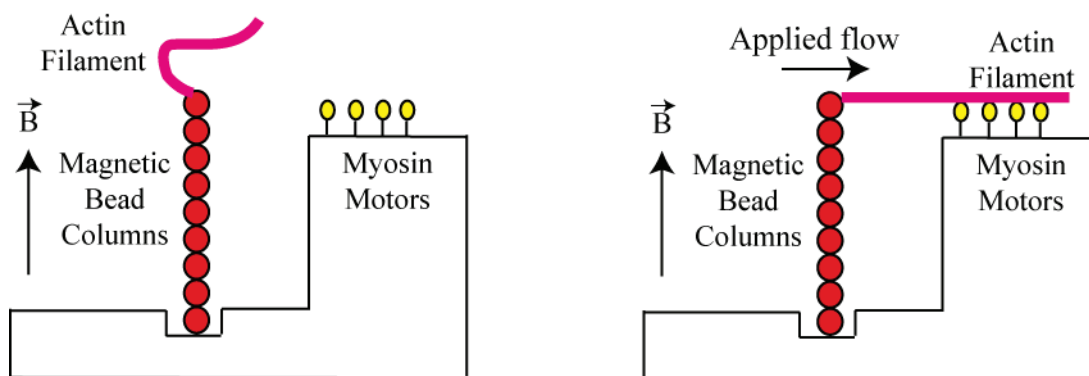


Figure 2.3.3 Diagram showing the possible use of a fluid flow to orient the actin filaments towards the myosin-covered surface in the idealized set-up.

In a sense, bundles due to their stiffer architecture would be easier to manipulate here. However this is a story for later, a perspective for the future, our characterization of the magnetic bead columns as force sensors is done.

Conclusion

A/. Part I: Molecular motor oscillations under elastic loading

At the onset of this thesis, our goal was to expand on the work performed previously (Plaçais, 2008). The spontaneous oscillations of a minimal acto-myosin system were a major breakthrough at the time and demonstrated that the oscillatory behaviour of many biological systems arise from an intrinsic oscillatory instability of motor collections under elastic loading. However, the parameters controlling shape of the waveform or the frequency are not yet experimentally characterized. Potential control parameters are the stiffness of the acto-myosin system, the number of engaged motors and the total force production of the active motor ensembles as well as the specific motors type. To investigate the effect of these parameters on the oscillations, the assay was further developed in this thesis along several lines

We have demonstrated that stiff polarized actin bundles could oscillate when driven by myosin II motors with an elastic load applied, making them interesting to study the effects of a stiffer system on the oscillation characteristics. However, our statistics on such events are low, and while still a promising venture that will be explored, the conclusions here are not clear. Moreover, our optical trap will need to be strengthened to retain the ‘stronger’ bundles i.e. the ones that engage a large number of motors and consequently are subjected to forces that are beyond the escape force of our trap.

And finally, we made a major achievement towards testing how the oscillations depend on the specific myosin type used. We succeeded in purifying fully functional myosin 1b in our laboratory. The perspectives will be to use myosin 1b in place of myosin II in the elastic loading experiment with the optical tweezers. This brings us closer to the final goal of a reconstitution of motor driven hair bundle oscillations with our *in vitro* system since myosin1b is a homologue of the hair bundle myosin1c.

B/. Part II: Auto-assembled magnetic bead columns as force sensors

The idea behind this project was to overcome the shortcomings of the optical tweezers namely the inability to probe a large number of molecular events. The auto-assembled magnetic bead columns were of great interest due to their mechanical properties and the possibility to organize them in relatively large arrays, hence the possibility to turn them into high throughput force sensors, able to probe a large number of molecular motor events at the same time. In this study, we characterized the mechanical behaviour and properties of the magnetic bead columns and discussed their viability as molecular force sensors.

Throughout this study, we have characterized the general mechanical behaviour of a bead column, successfully modelling them as rigid rods pivoting over their bases. As a side note, this unique property makes them suitable to potentially emulate the stereocilia of the hair cell bundle. We have also uncovered the parameters influencing the horizontal stiffness and the pivot stiffness such as the external magnetic field and the length of the column. Moreover our experimental results agreed remarkably well with the equations obtained from a theoretical study of the system.

We have demonstrated that the typical stiffnesses and time constants of the columns were in the appropriate range to probe molecular motor events and oscillations. In addition, the range of forces available is considerably larger than the typical force range of optical tweezers.

Having characterized the magnetic bead columns as viable force sensors to study forces exerted by molecular motors and motor-driven oscillations, the perspectives of this work are to successfully develop the technology to actually use them as high throughput molecular force sensors.

APPENDIX

List of buffer composition

G-buffer

Tris-HCl pH 8.0: 5 mM
CaCl₂: 0.2 mM
ATP : 0.2 mM
5% sucrose
5% dextran

F-buffer

Tris-HCl pH 7.4: 50 mM
KCl: 50 mM
MgCl₂: 1 mM
CaCl₂: 0.2 mM
DTT: 0.5 mM

Assay Buffer (AB)

Imidazole-HCl pH 7.4: 50 mM
KCl: 25 mM
MgCl₂: 4 mM
EGTA: 1 mM

AB-BSA

AB
BSA: 1 mg/mL

AB-GOC

AB
Glucose oxidase: 0.4 mg/mL
Catalase: 0.1 mg/mL
DTT: 40 mM
Glucose: 9 mg/mL

AB-GOC-CP

AB-GOC
Creatine Phosphate: 2 mM
Creatine Phosphokinase: 0.1 mg/mL

MES buffer

MES buffer pH 6: 50 mM

Borate buffer

Borate buffer pH 8.5

2× buffer

Hepes-HCl pH 7.5: 60 mM

KCl: 300 mM

MgCl₂: 8 mM

EGTA pH 7.5: 2 mM

Lysate buffer

2× buffer: 50% of final volume

Triton: 1%

ATP: 4 mM

DTT: 1mM

Protease Inhibitor Cocktail (PIC): 0.1% of final volume

Elution buffer

2× buffer: 50% of final volume

Methyl cellulose: 0.1%

ATP: 4 mM

DTT: 1 mM

PIC: 0.1% of final volume

Dialysis buffer

2× buffer: 50% of final volume

Methyl cellulose: 0.1%

ATP: 1 mM

DTT: 1 mM

PIC: 0.1% of final volume

Bibliography

- Adamek, N., Coluccio, L. M., & Geeves, M. A. (2008). Calcium sensitivity of the cross-bridge cycle of Myo1c, the adaptation motor in the inner ear. *Proc Natl Acad Sci U S A*, 105(15), 5710–5715.
- Alberts, B. (1994). *Molecular biology of the cell 4th edition*.
- Albet-Torres, N., O'Mahony, J., Charlton, C., Balaz, M., Lisboa, P., Aastrup, T., Månsson, A., et al. (2007). Mode of heavy meromyosin adsorption and motor function correlated with surface hydrophobicity and charge. *Langmuir : the ACS journal of surfaces and colloids*, 23(22), 11147–56. doi:10.1021/la7008682
- Batters, C., Arthur, C. P., Lin, A., Porter, J., Geeves, M. A., Milligan, R. A., Molloy, J. E., et al. (2004). Myo1c is designed for the adaptation response in the inner ear. *Embo J*, 23(7), 1433–1440.
- Batters, C., Wallace, M. I., Coluccio, L. M., & Molloy, J. E. (2004). A model of stereocilia adaptation based on single molecule mechanical studies of myosin I. *Philos Trans R Soc Lond B Biol Sci*, 359(1452), 1895–1905.
- Baumgart, J. (2010). *The Hair Bundle: Fluid-Structure Interaction in the Inner Ear*.
- Blanchoin, L., Pollard, T. D., & Mullins, R. D. (2000). Interactions of ADF/cofilin, Arp2/3 complex, capping protein and profilin in remodeling of branched actin filament networks. *Curr Biol*, 10(20), 1273–1282.
- Bourdieu, L., Magnasco, M. O., Winkelmann, D. A., & Libchaber, A. (1995). Actin filaments on myosin beds: The velocity distribution. *Phys Rev E Stat Phys Plasmas Fluids Relat Interdiscip Topics*, 52(6), 6573–6579.
- Brangbour, C., du Roure, O., Helfer, E., Démoulin, D., Mazurier, A., Fermigier, M., Carlier, M.-F., et al. (2011). Force-velocity measurements of a few growing actin filaments. *PLoS biology*, 9(4), e1000613. doi:10.1371/journal.pbio.1000613
- Bray, D., & White, J. G. (1988). Cortical flow in animal cells. *Science*, 239(4842), 883–888.
- Brenner, B., Schoenberg, M., Chalovich, J. M., Greene, L. E., & Eisenberg, E. (1982). Evidence for cross-bridge attachment in relaxed muscle at low ionic strength. *Proceedings of the National Academy of Sciences of the United States of America*, 79(23), 7288–91.
- Broersma, S. (1981). Viscous force and torque constants for a cylinder. *Journal of chemical physics*, 74(12).

- Capitanio, M., Canepari, M., Cacciafesta, P., Lombardi, V., Cicchi, R., Maffei, M., Pavone, F. S., et al. (2006). Two independent mechanical events in the interaction cycle of skeletal muscle myosin with actin. *Proc Natl Acad Sci U S A*, *103*(1), 87–92.
- Claudia Veigel, Stephan Schmitz, F. W. & J. R. S. (2005). Load-dependent kinetics of myosin-V can explain its high processivity. *Nature Cell Biology*, (7), 861 – 869.
- Cooke, R. (1997). Actomyosin interaction in striated muscle. *Physiol Rev*, *77*(3), 671–697.
- Cooke, R., & Pate, E. (1985). The effects of ADP and phosphate on the contraction of muscle fibers. *Biophys J*, *48*(5), 789–798.
- Coq, N., Bricard, A., Delapierre, F.-D., Malaquin, L., du Roure, O., Fermigier, M., & Bartolo, D. (2011). Collective Beating of Artificial Microcilia. *Physical Review Letters*, *107*(1), 1–4. doi:10.1103/PhysRevLett.107.014501
- Corey, D. P., & Hudspeth, A. J. (1983). Kinetics of the receptor current in bullfrog saccular hair cells. *J. Neurosci.*, *3*(5), 962–976.
- De La Cruz, E. M., & Ostap, E. M. (2004). Relating biochemistry and function in the myosin superfamily. *Curr Opin Cell Biol*, *16*(1), 61–67.
- Edman, K. A. (1988). Double-hyperbolic force-velocity relation in frog muscle fibres. *J Physiol*, *404*, 301–321.
- Edman, K. A., Mulieri, L. A., & Scubon-Mulieri, B. (1976). Non-hyperbolic force-velocity relationship in single muscle fibres. *Acta Physiol Scand*, *98*(2), 143–156.
- Endo, M. (1972). Stretch-induced increase in activation of skinned muscle fibres by calcium. *Nat New Biol*, *237*(76), 211–213.
- Fabiato, A., & Fabiato, F. (1978). Myofilament-generated tension oscillations during partial calcium activation and activation dependence of the sarcomere length-tension relation of skinned cardiac cells. *J Gen Physiol*, *72*(5), 667–699.
- Fenn, W. (1923). A QUANTITATIVE COMPARISON BETWEEN THE ENERGY LIBERATED AND THE WORK PERFORMED BY THE ISOLATED SARTORIUS MUSCLE OF THE FROG., (4).
- Finer, J. T., Simmons, R. M., & Spudich, J. A. (1994). Single myosin molecule mechanics: piconewton forces and nanometre steps. *Nature*, *368*(6467), 113–119.
- Fonnum, G., Johansson, C., Molteberg, A., Mørup, S., & Aksnes, E. (2005). Characterisation of Dynabeads® by magnetization measurements and Mössbauer spectroscopy. *Journal of Magnetism and Magnetic Materials*, *293*(1), 41 – 47.
- Ford, L. E., Huxley, A. F., & Simmons, R. M. (1985). Tension transients during steady shortening of frog muscle fibres. *J Physiol*, *361*, 131–150.

- Fukuda, N., Fujita, H., Fujita, T., & Ishiwata, S. (1996). Spontaneous tension oscillation in skinned bovine cardiac muscle. *Pflugers Arch*, 433(1-2), 1–8.
- Galbraith C, S. M. (1997). A micromachined device provides a new bend on fibroblast. *Biophysical journal*, 94(August), 9114–9118.
- Geeves, M. A., & Holmes, K. C. (1999). Structural mechanism of muscle contraction. *Annu Rev Biochem*, 68, 687–728.
- Gijs, M. a M., Lacharme, F., & Lehmann, U. (2010). Microfluidic applications of magnetic particles for biological analysis and catalysis. *Chemical reviews*, 110(3), 1518–63. doi:10.1021/cr9001929
- Gillespie, P. G., & Corey, D. P. (1997). Myosin and adaptation by hair cells. *Neuron*, 19(5), 955–8.
- Gillespie, P. G., & Cyr, J. L. (2004). Myosin-1c, the hair cell's adaptation motor. *Annu Rev Physiol*, 66, 521–545.
- Gittes, F., Mickey, B., Nettleton, J., & Howard, J. (1993). Flexural rigidity of microtubules and actin filaments measured from thermal fluctuations in shape. *J Cell Biol*, 120(4), 923–934.
- Gordon, A. M., Huxley, A. F., & Julian, F. J. (1966). The variation in isometric tension with sarcomere length in vertebrate muscle fibres. *J Physiol*, 184(1), 170–192.
- Greenberg, M. J., Lin, T., Goldman, Y. E., Shuman, H., & Ostap, E. M. (2012). Myosin IC generates power over a range of loads via a new tension-sensing mechanism. *Proceedings of the National Academy of Sciences of the United States of America*, 109(37), E2433–40. doi:10.1073/pnas.1207811109
- Guo, B., & Guilford, W. H. (2006). Mechanics of actomyosin bonds in different nucleotide states are tuned to muscle contraction. *Proc Natl Acad Sci U S A*, 103(26), 9844–9849.
- Haviv, L., Gillo, D., Backouche, F., & Bernheim-Groswasser, A. (2008). A cytoskeletal demolition worker: myosin II acts as an actin depolymerization agent. *J Mol Biol*, 375(2), 325–330.
- Houdusse, a, Silver, M., & Cohen, C. (1996). A model of Ca(2+)-free calmodulin binding to unconventional myosins reveals how calmodulin acts as a regulatory switch. *Structure (London, England : 1993)*, 4(12), 1475–90.
- Howard, J. (2001). *Mechanics of Motor Proteins and the Cytoskeleton*. Sunderland, MA: Sinauer Associates.
- Howard, J., & Ashmore, J. . (1986). Stiffness of sensory hair bundles in the sacculus of the frog. *Hearing Research*, 23(1), 93 – 104.
- Howard, J., Hudspeth, A. J., & Vale, R. D. (1989). Movement of microtubules by single kinesin molecules. *Nature*, 342(6246), 154–158.

- Hudspeth, A. J., & Gillespie, P. G. (1994). Pulling springs to tune transduction: adaptation by hair cells. *Neuron*, *12*(1), 1–9.
- Huxley, A. F. (1957). Muscle structure and theories of contraction. *Prog Biophys Biophys Chem*, *7*, 255 – 318.
- Huxley, A. F. (1974). Muscular contraction. *J Physiol*, *243*(1), 1–43.
- Huxley, A. F., & Simmons, R. M. (1971). Proposed mechanism of force generation in striated muscle. *Nature*, *233*(5321), 533–538.
- Isambert, H., Venier, P., Maggs, A. C., Fattoum, A., Kassab, R., Pantaloni, D., & Carlier, M. F. (1995). Flexibility of actin filaments derived from thermal fluctuations. Effect of bound nucleotide, phalloidin, and muscle regulatory proteins. *J Biol Chem*, *270*(19), 11437–11444.
- Ishijima, A., Kojima, H., Higuchi, H., Harada, Y., Funatsu, T., & Yanagida, T. (1996). Multiple- and single-molecule analysis of the actomyosin motor by nanometer-piconewton manipulation with a microneedle: unitary steps and forces. *Biophys J*, *70*(1), 383–400.
- Ishikawa, R., Sakamoto, T., Ando, T., Higashi-Fujime, S., & V in vitro. II and myosin Kohama, K. (2003). Polarized actin bundles formed by human fascin-1: their sliding and disassembly on myosin *Journal of Neurochemistry*, *87*(3), 676–685. doi:10.1046/j.1471-4159.2003.02058.x
- Ishiwata, S., Shimamoto, Y., Suzuki, M., & Sasaki, D. (2007). Regulation of muscle contraction by Ca²⁺ and ADP: focusing on the auto-oscillation (SPOC). *Adv Exp Med Biol*, *592*, 341–358.
- Ishiwata, S, Funatsu T, F. H. (1998). Contractile properties of thin (actin) filament-reconstituted muscle fibers. *Adv Exp Med Biol*, (453), 319 – 328.
- James D. Jontes, E. M. W.-K. & R. A. M. (1995). A 32° tail swing in brush border myosin I on ADP release. *Nature*, (378), 751 – 753.
- Joseph M. Laakso, John H. Lewis, Henry Shuman, E. M. O. (2008). Myosin I Can Act As a Molecular Force Sensor. *Science*, *321*, 133 – 136.
- Jülicher, F., & Prost, J. (1995). Cooperative molecular motors. *Phys. Rev. Lett.*, *75*(13), 2618–2621.
- Jülicher, F., & Prost, J. (1997). Spontaneous oscillations of collective molecular motors. *Phys. Rev. Lett.*, *78*(23), 4510–4513.
- Kojima, H., Ishijima, A., & Yanagida, T. (1994). Direct measurement of stiffness of single actin filaments with and without tropomyosin by in vitro nanomanipulation. *Proceedings of the National Academy of Sciences of the United States of America*, *91*(26), 12962–6.

- Kron, S. J., & Spudich, J. A. (1986). Fluorescent actin filaments move on myosin fixed to a glass surface. *Proc Natl Acad Sci U S A*, *83*(17), 6272–6276.
- Le Nel, A., Minc, N., Smadja, C., Slovakova, M., Bilkova, Z., Peyrin, J.-M., Viovy, J.-L., et al. (2008). Controlled proteolysis of normal and pathological prion protein in a microfluidic chip. *Lab on a chip*, *8*(2), 294–301. doi:10.1039/b715238h
- Lewalle, A., Steffen, W., Stevenson, O., Ouyang, Z., & Sleep, J. (2008). Single-molecule measurement of the stiffness of the rigor myosin head. *Biophysical journal*, *94*(6), 2160–9. doi:10.1529/biophysj.107.119396
- Lewis, J. H., Greenberg, M. J., Laakso, J. M., Shuman, H., & Ostap, E. M. (2012). Calcium regulation of myosin-I tension sensing. *Biophysical journal*, *102*(12), 2799–807. doi:10.1016/j.bpj.2012.05.014
- Lewis, J. H., Lin, T., Hokanson, D. E., & Ostap, E. M. (2006). Temperature dependence of nucleotide association and kinetic characterization of myo1b. *Biochemistry*, *45*(38), 11589–97. doi:10.1021/bi0611917
- Linari, M., Caremani, M., Piperio, C., Brandt, P., & Lombardi, V. (2007). Stiffness and fraction of Myosin motors responsible for active force in permeabilized muscle fibers from rabbit psoas. *Biophysical journal*, *92*(7), 2476–90. doi:10.1529/biophysj.106.099549
- Lowey, S., Slayter, H. S., Weeds, A. G., & Baker, H. (1969). Substructure of the myosin molecule. I. Subfragments of myosin by enzymic degradation. *J Mol Biol*, *42*(1), 1–29.
- Malaquin, L., Kraus, T., Schmid, H., Delamarque, E., & Wolf, H. (2007). Controlled particle placement through convective and capillary assembly. *Langmuir : the ACS journal of surfaces and colloids*, *23*(23), 11513–21. doi:10.1021/la700852c
- Manceva, S., Lin, T., Pham, H., Lewis, J. H., Goldman, Y. E., & Ostap, E. M. (2007). Calcium regulation of calmodulin binding to and dissociation from the myo1c regulatory domain. *Biochemistry*, *46*(42), 11718–26. doi:10.1021/bi700894h
- Margossian, S. S., & Lowey, S. (1982). Preparation of myosin and its subfragments from rabbit skeletal muscle. *Methods Enzymol*, *85 Pt B*, 55–71.
- Martin, P., Bozovic, D., Choe, Y., & Hudspeth, A. J. (2003). Spontaneous oscillation by hair bundles of the bullfrog's sacculus. *J Neurosci*, *23*(11), 4533–4548.
- Martin, P., & Hudspeth, A. J. (2001). Compressive nonlinearity in the hair bundle's active response to mechanical stimulation. *Proc. Natl. Acad. Sci. USA*, *98*(25), 14386–14391. Retrieved from <http://www.pnas.org/cgi/content/abstract/98/25/14386>
- Martin, P., Hudspeth, A. J., & Jülicher, F. (2001). Comparison of a hair bundle's spontaneous oscillations with its response to mechanical stimulation reveals the underlying active process. *Proc. Natl. Acad. Sci. USA*, *98*(25), 14380–14385.

- Martin, P, Mehta, A. D., & Hudspeth, A. J. (2000). Negative hair-bundle stiffness betrays a mechanism for mechanical amplification by the hair cell. *Proc. Natl. Acad. Sci. USA*, *97*(22), 12026–12031.
- Martin, P. (2008). Active processes and otoacoustic emissions in hearing. *Active processes and otoacoustic emissions in hearing*.
- Martin, Pascal, & Hudspeth, A. J. (1999). Active hair-bundle movements can amplify a hair cell's response to oscillatory mechanical stimuli. *Proc. Natl. Acad. Sci. USA*, *96*(25), 14306–14311.
- Mehta, A. D., Finer, J. T., & Spudich, J. A. (1997). Detection of single-molecule interactions using correlated thermal diffusion. *Proc Natl Acad Sci U S A*, *94*(15), 7927–7931.
- Mohamadi, M. R., Svobodova, Z., Verpillot, R., Esselmann, H., Wiltfang, J., Otto, M., Taverna, M., et al. (2010). Microchip electrophoresis profiling of A β peptides in the cerebrospinal fluid of patients with Alzheimer's disease. *Analytical chemistry*, *82*(18), 7611–7. doi:10.1021/ac101337n
- Molloy, J. E., Burns, J. E., Sparrow, J. C., Tregear, R. T., Kendrick-Jones, J., & White, D. C. (1995). Single-molecule mechanics of heavy meromyosin and S1 interacting with rabbit or *Drosophila* actins using optical tweezers. *Biophys J*, *68*(4 Suppl), 298S–303S; 303S–305S.
- Neuman, K. C., & Block, S. M. (2004). Optical trapping. *Rev Sci Instrum*, *75*(9), 2787–2809.
- Nishizaka, T., Seo, R., Tadakuma, H., Kinoshita Jr., K., & Ishiwata, S. (2000). Characterization of single actomyosin rigor bonds: load dependence of lifetime and mechanical properties. *Biophys J*, *79*(2), 962–974.
- Oiwa, K., Chaen, S., Kamitsubo, E., Shimmen, T., & Sugi, H. (1990). Steady-state force-velocity relation in the ATP-dependent sliding movement of myosin-coated beads on actin cables in vitro studied with a centrifuge microscope. *Proc Natl Acad Sci U S A*, *87*(20), 7893–7897.
- Okamura, N., & Ishiwata, S. (1988). Spontaneous oscillatory contraction of sarcomeres in skeletal myofibrils. *J Muscle Res Cell Motil*, *9*(2), 111–119.
- Petrov, A. (2007). Flexoelectricity and Mechanotransduction. *Current Topics in Membranes*, *58*, 121 – 150.
- Plastino, J., & Sykes, C. (2005). The actin slingshot. *Curr Opin Cell Biol*, *17*(1), 62–66.
- Plaçaïs, P.-Y. (2008). *Propriétés mécaniques de la myosine II in vitro : de la molécule unique aux effets collectifs*.
- Plaçaïs, P.-Y., Balland, M., Guérin, T., Joanny, J.-F., & Martin, P. (2009). Spontaneous Oscillations of a Minimal Actomyosin System under Elastic Loading. *Physical Review Letters*, *103*(15), 1–4. doi:10.1103/PhysRevLett.103.158102

- Pollard, T. D., Doberstein, S. K., & Zot, H. G. (1991). Myosin-I. *Annual review of physiology*, 53, 653–81. doi:10.1146/annurev.ph.53.030191.003253
- Pringle, J. W. (1978). The Croonian Lecture, 1977. Stretch activation of muscle: function and mechanism. *Proc R Soc Lond B Biol Sci*, 201(1143), 107–130.
- Rayment, I., Rypniewski, W. R., Schmidt-bdse, K., Smith, R., Tomchick, D. R., Benning, M. M., Winkelmann, D. A., et al. (1993). Three-Dimensional Structure of.
- Reymann, A.-C., Boujemaa-Paterski, R., Martiel, J.-L., Guérin, C., Cao, W., Chin, H. F., De La Cruz, E. M., et al. (2012). Actin network architecture can determine myosin motor activity. *Science (New York, N.Y.)*, 336(6086), 1310–4. doi:10.1126/science.1221708
- Riveline, D., Ott, A., Julicher, F., Winkelmann, D. A., Cardoso, O., Lacapere, J. J., Magnusdottir, S., et al. (1998). Acting on actin: the electric motility assay. *Eur. Biophys. J.*, 27(4), 403–408.
- Ruff, C., Furch, M., Brenner, B., Manstein, D. J., & Meyhofer, E. (2001). Single-molecule tracking of myosins with genetically engineered amplifier domains. *Nat Struct Biol*, 8(3), 226–229.
- Ruppert, C., Kroschewski, R., & Bähler, M. (1993). Identification, characterization and cloning of myr 1, a mammalian myosin-I. *The Journal of cell biology*, 120(6), 1393–403.
- Salbreux, G., Joanny, J. F., Prost, J., & Pullarkat, P. (2007). Shape oscillations of non-adhering fibroblast cells. *Phys Biol*, 4(4), 268–284.
- Saliba, A.-E., Saias, L., Psychari, E., Minc, N., Simon, D., Bidard, F.-C., Mathiot, C., et al. (2010). Microfluidic sorting and multimodal typing of cancer cells in self-assembled magnetic arrays. *Proceedings of the National Academy of Sciences of the United States of America*, 107(33), 14524–9. doi:10.1073/pnas.1001515107
- Sellers, J. R., & Veigel, C. (2010). Direct observation of the myosin-Va power stroke and its reversal. *Nature structural & molecular biology*, 17(5), 590–5. doi:10.1038/nsmb.1820
- Shimamoto, Y., Kono, F., Suzuki, M., & Ishiwata, S. (2007). Nonlinear force-length relationship in the ADP-induced contraction of skeletal myofibrils. *Biophys J*, 93(12), 4330–4341.
- Shimizu, H., Fujita, T., & Ishiwata, S. (1992). Regulation of tension development by MgADP and Pi without Ca²⁺. Role in spontaneous tension oscillation of skeletal muscle. *Biophys J*, 61(5), 1087–1098.
- Spudich, J. A. (2001). The myosin swinging cross-bridge model. *Nat Rev Mol Cell Biol*, 2(5), 387–392.
- Stauffer, E. A., Scarborough, J. D., Hirono, M., Miller, E. D., Shah, K., Mercer, J. A., Holt, J. R., et al. (2005). Fast adaptation in vestibular hair cells requires myosin-1c activity. *Neuron*, 47(4), 541–553.

- Takagi, Y., Homsher, E. E., Goldman, Y. E., & Shuman, H. (2006). Force generation in single conventional actomyosin complexes under high dynamic load. *Biophys J*, *90*(4), 1295–1307.
- Tan, J. L., Tien, J., Pirone, D. M., Gray, D. S., Bhadriraju, K., & Chen, C. S. (2003). Cells lying on a bed of microneedles: an approach to isolate mechanical force. *Proceedings of the National Academy of Sciences of the United States of America*, *100*(4), 1484–9. doi:10.1073/pnas.0235407100
- Tsuda, Y., Yasutake, H., Ishijima, A., & Yanagida, T. (1996). Torsional rigidity of single actin filaments and actin-actin bond breaking force under torsion measured directly by in vitro micromanipulation. *Proc Natl Acad Sci U S A*, *93*(23), 12937–12942.
- Unger, M. a. (2000). Monolithic Microfabricated Valves and Pumps by Multilayer Soft Lithography. *Science*, *288*(5463), 113–116. doi:10.1126/science.288.5463.113
- Veigel, C, Bartoo, M. L., White, D. C., Sparrow, J. C., & Molloy, J. E. (1998). The stiffness of rabbit skeletal actomyosin cross-bridges determined with an optical tweezers transducer. *Biophys J*, *75*(3), 1424–1438.
- Veigel, C, Coluccio, L. M., Jontes, J. D., Sparrow, J. C., Milligan, R. A., & Molloy, J. E. (1999). The motor protein myosin-I produces its working stroke in two steps. *Nature*, *398*(6727), 530–533.
- Veigel, C, Molloy, J. E., Schmitz, S., & Kendrick-Jones, J. (2003). Load-dependent kinetics of force production by smooth muscle myosin measured with optical tweezers. *Nat Cell Biol*, *5*(11), 980–986.
- Veigel, C, von Maydell, R. D., Kress, K. R., Molloy, J. E., & Fink, R. H. (1998). The effect of ionic strength on the kinetics of rigor development in skinned fast-twitch skeletal muscle fibres. *Pflugers Arch*, *435*(6), 753–761.
- Veigel, Claudia, Coluccio, L. M., Jontes, J. D., Sparrow, J. C., Milligan, R. A., & Molloy, J. E. (1999). letters to nature The motor protein myosin-I produces its working stroke in two steps, *398*(April), 530–533.
- Whittaker, M., Wilson-Kubalek, E. M., Smith, J. E., Faust, L., Milligan, R. A., & Sweeney, H. L. (1995). A 35-A movement of smooth muscle myosin on ADP release. *Nature*, *378*(6558), 748–751.
- Winkelmann, D. A., Bourdieu, L., Ott, A., Kinoshita, F., & Libchaber, A. (1995). Flexibility of myosin attachment to surfaces influences F-actin motion. *Biophys J*, *68*(6), 2444–2453.
- Wu, Y. C., Ricci, A. J., & Fettkoppe, R. (1999). Two components of transducer adaptation in auditory hair cells. *J. Neurophysiol.*, *82*(5), 2171–2181.
- Yasuda, K., Shindo, Y., & Ishiwata, S. (1996). Synchronous behavior of spontaneous oscillations of sarcomeres in skeletal myofibrils under isotonic conditions. *Biophys. J.*, *70*(4), 1823–1829.

- Yoko Yano Toyoshima, Stephen J. Kron, Elizabeth M. McNally*, Kenneth R. Niebling, C. T. & J. A. S. (1987). Myosin subfragment-1 is sufficient to move actin filaments in vitro. *Nature*, 328, 536–539.
- Zhu, T., Beckingham, K., & Ikebe, M. (1998). High affinity Ca²⁺ binding sites of calmodulin are critical for the regulation of myosin I beta motor function. *The Journal of biological chemistry*, 273(32), 20481–6.
- Zot, H. G., Doberstein, S. K., & Pollard, T. D. (1992). Myosin-I moves actin filaments on a phospholipid substrate: implications for membrane targeting. *The Journal of cell biology*, 116(2), 367–76.
- du Roure, O., Saez, A., Buguin, A., Austin, R. H., Chavrier, P., Silberzan, P., Siberzan, P., et al. (2005). Force mapping in epithelial cell migration. *Proceedings of the National Academy of Sciences of the United States of America*, 102(7), 2390–5.
doi:10.1073/pnas.0408482102

SUMMARY

Recent studies have suggested that minimal actomyosin systems have the intrinsic property to oscillate when subjected to an elastic load. A similar situation can be found in various biological systems, leading, both in-vivo and in-vitro, to spontaneous oscillations. In particular, muscular systems as well as mechanosensitive hair-cell bundles in the inner ear have been shown to oscillate spontaneously as the result of active force production by an acto-myosin protein complex. We attempt to shed light on the mechanism behind the oscillatory activity of the acto-myosin system, in particular by determining the parameters that control the frequency and amplitude of oscillation. The stiffness of the system, the total force developed by the motors and the type of motors have been proposed as being influential in this respect. To investigate this effect, we make use of a modified motility assay consisting of a motor-driven stiff polarized actin bundle subjected to an elastic load provided by optical tweezers. During the course of this work, we also characterized auto-assembled magnetic bead columns and assessed their viability as molecular force sensors to study the oscillations. The fact that they can easily be organized into large arrays makes them interesting as potential 'high-throughput' force sensors.